Delamination Initiation in Postbuckled Dropped-Ply Laminates

by

Carlos G. Dávila

Dissertation submitted to the Faculty of the

Virginia Polytechnic Institute and State University

in partial fulfillment of the requirements for the degree of

Doctor of Philosophy

in

Aerospace Engineering

APPROVED:

Eric R. Johnson, Chairman

Raphael T. Haftka

Michael W. Hyer

Rakesh K. Kapania

Junuthula N. Reddy

November 21, 1991

Blacksburg, Virginia

Delamination Initiation in Postbuckled Dropped-Ply Laminates

by

Carlos G. Dávila

Eric R. Johnson, Chairman

Aerospace Engineering

(ABSTRACT)

The compression strength of dropped-ply, graphite-epoxy laminated plates for the delamination mode of failure is studied by analysis and corroborated with experiments. The nonlinear response of the test specimens is modeled by a geometrically nonlinear finite element analysis. The methodology for predicting delamination is based on a quadratic interlaminar stress criterion evaluated at a characteristic distance from the ply drop-off.

The details of the complex state of stress in the region of the thickness discontinuity are studied using three-dimensional solid elements, while the uniform sections of the plate are modeled with quadrilateral shell elements. A geometrically nonlinear transition element was developed to couple the shell elements to the solid elements. The analysis was performed using the COmputational MEchanics Testbed (COMET), an advanced structural analysis software environment developed at the NASA Langley Research Center to provide a framework for research in structural analysis methods.

Uniaxial compression testing of dropped-ply, graphite-epoxy laminated plates has confirmed that delamination along the interfaces above and/or below the dropped plies is a common mode of failure initiation. The compression strength of specimens exhibiting a linear response is greater than the compression strength of specimens with the

same layup exhibiting geometrically nonlinear response. Experimental and analytical results also show a decrease in laminate strength with increasing number of dropped plies. For linear response there is a large decrease in compression strength with increasing number of dropped plies. For nonlinear response there is less of a reduction in compression strength with increasing number of dropped plies because the nonlinear response causes a redistribution and concentration of interlaminar stresses toward the unloaded edges of the laminate.

Acknowledgements

Professor Eric Johnson's teaching excellence is not limited to his classroom lectures. I want to thank him as much for his dedication to the ideals of education as for his guidance and infinite patience. His influence on me goes far beyond this dissertation. I also acknowledge the other members of my committee.

I wish to thank Dr. James Starnes Jr., head of the Aircraft Structures Branch at the NASA Langley Research Center, who monitored and funded this research through grant NAG1-537. His helpful insight enriched this work and is deeply appreciated.

This work would not have been possible without the computational facilities provided by the Computational Mechanics Branch at the NASA Langley Research Center. I would like to thank Dr. Jerrold Housner for this support, as well as Christine Lotts and Mohammad Aminpour for helping me master the COMET software environment.

I wish to thank my parents, Simonetta and Carlos, for their encouragement to excel in academics. Finally, I thank my fiancée, Maritza, whose constant emotional support and endless care have given me the strength to complete this work.

Table of Contents

List of Illustrations

List of Tables

1 Introduction

Radically new concepts for aircraft and spacecraft which exploit the properties of advanced composites are replacing everywhere older, less efficient designs. Only such radical departures from convention can utilize the full potential of the new breeds of fiber-reinforced materials. As experience progressively refines these new designs to the levels of more traditional techniques, the aerospace world is being revolutionized. The new shapes of things to come are taking form in the minds and art of people like Burt Rutan. His Voyager's 1986 unrefueled flight around the world[1], for instance, set records beyond the possibilities of previous technologies.

The learning experience, however, is always a difficult one. The potential of composites is often jeopardized by the lack of proper analysis and design methods. Indeed, the benefits of composite's anisotropic properties can be lost in design difficulties. Beechcraft's new Starship could be a case of such a failure[2]. While its Nomex honeycomb and graphite-epoxy construction are state of the art, at 14,400 lb. its takeoff weight compares unfavorably to the 10,810 lb. of its competition, the Piaggio Avanti. In spite of the Avanti's conventional construction materials, both planes have similar

payload-range characteristics, and the additional weight penalizes the composite plane's performance, particularly in cruise.

Details of composite structures quickly become so complex that successful designs easily require man-years to perfect. This is the case with the design of the Space Shuttle's filament wound motor case[3,4] shown in Figure 1. The transition region from the motor case joint to the membrane of the case in the aft segment of the booster is subjected to heavy compression when the Shuttle's main engines are fired. This transition section is a complicated design composed of various ply terminations which cause severe stress concentrations.

Although difficult to analyze, laminates with terminated plies are a common design feature wherever the stiffness of a structural member must be tailored. The design of a laminated wing skin, for example, calls for a taper in laminate thickness from the wing root, where thickness is beneficial, to the wing tip, where less rigidity is demanded. This gradual decrease in thickness is achieved by terminating internal plies in discrete steps along the span.

The stress distribution and the mechanics of deformation in the region around terminated plies has been the object of many a research effort, including the present. The complexity of the problem stems from its geometric discontinuities which imply the occurrence of three-dimensional deformations and stress concentrations. These stress risers must be fully understood for proper design since any anticipated increases in load-bearing capacity created by thickening the laminate could be negated by the through-the-thickness stresses generated at the ply-drop site.

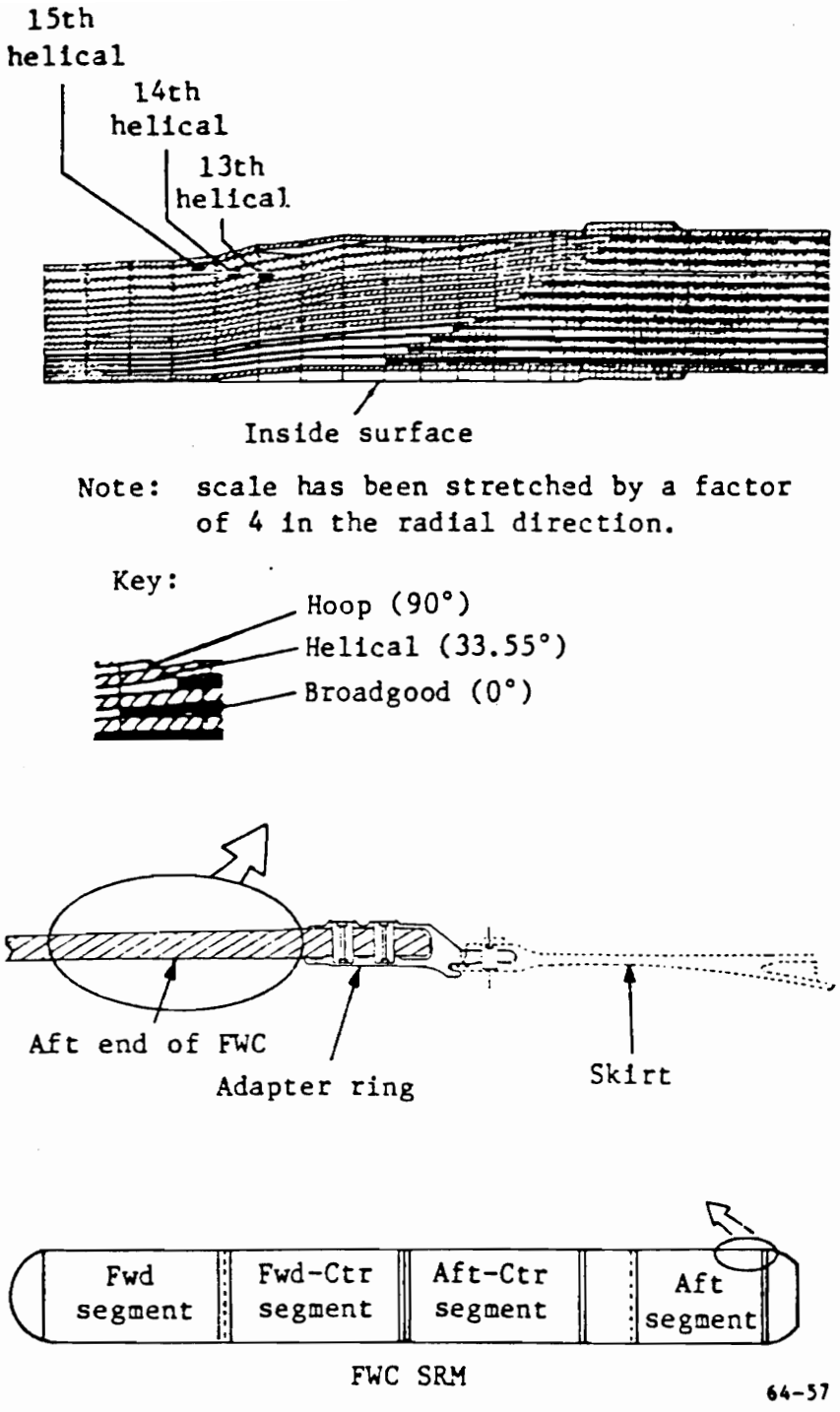

Figure 1. Detail of Shuttle filament wound case: transition region layup (approx. 40 in. long) Ref. 3

1.1 The dropped-ply problem.

Several authors have examined the deformations and stress gradients at the ply-drop site by using fully three-dimensional finite element models. Among the earliest were Adams et al.[5], who studied the effect of a dropped ply, moisture and residual thermal stresses on maximum compressive load. Their three-dimensional model included non-linear orthotropic material response but constrained the lateral surfaces to remain planar, essentially imposing plane strain conditions and not accounting for free edge effects. In addition, no longitudinal mesh refinement was made at the vicinity of the drop. They concluded that all the interlaminar stresses introduced by a single zero-degree dropped ply (out of 15 plies) were negligible compared to the in-plane stresses. However, they did not account for the low interlaminar strength of the composite compared to the in-plane strength.

Focusing on the design of hingeless composite helicopter rotor hubs, Daoust and Hoa[6] performed a study of the effects of several parameters on the strength of symmetrically tapered laminates under tension, bending and torsion. Different configurations were ranked by efficiency, which they defined as the strength ratio of a tapered laminate to a reference laminate with the same layup as the thin section of the tapered laminate. Strength was obtained from a two-dimensional finite element model of the cross-section by simple comparison of each stress component with its respective value obtained from uniaxial tests. Results showed that laminates with internally dropped plies are roughly twice as strong as external drop-offs. Maximum strength for laminates under tension was achieved with a fiber angle in the dropped plies equal to 22 degrees. Fiber angles

in the range of 45 to 90 degrees provided best efficiency under bending conditions, and 45 degrees was found to be the best compromise under combined bending and tension.

Fish and Lee[7] were also interested in the design of tapered laminates for rotor hubs, which they modeled with a refined three-dimensional finite element model of the ply drop-off region. Their interlaminar strength criterion was developed from the Tsai-Wu failure criterion and accounts for all three interlaminar stress components. The combined use of this criterion and the concept of stress averaging to predict delamination yielded good correlation with experiments. (Stress averaging is necessary to avoid stress singularities near geometric discontinuities such as free edges.) The averaging distance was assumed to be laminate-independent and equal to one ply thickness, as suggested by Kim and Soni[8]. Averaging distances have also been used in free-edge problems.†

Other authors avoided the expense of fully three-dimensional finite element models and used instead two-dimensional or quasi-three-dimensional analyses. Salpekar et al.[10] relied on a two-dimensional plane strain finite element analysis to show that the geometric discontinuities of the ply drop-off induce stress singularities which should not be applied in a maximum stress criterion. Instead, the authors recommend delamination analysis by strain energy release rates obtained from the virtual crack closure technique.

Wisnom[11], in one of the most recent publications on delamination of dropped-ply laminates, notes that the geometric complexity of tapered laminates investigated so far makes it inappropriate to extend conclusions about the underlying mechanisms involved

---

† Brewer and Lagace[9] applied the concept of averaging distance and quadratic failure criterion to the case of the straight free edge of a tensile coupon loaded in tension. They obtained best predictions with averaging distances ranging from 0.1 mm to 0.35 mm. These values are close to a single graphite/epoxy ply thickness (approximately 0.143 mm) but not equal to it.

and the applicability of the various methods proposed to other configurations. Wisnom focused, therefore, on symmetrically tapered, unidirectional glass fiber-epoxy laminates in tension. On the basis of his experiments and linear plane stress finite element analysis, he concluded, like Salpekar et al., that the critical parameter affecting delamination in tapered laminates is the strain energy release rate due to the terminating plies.

A different approach to the treatment of stress singularities at the edge of a ply drop-off is the one adopted by Wu[12]. This author performed a two-dimensional (x-z plane) nonlinear finite element analysis which accounted for yielding in the thin resin layer separating sublaminates. This yielding had the effect of reducing peak interlaminar stresses by about half.

The study of plates with dropped-plies in compression, as shown in Figure 2, was started in 1984 by Kemp and Johnson[13,14] who used a two-dimensional finite element analysis to determine the stress distribution in the vicinity of the dropped ply and to predict the initiation of delamination. Kemp recognized that the in-plane stresses in the dropped plies are small with respect to the through-the-thickness stresses at the drop-off. He found that axial forces are transfered to the terminated plies by shear rather than through the ends of the dropped ply fibers. Interlaminar stresses are largest at the discontinuity, decrease in exponential manner with increasing axial distance from the drop, and vanish in the far field. Kemp calculated that the axial distance required for the interlaminar stresses to vanish is a direct function of the number of dropped plies. For one ply dropped, Kemp calculated that the axial distance required for the interlaminar stresses to vanish is approximately 20 times the ply thickness. For each additional ply dropped, the axial distance increases by about 5 ply thicknesses.

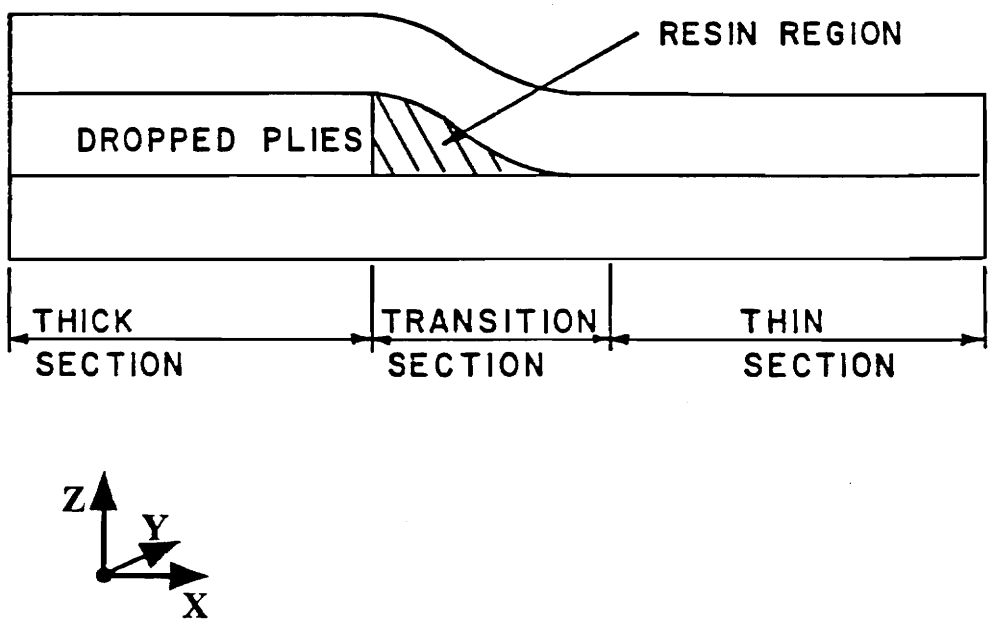

Figure 2. Dropped-Ply Laminate: Stiffness tailoring of a composite laminate results in abrupt thickness change

The finite element analysis started by Kemp was subsequently refined by Curry and Johnson[15,16] who found that width-wise (y-direction) effects neglected by Kemp were present in test specimens. To account for these effects, their model included a more general displacement field with states of stress dependent on only two coordinates. Curry's analysis was carried out at both a global level, which focused on the response of the entire test specimen, as well as a local level, which was confined to a through-the-thickness analysis near the transition section. The combined use of a global shell model and a local two-dimensional model results in an analysis which includes all six stress components. This type of analysis is referred to as "quasi three-dimensional" because it includes effects which are out of the plane of the two-dimensional local model, in this case width effects. These stresses were subsequently used in the Tsai-Wu criterion for intralaminar failure prediction. In addition, Curry used an interlaminar failure criterion adapted from Hashin which is based on matrix failure modes. No stress averaging was used. These criteria underestimated experimental failure loads by over 30%.

Curry's most important contribution to the dropped-ply problem, however, is his experimental work. He tested a large number of specimens of different dropped-ply configurations under both uniaxial tension and compression. He measured strains, displacements, and loads, and conducted a detailed study of the failure mechanisms by observing the formation and propagation of cracks.

The effect of specimen width on the compression strength of tapered laminates was one of the parameters studied by Curry. He tested specimens ten inches long of identical dropped-ply configuration, 1 inch, 1.5 inches, and 3 inches wide. While the two narrower specimens displayed a linear response until failure, the three-inch-wide specimen exhibited a geometrically nonlinear response prior to failure, and the load per unit width

at failure was substantially less than the one-inch-wide and 1.5-inch-wide specimens. It was this specific experiment of the three-inch-wide specimen that gave rise to the present work and which became the validation problem for the geometrically nonlinear analysis developed in this research.

1.2 Buckling and postbuckling of dropped-ply laminates

The investigation of structural instability starts with buckling. As early as 1974, Mikami et al.[17] calculated the buckling modes and loads for orthotropic plates with a symmetric step thickness change that resulted in a discontinuity in rigidity along the span. Their solution, based on a Galerkin solution to the stability equations, shows that the buckling load of a plate with a step thickness change is bound between the buckling loads of uniform plates of thicknesses corresponding to the thick and the thin sides of the plate. Their results also show that, unlike uniform plates, stepped plates do not exhibit abrupt mode changes at discrete plate aspect ratios, but instead the mode shapes vary in a progressive way.

The buckling analysis of orthotropic plates with a step thickness change was extended by Johnson and Dávila[18] to include transverse shearing deformation. This analysis and the unusual results obtained for thick plates are reported in the next chapter.

Aerodynamic and other design constraints usually impose that plies be dropped such that one side of the structure remains flat and uniform. There is, therefore, an ec-

centricity in the load path which couples the stretching (membrane) and bending (flexural) responses. It follows that dropped-ply laminates, like generally unsymmetric laminates, may not have any definable neutral surface, and consequently the concept of bifurcation buckling is not applicable. It becomes even more important, therefore, to investigate the nonlinear response of these laminates.

The influence of mechanical couplings on the buckling and postbuckling behavior of anisotropic plates was investigated by Jensen and Lagace[19]. Their experimental and analytical results on graphite-epoxy laminates showed that mechanical couplings have profound effects on the behavior of laminates. The authors obtained buckling loads by the Southwell method for a number of unsymmetric laminates chosen to isolate specific couplings. They concluded that the bifurcation buckling load serves little purpose except to give some rough comparison between various configurations. This was further reinforced by the fact that the buckling load did not usually correspond to any meaningful physical phenomenon or location on the load versus deflection curves.

Another important observation from Jensen and Lagace's paper is that two nominally identical plates do not necessarily display the same behavior. One laminate of particular interest is $[\,0_3\,//\,90_3\,//\,0_3\,//\,90_3\,]_T$, where the double slash // indicates a room temperature bondline joining previously cured sublaminates. The authors found that these laminates exhibit both primary bending until failure as well as a snap into a second mode. This indicates there are at least two stable equilibrium configurations for some values of the compressive load. The nonlinear Rayleigh-Ritz analysis developed by these authors could not predict snap-through into the second mode.

The similarity between unsymmetric laminates and dropped-ply laminates led Lagace et al.[20] to extend his research to the latter. This problem, however, was not well

suited for the Rayleigh-Ritz method because of the discontinuous nature of the plates. The analysis was instead performed through a shell analysis using finite elements. Lagace found that, like unsymmetric laminates, dropped-ply laminates showed considerable load-carrying capability beyond the (Southwell) buckling load, and the majority of them transitioned into higher order bending shapes at increased loads. Their results also indicated that the buckling load is bounded by the buckling loads of the basic flat plates with the same layup as the individual sections of the plate with the ply drop-offs. (This same conclusion was reached by Mikami et al.[17] with their linear buckling analysis of plates with a symmetric step thickness change). In addition, Lagace and his colleagues believe their experiments strongly indicate that the local eccentricity due to the thickness change is insignificant when compared to the effect of the bending stiffness changes. Finally, these authors found that plates with drop-offs exhibit very complex deflection shapes.

1.2 Objectives and approach

The objectives of this work are:

1. To obtain the geometrically nonlinear response of a dropped-ply laminated plate subject to axial compression, including three-dimensional effects at the thickness discontinuity.

2. To evaluate a methodology for delamination initiation based on a quadratic interlaminar stress criterion used in conjunction with a characteristic distance.

3. To corroborate the response and failure of the three-inch-wide compression specimens tested by Curry[15] with the analysis model developed in this study.

The computation of interlaminar stresses in postbuckling for a complex region like a ply drop-off requires a fully nonlinear three-dimensional finite element model. However, three-dimensional finite element analyses are computationally intensive, and prohibitively so when used to solve nonlinear problems by an iterative method. The approach taken here, therefore, is to develop a finite element model where three-dimensional elements are used only where three-dimensional effects are important, i.e., in the region of the dropped ply. Where thickness effects are insignificant (almost everywhere else), shell elements are substituted. A nonlinear solid-to-shell transition element for the connection of these two mutually incompatible elements is developed as part of the present study.

The remainder of this dissertation is divided as follows: Chapter 2 describes a method for the computation of buckling loads and buckling modes for simply supported thick orthotropic plates. This method allowed the investigation of the effects of plate aspect ratio and step thickness change on buckling. Chapter 3 is dedicated to the development of a nonlinear 20-node solid element and a 15-node linear and nonlinear transition element. A finite element model based on shell, solid and transition elements was developed for the evaluation of the interlaminar stress field in the region of the dropped ply. A parametric study on mesh size and the methodology for the prediction of delamination initiation are described in Chapter 4. The results for four case studies are presented and discussed in Chapter 5.

2 Buckling of Thick Orthotropic Plates with a Step Thickness Change

2.1 Introduction

As mentioned in Chapter 1, this investigation on structural instability of dropped-ply laminates was initiated with a bifurcation buckling analysis. The purpose of this chapter is to outline the method used to investigate the effect of step thickness change and plate aspect ratio on the bifurcation buckling behavior of specially orthotropic plates subject to compression. The approach taken is to use a first order shear deformation theory (SDT) to compute the buckling load, and compare it to the classical bifurcation load computed from classical lamination theory (CLT) (based on Kirchhoff hypotheses).

2.2 *Configuration and loading*

The geometry of the problem studied here is shown in Figure 3. It consists of a plate of length a and width b which is divided into two equal length parts ($a_1 = a_2 = a/2$) with different thicknesses t_1 and t_2. The loading is from a uniform compressive load $\overline{N}_x$ in the x direction applied along the width of the plate. The boundary conditions are simple support all around. The stiffnesses in each section are calculated for a $[0/90/0]_T$ laminate, where the fibers in a zero degree ply are parallel to the x-axis. Each lamina is orthotropic with the material properties shown in Fig. 3. Subscripts L and T on the material constants refer to longitudinal (fiber) and transverse directions, respectively.

2.3 *Transverse shear stiffness*

Shear deformation theories require the computation of the transverse shear stiffnesses A_{44}, A_{45}, A_{55}. In a first order shear deformation theory, the transverse shear strains are constant through the thickness of the laminate, and this violates interlaminar stress continuity in general. The stiffnesses A_{44}, A_{45}, and A_{55} computed on the basis of uniform transverse shear strains are considered too large, and shear correction factors are introduced to reduce their magnitudes. A review of the computation of shear correction factors for orthotropic plates is given in Whitney's[21] book (pp. 270-273). For example, in an isotropic homogeneous plate Reissner's method (static bending) gives

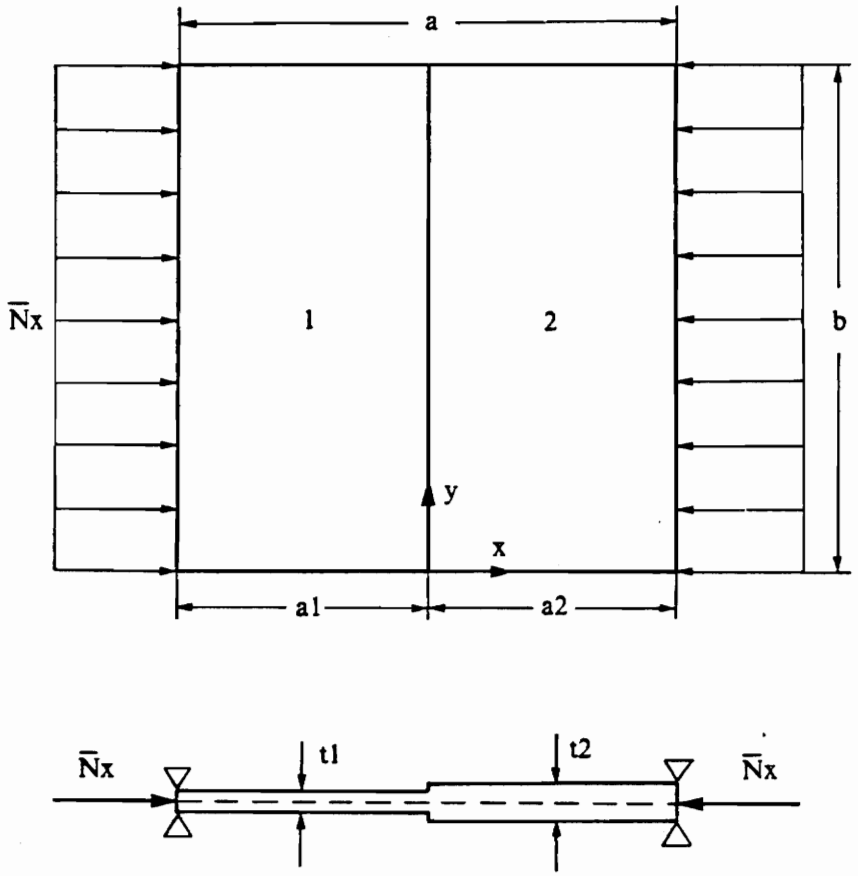

Stacking sequence:

$[0/90/0]_T$

Material Properties:

$$\frac{E_L}{E_T} = 30 \qquad \frac{G_{LT}}{E_T} = 0.6 \qquad \frac{G_{TT}}{E_T} = 0.5$$

$$\nu_{LT} = \nu_{TT} = 0.25$$

Thickness:

$$\frac{t_1 + t_2}{2} = t_{avg} = constant$$

Figure 3. Thick Orthotropic Plate with Symmetric Thickness Discontinuity

$A_{44} = A_{55} = (5/6)Gt$, $A_{45} = 0$, where G is the shear modulus, t is the plate thickness, and 5/6 is the shear correction factor. For laminates of general lay-up, there is a correction factor for each of the three stiffnesses A_{44}, A_{55}, and A_{45}. Cohen[22,23] provides a systematic method to compute the three stiffnesses A_{44}, A_{55}, and A_{45} for a general laminated shell wall construction. Cohen's method was used in the present study, and since it has not received the recognition it deserves, a summary of the method is presented below.

It is assumed that the material has monoclinic symmetry with respect to the reference plane of the plate. This uncouples the transverse shear strains γ from the in-plane strains e in Hooke's Law. Also, as is usual in plate analysis, the in-plane strains are assumed to have a linear distribution through the thickness. If e denotes the three-by-one vector of in-plane strains $(e_x, e_y, e_{xy})^T$, then

$$e = \varepsilon + z\kappa \tag{2.3.1}$$

where ε is the reference surface strain vector and κ is the curvature vector. Hooke's law for the in-plane stresses is

$$\sigma = Ee \tag{2.3.2}$$

in which E is the 3 X 3 matrix of elastic moduli, and σ is a three-by-one vector of in-plane stresses. The elements of matrix E are the transformed reduced stiffnesses, and these are piecewise constant in z.

Hooke's law for the transverse shear stresses and shear strains is

$$\tau = G\gamma \tag{2.3.3}$$

where

$$\tau = [\tau_{yz}, \tau_{zx}]^T$$
$$\gamma = [\gamma_{yz}, \gamma_{zx}]^T \tag{2.3.4}$$

and

$$G = \begin{bmatrix} c_{44} & c_{45} \\ c_{45} & c_{55} \end{bmatrix} \tag{2.3.5}$$

The elements of the elasticity matrix G are piecewise constant in z, and the transverse shear strains γ are constant in z.

The objective of the method is to determine the two-by two compliance matrix k in the relation

$$\gamma = k\,Q \tag{2.3.6}$$

where the two-by-two transverse shear resultant vector is

$$Q = [Q_y, Q_x]^T = \int_0^t \tau\, dz \tag{2.3.7}$$

and t denotes the total laminate thickness. For the purpose of deriving k Cohen takes the reference surface at the bottom surface of the laminate, but he shows the results are independent of the reference surface location. Cohen finds matrix k by considering the complementary strain energy per unit surface area in transverse shear, which is

$$V = 1/2 \int_0^t \tau^T G^{-1} \tau \, dz \tag{2.3.8}$$

In terms of matrix k this energy is represented as

$$V = 1/2 \, Q^T k \, Q \tag{2.3.9}$$

To proceed from Eq. (8) to Eq. (9), Cohen determines a statically admissible transverse shear stress distribution from the linear distribution of the in-plane stresses given by Eqs. (1) and (2). The result is

$$-\tau(z) = [\alpha_1(z) \; \alpha_2(z)] \; \xi + \beta(z) \, Q \tag{2.3.10}$$

in which the two-by-four matrices α_1 and α_2 are quadratic in z, the two-by-two matrix β is also quadratic in z, and the eight-by-one parameter vector ξ represents first order terms in the Taylor series expansion of the laminate membrane and bending moment resultants about a generic point on the reference surface. The matrices in Eq. (10) have properties that satisfy Eq. (7) and $\tau(0) = \tau(t) = 0$ for arbitrary vectors ξ and Q. Eq. (10) is substituted into Eq. (8) to get

$$2V = \xi^T A \, \xi + 2 \xi^T B \, Q + Q^T C \, Q \tag{2.3.11}$$

where

$$
\begin{aligned}
A &= \begin{bmatrix} A_{11} & A_{12} \\ A_{12}^T & A_{22} \end{bmatrix} && \text{(8X8)} \\
B &= \begin{bmatrix} B_1 \\ B_2 \end{bmatrix} && \text{(8X2)} \\
C &= \int_0^t \beta^T G^{-1} \beta \, dz && \text{(2X2)} \\
B_i &= \int_0^t \alpha_i^T G^{-1} \beta \, dz && \text{(4X2)} \\
A_{ij} &= \int_0^t \alpha_i^T G^{-1} \alpha_j \, dz && \text{(4X4)}
\end{aligned}
\tag{2.3.12}
$$

in which i and j can take on values 1 and 2, and the numbers in parentheses represent the size of the matrices.

The complementary energy in Eq. (11) is minimized with respect to the parameter vector ξ to get

$$A\xi + BQ = 0 \tag{2.3.13}$$

Finally Eq. (13) is solved for ξ and substituted into Eq. (11) to get

$$V = \frac{1}{2} Q^T \left[C - B^T A^{-1} B \right] Q \tag{2.3.14}$$

Comparing Eq. (14) with Eq. (9) yields the final result that

$$k = C - B^T A^{-1} B \tag{2.3.15}$$

For a single layer, isotropic and homogeneous material, Cohen's method gives $A_{44} = A_{55} = 5/6\ Gt$, $A_{45} = 0$, as expected.

Cohen also discusses the case when matrix A is singular, which occurs for most simple laminate constructions such as for a homogeneous single layer, for an isotropic heterogeneous laminate, or for cross-ply laminates with midsurface symmetry. Such cases require the computation of a "natural inverse" of A. Although in general the computation of this "inverse" of a singular matrix does not pose a problem, the author has had difficulties with some nonsymmetric stacking sequences where the rank of matrix A was not properly determined. For these cases, the implementation of Cohen's method could not be made entirely robust.

2.4 *Stability equations*

The buckling equations and associated boundary conditions for SDT theory are given in Whitney's[21] book (pp. 265-270). For the special case of symmetric othotropic laminates they reduce to three equations in the out-of-plane displacement w, the rotation α of the projection of the normal in the xz plane, and the rotation β of the projection of the normal in the yz plane. The stability equations are

$$\begin{aligned} A_{55}(\alpha_{,x} + w_{,xx}) + A_{44}(\beta_{,y} + w_{,yy}) - \overline{N}_x w_{,xx} &= 0 \\ D_{11}\alpha_{,xx} + (D_{12} + D_{66})\beta_{,xy} + D_{66}\alpha_{,yy} - A_{55}(\alpha + w_{,x}) &= 0 \\ (D_{12} + D_{66})\alpha_{,xy} + D_{22}\beta_{,yy} + D_{66}\beta_{,xx} - A_{44}(\beta + w_{,y}) &= 0 \end{aligned} \qquad (2.4.1)$$

The solution is obtained by assuming functions which satisfy the boundary conditions. For simple support at y = 0 and y = b, these boundary conditions are

$$w = 0 , \quad \alpha = 0 , \quad M_y = 0 , \tag{2.4.2}$$

and the solutions which satisfy these boundary conditions are

$$\begin{aligned} w(x,y) &= p_1 e^{\lambda x} \sin\left(\frac{m\pi y}{b}\right) \\ \alpha(x,y) &= p_2 e^{\lambda x} \sin\left(\frac{m\pi y}{b}\right) \\ \beta(x,y) &= p_3 e^{\lambda x} \cos\left(\frac{m\pi y}{b}\right) \end{aligned} \tag{2.4.3}$$

in which m is a positive integer, λ is a parameter, and p_1, p_2, and p_3 are buckling mode amplitudes.

Substitution of the assumed solution functions in Eq. (3) into the buckling equations yields the homogeneous system of equations

$$\begin{bmatrix} \lambda^2(\bar{N}_x + A_{55}) - A_{44}\left(\frac{m\pi}{b}\right)^2 & \lambda A_{55} & -A_{44}\left(\frac{m\pi}{b}\right) \\ -\lambda A_{55} & \lambda^2 D_{11}\left(D_{66}\left(\frac{m\pi}{b}\right)^2 + A_{55}\right) & -\lambda(D_{12}+D_{66})\left(\frac{m\pi}{b}\right) \\ -A_{44}\frac{m\pi}{b} & \lambda(D_{12}+D_{66})\left(\frac{m\pi}{b}\right) & \lambda^2 D_{66} - \left(D_{22}\left(\frac{m\pi}{b}\right)^2 + A_{44}\right) \end{bmatrix} \begin{bmatrix} p_1 \\ p_2 \\ p_3 \end{bmatrix} = 0$$

Solving the sixth order polynomial resulting from the vanishing of the system matrix in the above equation gives the characteristic roots λ_i, and the characteristic vectors $(p_1, p_2, p_3)^T$, where i = 1, ... , 6. Therefore, the displacements that satisfy the buckling differential equations in each uniform thickness portion of the plate are

$$\begin{bmatrix} w(x,y) \\ u(x,y) \\ v(x,y) \end{bmatrix} = \sum_{i=1}^{6} C_i \begin{bmatrix} p_1 \sin(m\pi y/b) \\ p_2 \sin(m\pi y/b) \\ p_3 \cos(m\pi y/b) \end{bmatrix}_{(i)} e^{\lambda_i x} \tag{2.4.4}$$

The remaining 12 constants C_i (6 per side) are obtained from the remaining boundary conditions. These conditions are:

$$\text{at x} = -a_1$$

$$w_1(-a_1, y) = 0 \quad M_{x1}(-a_1, y) = 0 \quad \beta_1(-a_1, y) = 0$$

$$\text{at x} = 0$$

$$\begin{aligned} w_1(0^-, y) - w_2(0^+, y) &= 0 \qquad (\bar{N}_x w_{,x} + Q_x)_1 - (\bar{N}_x w_{,x} + Q_x)_2 = 0 \\ \alpha_1(0^-, y) - \alpha_2(0^+, y) &= 0 \qquad M_{x1}(0^-, y) - M_{x2}(0^+, y) = 0 \\ \beta_1(0^-, y) - \beta_2(0^+, y) &= 0 \qquad M_{xy1}(0^-, y) - M_{xy2}(0^+, y) = 0 \end{aligned}$$

$$\text{at x} = a_2$$

$$w_2(a_2, y) = 0 \quad M_{x2}(a_2, y) = 0 \quad \beta_2(a_2, y) = 0$$

in which subscripts *1* and *2* denote the portions of the plate shown in Fig. 3.

The computations outlined above were implemented in a FORTRAN program according to the flowchart in Fig. 4. The program starts by computing an initial estimate of the buckling load $\bar{N}_x$ with CLT (Classical Lamination Theory), which provides an estimation of the characteristic values and vectors which satisfy the differential equations. Next, the determinant corresponding to the boundary conditions is evaluated. If the determinant is not equal to zero, a root finder routine is used to update the

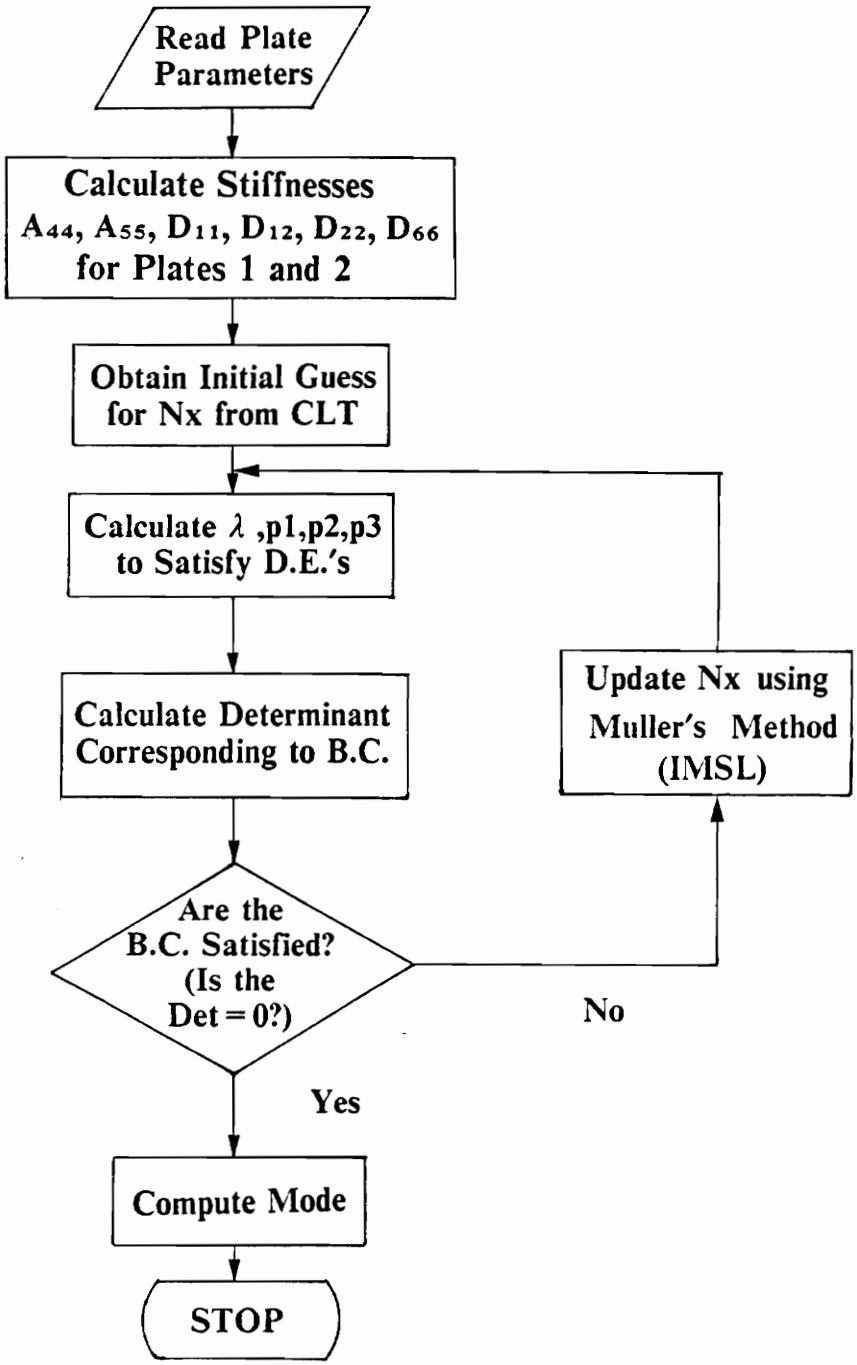

Figure 4. Procedure Flowchart: Calculation of buckling load by iteration

value of the buckling load. The procedure continues until convergence to a buckling load which satisfies all boundary conditions to within a specified tolerance.

2.5 *Results*

The following table shows the values of the shear correction factor computed by Cohen's method for the material properties of the orthotropic laminate given in Fig. 3. Reissner's commonly used correction factor (Whitney[21] pg. 270) is shown for comparison.

Table 1. Shear Correction Factors

Correction Factor	Cohen	Reissner
k_{44}	0.8507	0.8333
k_{55}	0.8653	0.8333

In the following results t is the average of the thicknesses t_1 and t_2, E_T is Young's modulus in the direction transverse to the fibers, and b is the laminate width. The variation of the dimensionless buckling coefficient $K = \overline{N}_{xcr}\, b^2/(E_T\, t^3)$ as a function of t_1/t_2 for CLT, and SDT for t/b = 0.1 and t/b = 0.2 is shown in Fig. 5. These are relatively thick plate geometries. The thicknesses t_1 and t_2 corresponding, respectively, to the thin and the thick sides of the laminate, are varied so as to maintain a constant average thickness (constant-weight variation in t_1 and t_2).

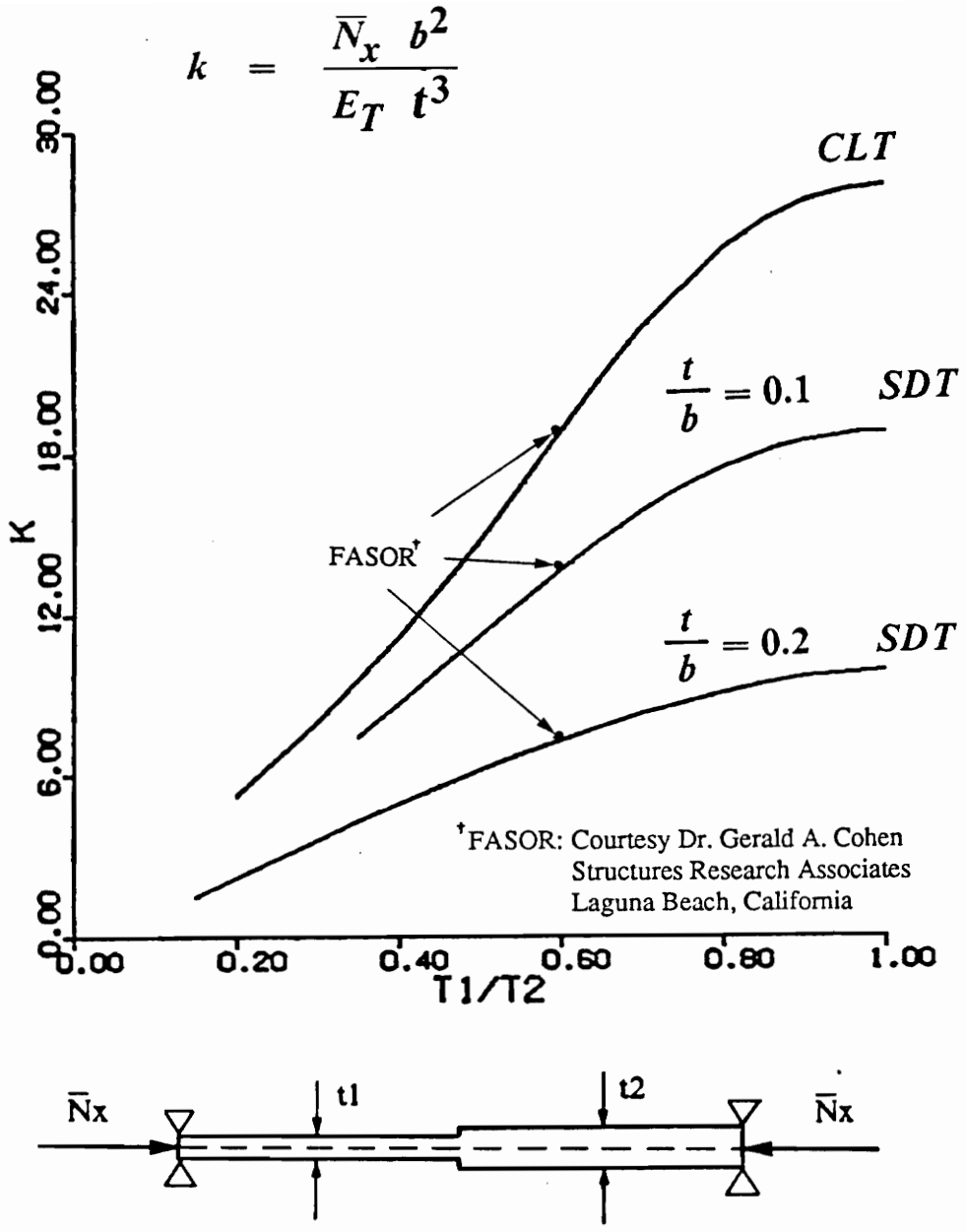

Figure 5. Buckling Coefficient vs. t_1/t_2 for square plate

The values for CLT were calculated by the author and the method was verified against the Mikami et al., Ref. 17, and the results were found to be identical (both analyses are based on identical assumptions).

For a t_1/t_2 ratio equal to one, the plate is of uniform thickness. The values obtained by the present analysis are within 3% of the values reported by Cohen[22], as shown in Table 2.

Table 2. Normal buckling load $K = \bar{N}_{xr} b^2/(E_T t^3)$ for thick uniform plate

Present Analysis	Elasticity[22]	Cohen[22]	CLT
	(a) t/b = 0.1		
18.8	19.3	19.1	27.9
	(b) t/b = 0.2		
9.90	10.4	10.2	27.9

As can be observed in both Table 2 and Fig. 5, SDT predicts a large decrease in buckling load compared to CLT for a uniform thickness plate ($t_1/t_2 = 1$). However, the discrepancy between SDT and CLT decreases for small t_1/t_2 ratios.

A plot of the buckling modes for a thickness ratio of $t_1/t_2 = 0.75$ is shown in Fig. 6. The mode predicted by CLT is close to the one for a moderately thick plate (t/b = 0.1), although the buckling load is overestimated by 30%. At a thickness ratio of t/b = 0.2, the predicted mode shape is very different from CLT and shows a curious "kink", or slope mismatch, at the transition of the two plates. This should not be surprising since, unlike CLT, SDT imposes no condition of slope continuity at the interface of the

two plates. However this kink would cause breakage of the fibers and is an artifice of the plate theory.

A plot of the buckling modes for different values of t_1/t_2 and with an average thickness ratio of $t/b = 0.2$ is shown in Fig. 7. For $t_1 = t_2$ the mode is a half sine wave. For increasing thickness difference, bending concentrates in the thin side of the plate, leaving little contribution from the thick side.

The plot in Figure 8 shows the variation of buckling coefficient with aspect ratio of the plate. The darker line line is for the stepped plate, and it is always bound by the buckling coefficients of uniform plates of thicknesses t_1 and t_2. The cusps in the lines for the uniform plates correspond to changes in mode shapes corresponding to specific plate aspect ratios. Stepped plates, however, do not exhibit any cusps, indicating that the mode shape changes gradually and without discontinuities.

The mode shapes of the stepped plate are compared with the uniform plates at three aspect ratios: 1.15, 1.75 and 2.25 in Fig. 9. At the lowest aspect ratio, 1.15, the modes for the thick and thin uniform plates are a half wave. At 1.75, the thick uniform plate is on the right of the first cusp, and its mode shape has changed to a full wave. At 2.25, the thin plate has also passed on the right of its first cusp and it too becomes a full wave. The mode of the stepped plate can be seen to change continuously and without abrupt changes.

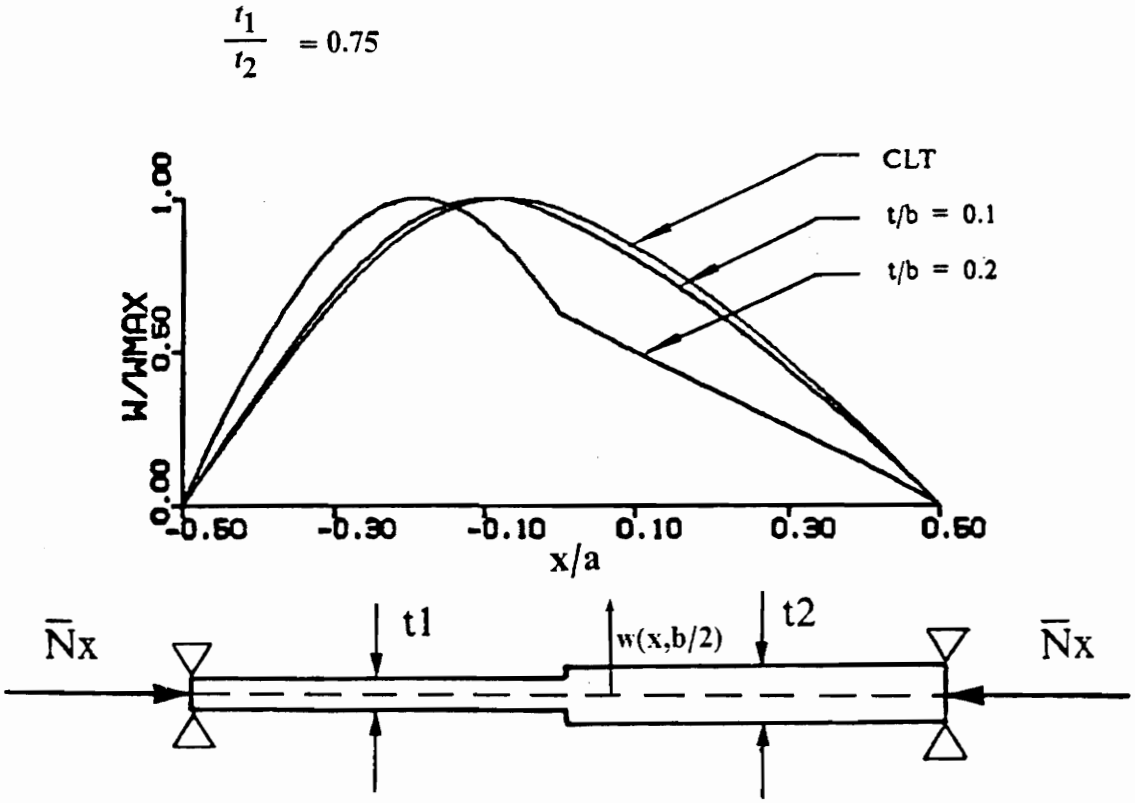

Figure 6. Buckling Modes for CLT and SDT at y = b/2 for square plate. $t_1/t_2 = 0.75$

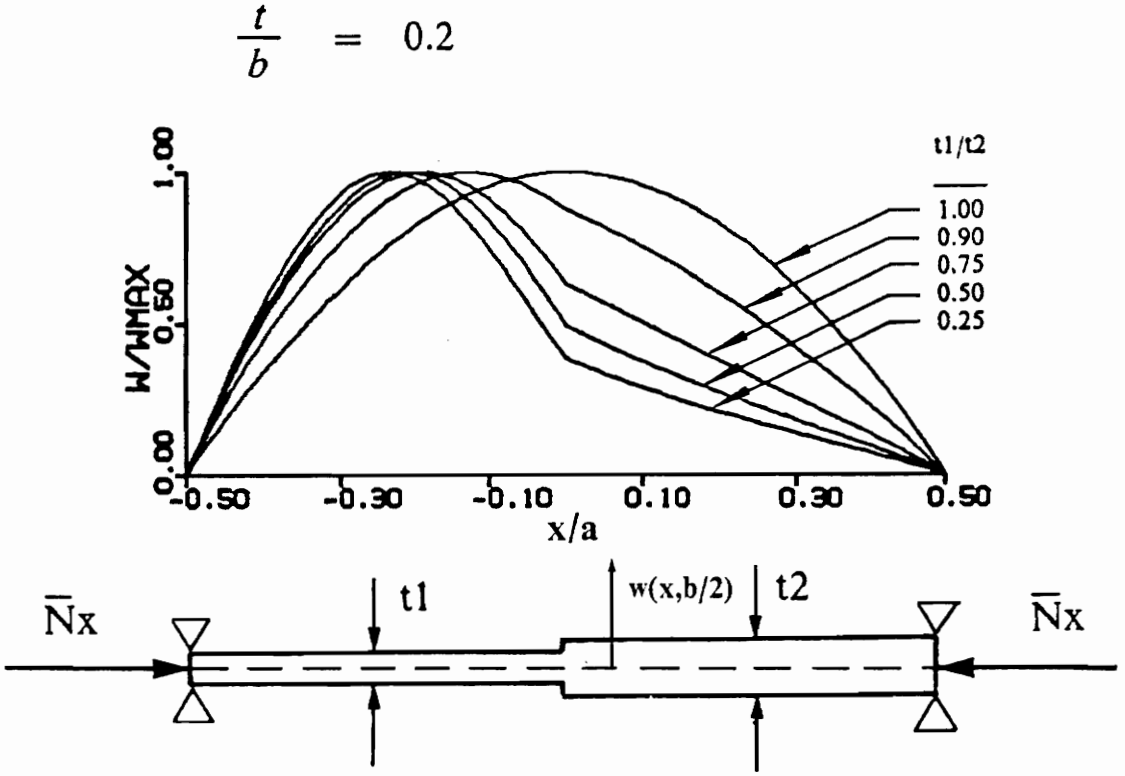

Figure 7. Buckling Modes from SDT at y = b/2 for square plate

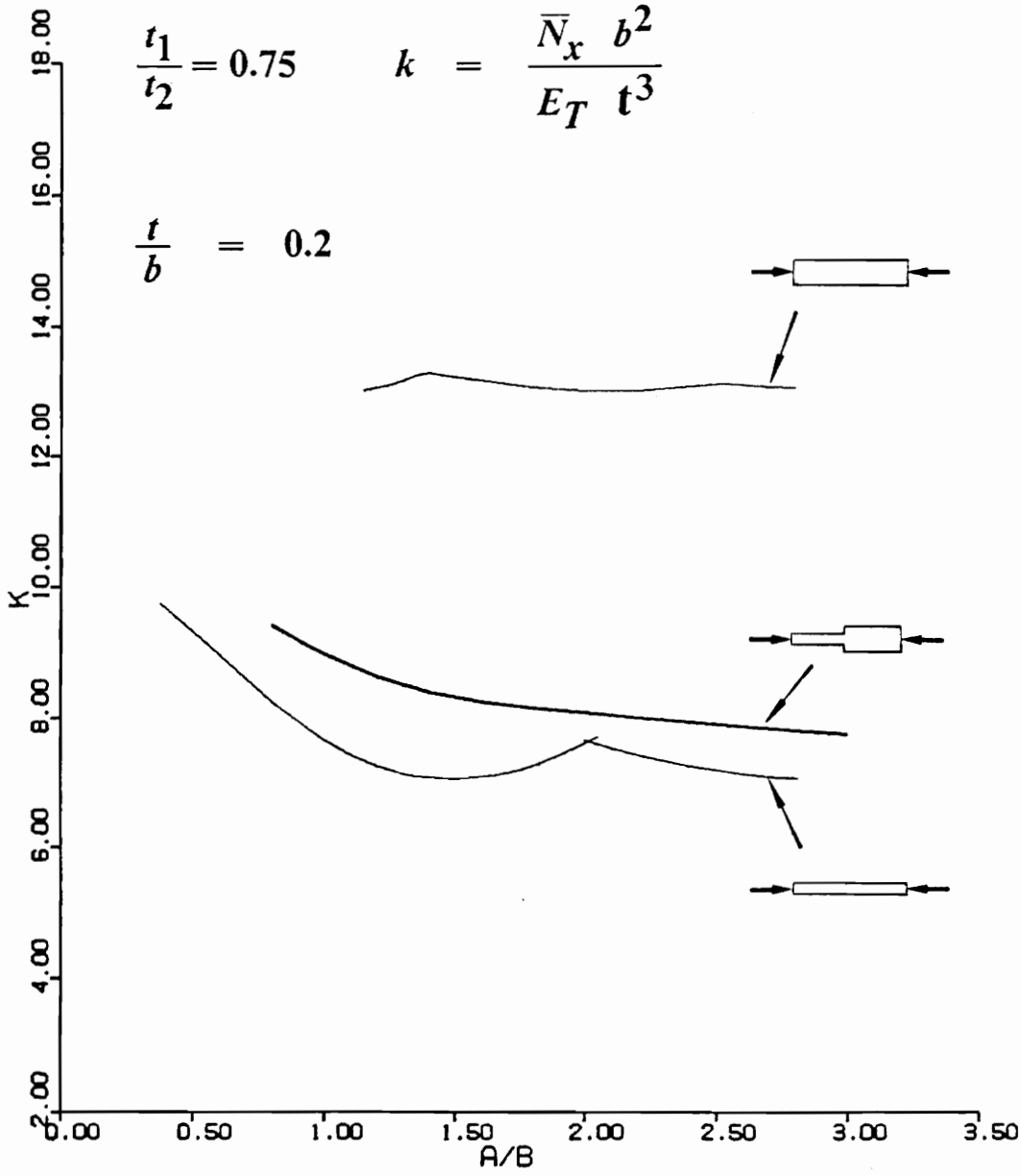

Figure 8. Buckling Coefficient vs. Aspect Ratio (SDT)

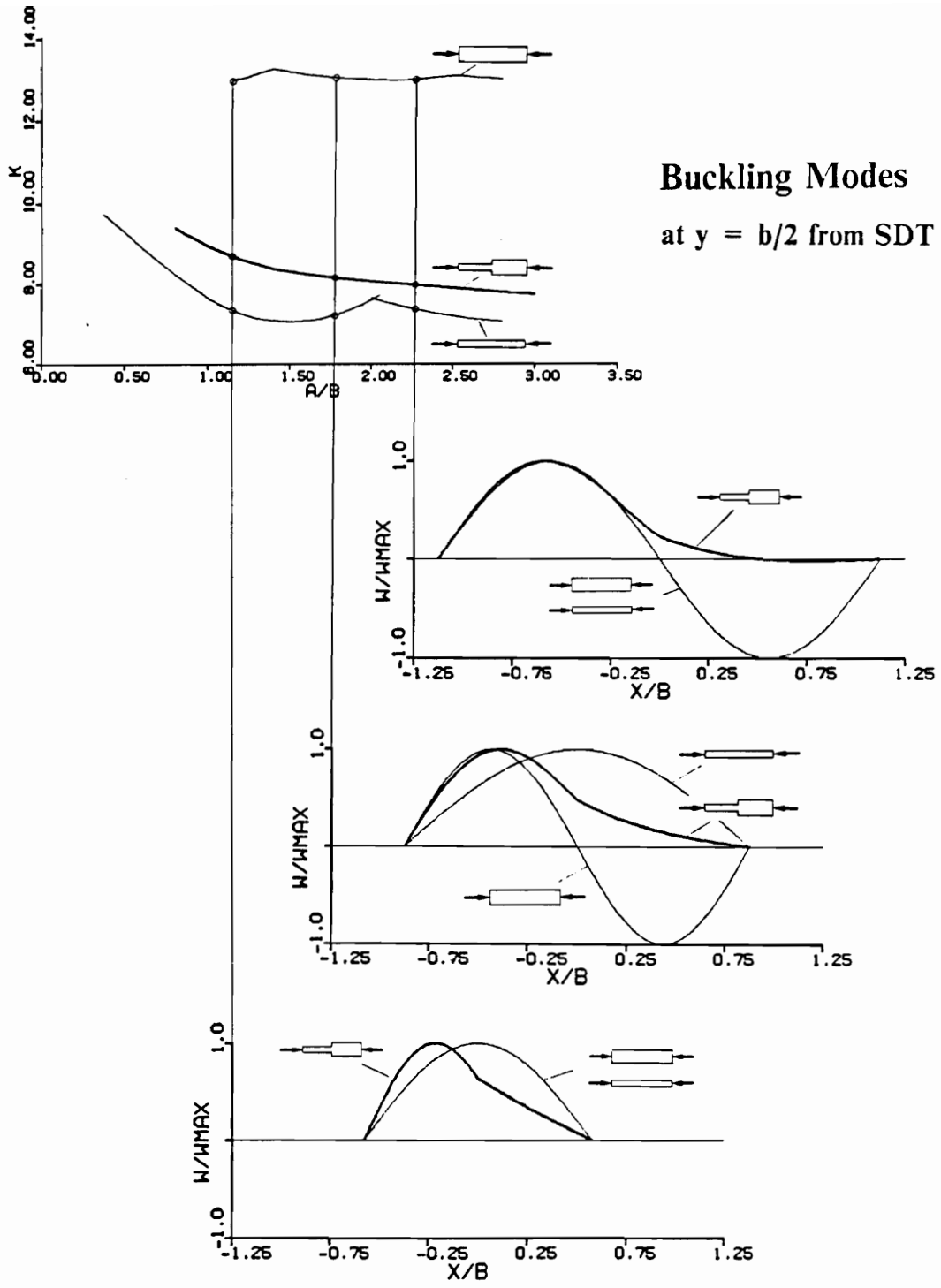

Figure 9. Buckling Modes vs. Aspect Ratio (SDT)

3 Element Development

3.1 Transition element for linear analysis

Refined finite element analyses of thin-walled laminated composite structures cannot always rely on two-dimensional shell elements to produce sufficient stress details. The shell theory assumptions of zero transverse strain and stress on which these elements are formulated usually do not provide the interlaminar stresses that cause delamination. On the other hand, discretizing thin-walled portions of a structure with solid elements can be computationally expensive and impractical. Also, it may lead to erroneous numerical results for thin structures owing to shear locking and membrane locking in the numerical solutions[24,25]. The ideal procedure is to model thin-walled areas of a structure - often the largest portion - with shell elements, and to use three-dimensional solid elements only where thickness deformations are significant. However, the nodal degrees of freedom of shell and solid elements are incompatible with each other and direct connection is not possible. One method to deal with this incompatibility is by way of a two-to-three dimensional Global/Local analysis - also called *zooming technique*[26] -

where results from a Global shell analysis are used to produce the boundary conditions for a three-dimensional Local analysis[27,28]. The inconvenience of dealing with two separate models, however, becomes compounded in nonlinear iterative analyses.

Another solution to the incompatibility between solid and shell elements was proposed by Bathe and his colleagues[29,30] and Surana[31]. These authors developed a transition element which provides the connection between three-dimensional solid elements and shell elements. Surana[32] later expanded the capabilities of this transition element to include geometrically nonlinear effects, and Liao, et al.[33] generalized its use to laminated composite structures.

In spite of their good accuracy and modeling convenience, the transition elements developed by these authors are of limited usefulness for this study because their shell-compatible nodes are located on the middle surface of the element. This implies that these transition elements can only link *one* solid element to *one* shell element. However, modeling a laminated structure typically involves several solid elements through the thickness, and the transition element does not provide any means of connecting them to the same shell element.

The transition element developed for this work does not suffer from the aforementioned limitations of previous transition elements. In addition, it was developed from an existing 20-node solid element with a relatively minor developmental effort.

The stiffness matrix $\boldsymbol{K}_{Tr}$ for the transition element was obtained from the known stiffness matrix $\boldsymbol{K}_S$ of a 20-node solid element developed by Griffin and Vidussoni (Refs. 34 and 35) by restricting the motion of one face of the element to be kinematically con-

strained by the Mindlin-Reissner plate theory†. This theory assumes that the normal to the surface before deformation remains rigid in the deformation. The connection between solid elements and shell elements is illustrated in Fig. 10. A stack of solid elements, each modeling a ply or a sublaminate group, needs to be coupled to a shell element. However, the formulation of these element types makes them incompatible with each other. For instance, the degrees of freedom of the solid element nodes (nodes 1 to 20 in Fig. 10a) are the three displacements u, v and w, while shell nodes (nodes 21 to 29) additionally include the rotations α and β of the normal.

The Mindlin-Reissner kinematic assumptions imply that the motion of the nodes on the "transition face" of the solid element (face with corner nodes 3,5,6,7 in Fig. 10a) is entirely prescribed by the displacements and rotations at the transition nodes (nodes 21, 24 and 28). Consequently, nodes 2, 3, 6, 7, 10, 14, 15 and 18 are no longer independent, and may be eliminated. The transition element is, therefore, shown complete in Fig. 10b, where it shown that the transition nodes 13, 14 and 15 do not necessarily lie on the boundaries of the element.

Except for the nodes on the transition face, all the nodes on the transition element correspond to a node on the solid element, as shown in Fig. 11. The degrees of freedom for the nodes on the transition element are, like on the solid element, u, v and w. However, the three transition nodes 13, 14 and 15 are shell nodes, so their degrees of freedom additionally include the rotations α and β of the normal. Therefore, the Mindlin-Reissner constraint can be imposed on one face of a 20-node solid element after reducing the number of nodes to 15 and the number of degrees of freedom from 60 to 51.

---

† For modeling a dropped-ply laminate it is necessary to constrain only one face of the solid element. However, constraining two faces of the element is possible and may be necessary in other applications. See the manual for the transition element in Appendix A.

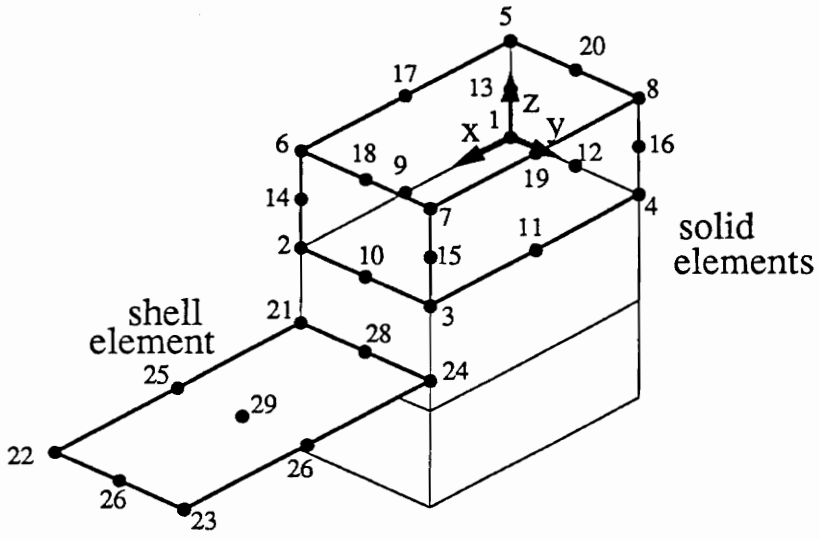

a) The connection between a stack of solid elements and a shell element can be made by applying the kinematic assumptions of plate theory to the transition face

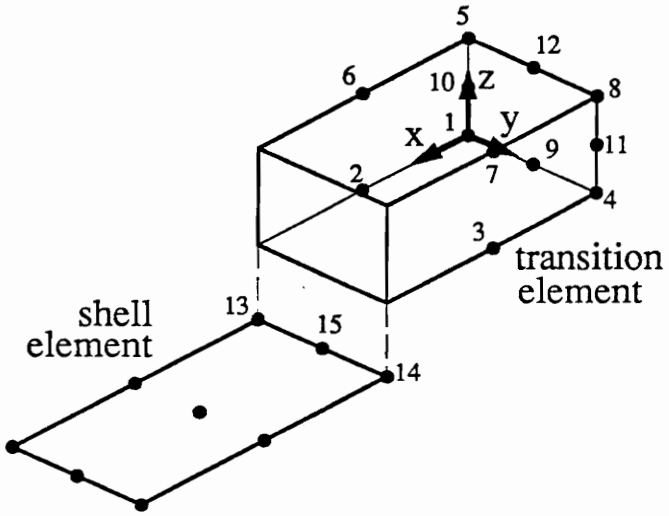

b) Displacements at solid element nodes on transition face are constrained by the kinematic assumptions, and the nodes can be eliminated. "Transition" nodes 13, 14 and 15 are not necessarily on the boundaries of the element

Figure 10. Kinematic restraints on transition face: the imposition of the Mindlin-Reissner plate assumptions implies that nodes 2,3,6,7,10,14,15 and 18 in Fig. 10a are dependent and can be eliminated (Fig. 10b)

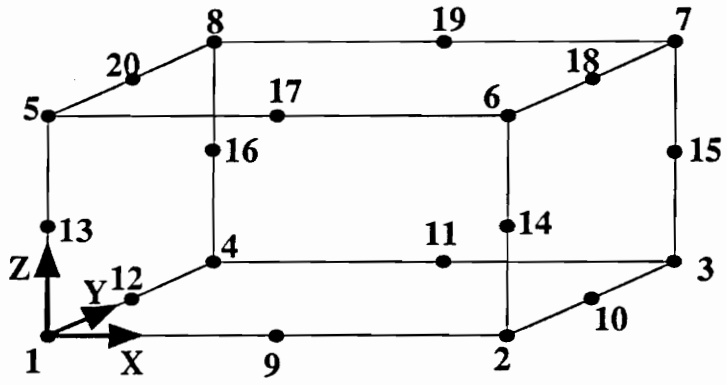

20-Node Solid Element

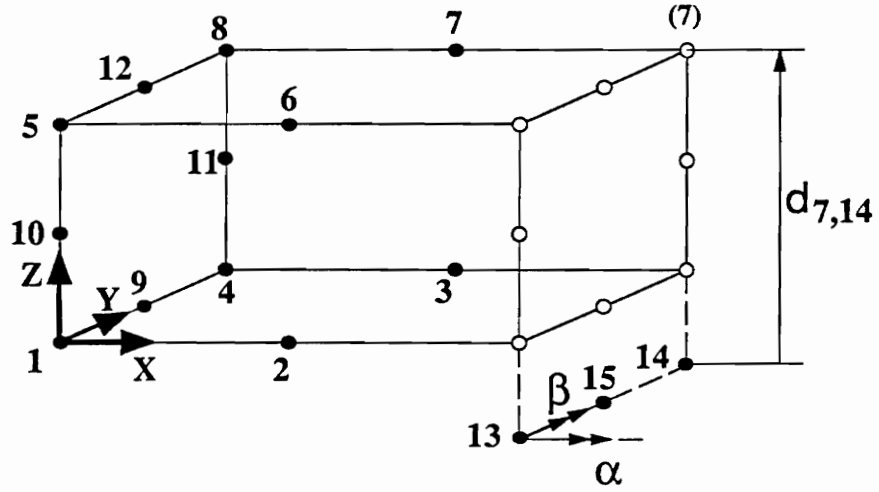

15-Node Transition Element

● solid element nodes

○ "missing" solid element nodes

Figure 11. Transition element: 20-node solid element with sixty degrees of freedom and derived 15-node transition element with fifty-one degrees of freedom

The kinematic relation between a solid element node k and its corresponding transition node j can be expressed as follows:

$$\begin{bmatrix} u_k \\ v_k \\ w_k \end{bmatrix}_S = \begin{bmatrix} 1 & 0 & 0 & 0 & d_{kj} \\ 0 & 1 & 0 & -d_{kj} & 0 \\ 0 & 0 & 1 & 0 & 0 \end{bmatrix} \begin{bmatrix} u_j \\ v_j \\ w_j \\ \alpha_j \\ \beta_j \end{bmatrix}_{Tr} \tag{3.1.1}$$

where the term $| d_{kj} |$ is the distance from the transition node j to the solid element node k. Equation (1) is succinctly written as $\{\hat{u}_k\}_S = [R_{kj}]\{\hat{u}_j\}_{Tr}$.

If $\hat{\boldsymbol{u}}_S$ is the complete displacement vector for the solid element (60X1) and $\hat{\boldsymbol{u}}_{Tr}$ is the vector of displacements and rotations for the transition element (51X1), the restraint matrix $\boldsymbol{R}$ (60X51) is defined as

$$\hat{\boldsymbol{u}}_S = \boldsymbol{R}\,\hat{\boldsymbol{u}}_{Tr} \tag{3.1.2}$$

in which

$$\hat{\boldsymbol{u}}_S^T = \{u_1, v_1, w_1, \ldots, u_k, v_k, w_k, \ldots, w_N\}$$
$$\hat{\boldsymbol{u}}_{Tr}^T = \{u_1, v_1, w_1, \ldots, u_j, v_j, w_j, \alpha_j, \beta_j, \ldots, \beta_N\}$$

The transition node j is related to the solid element node k through Eq. (1). Using this notation, the restraint matrix $\boldsymbol{R}$ can therefore be written as

$$
\begin{bmatrix} \\ \hat{u}_1 \\ \hat{u}_2 \\ \hat{u}_3 \\ \hat{u}_4 \\ \hat{u}_5 \\ \hat{u}_6 \\ \hat{u}_7 \\ \hat{u}_8 \\ \hat{u}_9 \\ \hat{u}_{10} \\ \hat{u}_{11} \\ \hat{u}_{12} \\ \hat{u}_{13} \\ \hat{u}_{14} \\ \hat{u}_{15} \\ \hat{u}_{16} \\ \hat{u}_{17} \\ \hat{u}_{18} \\ \hat{u}_{19} \\ \hat{u}_{20} \\ \\ \end{bmatrix}_S
=
\begin{bmatrix}
\mathbf{I} & 0 & 0 & 0 & 0 & 0 & 0 & 0 & 0 & 0 & 0 & 0 & 0 & 0 & 0 \\
0 & 0 & 0 & 0 & 0 & 0 & 0 & 0 & 0 & 0 & 0 & 0 & R_{2,13} & 0 & 0 \\
0 & 0 & 0 & 0 & 0 & 0 & 0 & 0 & 0 & 0 & 0 & 0 & 0 & R_{3,14} & 0 \\
0 & 0 & 0 & \mathbf{I} & 0 & 0 & 0 & 0 & 0 & 0 & 0 & 0 & 0 & 0 & 0 \\
0 & 0 & 0 & 0 & \mathbf{I} & 0 & 0 & 0 & 0 & 0 & 0 & 0 & 0 & 0 & 0 \\
0 & 0 & 0 & 0 & 0 & 0 & 0 & 0 & 0 & 0 & 0 & 0 & R_{6,13} & 0 & 0 \\
0 & 0 & 0 & 0 & 0 & 0 & 0 & 0 & 0 & 0 & 0 & 0 & 0 & R_{7,14} & 0 \\
0 & 0 & 0 & 0 & 0 & 0 & 0 & \mathbf{I} & 0 & 0 & 0 & 0 & 0 & 0 & 0 \\
0 & \mathbf{I} & 0 & 0 & 0 & 0 & 0 & 0 & 0 & 0 & 0 & 0 & 0 & 0 & 0 \\
0 & 0 & 0 & 0 & 0 & 0 & 0 & 0 & 0 & 0 & 0 & 0 & 0 & 0 & R_{10,15} \\
0 & 0 & \mathbf{I} & 0 & 0 & 0 & 0 & 0 & 0 & 0 & 0 & 0 & 0 & 0 & 0 \\
0 & 0 & 0 & 0 & 0 & 0 & 0 & 0 & \mathbf{I} & 0 & 0 & 0 & 0 & 0 & 0 \\
0 & 0 & 0 & 0 & 0 & 0 & 0 & 0 & 0 & \mathbf{I} & 0 & 0 & 0 & 0 & 0 \\
0 & 0 & 0 & 0 & 0 & 0 & 0 & 0 & 0 & 0 & 0 & 0 & R_{14,13} & 0 & 0 \\
0 & 0 & 0 & 0 & 0 & 0 & 0 & 0 & 0 & 0 & 0 & 0 & 0 & R_{15,14} & 0 \\
0 & 0 & 0 & 0 & 0 & 0 & 0 & 0 & 0 & 0 & \mathbf{I} & 0 & 0 & 0 & 0 \\
0 & 0 & 0 & 0 & 0 & \mathbf{I} & 0 & 0 & 0 & 0 & 0 & 0 & 0 & 0 & 0 \\
0 & 0 & 0 & 0 & 0 & 0 & 0 & 0 & 0 & 0 & 0 & 0 & 0 & 0 & R_{18,15} \\
0 & 0 & 0 & 0 & 0 & 0 & \mathbf{I} & 0 & 0 & 0 & 0 & 0 & 0 & 0 & 0 \\
0 & 0 & 0 & 0 & 0 & 0 & 0 & 0 & 0 & 0 & 0 & \mathbf{I} & 0 & 0 & 0
\end{bmatrix}
\begin{bmatrix} \\ \hat{u}_1 \\ \hat{u}_2 \\ \hat{u}_3 \\ \hat{u}_4 \\ \hat{u}_5 \\ \hat{u}_6 \\ \hat{u}_7 \\ \hat{u}_8 \\ \hat{u}_9 \\ \hat{u}_{10} \\ \hat{u}_{11} \\ \hat{u}_{12} \\ \hat{u}_{13} \\ \hat{u}_{14} \\ \hat{u}_{15} \\ \\ \end{bmatrix}_{Tr}
\tag{3.1.3}
$$

in which $\hat{u}_i$ denotes a three-by-one subvector of nodal displacements except for $\hat{u}_{13}$, $\hat{u}_{14}$, and $\hat{u}_{15}$ on the transition element, which are five-by-one subvectors containing displacements and rotation components. Matrix **I** is the three-by-three identity matrix which relates the nodal displacements of the solid element to the nodal displacements of the transition element where there is a one-to-one correspondence.

The internal virtual work for the solid element is

$$\int_V \delta\varepsilon^T \sigma \, dV = \delta \hat{u}_S^T \, K_S \, \hat{u}_S \tag{3.1.4}$$

By substituting Eq. (2) into Eq. (4) the virtual work statement for the transition element is

$$\int_V \delta\varepsilon^T \sigma dV = \delta \hat{u}_{Tr}^T \, R^T K_S R \, \hat{u}_{Tr} \tag{3.1.5}$$

from which it is clear that the stiffness matrix of the transition element is simply

$$K_{Tr} = R^T K_S R \tag{3.1.6}$$

Although similar in form to a multi-point constraint†, Eq. (6) is applied to the solid element stiffness matrix *before* assembly of the matrix. This frees the user from all matrix manipulations and allows the use of standard solver and finite element libraries.

3.2 *Verification of transition element*

The following test case illustrates the good accuracy of the transition element by comparing results to Surana[31], and to solutions with shell elements.

---

† A multi-point constraint is a procedure with which some of the field variables (called *dependent* or *slave* variables) are expressed in terms of others (the so-called *independent* or *master* variables) through the application of appropriate transformations which eliminate the dependent variables as the system is assembled. Applications for this procedure include *adaptive refinement*, contact-point constraints, multi-body dynamics and *transition* regions. See the COMET's User's Manual, Sect. 6.9, Ref. 34.

3.2.1 Case 1

Consider the cantilever plate shown in Figure 12. The plate consists of a short, thick metal slab ($2in. \times 1.in. \times 0.7in.$) and a very thin long plate ($10in. \times 1.in. \times 0.1in.$) joined together at the mid-plane. The plate is subjected to a bending load of p = 3 lb/in. (loading I) and an inplane load of $p = 12 \times 10^4$ lb/in. (loading II), both acting at the free end (x = 12in) of the plate. The end x = 0 of the plate is clamped. The material properties of the plate are the modulus of elasticity $E = 30 \times 10^6$ psi, and Poisson's ratio $\nu = 0$. The following section details the finite element models implemented on the COMET at the NASA Langley Research Center[34,36].

Model A. The finite element model shown in Figure 12 (b) uses ten 20-node solid elements, one transition element as developed in this study, and six nine-node (EX97 in Testbed) Assumed Natural Strain shell elements.

Model B. The model studied by Surana[31] differs from model A only in the formulation of the transition element (Surana's) and in the number of nodes per shell element (eight instead of nine).

Model C. The model in Fig. 12 (c) consists only of nine 9-node EX97 shell elements.

Deflections are calculated for models A and C described above, and are compared to Surana's results (Model B) for both loading cases.

Loading I. The axial displacement u as a function of the thickness is shown in Fig. 13. at two spanwise locations. Model C differs most significantly from the other two at x = 2. in. where the thickness is discontinuous and the shell model fails to capture the

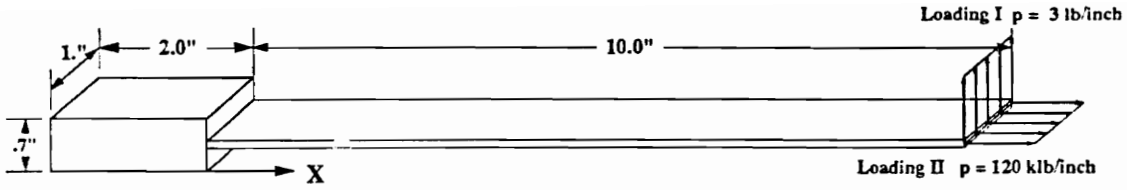

a) Cantilever plate: details of geometry

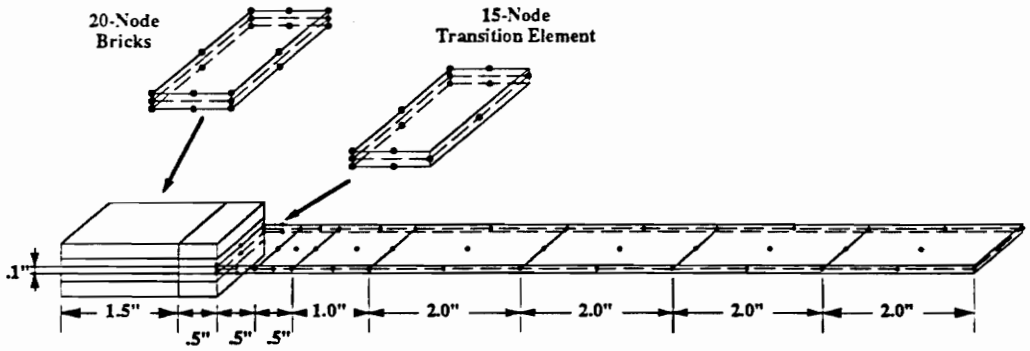

b) Model A : Finite element model with solid, transition and shell elements

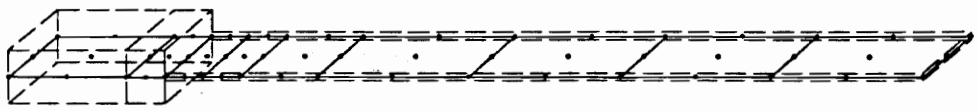

c) Model C : Finite element model with shell elements

Figure 12. Cantilever plate (Case 1): Details of finite element models

Model A : present study

Model B : Surana[31]

Model C : all shell elements

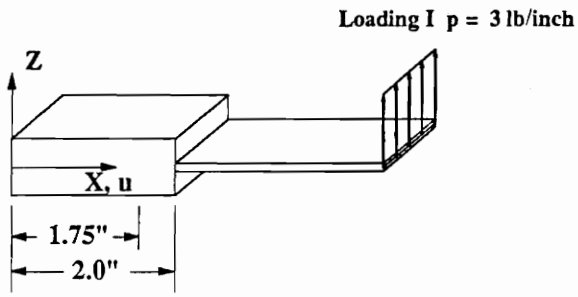

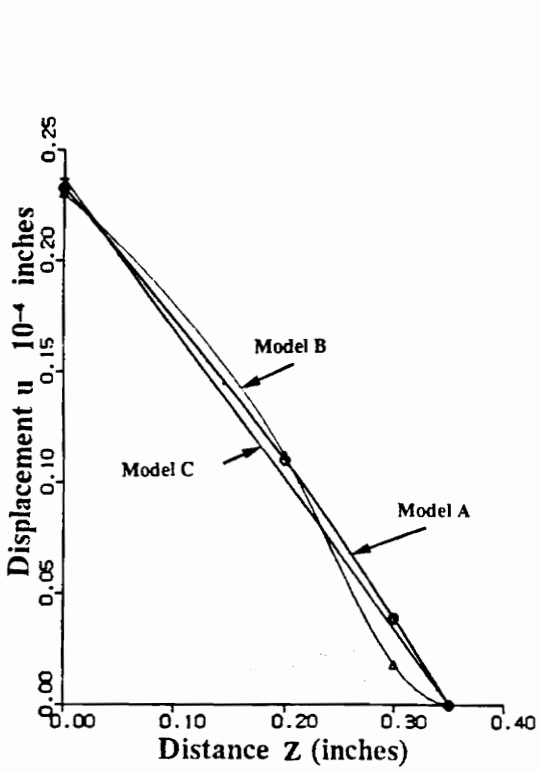

at x = 1.75 in., y = 0.5 in

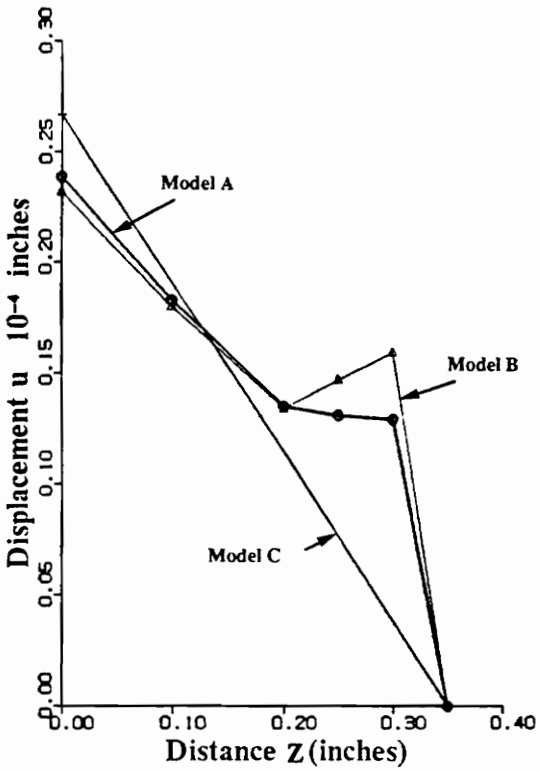

at x = 2.00 in., y = 0.5 in

Figure 13. Loading I: Axial displacement u along the depth of the plate (Case 1)

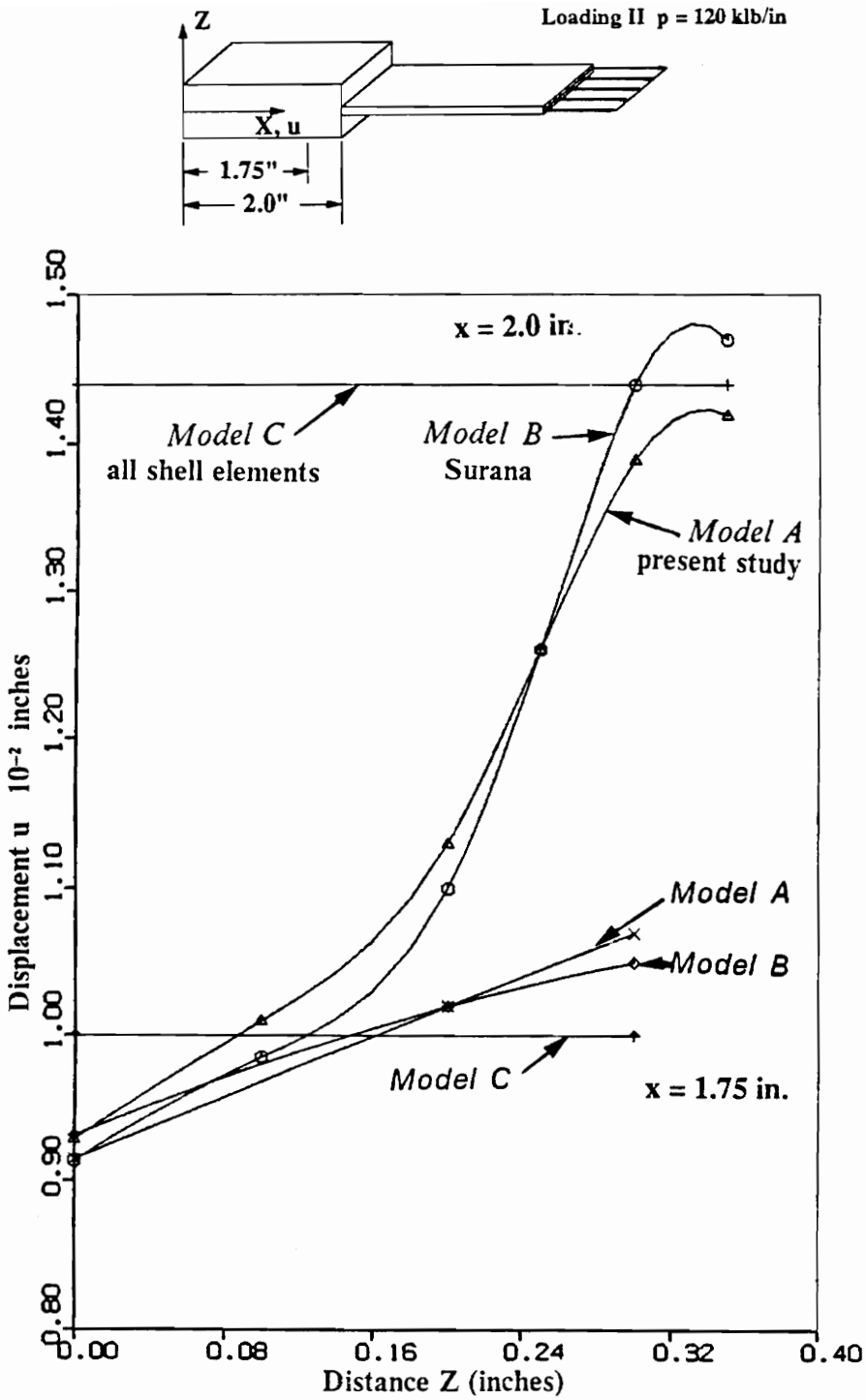

Figure 14. Loading II: Axial displacement u along the depth of the plate (Case 1)

correct deformation. At locations further away from the discontinuity, the correlation between the models substantially improves.

Loading II. A plot of the axial displacement u along the depth of the beam at several spanwise locations is shown in Fig. 14. Once again, Model C fails to capture the correct deformation, in particular at the location of the thickness discontinuity. However, the results of the present study (Model A) are in good agreement with those of Surana (Model B).

3.2.2 Case 2

The purpose of the preceding example was to validate the displacement fields of the transition element developed here. The object of this second case is to illustrate the stress fields in a model consisting of solid elements only (Model A, Fig. 15 a), and compare them against a model consisting of a combination of shell, transition and solid elements (Model B, Fig. 15b). Since transition elements are not recommended for the evaluation of stresses (because the kinematic constraint can introduce stress concentrations), the stresses are calculated only in the solid elements.

The example consists of a twenty-inch long cantilever beam composed of nine plies: a single zero-degree ply above an eight-layer quasi-isotropic sublaminate. (This configuration is somewhat similar to the lower half of the thick side of a dropped-ply laminate). The width of the laminate is five inches, and the thickness is four and a half inches. An inplane load of 6,000 lbs is applied at the free end of the top ply (0-degree) only, as shown in Fig. 15. The mesh is refined near the free end of the beam in order

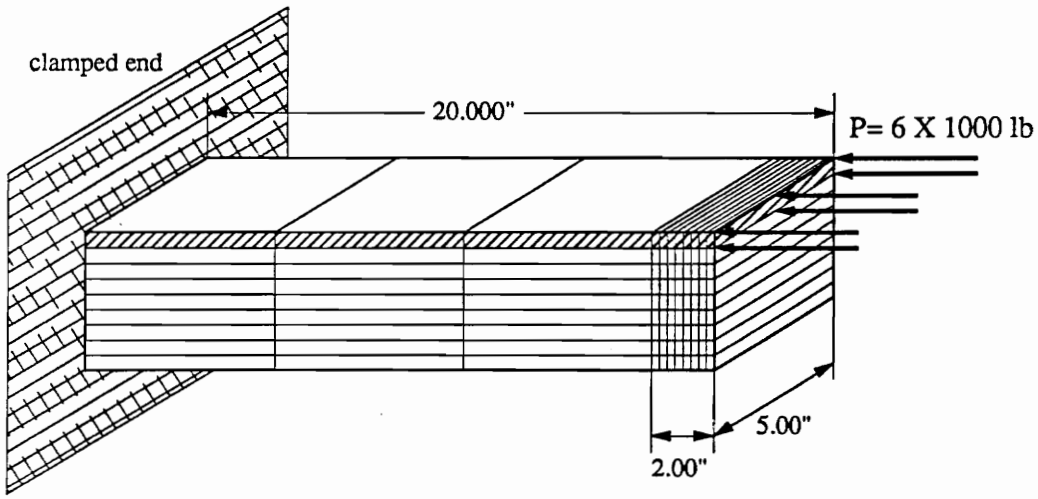

a) Model A: all-solid element model

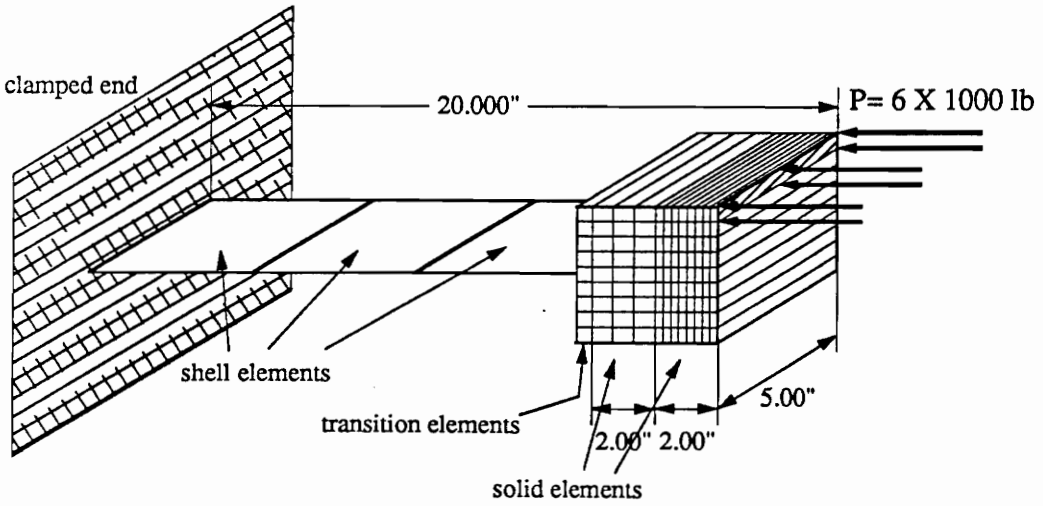

b) Model B: model composed of shell, transition and solid elements

Figure 15. Case 2: cantilever beam

to capture the boundary layer of the stresses near the edge. Model A is thus composed of nine layers of (3+8) 20-node solid elements, for a total of 99 solid elements. Model B is composed of three nine-node shell elements, nine transition elements, and 99 solid elements.

The resulting interlaminar stresses are shown for both models at y = b/2 in Figs. 16a and 16b. The dominant stress is the interlaminar shear stress τ_{xz} shown in Fig. 16a, which results from the load transfer from the zero-degree plies to the quasi-isotropic sublaminate. The agreement between the model consisting of solid elements only and the model composed of the combination of elements is good for both the interlaminar shear stress and normal stress. Although the error is as high as 15% closer to the transition elements, it remains below 4% in the range of highest stresses (last 0.5 inches of span).

3.2.3 Discussion and conclusions on the transition element

Transitions between shell elements and solid elements have usually been effected in one of two ways: 1) a constraint is applied to the finite element model at the transition, or 2) a transition element is developed with its own particular set of node sequences and interpolation functions. The first approach is often difficult to apply and requires a high level of competence from the user. Transition elements such as those developed by Surana[31] and Liao[33], on the other hand, are developed with a set of interpolations based on the positions of the nodes in their natural coordinates. This implies that these elements are designed to have their transition nodes at particular relative locations, such as at the center of the transition face, or at the center of an edge. This excludes the

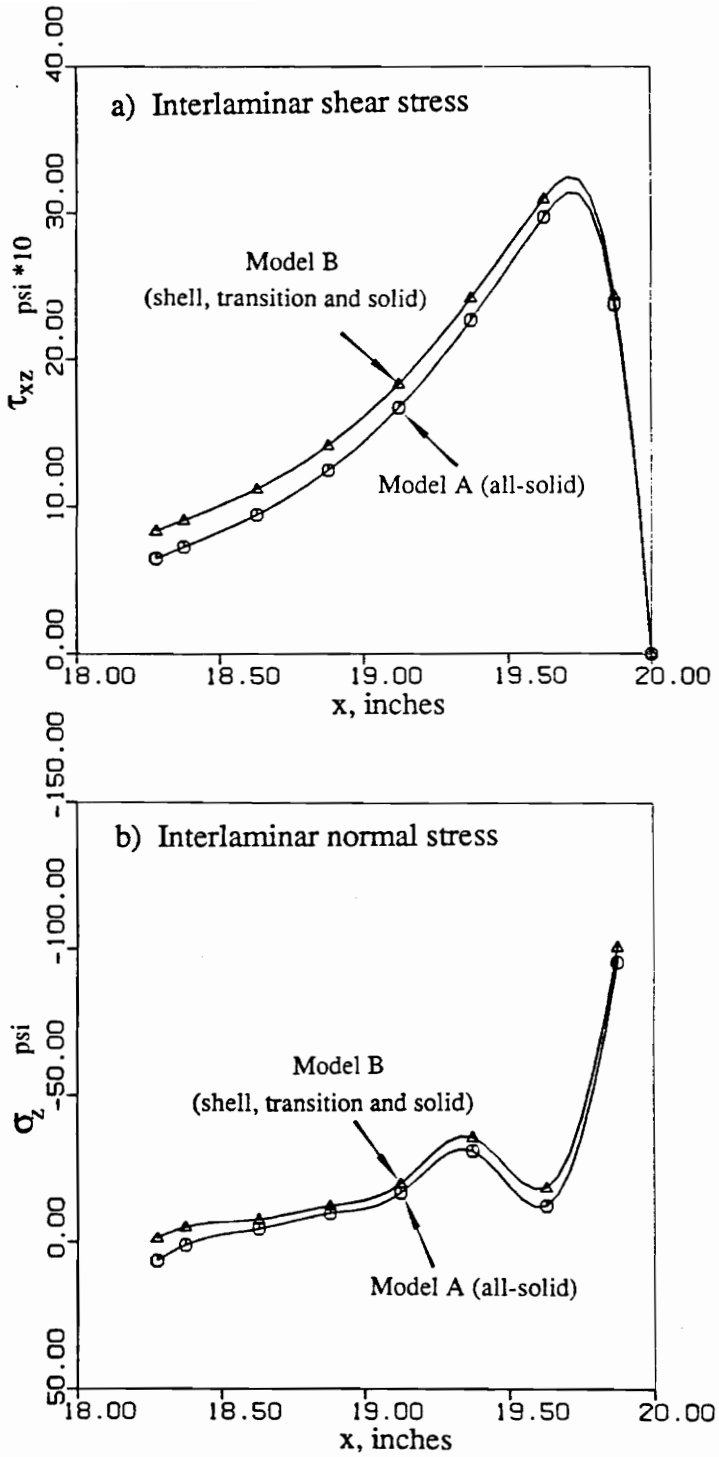

Figure 16. **Interlaminar stresses for cantilever beam at y = b/2:** all-solid model (Model A) and mixed formulation model (Model B) show good agreement near free edge

possibility of connecting more than one of these elements to the same nodes of a shell element.

The method developed here, however, is a combination of the two approaches mentioned above: the transition element is based on a kinematic constraint, but the constraint is applied at an element level where it becomes transparent to the user. The element has its particular node sequence, yet the transition nodes are not constrained by the formulation of the element to specific locations on the transition face. The element developed here provides, therefore, the modeling capabilities of a multi-point constraint and the ease of implementation of a transition element.

Two penalties are associated with the use of a kinematic restraint. Firstly, because it allows the connection of a shell element to any number of solid elements, the bandwidth of the system of equations can become arbitrarily large. This may result in considerably longer execution times. The second penalty concerns the stress gradients that the restraint can introduce, in particular where three-dimensional effects are important. This precludes the use of these elements for the calculation of stresses. In addition, they should be used far enough from the regions of three-dimensional effects in order to prevent the poisoning of stress gradients in their proximity.

The preceding examples demonstrate the use of the transition element in connecting solid elements to shells. The combined use of shell and solid elements allows greater flexibility and optimization in the generation of finite element models.

3.3 Geometrically nonlinear solid element in an incremental formulation

3.3.1 Variational principle

The principle of virtual displacements, or virtual work, for finite displacements of the body is the governing variational principle. This variational statement is given by Eqs. (50) to (52) at the end of this subsection. Its derivation here is given for completeness. Much of what is presented is synthesized from chapter six in Bathe's[29] text on finite elements and chapters four and five of Malvern's[37] text on continuum mechanics.

Let the body in its undeformed, or natural, state have volume designated ${}^0V$, external surface area ${}^0S$, mass density ${}^0\rho$, and reference the material points of the body to cartesian coordinates ${}^0x_i$, i = 1,2,3. The body is subjected to quasi-static loads and displaces to a deformed configuration in equilibrium at time t. Denote the volume of the deformed configuration ${}^tV$, external surface are ${}^tS$, and denote the mass density of the deformed body as ${}^t\rho$. The material point at ${}^0x_i$ in the natural state occupies the spatial point ${}^tx_i$ in the deformed state measured in the same cartesian system. The displacement of this material point is designated ${}^tu_i$, and is given by

$$ {}^tu_i = {}^tx_i - {}^0x_i \tag{3.3.1} $$

For quasi-statically applied loads, ${}^tu_i$ is the displacement of the material points of the body in static equilibrium, and consequently its time derivative is zero. The pre-

superscript "t" on the dependent variables is, then, a notational device to denote a particular static equilibrium state under a given set of loads.

The loads at time t are prescribed tractions ${}^tT_i$ over portion ${}^tS_1$ of the external surface ${}^tS$, and/or prescribed displacements U_i over portion ${}^tS_2$, where ${}^tS = {}^tS_1 \cup {}^tS_2$, ${}^tS_1 \cap {}^tS_2 = 0$. Let ${}^t\tau_{ij}$ denote the cartesian components of the Cauchy stress tensor in the deformed configuration of the body at time t. In the nonpolar case, moment equilibrium shows the Cauchy stress tensor is symmetric. The prescribed surface tractions are related by Cauchy's formula to the stresses as

$$ {}^tT_i = {}^t\tau_{ji}\, {}^tn_j \qquad \text{on } {}^tS_1 \tag{3.3.2} $$

in which ${}^tn_j$ are the cartesian components of the outward unit normal to the external surface ${}^tS_1$. The displacement boundary conditions are

$$ {}^tu_i = {}^tU_i \qquad \text{on } {}^tS_2 \tag{3.3.3} $$

Equilibrium of the body at time t requires

$$ \int_{{}^tS} {}^tT_i \, d\,{}^tS + \int_{{}^tV} {}^tf_i \, d\,{}^tV = 0 \tag{3.3.4} $$

in which ${}^tf_i$ are the cartesian components of the body force per unit volume. Note that the integral of the surface tractions is over the entire surface area in Eq. (4). Substituting for ${}^tT_i$ using Cauchy's formula in Eq. (2) to get

$$ \int_{{}^tS} {}^t\tau_{ji}\, {}^tn_j \, d\,{}^tS + \int_{{}^tV} {}^tf_i \, d\,{}^tV = 0 $$

and then using Gauss' theorem on the surface integral, equilibrium condition (4) becomes

$$\int_{{}^tV} \left(\frac{\partial {}^t\tau_{ji}}{\partial {}^tx_j} + {}^tf_i \right) d\,{}^tV = 0 \tag{3.3.5}$$

Equation (5) is valid for every elemental volume in ${}^tV$ so

$$\frac{\partial {}^t\tau_{ji}}{\partial {}^tx_j} + {}^tf_i = 0 , \quad \text{in } {}^tV \tag{3.3.6}$$

The principle of virtual displacements, or virtual work, is a variational statement of equilibrium. Let δu_i denote the cartesian components of a virtual (infinitesimal) displacement field defined with respect to the body in equilibrium at time t. The virtual field is to be continuous, single-valued, have continuous first derivatives, and vanish on ${}^tS_2$ where displacements are prescribed (kinematically admissible). The virtual work of the stresses, which are constant with respect to the infinitesimal virtual displacements, is

$$\delta W_{\text{int}} = \int_{{}^tV} {}^t\tau_{\text{ij}}\ \delta e_{\text{ij}}\ d\,{}^tV \tag{3.3.7}$$

where the virtual strains accompanying the virtual displacements are

$$\delta e_{\text{ij}} = \frac{1}{2}\left[\frac{\partial \delta {}^tu_i}{\partial {}^tx_j} + \frac{\partial \delta {}^tu_j}{\partial {}^tx_i} \right] \tag{3.3.8}$$

The external virtual work is

$$\delta W_{ext} = \int_{{}^tS_1} {}^tT_i \, \delta u_i \, d\,{}^tS + \int_{{}^tV} {}^tf_i \, \delta u_i \, d\,{}^tV \tag{3.3.9}$$

The principle of virtual displacements states that, if

$$\delta W_{\text{int}} = \delta W_{ext} \tag{3.3.10}$$

for every kinematically admissible virtual displacement field δu_i with respect to the actual field u_i, then the static field is statically admissible. The static field consists of the symmetric stress tensor ${}^t\tau_{ij}$ in ${}^tV$ and the prescribed tractions ${}^tT_i$ on ${}^tS_1$. The static field is statically admissible if it satisfies Eqs. (2) and (6).

The principle of virtual work may be written in terms of variables defined in the natural state. Since the Cauchy stresses are symmetric, Eqs. (7) and (8) imply

$$\delta W_{\text{int}} = \int_{{}^tV} {}^t\tau_{ji} \frac{\partial(\delta \, {}^tu_i)}{\partial \, {}^tx_j} \, d\,{}^tV \tag{3.3.11}$$

Consider the displacements in Eq. (1) as functions of the coordinates of the material points in the natural state, and write Eq. (1) as

$${}^tx_i = {}^0x_i + {}^tu_i({}^0x_j) \tag{3.3.12}$$

Equation (12) defines continuous, single-valued functions ${}^tx_i$ in terms of ${}^0x_i$ in continuum mechanics. The gradient term in the integrand of Eq. (11) may be written using the chain rule as

$$\frac{\partial(\delta\,{}^t u_i)}{\partial {}^t x_j} = \frac{\partial(\delta\,{}^t u_i)}{\partial {}^0 x_k}\,\frac{\partial {}^0 x_k}{\partial {}^t x_j} = \delta\left(\frac{\partial {}^t u_i}{\partial {}^0 x_k}\right)\frac{\partial {}^0 x_k}{\partial {}^t x_j} \tag{3.3.13}$$

The variational operator δ and the differential operator $\partial(\,)/\partial {}^0 x_k$ may be interchanged, as is done in Eq. (13), because the variation implies the change in displacement of a material point and this material point is identified by fixed values of the coordinates ${}^0 x_i$, i.e., the variation is done holding ${}^0 x_i$ fixed. The differential volume element in the deformed configuration is given by the scalar triple product

$$d\,{}^t V = \left[\frac{\partial {}^t x}{\partial {}^0 x_1}\;\frac{\partial {}^t x}{\partial {}^0 x_2}\;\frac{\partial {}^t x}{\partial {}^0 x_3}\right] d^0 x_1\, d^0 x_2\, d^0 x_3 = J\, d\,{}^0 V \tag{3.3.14}$$

in which ${}^t x$ is the position vector of the material point in the deformed state, $d^0 V = d^0 x_1\; d^0 x_2\; d^0 x_3$, and the Jacobian J is

$$J = \det\left(\frac{\partial {}^t x_i}{\partial {}^0 x_j}\right) \tag{3.3.15}$$

The Jacobian is positive under a continuous deformation of matter because Eq. (14) and the conservation of mass (${}^0\rho\, d^0 V = {}^t\rho\, d^t V$) imply

$$J = \frac{{}^0\rho}{{}^t\rho} \tag{3.3.16}$$

with the mass densities always positive. From Eqs. (13) and (14), the transformation of the volume integral in the internal virtual work to the natural state is

$$\delta W_{\text{int}} = \int_{{}_0V} {}^t\tau_{ji}\, \delta\left(\frac{\partial {}^t u_i}{\partial {}^0 x_k}\right) \frac{\partial {}^0 x_k}{\partial {}^t x_j}\, J\, d{}^0V \tag{3.3.17}$$

or

$$\delta W_{\text{int}} = \int_{{}_0V} {}_0^tT_{ki}\, \delta\left(\frac{\partial {}^t u_i}{\partial {}^0 x_k}\right) d{}^0V \tag{3.3.18}$$

in which the first Piola-Kirchhoff stress tensor components are defined by

$${}_0^tT_{ki} = J\, \frac{\partial {}^0 x_k}{\partial {}^t x_j}\, {}^t\tau_{ji} \tag{3.3.19}$$

The notation ${}_0T_{ki}$ means the cartesian stress component "ki" is measured in the natural state, but corresponds to stresses occuring in the deformed state at time t.

The definition of the first Piola-Kirchhoff stress components in terms of the Cauchy stress components in Eq. (19) has a physical basis. Let dP denote the actual force transmitted across an element of area of magnitude $d{}^tS$, and with unit normal components ${}^tn_i$, in the deformed state. Then

$$dP = {}^t\boldsymbol{T}^{(n)}\, d{}^tS \tag{3.3.20}$$

where ${}^t\boldsymbol{T}^{(n)}$ is the Cauchy stress vector (measured in the deformed state). The first Piola-Kirchhoff stress vector ${}_0\boldsymbol{T}^{(n)}$ is defined with respect to the area element in the natural state

$$dP = {}_0^t\boldsymbol{T}^{(n)}\, d{}^0S \tag{3.3.21}$$

That is, the first Piola-Kirchhoff stress vector determines the force transmitted across an area element in the deformed state in terms of the area of the element in the natural state. The stress vectors in the natural and deformed states are related to their respective components by Cauchy's formula. Let $\hat{i}_i$ denote the cartesian unit vectors, then Cauchy's formulae are

$$ {}_0^t T^{(n)} = {}_0^t T_{ji}\ {}^0 n_j\ \hat{i}_i \quad \text{in } {}^0V \tag{3.3.22} $$

$$ {}^t T^{(n)} = {}^t \tau_{ji}\ {}^t n_j\ \hat{i}_i \quad \text{in } {}^t V \tag{3.3.23} $$

Equating the differential forces given by Eqs. (20) and (21), then using (22) and (23), the i^{th} direction components of the equality are

$$ {}_0^t T_{ji}\ {}^0 n_j\ d^0 S = {}^t \tau_{ji}\ {}^t n_j\ d^t S \tag{3.3.24} $$

The relationship for the area change of an infinitesimal area $d^0 S$ in the initial configuration into an area $d^t S$ in the deformed configuration is (see Malvern[37], p.169)

$$ {}^t n_i\ d^t S = J\ \frac{\partial^0 x_j}{\partial^t x_i}\ {}^0 n_j\ d^0 S \tag{3.3.25} $$

Substitute Eq. (25) for ${}^t n_j\, d^t S$ on the right-hand side of (24) to get

$$ {}_0^t T_{ji}\ {}^0 n_j\ d^0 S = {}^t \tau_{ji}\ J\ \frac{\partial^0 x_k}{\partial^t x_j}\ {}^0 n_k\ d^0 S $$

After rearrangement this becomes

$$ \left({}_0^t T_{ki} - J\ \frac{\partial^0 x_k}{\partial^t x_j}\ {}^t \tau_{ji} \right) {}^0 n_k\ d^0 S = 0 \tag{3.3.26} $$

Equation (26) must be valid for every area element at the point in the natural state, so

$$ {}_0^tT_{ki} = J \frac{\partial {}^0x_k}{\partial {}^tx_j} {}^t\tau_{ji} \tag{3.3.27} $$

Equation (27) is the same as (19), and the physical basis of the first Piola-Kirchhoff stress tensor is established.

The integrand of the internal virtual work integral (18) represents the internal virtual work in the deformed state per unit undeformed volume. This integrand is the inner product of the first Piola-Kirchhoff stress tensor and the virtual displacement gradient tensor. The first Piola-Kirchhoff stress tensor and the displacement gradient tensor are said to be conjugate variables. However, neither of these tensors is symmetric. In constitutive equations, it is convenient to use symmetric stress and strain tensors. A stress tensor defined in the natural state that is symmetric is the second Piola-Kirchhoff stress tensor.

The physical basis for the second Piola-Kirchhoff stress tensor is to define the infinitesimal force dP^* acting over an element of area d^0S in the natural state in terms of the actual force dP acting over the element of area d^tS in the deformed state by

$$ dP_i^* = \frac{\partial {}^0x_i}{\partial {}^tx_j} dP_j \tag{3.3.28} $$

in which $\partial {}^0x_i/\partial {}^tx_j$ are the cartesian components of the inverse deformation gradient tensor. The inverse deformation gradient tensor in Eq. (28) is interpreted as operating on the force vector dP_i acting over area d^tS at ${}^tx_i$ in the deformed state to associate with it force vector dP_i^* acting over area d^0S at ${}^0x_i$ in the natural state. From the polar

decomposition theorem, the inverse deformation gradient tensor is equal to the product of an orthogonal rotation tensor and a symmetric positive definite stretch tensor. Thus, definition (28) is equivalent to a stretch of dP_i followed by a rotation to get the force vector dP_i^*.

Denote the second Piola stress vector associated with the infinitesimal force vector dP_i^* by ${}_{\delta}S_i$. Then

$$dP_i^* = {}_0^tS_i \, d^0S \tag{3.3.29}$$

and by Cauchy's formula this stress vector is related to the cartesian components of the second Piola-Kirchhoff stress tensor by

$${}_0^tS_i = {}_0^tS_{ji} \, {}^0n_j \tag{3.3.30}$$

where ${}^0n_j$ is the unit normal to area element d^0S. Combine Eqs. (29) and (30) to get

$$dP_i^* = {}_0^tS_{ji} \, {}^0n_j \, d^0S \quad , \text{ in } {}^0V \tag{3.3.31}$$

In the deformed state the actual force is determined by the Cauchy stresses as

$$dP_i = {}^t\tau_{ji} \, {}^tn_j \, d^tS \quad , \text{ in } {}^tV \tag{3.3.32}$$

Substitute Eqs. (31) and (32) into (28) to obtain

$${}_0^tS_{ji} \, {}^0n_j \, d^0S = \frac{\partial {}^0x_i}{\partial {}^tx_j} \, {}^t\tau_{kj} \, {}^tn_k \, d^tS \tag{3.3.33}$$

Use the formula (25) for the area change in (33) and then rearrange terms to get

$$\left[{}_0^tS_{ji} - J \frac{\partial^0 x_i}{\partial^t x_l} \frac{\partial^0 x_j}{\partial^t x_k} {}^t\tau_{kl} \right] {}^0n_j \, d^0S = 0 \tag{3.3.34}$$

Equation (34) is valid for every area element ${}^0n_j \, d^0S$ at ${}^0x_j$, so the bracketed term in (34) must vanish; i.e., after rearrangement of subscripts,

$${}_0^tS_{ij} = J \frac{\partial^0 x_i}{\partial^t x_k} \frac{\partial^0 x_j}{\partial^t x_l} {}^t\tau_{kl} \tag{3.3.35}$$

Equation (35) relates the Cauchy stresses τ_{kl} to the second Piola-Kirchhoff stresses ${}_0^tS_{ij}$, and, since the former are symmetric, Eq. (35) shows the second Piola-Kirchhoff stresses are also symmetric. Comparing Eqs. (27) and (35), it is seen that the two Piola-Kirchhoff stress tensors are related by

$${}_0^tS_{ij} = \frac{\partial^0 x_j}{\partial^t x_l} {}_0^tT_{il} \tag{3.3.36}$$

or by the inverse relation

$${}_0^tT_{ij} = \frac{\partial^t x_j}{\partial^0 x_k} {}_0^tS_{ik} \tag{3.3.37}$$

Now return to expression (18) for the internal virtual work. Use Eq. (37) to replace the first Piola-Kirchhoff stress tensor by the second Piola Kirchhoff stress tensor and rearrange the subscripts to get

$$\delta W_{\text{int}} = \int_{{}_0V} {}_0^tS_{ij} \frac{\partial^t x_k}{\partial^0 x_j} \delta \left(\frac{\partial^t u_k}{\partial^0 x_i} \right) d^0V \tag{3.3.38}$$

The gradient terms in the integrand of the internal virtual work Eq. (38) can be interpreted in terms of Green's strain tensor whose cartesian components are denoted E_{ij}. Green's strain tensor is defined by the relation

$$(d\,{}^{t}s)^2 - (d\,{}^{0}s)^2 = 2\,{}_{0}^{t}E_{ij}\,d\,{}^{0}x_i\,d\,{}^{0}x_j \tag{3.3.39}$$

in which $d{}^{t}s$ is the length of line element $d{}^{t}x_i$ at ${}^{t}x_i$ in ${}^{t}V$, and $d{}^{0}s$ is the length of line element $d{}^{0}x_i$ at ${}^{0}x_i$ in ${}^{0}V$. Using the pythagorean theorem to compute the squares of the lengths of these line elements, and that the direct transformations ${}^{t}x_i = {}^{t}x_i({}^{0}x_j)$ are continuous functions, Green's strain components defined in Eq. (39) can be written as

$${}_{0}^{t}E_{ij} = \frac{1}{2}\left(\frac{\partial {}^{t}x_k}{\partial {}^{0}x_i}\,\frac{\partial {}^{t}x_k}{\partial {}^{0}x_j} - \delta_{ij}\right) \tag{3.3.40}$$

or

$${}_{0}^{t}E_{ij} = \frac{1}{2}\left(\frac{\partial {}^{t}u_i}{\partial {}^{0}x_j} + \frac{\partial {}^{t}u_j}{\partial {}^{0}x_i} + \frac{\partial {}^{t}u_k}{\partial {}^{0}x_i}\,\frac{\partial {}^{t}u_k}{\partial {}^{0}x_j}\right) \tag{3.3.41}$$

Equation (41) follows from (39) using the definition of displacements in Eq. (1). From Eqs. (40) and (41) it is observed that Green's strain tensor is symmetric.

The first variation of the Green strain components in Eq. (40) is

$$\delta E_{ij} = \frac{1}{2}\left[\delta\left(\frac{\partial {}^{t}x_k}{\partial {}^{0}x_i}\right)\frac{\partial {}^{t}x_k}{\partial {}^{0}x_j} + \frac{\partial {}^{t}x_k}{\partial {}^{0}x_i}\,\delta\left(\frac{\partial {}^{t}x_k}{\partial {}^{0}x_j}\right)\right] \tag{3.3.42}$$

The operations of variation and partial differentiation may be interchanged and $\delta {}^{t}x_k = \delta {}^{t}u_k$, since the variation in position of a material point in the deformed state is done for fixed values of ${}^{0}x_i$. Thus, Eq. (42) becomes

$$\delta E_{ij} = \frac{1}{2}\left[\delta\left(\frac{\partial^t u_k}{\partial^0 x_i}\right)\frac{\partial^t x_k}{\partial^0 x_j} + \frac{\partial^t x_k}{\partial^0 x_i}\,\delta\left(\frac{\partial^t u_k}{\partial^0 x_j}\right)\right] \tag{3.3.43}$$

Now take the inner product of the first variation of the Green strain tensor with the second Piola-Kirchhoff stress tensor to get

$${}_0^tS_{ij}\,\delta E_{ij} = \frac{1}{2}\left[{}_0^tS_{ij}\,\delta\left(\frac{\partial^t u_k}{\partial^0 x_i}\right)\frac{\partial^t x_k}{\partial^0 x_j} + {}_0^tS_{ij}\,\frac{\partial^t x_k}{\partial^0 x_i}\,\delta\left(\frac{\partial^t u_k}{\partial^0 x_j}\right)\right] \tag{3.3.44}$$

Interchange indices i and j in the second term on the right-hand side of Eq. (44), and use symmetry of the second Piola-Kirchhoff stress tensor to obtain

$${}_0^tS_{ij}\,\delta E_{ij} = {}_0^tS_{ij}\,\delta\left(\frac{\partial^t u_k}{\partial^0 x_i}\right)\frac{\partial^t x_k}{\partial^0 x_j} \tag{3.3.45}$$

The right-hand side of Eq. (45) is the integrand in the internal virtual work integral (38). Thus, Eq. (38) becomes

$$\delta W_{\text{int}} = \int_{{}_0V} {}_0^tS_{ij}\,\delta E_{ij}\,d^0V \tag{3.3.46}$$

which shows the internal virtual work in the deformed configuration per unit undeformed volume is the inner product of the second Piola-Kirchhoff stress tensor and the virtual strains obtained from Green's strain tensor. (Note that the variation in the strain components is equivalent to the use of virtual strains.) The advantage to the form of the internal virtual work in Eq. (46) is that both the second Piola-Kirchhoff stress tensor and Green's strain tensor are symmetric. Additionally, the second Piola-

Kirchhoff stress tensor and Green's strain do not change if the body undergoes a rigid body rotation.

In regard to the external virtual work given in Eq. (9), it is assumed that the loads are independent of the deformation. On the basis of Eqs. (20) and (21), the load dP_i acting on the external surface d^tS in the deformed state is defined equal to the load acting over surface d^0S in the natural state. That is,

$$dP_i = {}^tT_i\, d^tS = {}_0^tT_i\, d^0S \tag{3.3.47}$$

in which ${}^tT_i$ is the traction vector in the deformed state and ${}_0^tT_i$ is the first Piola-Kirchhoff traction vector defined in the natural state. With definition (47) and conservation of mass (${}^0\rho\, d^0V = {}^t\rho\, d^tV$), the integrals in the external virtual work Eq. (9) can be transformed from the deformed state to the natural state. For deformation-independent loading, the external virtual work is evaluated by

$$\delta W_{\text{ext}} = \int_{{}^0S_1} {}_0^tT_i\, \delta u_i\, d^0S + \int_{{}^0V} {}_0^tf_i\, \delta u_i\, d^0V \tag{3.3.48}$$

in which the body force per unit volume in the natural state is defined by

$${}_0^tf_i = \frac{{}^0\rho}{{}^t\rho}\, {}^tf_i \tag{3.3.49}$$

Equation (49) implies the body force per unit mass acting on the particle of mass ${}^t\rho\, d^tV$ at position ${}^tx_i$ in the deformed state is equal, by definition, to the body force per unit mass on the particle of mass ${}^0\rho\, d^0V$ at position ${}^0x_i$ in the natural state. The external loads ${}_0^tT_i$ over ${}^0S_1$ and ${}_0^tf_i$ in ${}^0V$ are assumed to be prescribed prior to the analysis to determine the deformed configuration.

In summary, the variational principle that is employed in the finite element formulation is the principle of virtual work. The principle is written in terms of quantities defined in the natural state but it is a statement of equilibrium of the body in its deformed configuration. It is assumed the external loads are independent of the deformation. The variational principle is

$$\delta W_{\text{int}} = \delta W_{\text{ext}} \tag{3.3.50}$$

in which

$$\delta W_{\text{int}} = \int_{{}^0V} {}_0^tS_{ij}\, \delta E_{ij}\, d^0V \tag{3.3.51}$$

and

$$\delta W_{\text{ext}} = \int_{{}^0S_1} {}_0^tT_i\, \delta u_i\, d^0S + \int_{{}^0V} {}_0^tf_i\, \delta u_i\, d^0V \tag{3.3.52}$$

for every kinematically admissible virtual displacement field δu_i with respect to actual displacements ${}^tu_i$. The corresponding virtual change in Green's strain is given by Eq. (43).

3.3.2 Incremental functional for Newton's method

A direct application of the finite element method to the variational principle developed in the previous section is called a total Lagrangian formulation since all dependent variables are referenced to the natural state. The algebraic equations resulting from this functional would be nonlinear, and iteration is necessary to solve these equations. Rather than proceeding in this manner, an incremental functional is devel-

oped from the principle of virtual work, and then the finite element method is applied to it. Consequently, the algebraic equations for iteration by Newton's method are derived directly.

For fixed values of the external loads ${}^{t}T_i$ and ${}^{t}f_i$ in Eq. (52), consider replacing the actual displacement ${}^{t}u_i$ at equilibrium in the principle of virtual work by an approximation. Let this approximation represent a known displacement plus a small increment. The approximation is substituted into the principle of virtual work and the functional is linearized in the increment. The replacement proceeds as follows. Let

$$ {}_0^t u_i \rightarrow {}_0^t u_i + \Delta u_i \tag{3.3.53} $$

in which ${}^{t}u_i$ on the right hand side of this expression is assumed to be known and Δu_i is an unknown small increment. As a result of the replacement (53), Green's strain becomes

$$ {}_0^t E_{ij} \rightarrow {}_0^t E_{ij} + \Delta {}_0^t E_{ij} \tag{3.3.54} $$

in which ${}^{t}E_{ij}$ is determined from the known displacements and the linearized incremental strains are

$$ \Delta {}_0^t E_{ij} = \frac{1}{2} \left[\frac{\partial \Delta u_i}{\partial x_j} + \frac{\partial \Delta u_j}{\partial x_i} + \frac{\partial \Delta u_k}{\partial x_i} \frac{\partial {}_0^t u_k}{\partial x_j} + \frac{\partial {}_0^t u_k}{\partial x_i} \frac{\partial \Delta u_k}{\partial x_j} \right] \tag{3.3.55} $$

in which x_i is understood to be ${}^{0}x_i$ of the natural state. The stresses are replaced as

$$ {}_0^t S_{ij} \rightarrow {}_0^t S_{ij} + \Delta S_{ij} \tag{3.3.56} $$

in which the stresses ${}^{t}S_{ij}$ are determined from strains ${}^{t}E_{ij}$ by the constitutive law. It is assumed that a strain energy density function $u({}^{t}E_{ij})$ exists such that

$$ {}_0^tS_{ij} = \frac{\partial u}{\partial {}_0^tE_{ij}} \tag{3.3.57} $$

so that the stress increment becomes

$$ \Delta S_{ij} = C_{ijkl}\,\Delta E_{kl} \tag{3.3.58} $$

where

$$ C_{ijkl} = \frac{\partial^2 u}{\partial {}_0^tE_{ij}\;\partial {}_0^tE_{kl}} \tag{3.3.59} $$

The replacements (53), (54), and (56) are substituted into the principle of virtual work (52), and then linearized in the increments to get

$$ \begin{aligned} \int_{{}_0V} \left[\Delta S_{ij}\,\delta E_{ij} + {}_0^tS_{ij}\,\delta(\Delta E_{ij}) \right] d^0V = \\ \int_{{}_0S_1} {}_0^tT_i\,\delta u_i\,d^0S + \int_{{}_0V} {}_0^tf_i\,\delta u_i\,d^0V - \int_{{}_0V} {}_0^tS_{ij}\,\delta E_{ij}\,d^0V \end{aligned} \tag{3.3.60} $$

The virtual displacements are not incremented since they are any of a set of kinematically admissible (test) functions, and it is only the actual displacements (in the space of trial functions) that are being determined by iteration. Consequently, the variation of Green's strain and its increment in Eq. (60) are given by

$$ \delta E_{ij} = \frac{1}{2}\left[\frac{\partial \delta u_i}{\partial x_j} + \frac{\partial \delta u_j}{\partial x_i} + \frac{\partial \delta u_k}{\partial x_i}\,\frac{\partial u_k}{\partial x_j} + \frac{\partial u_k}{\partial x_i}\,\frac{\partial \delta u_k}{\partial x_j} \right] \tag{3.3.61} $$

$$ \delta(\Delta E_{ij}) = \frac{1}{2}\left[\frac{\partial \delta u_k}{\partial x_i}\,\frac{\partial \Delta u_k}{\partial x_j} + \frac{\partial \Delta u_k}{\partial x_i}\,\frac{\partial \delta u_k}{\partial x_j} \right] \tag{3.3.62} $$

3.3.3 Isoparametric element formulation

The geometry and displacements of an element are represented by

$$x_i = \sum_{k=1}^{N} h_k(\xi_i)\, x_i^k \tag{3.3.63}$$

$${}_0^t u_i = \sum_{k=1}^{N} h_k(\xi_i)\, \hat{u}_i^k \tag{3.3.64}$$

in which N is the number of nodes in an element, $h_k(\xi_i)$ are the interpolation functions in terms of the normalized coordinates ξ_i, $\xi_i \in (-1,1)$, x_i^k are the nodal coordinates, and $\hat{u}_i^k$ are the nodal displacements. Similarly, the incremental displacements are represented as

$$\Delta u_i = \sum_{k=1}^{N} h_k(\xi_i)\, \Delta\hat{u}_i^k \tag{3.3.65}$$

As a result of Eqs. (64) and (65), the incremental strains in Eq. (55) become

$$
\begin{aligned}
{}_0^t\Delta E_{ij} = \frac{1}{2}\sum_{m=1}^{N}\left[\frac{\partial h_m}{\partial x_j}\,\Delta\hat{u}_i^m + \frac{\partial h_m}{\partial x_i}\,\Delta\hat{u}_j^m\right] \\
+ \frac{1}{2}\left[\sum_{m=1}^{N}\left(\sum_{l=1}^{N}\frac{\partial h_l}{\partial x_j}\,\hat{u}_k^l\right)\frac{\partial h_m}{\partial x_i}\,\Delta\hat{u}_k^m\right. \\
\left. + \sum_{m=1}^{N}\left(\sum_{l=1}^{N}\frac{\partial h_l}{\partial x_i}\,\hat{u}_k^l\right)\frac{\partial h_m}{\partial x_j}\,\Delta\hat{u}_k^m\right]
\end{aligned}
\tag{3.3.66}
$$

It is convenient to introduce a vector notation. Define the six-by-one engineering strain vector as

$$
{}_0^t\boldsymbol{\varepsilon} = \left[{}_0^tE_{11},\ {}_0^tE_{22},\ {}_0^tE_{33},\ 2\,{}_0^tE_{23},\ 2\,{}_0^tE_{31},\ 2\,{}_0^tE_{12}\right]^T \tag{3.3.67}
$$

and the 3N X 1 nodal displacement vector

$$
{}_0^t\hat{\boldsymbol{u}} = \left[\hat{u}_1^1,\ \hat{u}_2^1,\ \hat{u}_3^1,\ \ldots,\ \hat{u}_1^m,\ \hat{u}_2^m,\ \hat{u}_3^m,\ \ldots,\ \hat{u}_1^N,\ \hat{u}_2^N,\ \hat{u}_3^N\right]^T \tag{3.3.68}
$$

The six-by-one incremental strain vector, obtained from Eq. (66), is

$$
\Delta\,{}_0^t\boldsymbol{\varepsilon} = {}_0^t\boldsymbol{B}_L\,\Delta\,\hat{\boldsymbol{u}} \tag{3.3.69}
$$

where ${}_0^t\boldsymbol{B}_L$ is a 6 X 3N strain-displacement matrix. It is written as the sum of two matrices, that is

$$
{}_0^t\boldsymbol{B}_L = \boldsymbol{B}_{L0} + \boldsymbol{B}_{L1} \tag{3.3.70}
$$

Matrix $\boldsymbol{B}_{L0}$ is independent of the displacements and $\boldsymbol{B}_{L1}$ is linearly dependent on the displacements. Each of these matrices can be written in the partitioned form

$$\boldsymbol{B}_{L0} = \left[\boldsymbol{B}_{L0}^{1},\ \boldsymbol{B}_{L0}^{2},\ \ldots,\ \boldsymbol{B}_{L0}^{m},\ \ldots,\ \boldsymbol{B}_{L0}^{N}\right] \tag{3.3.71}$$

$$\boldsymbol{B}_{L1} = \left[\boldsymbol{B}_{L1}^{1},\ \boldsymbol{B}_{L1}^{2},\ \ldots,\ \boldsymbol{B}_{L1}^{m},\ \ldots,\ \boldsymbol{B}_{L1}^{N}\right] \tag{3.3.72}$$

in which the six-by-three submatrices are

$$\boldsymbol{B}_{L0}^{m} = \begin{bmatrix} \dfrac{\partial h_m}{\partial x_1} & 0 & 0 \\ 0 & \dfrac{\partial h_m}{\partial x_2} & 0 \\ 0 & 0 & \dfrac{\partial h_m}{\partial x_3} \\ 0 & \dfrac{\partial h_m}{\partial x_3} & \dfrac{\partial h_m}{\partial x_2} \\ \dfrac{\partial h_m}{\partial x_3} & 0 & \dfrac{\partial h_m}{\partial x_1} \\ \dfrac{\partial h_m}{\partial x_2} & \dfrac{\partial h_m}{\partial x_1} & 0 \end{bmatrix} \tag{3.3.73}$$

$$\boldsymbol{B}_{L1}^{m} = \begin{bmatrix} l_{11}\dfrac{\partial h_m}{\partial x_1} & l_{21}\dfrac{\partial h_m}{\partial x_1} & l_{31}\dfrac{\partial h_m}{\partial x_1} \\ l_{12}\dfrac{\partial h_m}{\partial x_2} & l_{22}\dfrac{\partial h_m}{\partial x_2} & l_{32}\dfrac{\partial h_m}{\partial x_2} \\ l_{13}\dfrac{\partial h_m}{\partial x_3} & l_{23}\dfrac{\partial h_m}{\partial x_3} & l_{33}\dfrac{\partial h_m}{\partial x_3} \\ l_{13}\dfrac{\partial h_m}{\partial x_2} + l_{12}\dfrac{\partial h_m}{\partial x_3} & l_{23}\dfrac{\partial h_m}{\partial x_2} + l_{22}\dfrac{\partial h_m}{\partial x_3} & l_{33}\dfrac{\partial h_m}{\partial x_2} + l_{32}\dfrac{\partial h_m}{\partial x_3} \\ l_{11}\dfrac{\partial h_m}{\partial x_3} + l_{13}\dfrac{\partial h_m}{\partial x_1} & l_{21}\dfrac{\partial h_m}{\partial x_3} + l_{23}\dfrac{\partial h_m}{\partial x_1} & l_{31}\dfrac{\partial h_m}{\partial x_3} + l_{33}\dfrac{\partial h_m}{\partial x_1} \\ l_{12}\dfrac{\partial h_m}{\partial x_1} + l_{11}\dfrac{\partial h_m}{\partial x_2} & l_{22}\dfrac{\partial h_m}{\partial x_1} + l_{21}\dfrac{\partial h_m}{\partial x_2} & l_{32}\dfrac{\partial h_m}{\partial x_1} + l_{31}\dfrac{\partial h_m}{\partial x_2} \end{bmatrix} \tag{3.3.74}$$

in which

$$l_{ij} = \sum_{k=1}^{N} \frac{\partial h_k}{\partial x_j} \hat{u}_i^k = \frac{\partial u_i}{\partial x_j} \tag{3.3.75}$$

The virtual displacements are taken to be in the same space of functions as the finite element space of functions. Thus

$$\delta u_i = \sum_{k=1}^{N} h_k \delta \hat{u}_i^k \tag{3.3.76}$$

and, as a consequence, the virtual engineering strain vector is

$$\delta {}_0^t\boldsymbol{\varepsilon} = {}_0^t\boldsymbol{B}_L \delta \hat{\boldsymbol{u}} \tag{3.3.77}$$

The constitutive law for the incremental stresses in the finite element representation becomes

$$\Delta \tilde{\boldsymbol{S}} = \boldsymbol{C} \Delta {}_0^t\boldsymbol{\varepsilon} \tag{3.3.78}$$

in which the vector of stress increments is

$$\Delta \tilde{\boldsymbol{S}} = [\Delta S_{11}, \Delta S_{22}, \Delta S_{33}, \Delta S_{23}, \Delta S_{31}, \Delta S_{12}]^T \tag{3.3.79}$$

and the matrix $\boldsymbol{C}$ is a symmetric six-by-six matrix of elastic constants that can be related to the fourth order tensor in Eq. (59).

The principle of virtual work in the incremental form of Eq. (60) may be written as a sum over the elements composing the body. Rewriting the first term on the left-hand side of Eq. (60), for an element, in terms of the vector notation gives

$$\int_{{}^0V_e} \Delta S_{ij}\, \delta E_{ij}\, d^0V = \int_{{}^0V_e} \delta {}_0^t\boldsymbol{\varepsilon}^T\, \Delta \tilde{\boldsymbol{S}}\, d^0V \tag{3.3.80}$$

Substituting Eqs. (69), (77), and (78) for the finite element representations of the strains and stresses into Eq. (80) results in

$$\int_{{}^0V_e} \Delta S_{ij}\, \delta E_{ij}\, d^0V = \delta \hat{\boldsymbol{u}}^T \boldsymbol{K}\, \Delta \hat{\boldsymbol{u}} \tag{3.3.81}$$

in which the 3N X 3N stiffness matrix $\boldsymbol{K}$ is

$$\boldsymbol{K} = \int_{{}^0V_e} {}_0^t\boldsymbol{B}_L^T\, \boldsymbol{C}\, {}_0^t\boldsymbol{B}_L\, d^0V \tag{3.3.82}$$

For an element, the second term on the left-hand side of Eq. (60) is, upon using Eq. (62), rewritten as

$$\int_{{}^0V_e} {}_0^tS_{ij}\, \delta(\Delta E_{ij})\, d^0V = \int_{{}^0V_e} {}_0^tS_{ij}\, \frac{\partial \delta u_k}{\partial x_i}\, \frac{\partial \Delta u_k}{\partial x_j}\, d^0V \tag{3.3.83}$$

since ${}_0^tS_{ij}$ is symmetric. Substituting Eq. (64) for the displacements, and Eq. (76) for the virtual displacements, into Eq. (83) gives

$$\int_{{}_0V_e} {}_0^tS_{ij}\,\delta(\Delta E_{ij})\,d^0V = \sum_{l=1}^{N}\sum_{m=1}^{N} \delta\hat{u}_k^l \int_{{}_0V_e} \frac{\partial h_l}{\partial x_i}\,{}_0^tS_{ij}\,\frac{\partial h_m}{\partial x_j}\,d^0V\,\Delta\hat{u}_k^m \tag{3.3.84}$$

The summation on indices i, j, and k from one to three on the right-hand side of Eq. (84) may be written in vector notation. Let ∇h_m denote the three-by-one gradient vector of the interpolation function for the m^{th} node, i.e.,

$$\nabla h_m = \left[\frac{\partial h_m}{\partial x_1}\,,\ \frac{\partial h_m}{\partial x_2}\,,\ \frac{\partial h_m}{\partial x_3}\right]^T \tag{3.3.85}$$

Define a nine-by-three gradient matrix $(\boldsymbol{B}_{NL})_m$ for the m^{th} node as

$$(\boldsymbol{B}_{NL})_m = \begin{bmatrix} \nabla h_m & \tilde{0} & \tilde{0} \\ \tilde{0} & \nabla h_m & \tilde{0} \\ \tilde{0} & \tilde{0} & \nabla h_m \end{bmatrix} \tag{3.3.86}$$

in which the three-by-one null vector is

$$\tilde{0} = [0\ \ 0\ \ 0]^T \tag{3.3.87}$$

Equation (84) in vector notation (which is equivalent to indices i, j, and k summed out) is

$$\int_{{}_0V_e} {}_0^t\boldsymbol{S}\,\delta\,(\Delta\boldsymbol{E})\,d^0V = \sum_{l=1}^{N}\sum_{m=1}^{N} (\delta\hat{\boldsymbol{u}}^l)^T \int_{{}_0V_e} (\boldsymbol{B}_{NL})_l^T\,{}_0^t\boldsymbol{S}\,(\boldsymbol{B}_{NL})_m\,d^0V\,\Delta\hat{\boldsymbol{u}}^m \tag{3.3.88}$$

in which the nine-by-nine stress matrix in partitioned form is

$$ {}_0^t\boldsymbol{S} = \begin{bmatrix} {}_0^t\tilde{\boldsymbol{S}} & 0 & 0 \\ 0 & {}_0^t\tilde{\boldsymbol{S}} & 0 \\ 0 & 0 & {}_0^t\tilde{\boldsymbol{S}} \end{bmatrix} \tag{3.3.90} $$

Finally, the double summation over the N-nodes of the element in Eq. (88) may be replaced by the vector notation

$$ \int_{{}^0V_e} S_{ij}\, \delta\,(\Delta E_{ij})\, d\,{}^0V = \delta\hat{\boldsymbol{u}}^T\, \boldsymbol{K}_{NL}\, \Delta\hat{\boldsymbol{u}} \tag{3.3.91} $$

in which the 3N by 3N initial stress matrix, or geometric stiffness matrix, $\boldsymbol{K}_{NL}$ is defined by

$$ \boldsymbol{K}_{NL} = \int_{{}^0V_e} \boldsymbol{B}_{NL}^T\, {}_0^t\boldsymbol{S}\, \boldsymbol{B}_{NL}\, d\,{}^0V \tag{3.3.92} $$

and the 9-by-3N gradient matrix is defined in the partitioned form

$$ \boldsymbol{B}_{NL} = [(\boldsymbol{B}_{NL})_1\,,\ (\boldsymbol{B}_{NL})_2\,,\ \ldots\,,\ (\boldsymbol{B}_{NL})_N] \tag{3.3.93} $$

Using the virtual displacement (76) for an element, the external virtual work term on the right-hand side of Eq. (60) becomes

$$ \int_{{}^0S_{1e}} {}_0^tT_i\, \delta u_i\, d\,{}^0S + \int_{{}^0V} {}_0^tf_i\, \delta u_i\, d\,{}^0V = \delta\hat{\boldsymbol{u}}^T\, \boldsymbol{R} \tag{3.3.94} $$

in which the 3N X 1 external force vector is

$$\boldsymbol{R} = \left[R_1^1,\ R_2^1,\ R_3^1,\ \ldots,\ R_1^m,\ R_2^m,\ R_3^m,\ \ldots,\ R_1^N,\ R_2^N,\ R_3^N\right]^T \tag{3.3.95}$$

and element

$$R_i^m = \int_{{}_0S_{1\sigma}} {}_0^tT_i\, h_m\, d^0S + \int_{{}_0V_\sigma} {}_0f_i\, h_m\, d^0V \tag{3.3.96}$$

The second term on the right-hand side of the incremental functional in Eq. (60) can be rewritten using matrix notation as

$$\int_{{}_0V_\sigma} {}_0^tS_{ij}\, \delta E_{ij}\, d^0V = \int_{{}_0V_\sigma} \delta {}_0^t\boldsymbol{\varepsilon}^T\, {}_0^t\hat{\boldsymbol{S}}\, d^0V \tag{3.3.97}$$

where the six-by-one stress vector is

$${}_0^t\hat{\boldsymbol{S}} = \left[{}_0^tS_{11},\ {}_0^tS_{22},\ {}_0^tS_{33},\ {}_0^tS_{23},\ {}_0^tS_{31},\ {}_0^tS_{12}\right]^T \tag{3.3.98}$$

Substitution of Eq. (77) into (93) gives

$$\int_{{}_0V_\sigma} {}_0^tS_{ij}\, \delta E_{ij}\, d^0V = \delta\hat{\boldsymbol{u}}^T \int_{{}_0V_\sigma} {}_0^t\boldsymbol{B}_L^T\, {}_0^t\hat{\boldsymbol{S}}\, d^0V = \delta\hat{\boldsymbol{u}}^T\boldsymbol{F} \tag{3.3.99}$$

in which the internal force vector is

$$\begin{aligned}\boldsymbol{F} &= \int_{{}_0V_\sigma} {}_0^t\boldsymbol{B}_L^T\, {}_0^t\hat{\boldsymbol{S}}\, d^0V \\ &= \left[F_1^1,\ F_2^1,\ F_3^1,\ \ldots,\ F_1^m,\ F_2^m,\ F_3^m,\ \ldots,\ F_1^N,\ F_2^N,\ F_3^N\right]^T\end{aligned} \tag{3.3.100}$$

3.3.4 Solution procedure: Crisfield's algorithm

The solution procedure used to solve equations (50) is based on a modified Newton/Raphson incremental strategy with automatic load-step control. The procedure was written by G.M. Stanley of Lockheed Palo Alto Research Laboratory, as described in Ref. 38, and is based on a variant of Crisfield's algorithm. This procedure solves an "extended" system of equations which can be written:

$$\begin{aligned} \boldsymbol{r}(\boldsymbol{d}, \lambda) &= 0 \qquad \text{(equilibrium)} \\ c(\boldsymbol{d}, \lambda) &= 0 \qquad \text{(arc-length constraint)} \end{aligned} \tag{3.3.101}$$

where $\boldsymbol{r}$ represents the residual (or out-of-balance) force vector, $\boldsymbol{d}$ is the displacement vector for the assembled model, λ is the external load parameter, and c is a single constraint equation governing the maximum "arc-length" to be traversed in a single solution increment along a load-displacement curve. The purpose of the procedure is to determine a statically connected set of configurations $(\boldsymbol{d}, \lambda)$ representing the load-displacement history of the finite element model.

The arc-length constraint is added to the set of equations so that i) the user does not have to select the load increment, and ii) the solution algorithm can automatically traverse limit points, i.e., maxima and minima on the load-displacement curve.

The algorithm features i) polynomial extrapolation of converged solutions, ii) an energy error norm that properly weighs translational and rotational freedoms, and iii) generalization to large rotations, specified displacements and live loads.

3.4 *Transition element for geometrically nonlinear analysis via an incremental formulation*

The restraint matrix $\boldsymbol{R}$ shown in Eq. (3.1.3) for a linear analysis is a function only of the difference in thickness coordinates d_{kj} from the solid element node k to the transition node j in the undeformed configuration. This linear approximation, where displacements are proportional to rotation angles, is not valid for large rotations, in which case displacements are trigonometric functions of the rotations.

An incremental restraint matrix $\boldsymbol{R}$ for geometrically nonlinear problems is developed below for use in conjunction with iterative methods for the solution of nonlinear problems. It will be shown that $\boldsymbol{R}$, like the tangent stiffness, is a function of displacements as well as geometry.

Let ${}^0\overline{P} = (0, 0, d_{kj})^T$ be a normal to the undeformed surface of length $|d_{kj}|$ at node j. As mentioned earlier, the element and local reference frame are defined so that the undeformed normal is in the z direction. At time t, the normal at node j has rotated to position ${}^t\overline{P}$ by the angles α_j and β_j as shown in Fig. 17. In accordance with Mindlin-Reissner plate theory, the normal rotates while remaining rigid under deformation. Its length stays equal to $|d_{kj}|$. The components of ${}^t\overline{P}$ are

$$ {}^t\overline{P} = d_{kj} \begin{bmatrix} {}^t\lambda_1 \\ {}^t\lambda_2 \\ {}^t\lambda_3 \end{bmatrix} \tag{3.4.1} $$

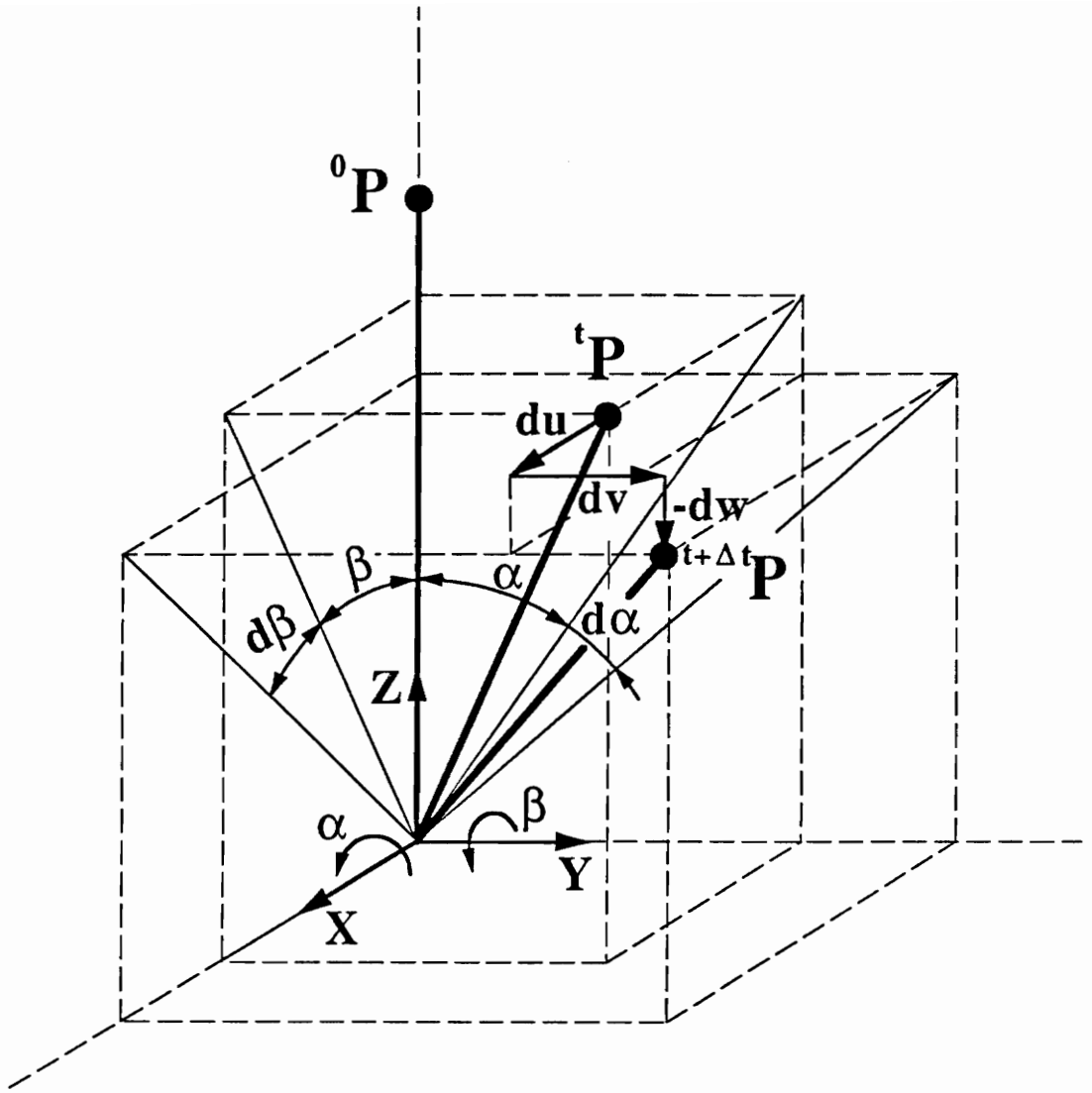

Figure 17. Rotation of Normal to Surface: Incremental displacements obtained from incremental rotations

where ${}^t\lambda_1$, ${}^t\lambda_2$, and ${}^t\lambda_3$ are the direction cosines of the normal. They are related to the angles α_j and β_j as

$$
\begin{aligned}
{}^t\lambda_3 &= \frac{\cos\alpha_j \;\cos\beta_j}{\sqrt{\cos^2\alpha_j + \cos^2\beta_j - \cos^2\alpha_j\,\cos^2\beta_j}} \\
{}^t\lambda_2 &= -\tan\alpha_j\,\lambda_3 \\
{}^t\lambda_1 &= \frac{\cos\alpha_j \;\sin\beta_j}{\sqrt{\cos^2\alpha_j + \cos^2\beta_j - \cos^2\alpha_j\,\cos^2\beta_j}}
\end{aligned}
\tag{3.4.2}
$$

where the signs are chosen to make the expressions valid in the range $-\pi/2 < \alpha_j,\ \beta_j < \pi/2$.

For small to moderate incremental rotations the following approximations are valid:

$$
\begin{aligned}
{}^{t+\Delta t}\alpha &= {}^t\alpha + d\alpha \\
{}^{t+\Delta t}\beta &= {}^t\beta + d\beta
\end{aligned}
\tag{3.4.3}
$$

The effect of rotation at node j on the translational displacements of the solid-element at node k is obtained from the difference of the position vectors:

$$
(\mathrm{du},\ \mathrm{dv},\ \mathrm{dw})_k^T = {}^{t+\Delta t}\overline{P} - {}^t\overline{P} \tag{3.4.4}
$$

At time $t + \Delta t$ the director cosine ${}^{t+\Delta t}\lambda_3$ is

$$
{}^{t+\Delta t}\lambda_3 = \frac{\cos(\alpha_j + d\alpha_j)\;\cos(\beta_j + d\beta_j)}{\sqrt{\cos^2(\alpha_j + d\alpha_j) + \cos^2(\beta_j + d\beta_j) - \cos^2(\alpha_j + d\alpha_j)\;\cos^2(\beta_j + d\beta_j)}} \tag{3.4.5}
$$

Since the angles $d\alpha_j$ and $d\beta_j$ are assumed to be small, the application of trigonometric identities to the sines and cosines of sums of angles yields the expression

$$ {}^{t+\Delta t}\lambda_3 = \frac{N_1 + N_2\, d\alpha + N_3\, d\beta}{\sqrt{D_1 + D_2\, d\alpha + D_3\, d\beta}} \tag{3.4.6} $$

where the terms N_1, N_2, N_3, D_1, D_2 and D_3 are defined as follows:

$$ \begin{aligned} N_1 &= \cos\alpha_j \cos\beta_j \\ N_2 &= -\sin\alpha_j \cos\beta_j \\ N_3 &= -\cos\alpha_j \sin\beta_j \\ D_1 &= \cos^2\alpha_j + \cos^2\beta_j - \cos^2\alpha_j \cos^2\beta_j \\ D_2 &= -\sin^2\beta_j \sin 2\alpha_j \\ D_3 &= -\sin^2\alpha_j \sin 2\beta_j \end{aligned} \tag{3.4.7} $$

The quotient in Eq. (6) is linearized by developing it in a Taylor series in dα and dβ. Truncation of the series to include only linear terms yields the following approximation:

$$ {}^{t+\Delta t}\lambda_3 \simeq \frac{N_1}{\sqrt{D_1}} + \frac{N_2\sqrt{D_1} - \dfrac{N_1 D_2}{2\sqrt{D_1}}}{D_1}\, d\alpha + \frac{N_3\sqrt{D_1} - \dfrac{N_1 D_3}{2\sqrt{D_1}}}{D_1}\, d\beta \tag{3.4.8} $$

Remembering that ${}^t\lambda_3 = N_1/\sqrt{D_1}$, then the component of the incremental displacement in the z direction (including effect of rotation only) is

$$ dw \simeq d_{kj}({}^{t+\Delta t}\lambda_3 - {}^t\lambda_3) = d_{kj}(fw_{\alpha j} + fw_{\beta j}) \tag{3.4.9} $$

where the functions $fw_{\alpha j}$ and $fw_{\beta j}$ are the coefficients of dα and dβ in Eq. (8).

The translation components in the x and y directions can be expressed in a similar manner, and the linearized displacements are expressed in their final form:

$$\begin{aligned} \Delta u_k &= d_{kj}\,(fu_{\alpha j}\,\Delta\alpha \;+\; fu_{\beta j}\,\Delta\beta\,) \\ \Delta v_k &= d_{kj}\,(fv_{\alpha j}\,\Delta\alpha \;+\; fv_{\beta j}\,\Delta\beta\,) \\ \Delta w_k &= d_{kj}\,(fw_{\alpha j}\,\Delta\alpha \;+\; fw_{\beta j}\,\Delta\beta\,) \end{aligned} \tag{3.4.10}$$

where the functions used above are:

$$fu_{\alpha j} = \frac{-\sin\alpha_j\,\sin\beta_j + \cos\alpha_j\,\sin\beta_j\,\dfrac{\sin 2\alpha_j\,\sin^2\beta_j}{2(\cos^2\alpha_j+\cos^2\beta_j-\cos^2\alpha_j\,\cos^2\beta_j)}}{\sqrt{\cos^2\alpha_j+\cos^2\beta_j-\cos^2\alpha_j\,\cos^2\beta_j}}$$

$$fu_{\beta j} = \frac{\cos\alpha_j\,\cos\beta_j + \cos\alpha_j\,\sin\beta_j\,\dfrac{\sin 2\beta_j\,\sin^2\alpha_j}{2(\cos^2\alpha_j+\cos^2\beta_j-\cos^2\alpha_j\,\cos^2\beta_j)}}{\sqrt{\cos^2\alpha_j+\cos^2\beta_j-\cos^2\alpha_j\,\cos^2\beta_j}}$$

$$fv_{\alpha j} = \frac{-\cos\alpha_j\cos\beta_j - \sin\alpha_j\cos\beta_j\,\dfrac{\sin 2\alpha_j\,\sin^2\beta_j}{2(\cos^2\alpha_j+\cos^2\beta_j-\cos^2\alpha_j\,\cos^2\beta_j)}}{\sqrt{\cos^2\alpha_j+\cos^2\beta_j-\cos^2\alpha_j\,\cos^2\beta_j}}$$

$$fv_{\beta j} = \frac{\sin\alpha_j\,\sin\beta_j - \sin\alpha_j\,\cos\beta_j\,\dfrac{\sin 2\beta_j\,\sin^2\alpha_j}{2(\cos^2\alpha_j+\cos^2\beta_j-\cos^2\alpha_j\,\cos^2\beta_j)}}{\sqrt{\cos^2\alpha_j+\cos^2\beta_j-\cos^2\alpha_j\,\cos^2\beta_j}} \tag{3.4.11}$$

$$fw_{\alpha j} = \frac{-\sin\alpha_j\,\cos\beta_j + \cos\alpha_j\,\cos\beta_j\,\dfrac{\sin 2\alpha_j\,\sin^2\beta_j}{2(\cos^2\alpha_j+\cos^2\beta_j-\cos^2\alpha_j\,\cos^2\beta_j)}}{\sqrt{\cos^2\alpha_j+\cos^2\beta_j-\cos^2\alpha_j\,\cos^2\beta_j}}$$

$$fw_{\beta j} = \frac{-\cos\alpha_j\,\sin\beta_j + \cos\alpha_j\,\cos\beta_j\,\dfrac{\sin 2\beta_j\,\sin^2\alpha_j}{2(\cos^2\alpha_j+\cos^2\beta_j-\cos^2\alpha_j\,\cos^2\beta_j)}}{\sqrt{\cos^2\alpha_j+\cos^2\beta_j-\cos^2\alpha_j\,\cos^2\beta_j}}$$

Equation (10) can more conveniently be written in matrix form:

$$ {}^{t+\Delta t}\overline{P} - {}^{t}\overline{P} = \begin{Bmatrix} \Delta u_k \\ \Delta v_k \\ \Delta w_k \end{Bmatrix} = d_{kj} \begin{bmatrix} fu_{\alpha j} & fu_{\beta j} \\ fv_{\alpha j} & fv_{\beta j} \\ fw_{\alpha j} & fw_{\beta j} \end{bmatrix} \begin{bmatrix} \Delta\alpha_j \\ \Delta\beta_j \end{bmatrix} \tag{3.4.12} $$

The submatrix $[R_{kj}]$ which takes into account the combined effect of rotations and translations at the transition node can now be written in a form similar to its linear counterpart, Eq. (3.1.1). The total incremental displacement of solid-element node k in terms of the transition element node j is, therefore:

$$ \begin{bmatrix} \Delta u_k \\ \Delta v_k \\ \Delta w_k \end{bmatrix}_S = [R_{kj}]\,\{\Delta\hat{u}_j\}_{Tr} = \begin{bmatrix} 1 & 0 & 0 & d_{kj}fu_{\alpha j} & d_{kj}fu_{\beta j} \\ 0 & 1 & 0 & d_{kj}fv_{\alpha j} & d_{kj}fv_{\beta j} \\ 0 & 0 & 1 & d_{kj}fw_{\alpha j} & d_{kj}fw_{\beta j} \end{bmatrix} \begin{bmatrix} \Delta u_j \\ \Delta v_j \\ \Delta w_j \\ \Delta\alpha_j \\ \Delta\beta_j \end{bmatrix}_{Tr} \tag{3.4.13} $$

The formulation of the finite element stiffness matrix and internal force vector for the transition element are obtained directly from the formulations of the nonlinear solid element derived in the previous section. Denoting by $\Delta\hat{u}_S$ the incremental displacement vector of the solid element and $\Delta\hat{u}_{Tr}$ the incremental vector of the transition element, Eq. (3.3.81) gives the linear component of the tangential stiffness

$$ \int_{{}^0V_e} \Delta S_{ij}\,\delta E_{ij}\,d\,{}^0V = \delta\hat{u}_S^T\,[K]_S\,\Delta\hat{u}_S \tag{3.4.14} $$

The geometric stiffness term is given by Eq. (3.3.91)

$$\int_{{}^0V_e} {}_0^tS_{ij}\,\delta(\Delta E_{ij})\,d\,{}^0V = \delta\hat{u}_S^T\,[K_{NL}]_S\,\Delta\hat{u}_S \tag{3.4.15}$$

The internal force vector is given by Eq. (3.3.99)

$$\int_{{}^0V_e} {}_0^tS_{ij}\,\delta E_{ij}\,d\,{}^0V = \delta\hat{u}_S^T F_S \tag{3.4.16}$$

By substituting $\Delta\hat{u}_S = R\,\Delta\hat{u}_{Tr}$ into expressions (14), (15) and (16), it is readily observed that, like in the linear case, the nonlinear transition element is easily constructed from the solid element and its associated constraint matrix:

$$\begin{aligned} [K]_{Tr} &= R^T[K]_S R \\ [K_{NL}]_{Tr} &= R^T[K_{NL}]_S R \\ F_{Tr} &= R^T F_S \end{aligned} \tag{3.4.17}$$

3.5 *Validation of the geometrically nonlinear solid and transition Elements*

The geometrically nonlinear 20-node solid element and the 15-node transition element developed above were validated with the following test cases: The first test case compares the accuracy of the elements against a one-dimensional exact solution. The

second case compares the two elements against a nonlinear solution using well proven shell elements[34].

3.5.1 Case 1

This first case consists of a one-dimensional response problem using a single-element, and tests the nonlinear behavior of the elements under large extensional strains. The geometry of the problem for the solid and transition elements is illustrated in Figs. 18a and 18b, respectively. It consists of a homogeneous cube two centimeters long which has a uniform displacement applied at all nodes of one face while the opposite face is restrained. All degrees of freedom v and w in the y and z directions, respectively, are restrained to remain zero.

It can be shown (Bathe[29], p. 385) that the Green-Lagrange strain is

$$ {}^{t}_{0}\varepsilon_{11} = \frac{1}{2}\left[\left(\frac{{}^{t}L}{{}^{0}L}\right)^{2} - 1\right] \tag{3.5.1} $$

where ${}^{t}L$ and ${}^{0}L$ are the lengths of the cube at time t and in the undeformed configuration, respectively. The 2nd Piola-Kirchhoff stress is related to the applied load ${}^{t}P$ by:

$$ {}^{t}_{0}S_{11} = \left(\frac{{}^{t}P}{\overline{A}}\right)\left(\frac{{}^{0}L}{{}^{t}L}\right) \tag{3.5.2} $$

where $\overline{A}$ is the area of a face of the undeformed cube.

For the purpose of this example, Hooke's law is assumed applicable to very large strains (Hooke's law is usually only applicable to small strains). This can be written as

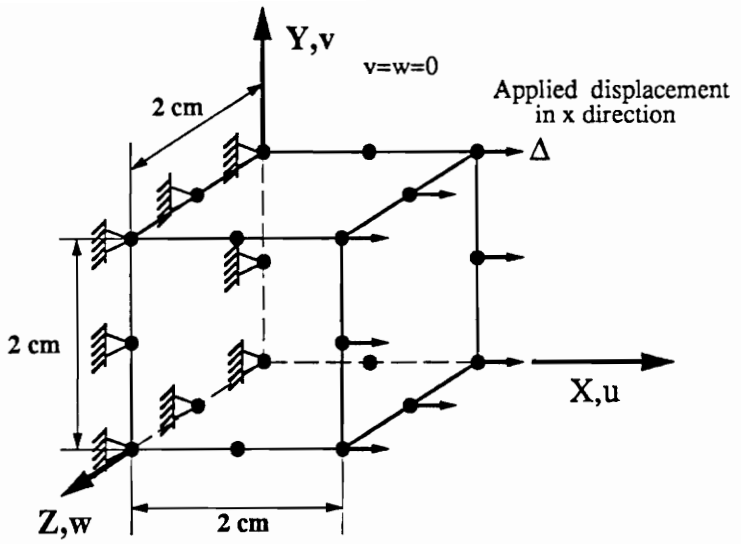

a) 20-Node Solid Element

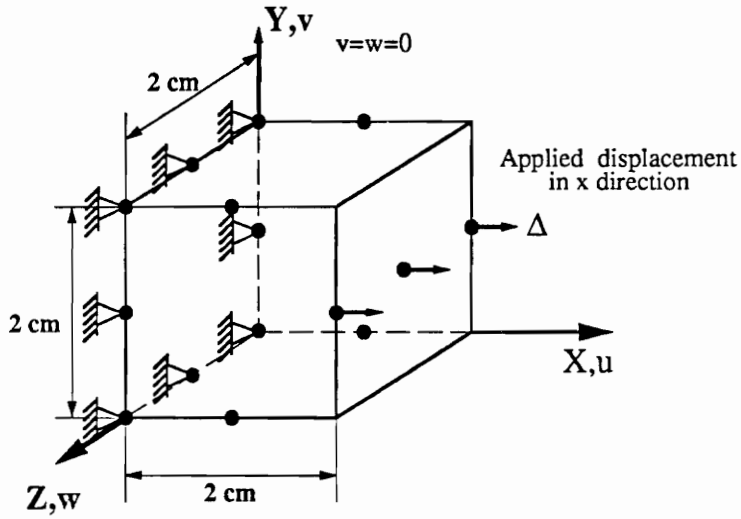

b) 15-Node Transition Element

Figure 18. Test of nonlinear behavior of elements under large strains: configuration and loading of the problem

$$ {}_0^tS_{11} = \frac{E(1-\nu)}{(1+\nu)(1-2\nu)} {}_0^t\varepsilon_{11} \tag{3.5.3} $$

since $\delta\varepsilon_{22} = \delta\varepsilon_{33} = 0$

The agreement between the exact solution and the finite element solution is excellent for both the 20-node solid element and the 15-node transition element, as shown in Fig. 19.

3.5.2 Case 2

The problem for this case consists of an 8-ply quasi-isotropic laminate, $[\pm 45, 0, 90]_s$, 20 inches long and one inch wide. The plate is simply-supported at both ends. The supports are fixed against longitudinal motion u, and in out-of-plane deflection w. The transverse displacement v is unrestricted. The plies are 0.00536 inches thick. The material properties are: $E_1 = 18.5\ 10^6$ psi., $E_2 = E_3 = 1.64\ 10^6$ psi., $\nu_{12} = \nu_{13} = 0.3$, $\nu_{23} = 0.35$, $G_{12} = G_{13} = 0.87\ 10^6$ psi., $G_{23} = 0.49\ 10^6$ psi..

The four finite element models shown in Fig. 20 are used to assess the accuracy of the solid and transition elements.

Model A: This model consists of ten 20-node solid elements along the span of the plate. Symmetry at midspan and widthwise is used to reduce the size of the model and to conserve acceptable element proportions (the height/width and height/length ratios have been limited to about 1/20 or less).

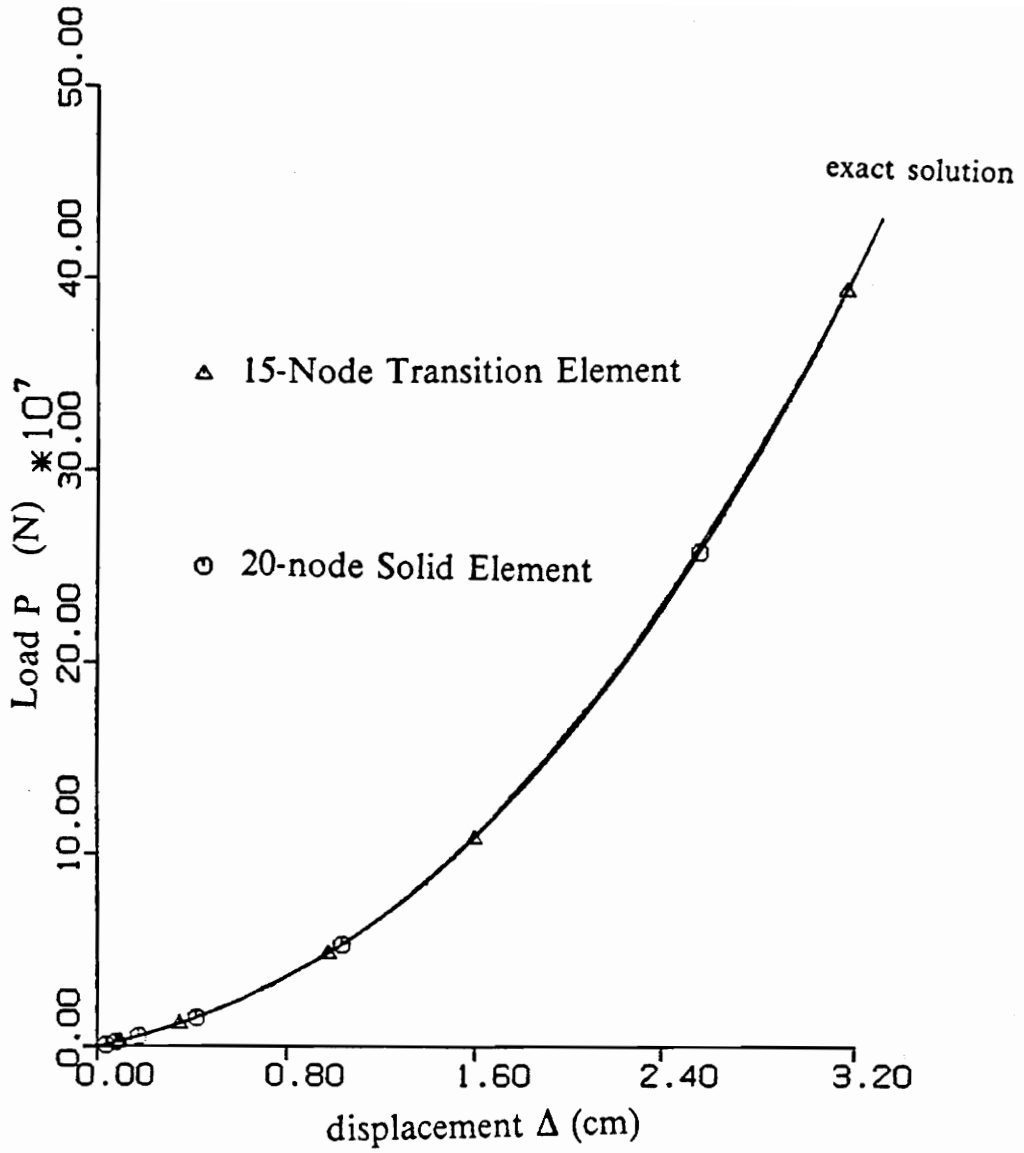

Figure 19. Axial load-displacement: response of nonlinear elements ($E = 10^7$ N/cm^2, $\nu = 0.30$)

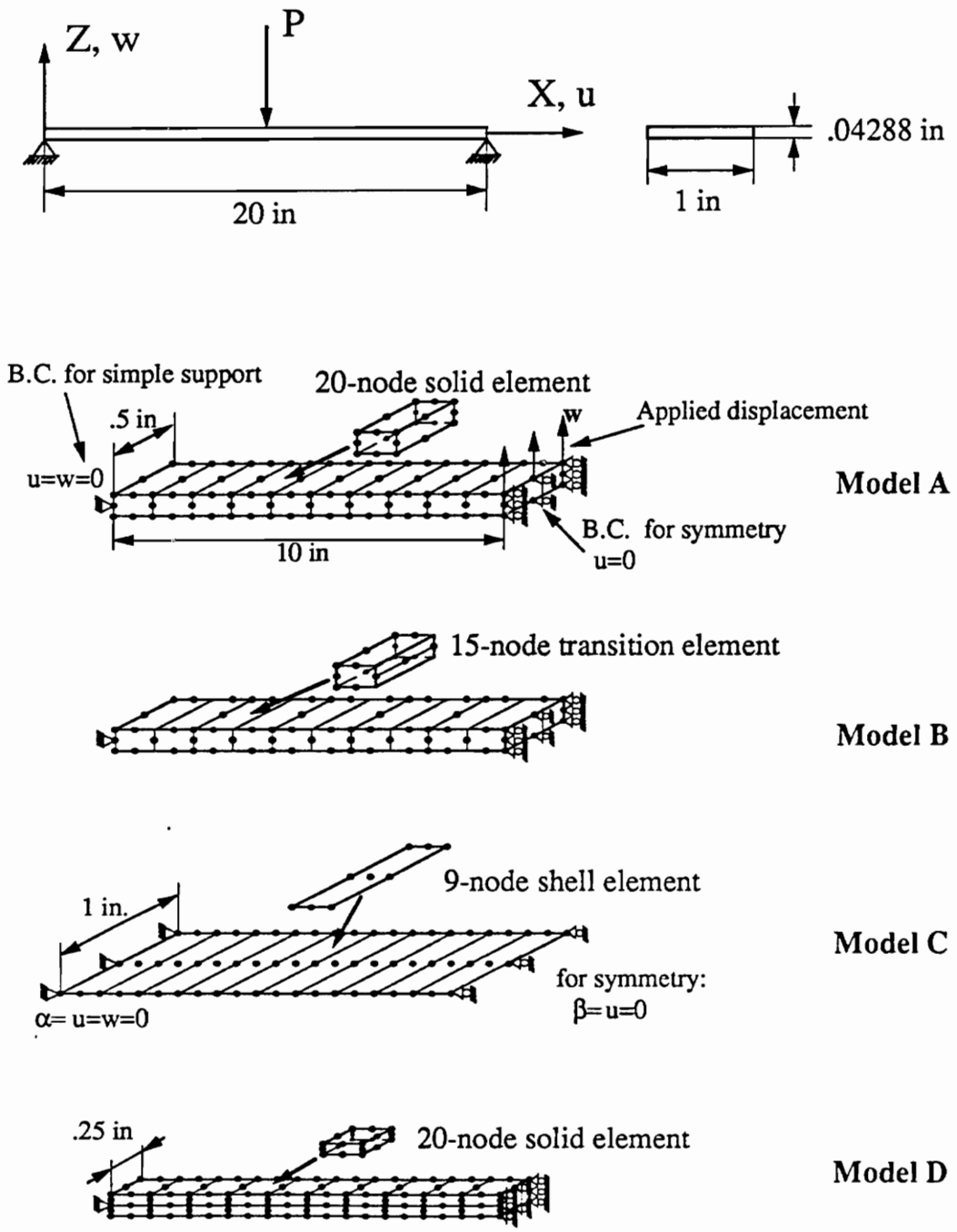

Figure 20. Geometry and finite element models of a simply-supported plate

Model B: This model is similar to Model A except that the elements are 15-node transition elements joined in pairs by their shell nodes.

Model C: Composed of ten 9-node ANS shell elements, this model is taken as a reference since its performance in this type of environment has been demonstrated.

Model D: The last model for this problem is similar to Model A except that two elements are used through the thickness. The width has been cut again in half to maintain an acceptable height/length ratio. (Although the symmetry plane is at $y = b/2$, width effects in this problem are negligible, and acceptable results are obtained with a 1/4 width model of the plate.)

3.5.3 Results

The results in Fig. 21 show the large stiffening effect caused by the end loads introduced by the immovable supports. The applied load P is normalized by the plate width, *b*. As expected, Models A and B are somewhat more compliant than the plate solution, Model C.

This figure also shows that the transition element and the solid element give very similar results. However, it can be seen from their respective step sizes that the solid element progresses much faster at large loads than the transition element. This can be attributed to the small increments in the angle approximations that were made on the restraint matrix of the transition element. These approximations decrease the accuracy

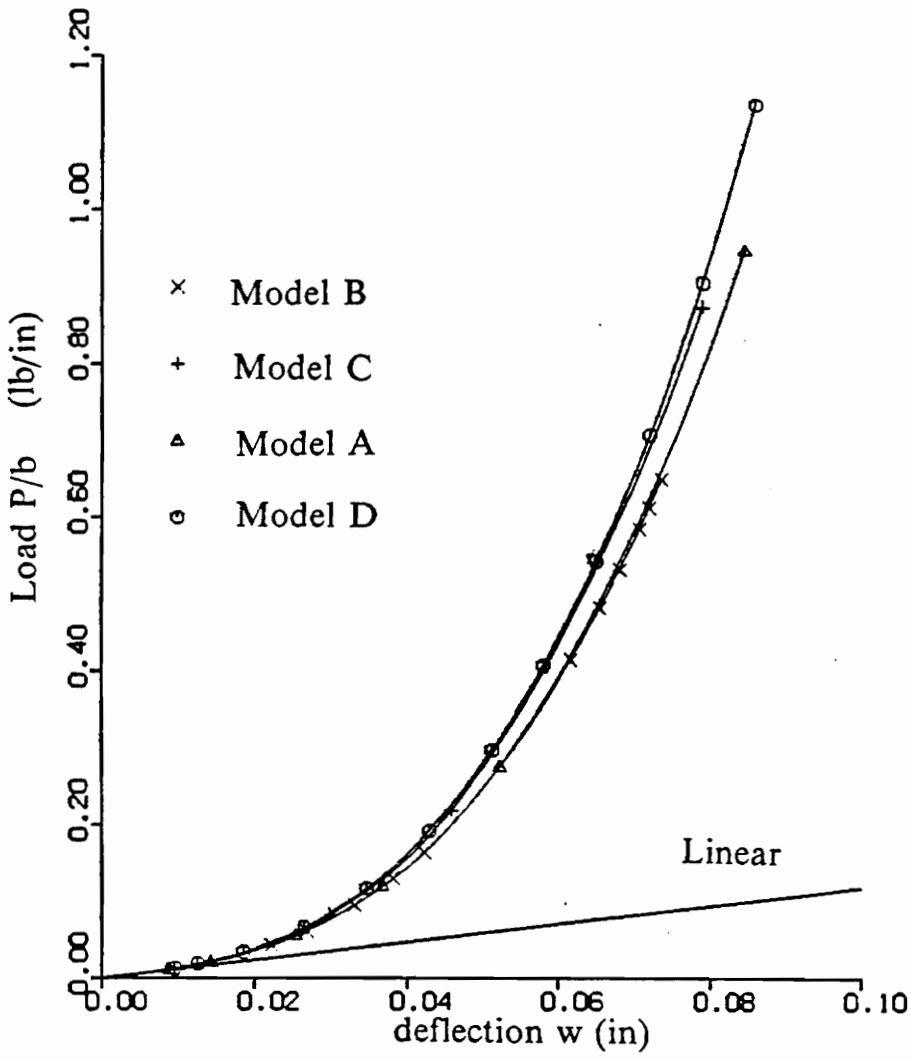

Figure 21. Geometric nonlinear response of quasi-isotropic plate under central point load

of the tangent stiffness matrix, which results in a slower convergence and, therefore, a smaller load increment.

The results for Model D address the possible danger in the use of solid elements with homogenized material properties obtained from unsymmetric laminates. Homogenization is a method by which the equivalent homogeneous anisotropic properties of a sublaminate group are obtained through the use of equilibrium and compatibility assumptions. The method of homogenization of the material properties implemented in COMET for the transition and solid elements may result in incorrect results for nonsymmetric laminates. By modeling the 8-ply symmetric laminate with two solid elements through the thickness, the elements model unsymmetric portions of the laminate. Please refer to Appendix B for a more complete discussion on the limitations of the homogenization method.

The response of Model D illustrates that acceptable accuracy can be obtained when the elements constitute sublaminates of a symmetric laminate.

3.5.4 Conclusions

It was concluded in Section 3.2.2 that the linear transition elements developed in this work produced results which compared well with the elements developed by Surana[31]. A similar conclusion can be reached on the nonlinear transition elements which were compared to the data available from the elements developed by Surana[32] and Liao[33], to geometrically nonlinear all-shell finite element models, and to one analytical large-strain problem. All of these examples show that the transition elements developed here provide reliable results under a variety of conditions.

It must be emphasized again that transition elements are not designed to be used for the computation of stress and strain fields. Furthermore, they should not be used where thickness effects are important. For this reason the evaluation of the transition elements developed here does not include any stress computations.

4 Finite Element Model and Delamination Analysis

4.1 Software environment

The analyses of this study were performed using the COmputational MEchanics Testbed (COMET), an advanced structural analysis software system developed at NASA Langley Research Center to provide a framework for research in structural analysis methods. COMET is a computational environment containing FORTRAN processors as well as a high-level command language designed for the development and assessment of new techniques in an "everything-else-constant" environment. COMET's "open architecture" accepts independent processors such as equation solvers, mesh generators and element stiffness matrix processors, which allows researchers to concentrate on their areas of expertise without spending large amounts of time developing the supporting software.

4.2 Configuration of shell and solid elements

The finite element model of the dropped-ply laminate developed for this study is composed of shell elements, solid elements and transition elements. The shell element is denoted within COMET as EX97 and is a 9-node assumed natural strain (ANS) element with five degrees of freedom per node (no drilling rotation). The element formulation includes transverse shearing deformation and has proven to be of superior accuracy with respect to more conventional elements[24,25,39]. The nonlinear strain-displacement relations in EX97 have been extensively tested, even in cases that involved extremely nonlinear, large rotation, structural response. The 20-node solid element and the 15-node transition element have been described in the previous chapter.

The geometry of the finite element model is represented in Fig. 22. By far, the largest the area of the laminate is modeled by EX97 shell elements, while only the region closest to the ply drop-off (4% of total area) is composed of three-dimensional elements. Although the laminates studied here are not strictly symmetric about the longitudinal centerline (because of the $\pm$45-degree layers), it was determined from a full width model that this asymmetric effect is negligible. The model for this study was therefore chosen to be a half-width model with a plane of symmetry specified at $y = b/2$.

The length of the region modeled with solid elements, or the 3-D region, was chosen to be 0.4 inches long, or from 0.25 inches before the ply drop-off to 0.15 inches after the drop-off. These choices resulted from Curry's analysis and his observations on the lengths of decay of the boundary layers of the interlaminar stresses in the vicinity of the drop-off. A length of 0.4 inches was found to be a good compromise between efficiency and accuracy by allowing most of the interlaminar stress boundary layers to be con-

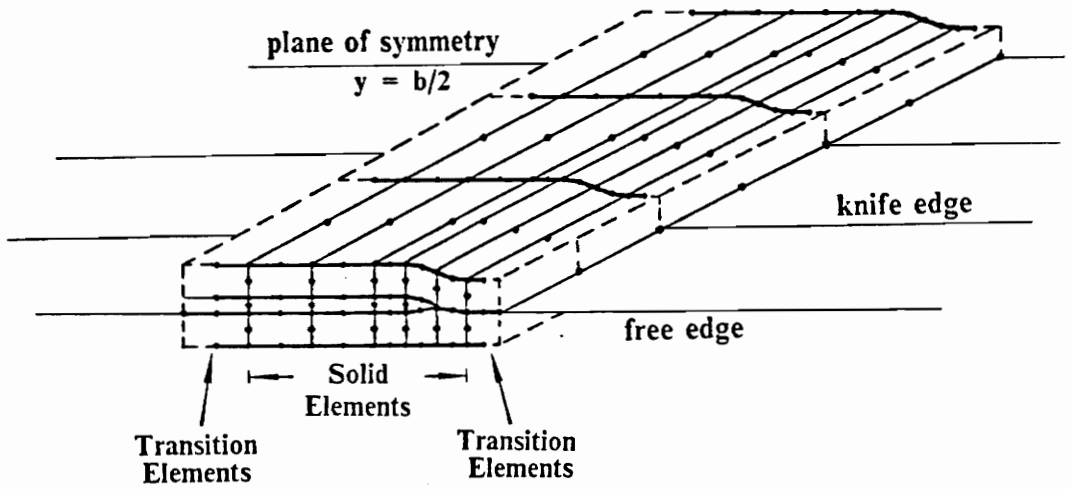

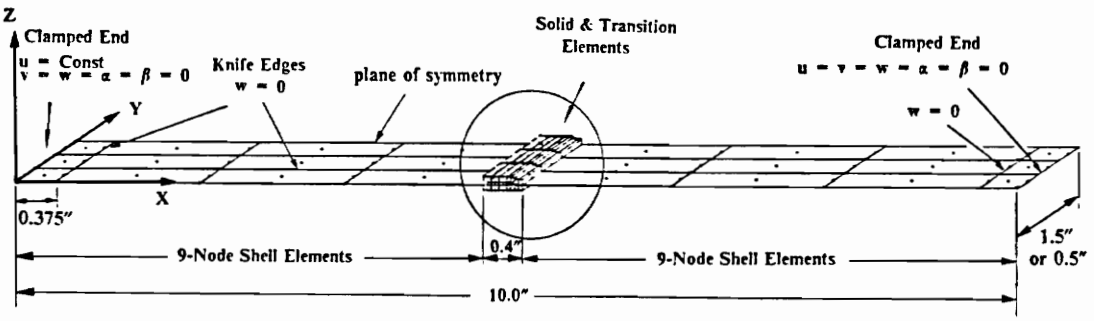

Figure 22. **Finite element model of dropped-ply laminate:** detail shows solid elements and transition elements

tained within the 3-D region. Because they are located outside the areas of 3-D effects, the transition elements are prevented from introducing an artificial boundary layer.

The error introduced by using a combination of solid, transition and solid elements rather than only solid elements is expected to be below 5%, as illustrated by the test case 2 of the transition element, Sect. 3.2.2.

4.3 Boundary conditions and material properties

The boundary conditions on the finite element model closely reflect the supports in the experimental setup. The end fixtures have a grip length of 0.375 inches. The corresponding boundary conditions impose a uniform u displacement (x-direction) along the end of the thick side, and set to zero the w-displacement of the nodes within the grips. All degrees of freedom along the thin end are set to zero (clamped). Knife edges run along the length of the plate, 0.125 inches inward from the free edge of the laminate. For shell elements, knife edges are specified by imposing $w = 0$. For solid elements, a clamping action of the knife edges was simulated by specifying $w = 0$ at the bottom (uniformly flat) face of the laminate, while a small pinching displacement $w = -h/10^4$ was applied to the top face, but only along the thick side of the laminate, where h is the thickness of the thick side of the laminate.

Symmetry conditions are specified at the plane $y = b/2$ by setting all transverse displacements v (y-direction) to zero. In addition, the rotation α of the normal around the x-axis at all shell nodes on the symmetry plane were also set to zero (see Fig. 17).

The material properties for AS4/3502 graphite-epoxy unidirectional tape used in the analysis are as reported by Tsai[40] and subsequently used by Curry[15]. They are shown in Table 3.

Table 3. Material Properties

Material Properties of Unidirectional AS4/3502 Graphite-Epoxy		
E_1	18.5 10^6 psi	Young's modulus in 1 direction
E_2	1.64 10^6 psi	Young's modulus in 2 direction
E_3	1.64 10^6 psi	Young's modulus in 3 direction
ν_{12}	0.3	Poisson's ratio
ν_{13}	0.3	Poisson's ratio
ν_{23}	0.3	Poisson's ratio
G_{12}	0.87 10^6 psi	Shear modulus in the 1-2 plane
G_{13}	0.87 10^6 psi	Shear modulus in the 1-3 plane
G_{23}	0.49 10^6 psi	Shear modulus in the 2-3 plane
Material Properties of Neat Resin		
E_{resin}	0.5 10^6 psi	Young's modulus of resin
ν_{resin}	0.41	Poisson's ratio of resin
G_{resin}	0.195 10^6 psi	Shear modulus of resin
Interlaminar Strengths		
Z^{S1}	13.5 ksi	Shear strength in 1-3 plane
Z^{S2}	13.5 ksi	Shear strength in 2-3 plane
Z^T	7.54 ksi	Transverse tensile strength

4.4 Mesh development

The mesh generation was programed parametrically so that the basic mesh could be easily refined longitudinally and/or across the width without need of constructing a new model. (Mesh refinement in the thickness direction was not programmed parametrically.) The runstream for the generation of the finite element model is included in Appendix C, and it was used to conduct a parametric study to determine the optimal

mesh refinement and element size for a good compromise between efficiency and accuracy in the prediction of interlaminar stresses.

The solid element region of the model is shown in Fig. 23 for four different mesh refinements. Figure 23a represents a "basic" mesh, i.e., the basic mesh pattern has not been refined, and each sublaminate is composed of only one layer of solid elements. The thick side of the laminate is, therefore, three elements thick; one element through the dropped plies sandwiched between the elements of the outer eight-layer quasi-isotropic sublaminates. The three-dimensional elastic properties of the individual layers are "smeared" by the homogenization processor LAU[34] in COMET.

4.4.1 Refinement in longitudinal direction

A parametric study on longitudinal (x-direction) mesh refinement was essential to determine the size of the elements that would be required to capture the stress gradients at the corner of the ply drop-off. The relative magnitude of the local effects is illustrated by Fig. 24, which shows the deformation of the grid at $y = b/2$ for a linear analysis of a 1-inch-wide $[0_4]_T$ dropped ply sublaminate. The distortion at the corner of the ply drop-off clearly indicates the presence of severe shear and tensile stresses in the area. The applied compressive load is 300 lb/in, and the magnitudes of the displacements have been exaggerated 200 times. The vertical scale is magnified four times relative to the horizontal scale.

The basic mesh was too coarse in the neighborhood of the ply drop-off to capture the large stress gradients, and a mesh twice as refined as the basic mesh in the longitudinal direction (Fig. 23b) gave better results. A three-times mesh refinement (Fig. 23d)

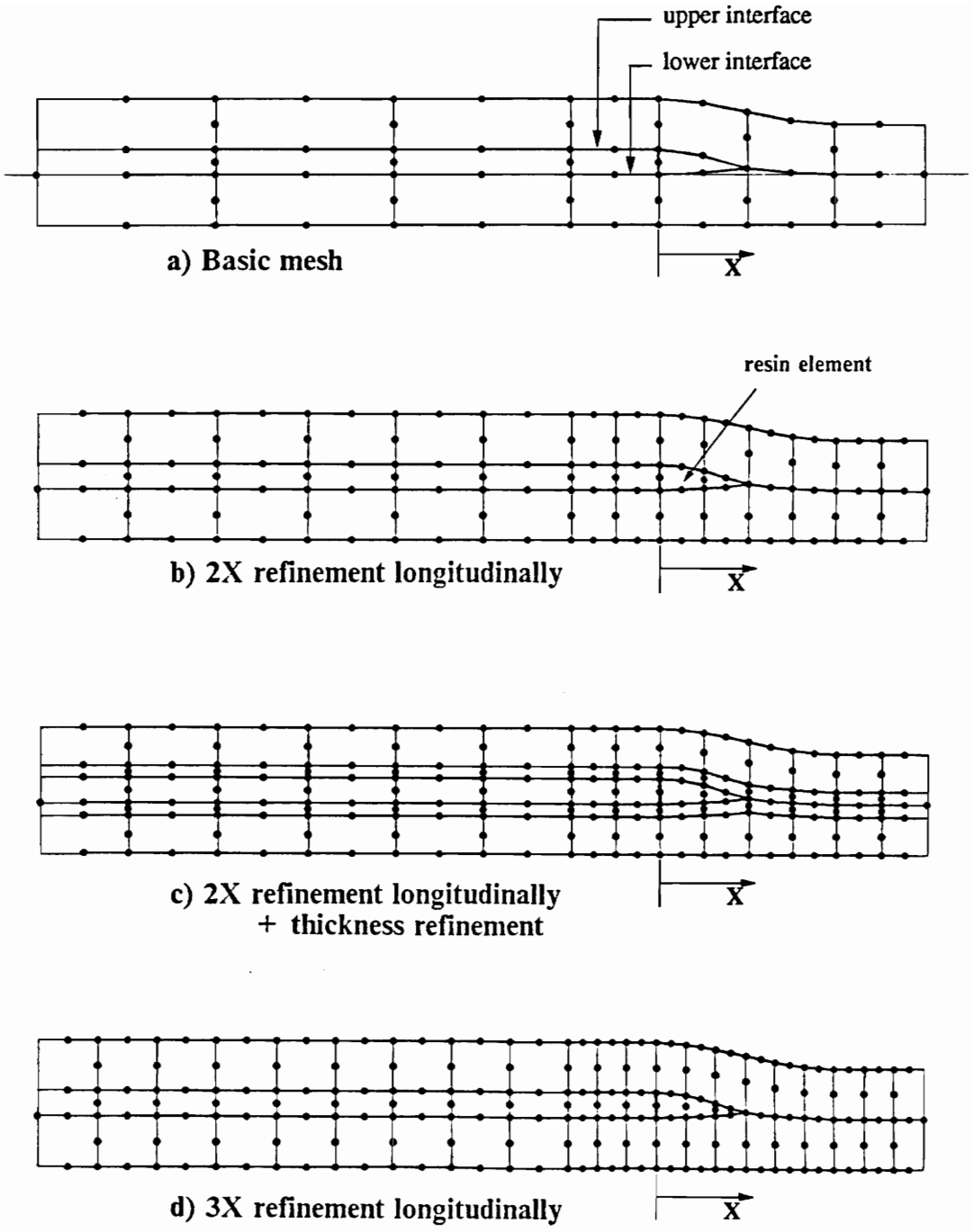

Figure 23. Four finite element meshes near ply drop-off: x = 0 at ply drop-off

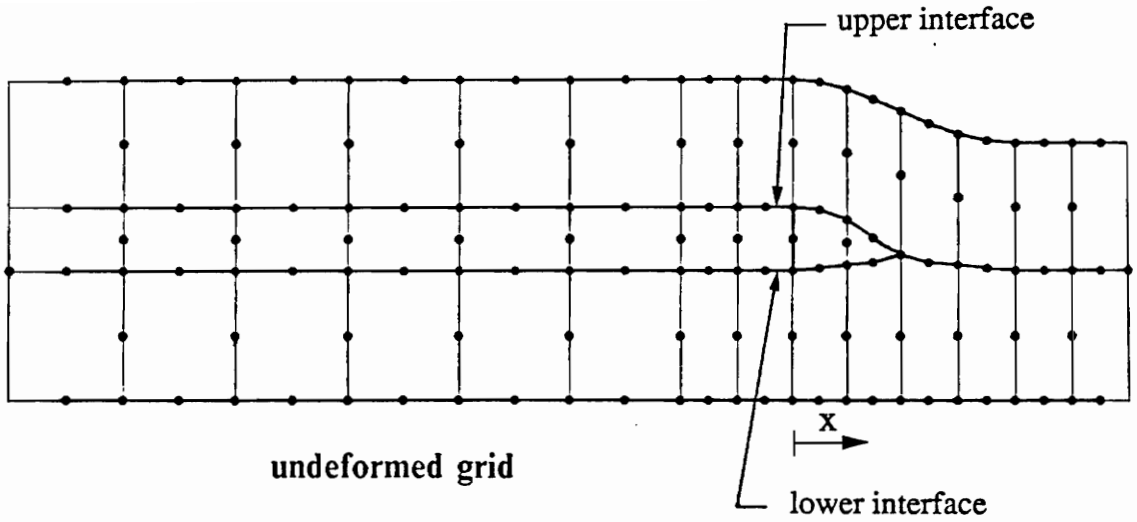

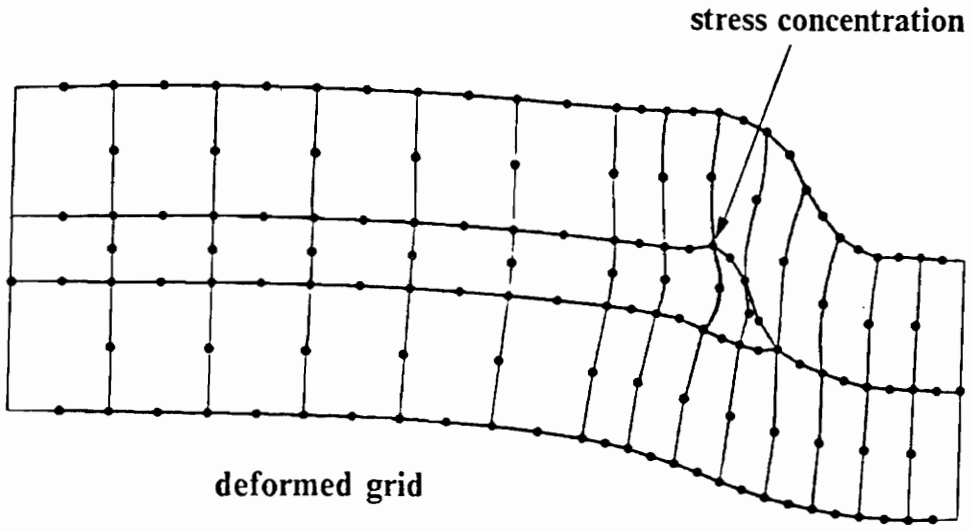

Figure 24. Undeformed and deformed grids indicate the presence of large tensile and shear stresses at the ply drop-off

substantially increased execution time relative to the mesh shown in Fig. 23b, but had only a moderate effect on the stresses.

Longitudinal mesh refinement provided an additional benefit. Because a pentahedral element (or wedge element) was not available, the resin-rich cavity next to the dropped plies had to be left empty in the basic mesh. However, some longitudinal mesh refinement allows one or more "resin" solid elements to be used. The mesh shown in Fig. 23b is refined twice along the span, and for this mesh one resin element can be used. It was found that the presence of this resin element reduces the interlaminar stresses at the neighborhood of the drop-off by about ten percent. The reduction in interlaminar normal stress σ_z at the upper and lower interfaces (see Figs 23a and 24) near the ply drop-off for a 1-in.-wide specimen with four 0-degree plies dropped is shown in Fig. 25. The applied compressive load is 290.4 lb/in., and the longitudinal stress distributions are shown along the centerline of the laminate ($y = b/2$). The mesh is three times refined longitudinally (Fig. 23d). Overlaid for comparison are Curry's results[15] with the quasi-three-dimensional analysis described in the introduction. The agreement between the present analysis and Curry's analysis is excellent.

A similar reduction in stresses affects the interlaminar shear stress, τ_{xz}, as shown in Fig. 26. As can be observed from the last three points on the curves in Fig. 26, the 20-node solid elements used here can only represent a linear longitudinal distribution of the transverse shear stress τ_{xz}. The stresses are accurate in an average sense. However, even with this fine mesh, the elements do not capture the exact gradients near the ply drop-off.

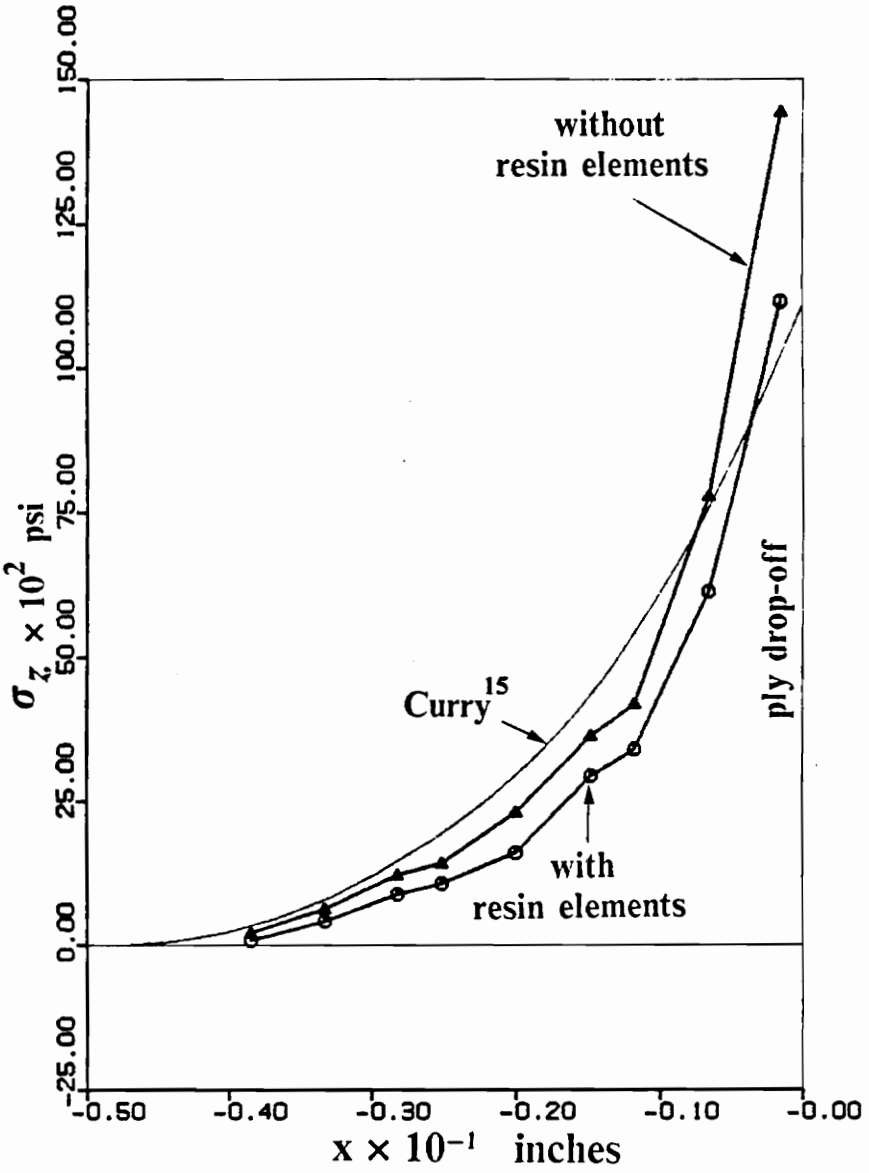

Figure 25. Longitudinal distribution of interlaminar normal stress at upper interface near ply drop-off at y = b/2: (1-in.-wide, $[0_4]$s insert)

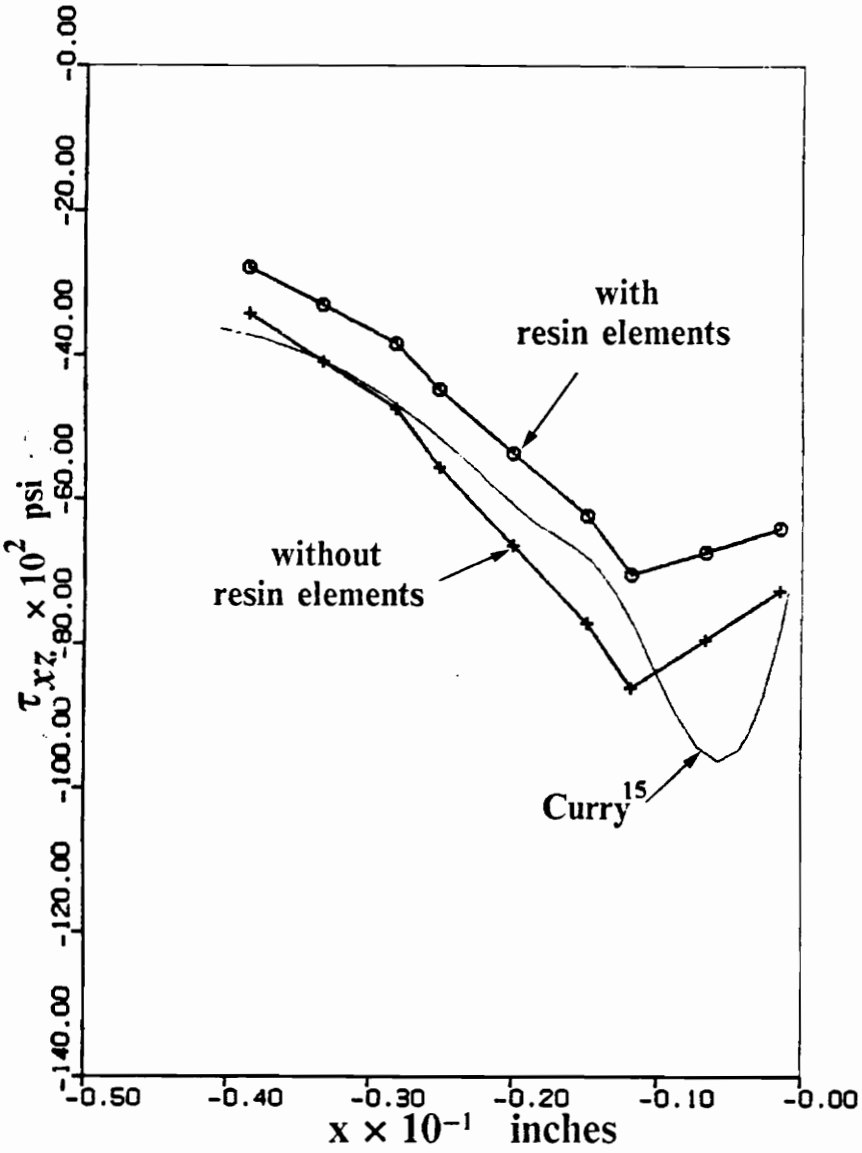

Figure 26. Longitudinal distribution of interlaminar shear stress at upper interface near ply drop-off at y = b/2: (1-in.-wide, $[0_4]_S$ insert)

4.4.2 Refinement in the width direction

A second parametric study involved the number of elements in the width direction (y-direction). A concern was that a small longitudinal grid spacing would dictate a similarly small grid spacing across the width in order to avoid element width to length ratios (or aspect ratios) greater than one order of magnitude. However, it was found that aspect ratio per se is not nearly as important a factor as to whether or not the elements are small enough in any direction to accurately represent the stress gradients. Since the width-wise gradients in the stresses are relatively slow and small compared to the longitudinal gradients, it was found that only three elements were needed to span the half-width of the laminate. This corresponds to an aspect ratio of up to 130-to-1 for some elements in the case of two plies dropped.

4.4.3 Refinement in the thickness direction

The model configuration shown in Fig. 23c has two additional layers of elements. This model uses what was termed H2 homogenization in Appendix B for the quasi-isotropic sublaminates. This type of discretization, where the ±45-degree layers in contact with the dropped plies are modeled with one element through the thickness, was found to provide excellent accuracy at a moderate penalty in execution time (see Appendix B). The interlaminar normal stress distributions for two models with and without the thickness refinement, and each for a three-times longitudinal refinement, are shown in Fig. 27 for a linear analysis of the $[0_4]_T$ specimen. The applied load is 290.4 lb/in., the same load as for the cases shown in Figs. 25 and 26. At some locations the differences in the interlaminar normal stress σ_z are significant.

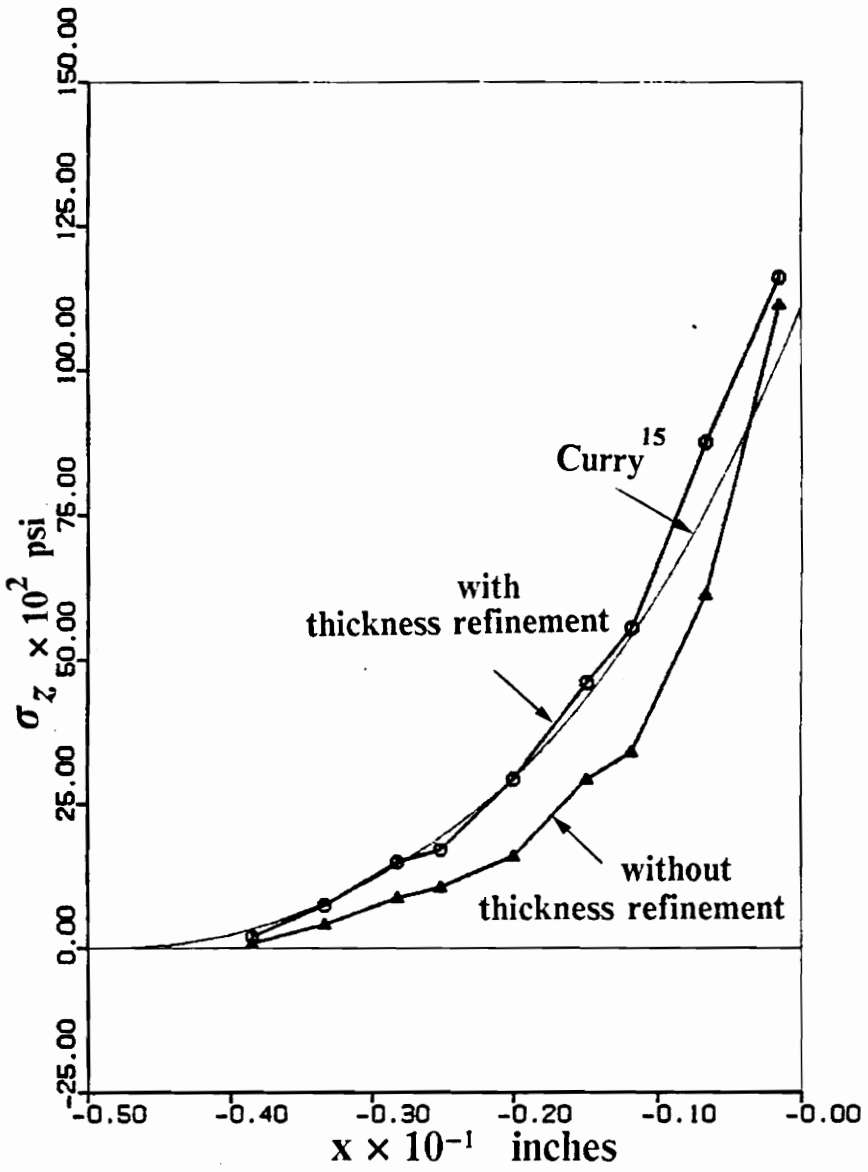

Figure 27. Interlaminar normal stress at upper interface: effect of thickness refinement compared to the case shown in Fig. 25.

4.4.4 Final mesh selected

The final configuration selected after the parametric study of mesh refinement is the one represented in Fig. 23b. It has three rows of elements across the half-width, one of them representing the strip out-board of the knife edges. The basic mesh is refined twice along the span. Although a three-times longitudinal mesh refinement produced somewhat different results, it was decided that the characteristic distance used in the delamination methodology (see Chapter 5) would compensate for the coarse stress distribution obtained from discretizing the mesh only twice in the axial direction. The model consists of 24 shell elements, 15 transition elements and 45 solid elements. There are 126 shell nodes, 684 solid element nodes and 2361 active degrees of freedom. A linear analysis with this model employs 350 seconds of CPU time on the four-processor CONVEX computer at NASA Langley's Computational Mechanics Branch. Storage requirements for one analysis are of the order of 80 Mbytes. A typical nonlinear analysis uses 7000 seconds of CPU time.

The z = constant plane that coincides with the upper interface of the dropped plies (Fig. 23a) for a one-inch wide laminate is shown in Fig. 28. In this figure, x = 0 at the ply drop-off, y = 0 at the free edge, y = 0.125 inches at the knife edge, and y = 0.50 inches at the longitudinal centerline. The positive z-faces of the six solid elements that span the thickness of the dropped plies are outlined in this plane as is shown in Fig. 28. The "+" signs in the figure correspond to the position in the upper interface of the projection of of the integration points, or Gauss points, of these solid elements. The values of the interlaminar stresses were obtained at those locations by interpolating the stresses from the elements immediately above and below the interface.

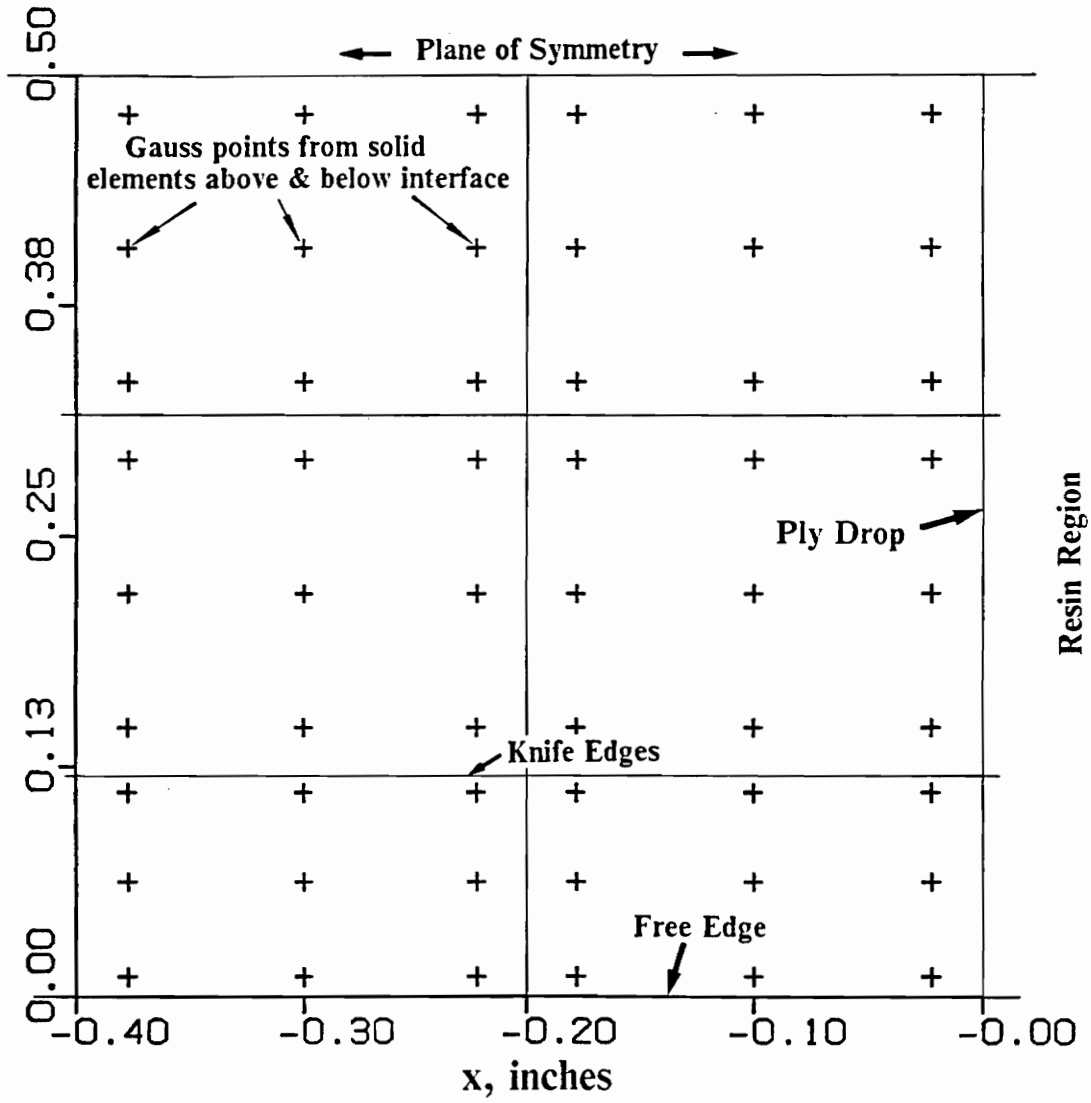

Figure 28. Top view of interface: (+) signs indicate location of integration points.

4.5 Delamination analysis

One of the most important failure modes in laminated structures is delamination. Delamination is the separation of individual laminae of a laminate due to the interlaminar stresses. In general, the delamination initiation load is not the ultimate load. After initiation, delamination may undergo stable growth or, as the loads redistribute, may jump to seemingly unpredictable locations or may also interact with in-plane failure mechanisms. Predicting delamination initiation is considerably easier than predicting failure propagation.

Two approaches to the prediction of delamination initiation are commonly used. The first method predicts failure initiation from a *delamination tolerance* methodology, while the second approach estimates initiation from the standpoint of *delamination resistance*.

The delamination tolerance methodology is based on fracture mechanics techniques, usually on the strain energy release rate. Typically, a crack is assumed to exist at a critical interface of the finite element model and the strain energy released by a small increase in the crack length is calculated at a fixed value of the load. If the strain energy release rate is computed for several initial crack lengths, then by extrapolation the strain energy release rate at zero crack length can be estimated. At some load this rate becomes higher than the critical value G_c for the laminate, the crack can propagate and delamination is assumed to occur[11].

The approach adopted in this work, on the other hand, predicts the failure initiation load by estimating the delamination resistance of the laminate. This approach is

based on a mechanics of materials point of view, where the local state of the interlaminar stresses in the interface at a critical location are compared with relevant strength parameters. A major difficulty associated with this method is the calculation of the interlaminar stress field. In particular, the stress singularities often produced by idealized mathematical models near geometric discontinuities do not correlate with experimental observations. These singularities are a mathematical artifice due to a lack of modeling detail at a ply level. At a ply drop-off, for instance, the presence of a resin-rich bond line, say one to three fiber diameters thick which separates laminae of different fiber orientations, mitigates the step change in material properties across the zero-thickness interface of the idealized model. This fact and that plasticity effects may occur in the resin-rich interface[12] reduce the sharp stress peaks that would otherwise cause immediate delamination. It is clear that the presence of stress singularities in idealized mathematical models renders point stress criteria meaningless.

The introduction to this dissertation mentions the work of Fish and Lee[7] and others[8,9] who have obtained good correlation with experiment by using a quadratic delamination criterion with average values of the interlaminar stresses instead of point-wise values. The averaging distance was found to be a function of material properties and layup configuration. This method of averaging the stresses over a specified distance was rejected for the present work because the calculation of averages requires curve-fitting of the stress distribution through the few points closest to the ply drop-off and extrapolation beyond the Gauss point closest to the singularity. The extrapolation is possible either by making assumptions on the unknown values of the stresses at the singularity, or by using much greater longitudinal mesh refinement. Instead, the the criterion used here is the point stress criterion proposed by Nuismer and Whitney[41] for determining the notch strength of laminates, but it is modified here to account for failure by delam-

ination. It consists of determining a characteristic distance that defines a location close to the singularity where the stresses from the approximate analysis are assumed to be representative of the actual stresses.

This work is concerned exclusively with predicting laminate failure initiation by delamination near the ply drop-off. That is, a critical failure mode is assumed and the load to initiate it is computed. The next chapter contains the failure analyses of several such cases. The analysis of each specimen consists of: 1) a linear analysis of the 1-in.-wide specimen to determine the characteristic distance for the laminate, and 2) a nonlinear analysis of the corresponding 3-in.-wide specimen which uses the previously determined characteristic distance to predict the initial failure domain and delamination initiation load. In more detail, the analysis proceeds as follows.

1. **Linear Analysis**: The distribution of the failure index F is calculated at the experimentally determined delamination initiation load of the 1-in.-wide specimen in the critical interface(s) near the ply drop-off. The failure index is defined as

$$F = \left(\frac{\bar{\tau}_{xz}}{Z^{S1}} \right)^2 + \left(\frac{\bar{\tau}_{yz}}{Z^{S2}} \right)^2 + \left(\frac{\bar{\sigma}_z}{Z^T} \right)^2 \qquad (4.3.1)$$

where $\bar{\tau}_{xz}$, $\bar{\tau}_{xz}$, and $\bar{\sigma}_z$ are the interlaminar stresses evaluated at the characteristic distance from the drop-off, and Z^{S1}, Z^{S2}, and Z^T are the corresponding allowable stresses (see Table 3). The characteristic distance d is defined as the largest longitudinal distance from the drop-off where F = 1. That is, failure is assumed to occur in the domain $-d \leq x \leq 0$, $0 \leq y \leq b$, in the interface where values of F exceed unity.

2. **Nonlinear Analysis**: The distribution of F is calculated at every load step. The largest value of F anywhere at a characteristic distance from the drop-off is recorded. The delamination load is reached when F attains unity.

5 Results and Discussion

5.1 Dropped-ply specimens selected for analysis

The objective of this work is not to perform a study of all of the possible failure mechanisms in the dropped-ply specimens. Instead, the purpose is to develop and assess a failure analysis methodology for the prediction of delamination in postbuckling, which was the first major failure event for most of the specimens tested by Curry[16]. Consequently, the four laminates analyzed here were selected among other specimens because in Curry's experiments they failed in delamination in the region of the dropped ply. The specimens selected are labeled 82-2, 83-2, 84-2, and 85-2 in Table 4. (These specimen numbers are taken from Ref. 16). The analyses described in this work do not attempt, therefore, to predict failure modes or failure locations other than the delamination observed along the upper and lower interfaces of the dropped-ply sublaminate.

This chapter contains the analysis of the following four cases.

- Case 1: $[0_4]_T$ dropped-ply sublaminate (specimen 84-2)

Table 4. Summary of compression specimens tested by Curry

Ply drop	Specimen no.	Avg width inches †	Avg ply thickness thin side (10^{-3} in)	Avg ply thickness thick side (10^{-3} in)	Failure ‡ initiation (lb/in)	Ultimate ‡ failure (lb/in)	Failure location and mode
$[\pm 45/0/90]_S$	11-3	1.	-	-	4320	4320	Delamination at drop-off
	11-4	1.	-	-	4630	4630	"
	11-5	1.	-	-	4270	4270	"
	81-2	3.	-	-	3780	3780	Fail. 1.75" from thin end
$[\pm 45/0_2]_S$	12-3	1.	-	-	3940	4005	Delamination at drop-off
	12-4	1.005	5.00	5.00	3800	4070	"
	12-5	1.003	5.01	5.00	3780	3780	"
	82-2	3.006	5.01	5.00	3475	3475	"
$[0_2]_T$	13-3	1.	-	-	5100	5600	Delamination at drop-off
	13-4	1.003	5.00	5.00	5280	5305	"
	13-5	1.002	4.95	4.88	5060	5130	"
	83-2	3.000	5.40	5.38	3520	3520	"
$[0_4]_T$	14-3	1.	-	-	3750	4255	Delamination at drop-off
	14-4	1.003	5.00	4.95	3680	4335	"
	14-5	1.004	4.94	4.90	3650	4035	"
	84-2	3.006	5.40	5.30	3420	3420	"
$[0_8]_T$	15-3	1.	-	-	3640	3700	Delamination at drop-off
	15-4	1.003	5.08	5.00	3450	3650	"
	15-5	1.001	5.08	5.00	3390	3390	"
	85-2	3.001	5.08	5.00	2920	2920	"
$[90_2]_T$	86-1	1.5	-	-	-	5990	End failure in thin sect.
	86-2	3.	-	-	3470	3470	Failure 3" from thin end
$[90_4]_T$	87-1	1.5	-	-	-	6630	Delamination at drop-off
	87-2	3.	-	-	3535	3695	Fail. in thin sect. & drop
$[90_8]_T$	88Ra-1	1.	-	-	-	5829	End failure in thin sect
	88Ra-2	3.	-	-	-	3880	Fail. 1/4" below drop-off

† Nominal values are given when exect measurements were not available

‡ Some values are from Curry's raw experimental data and may differ somewhat from Refs. 15 and 16

- Case 2: $[0_2]_T$ dropped-ply sublaminate (specimen 83-2)
- Case 3: $[0_8]_T$ dropped-ply sublaminate (specimen 85-2)
- Case 4: $[\pm 45/0_2]_S$ dropped-ply sublaminate (specimen 82-2)

All four cases consist of a dropped-ply sublaminate composed of two, four or eight contiguous plies, sandwiched between two eight-ply $[\pm 45/0/90]_S$ quasi-isotropic sublaminates. The results of the four cases are compared and discussed at the end of this chapter.

5.2 Case 1 $[0_4]_T$ dropped-ply sublaminate

5.2.1 Linear analysis

Curry tested three nominally identical $[0_4]_T$ 1-in.-wide specimens in compression (specimen nos. 14-3, 14-4, and 14-5) and determined initial delamination loads of 3750, 3680 and 3650 lbs, as shown in Table 4. The second specimen was selected for analysis since its failure load was closest to the average of the replicate specimens. The actual measurements of specimen no. 14-4 were used in the finite element model: average width = 1.003 in. and average ply thickness in the thin side = 0.00500 in., average ply thickness in the thick side = 0.00495 in. The stresses and the corresponding delamination index F were computed for an applied compressive load of 3680 lbs. The distribution of F at the upper interface in the vicinity of the ply drop is shown in Fig. 29. The distribution at the lower interface was also computed but the stresses were found to be less critical.

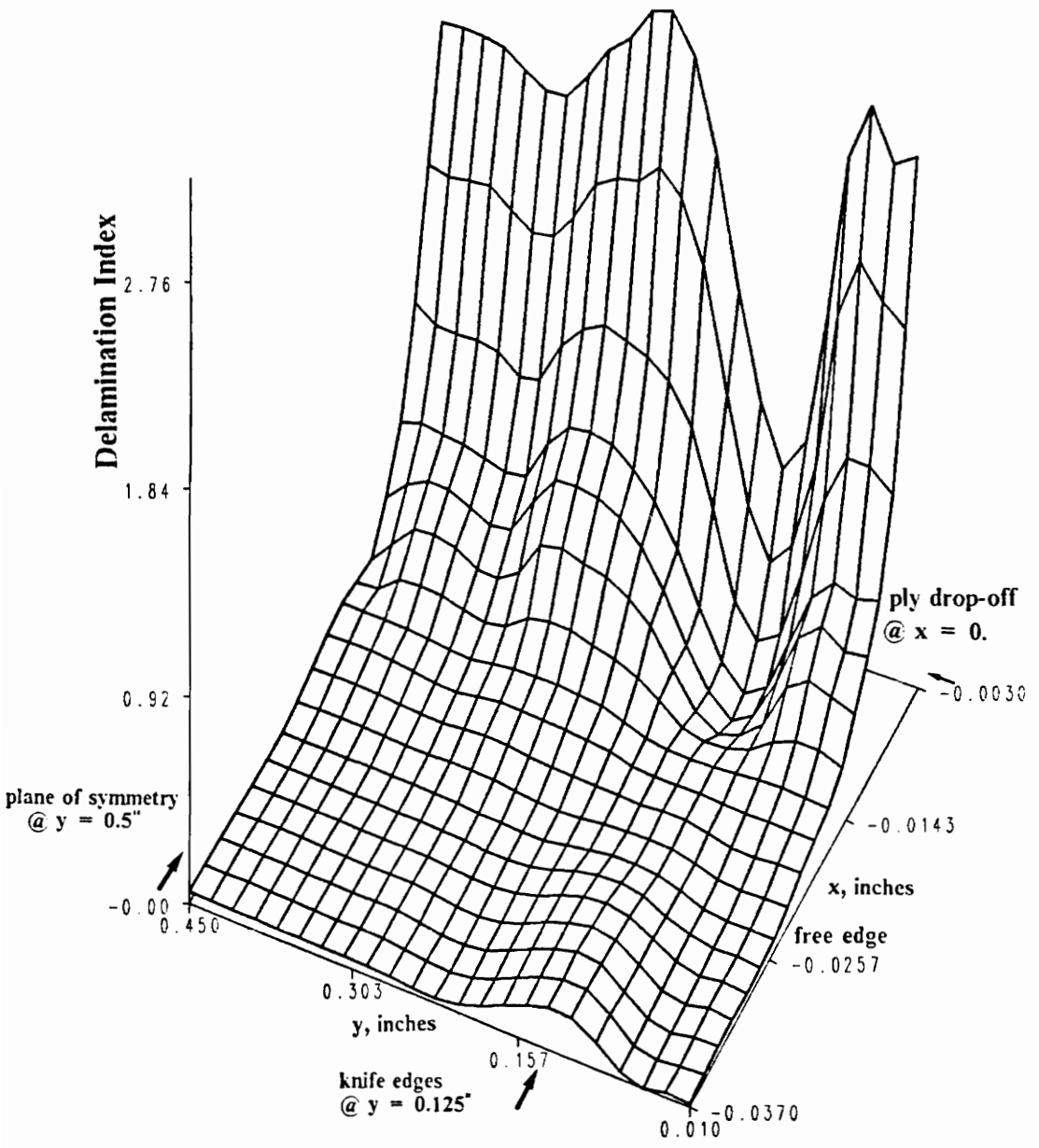

Figure 29. Distribution of the delamination index in the upper interface for a linear analysis: 1-in.-wide $[0_4]_T$ dropped-ply specimen at $N_x = 3{,}680$ lb/in, compression.

The two dominant features of the the distribution of the failure index F shown in Fig. 29 are 1) the large gradient in x near the ply drop-off, and 2) the trough caused by the clamping action of the knife edges. This support introduces a compressive force which reduces the peeling stress σ_z.

The definition of the delamination index by the quadratic criterion, Eq. (4.3.1), does not account for the sign of σ_z. It is debatable if compressive interlaminar stresses should be included in the computation of the delamination index. Although it was decided to include the compressive values of σ_z in Eq. (4.3.1), the results of this study are not affected by either including or excluding it. The reason for the lack of sensitivity in the sign of σ_z in the failure analysis of this problem is that the critical stresses are always tensile. The only region in the upper interface where compressive interlaminar normal stresses were observed is along the knife edges, ahead of the ply drop-off where the influence of the knife edge pre-compression dominates. In this region, the trough at the ply drop-off becomes a small ridge.

Another important observation from Fig. 29 is that the stresses along the centerline of the laminate (y = 0.5 in) are not significantly lower than those at any other y = constant location. This indicates that, for this problem, a two-dimensional analysis along the centerline of the laminate (such as Curry's analysis) can produce excellent predictions of the highest stresses in the laminate. It will be shown, however, that the nonlinear analyses of the wider 3-in.-wide specimens support the opposite conclusion.

The contour lines of the index F over the upper interface are shown in Fig. 30. Also shown in this figure is the location of the characteristic line, which is defined as a line parallel to the ply drop-off which is tangent to the contour F = 1 at its farthest point

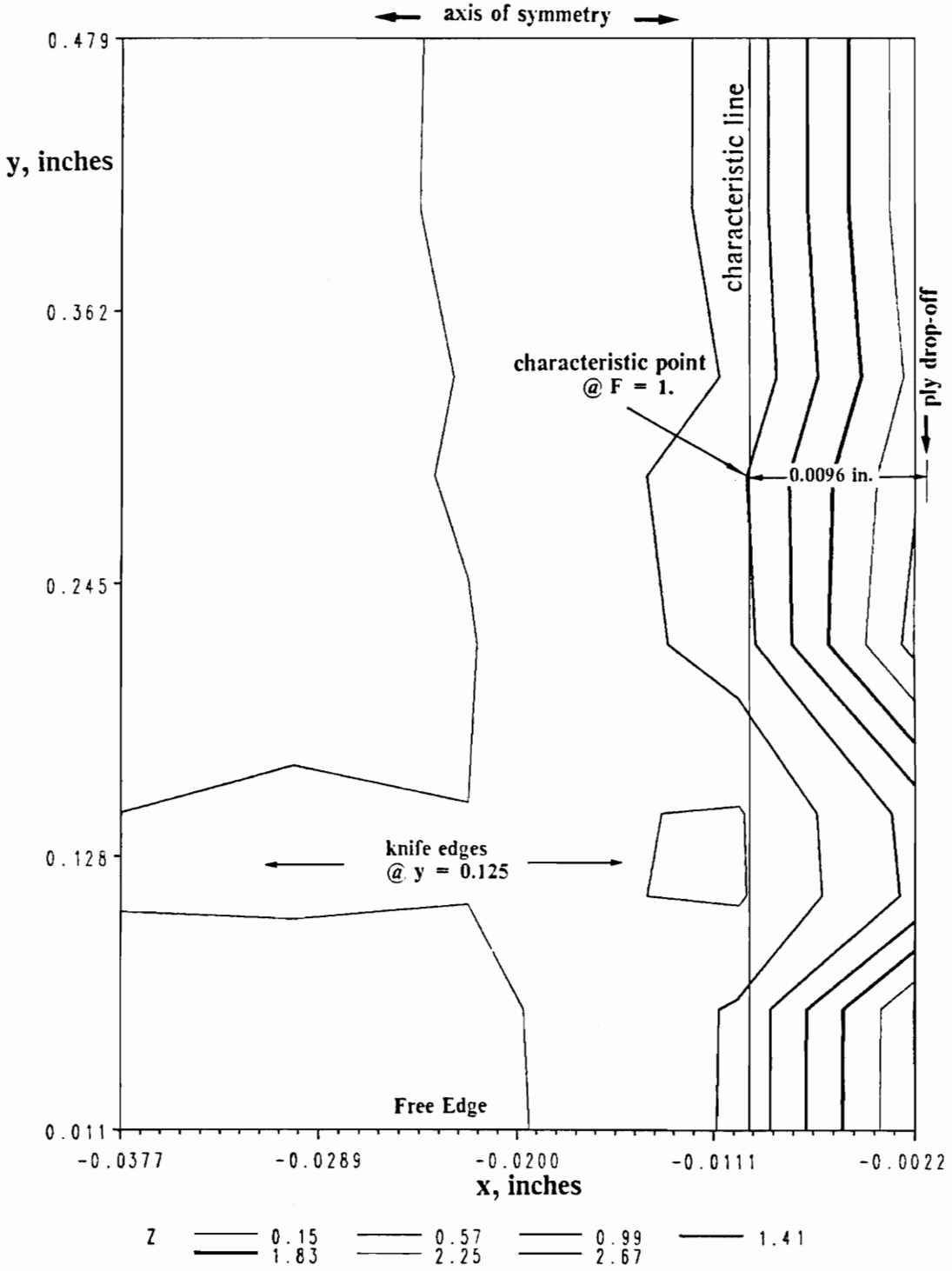

Figure 30. Contours of the delamination index in the upper interface for a linear analysis: 1-in.-wide $[0_4]_T$ dropped-ply specimen at N_x = 3,680 lb/in, compression.

from the ply drop-off. The longitudinal distance from the ply drop-off to the characteristic line is the characteristic distance, and it was found to be equal to 0.0096 inches.

The x and y coordinates of the point of tangency of the F = 1 contour and the characteristic line is labeled the characteristic point in Fig. 30. With the present analysis methodology it cannot be said that delamination initiates at the characteristic point, but only that delamination initiates somewhere in the region between the ply drop-off and the characteristic line. However, comparing the position of the characteristic point between dropped-ply laminates does provide qualitative evidence as to the shifting of the failure location.

5.2.2 Nonlinear analysis

A nonlinear analysis was performed on the 3-in.-wide specimen no. 84-2 (see Table 4) of otherwise similar configuration to the 1-in.-wide specimen no. 14-4 analyzed above. The nonlinear finite element model was identical to the linear model except for the width (3.006 in) and thicknesses of the laminate. The measured lamina thicknesses were 0.0053 and 0.0054 inches for the thick and thin sides, respectively.

The plots shown in Fig. 31 are the out-of-plane deflection (w) of the laminate at y = b/2. For very low loads (or linear analysis) the bending shape consists of two half-waves, but it immediately transitions to three-half waves. A comparison of out-of-plane deflection at three different locations along the length is shown in Fig 32. It can be observed that the initial bending response of the laminate is nearly linear. After a load of about 2000 lbs/in., the deflections increase rapidly with load, indicating a nonlinear (postbuckling) regime. The finite element model predicts the experimentally measured

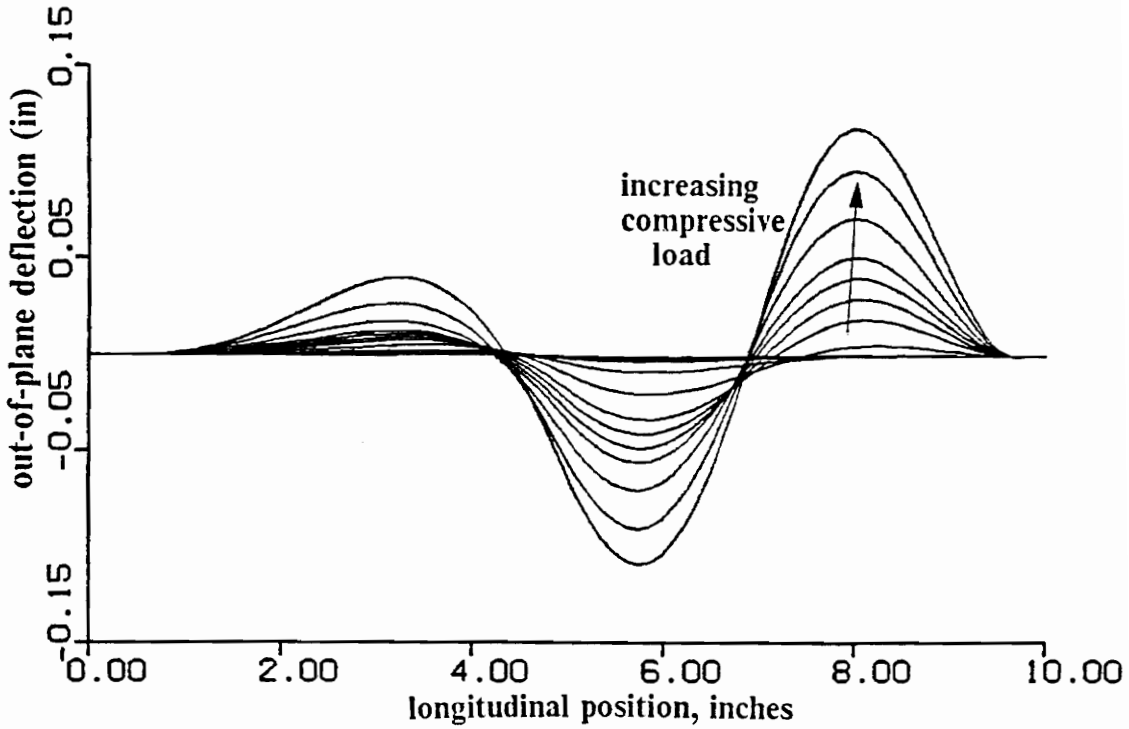

Figure 31. Out-of-plane displacements at y = b/2: $[0_4]_T$ dropped-ply specimen at several compressive loads

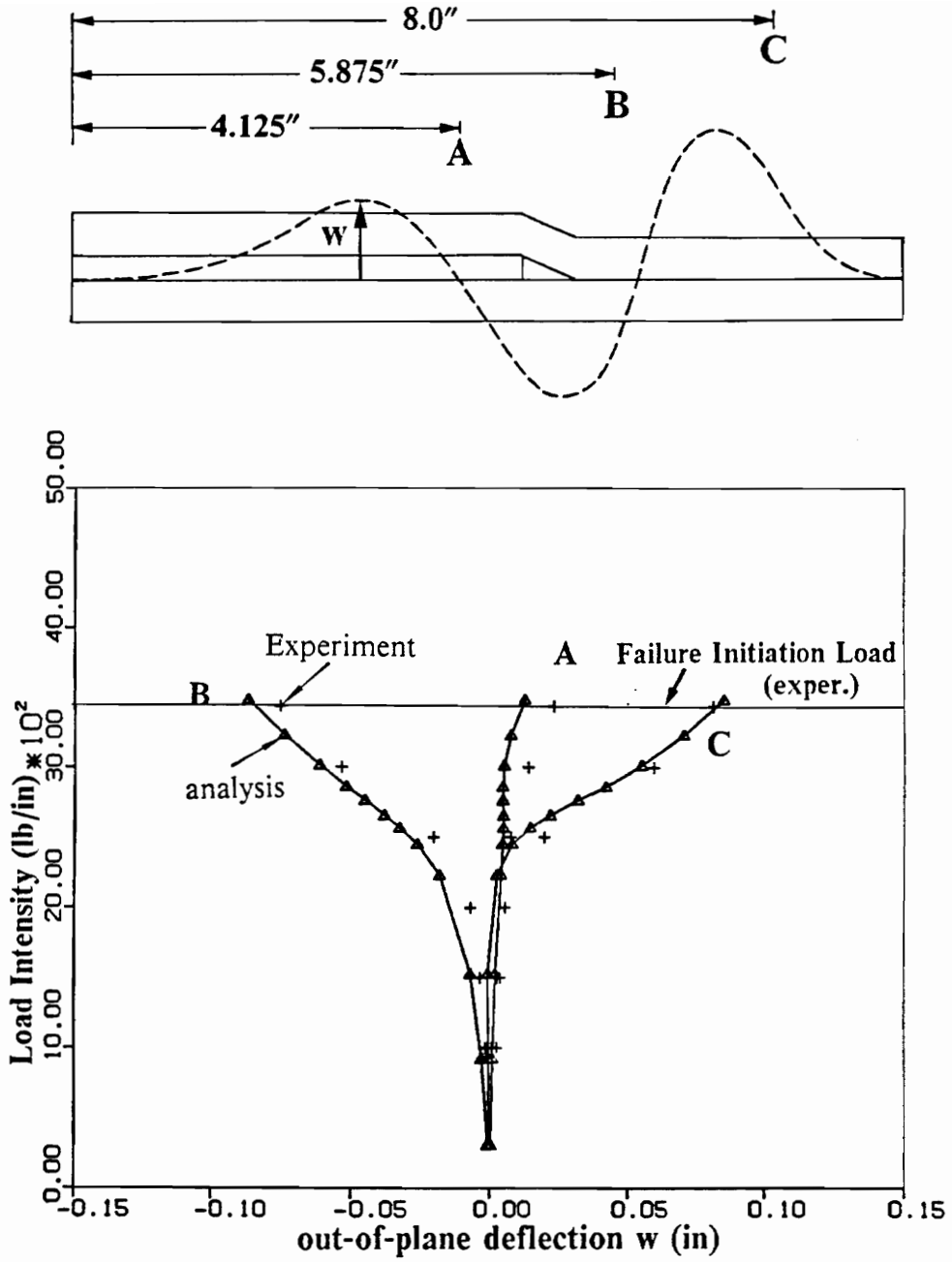

Figure 32. Compressive load intensity vs. out-of-plane deflection: 3-in.-wide $[0_4]_T$ dropped-ply specimen

deflections well, yet it is believed that even closer agreement could have been achieved with more precise measurements of the locations of the displacement transducers.

The distribution of the delamination index at load step 15 in the nonlinear analysis ($N_x = 3480$ lb/in. in compression, which is close to the failure load) is shown in Fig. 33, and Fig. 34 is the corresponding contour plot. Although the overall distribution of F has some similarity to that of the 1-in.-wide specimen, it is significant that the stresses along the centerline ($y = b/2$) have decreased. The large deflections at the center of the laminate cause the center to unload at the expense of increasing interlaminar stresses in the region closer to the knife edge supports.

In summary, the combined use of a linear and a nonlinear analysis can be represented by the plots shown in Fig 35, which represent the longitudinal profiles of index F at the various width-wise locations of integration points. The characteristic distance is determined from the linear analysis from $F = 1$ at failure, as shown in Fig 35a. This distance is used in Fig. 35b to determine the highest value of F on the characteristic line at each load step. For instance, at the 15th load step $N_x = 3480$ lb/in. and $F = 1.15$, so the delamination load is exceeded. The predicted value of the initial delamination load is obtained by interpolating the stress index, defined as the square root of the failure index F, between load steps 14 and 15. This procedure is illustrated on the graph shown in Fig. 36 where the square root of the delamination index (a measure of the stress state) is plotted versus applied load N_x. Interpolation between steps 14 and 15 yields a prediction of 3320 lb/in. for the compressive failure load, and this is in error with respect to experiment by only 3%.

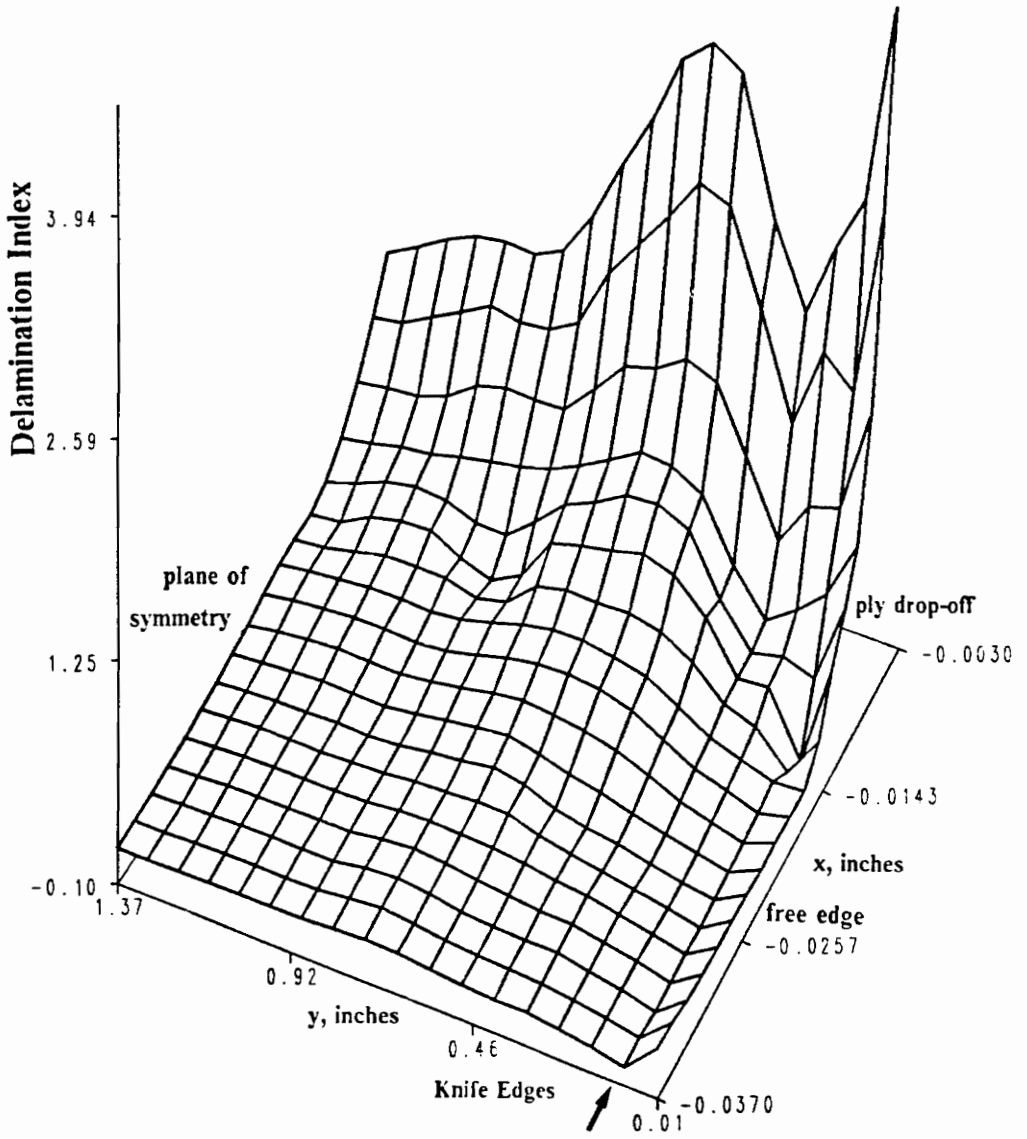

Figure 33. Distribution of the delamination index in the upper interface for a nonlinear analysis: 3-in.-wide $[0_4]_T$ dropped-ply specimen at N_x = 3,480 lb/in, compression.

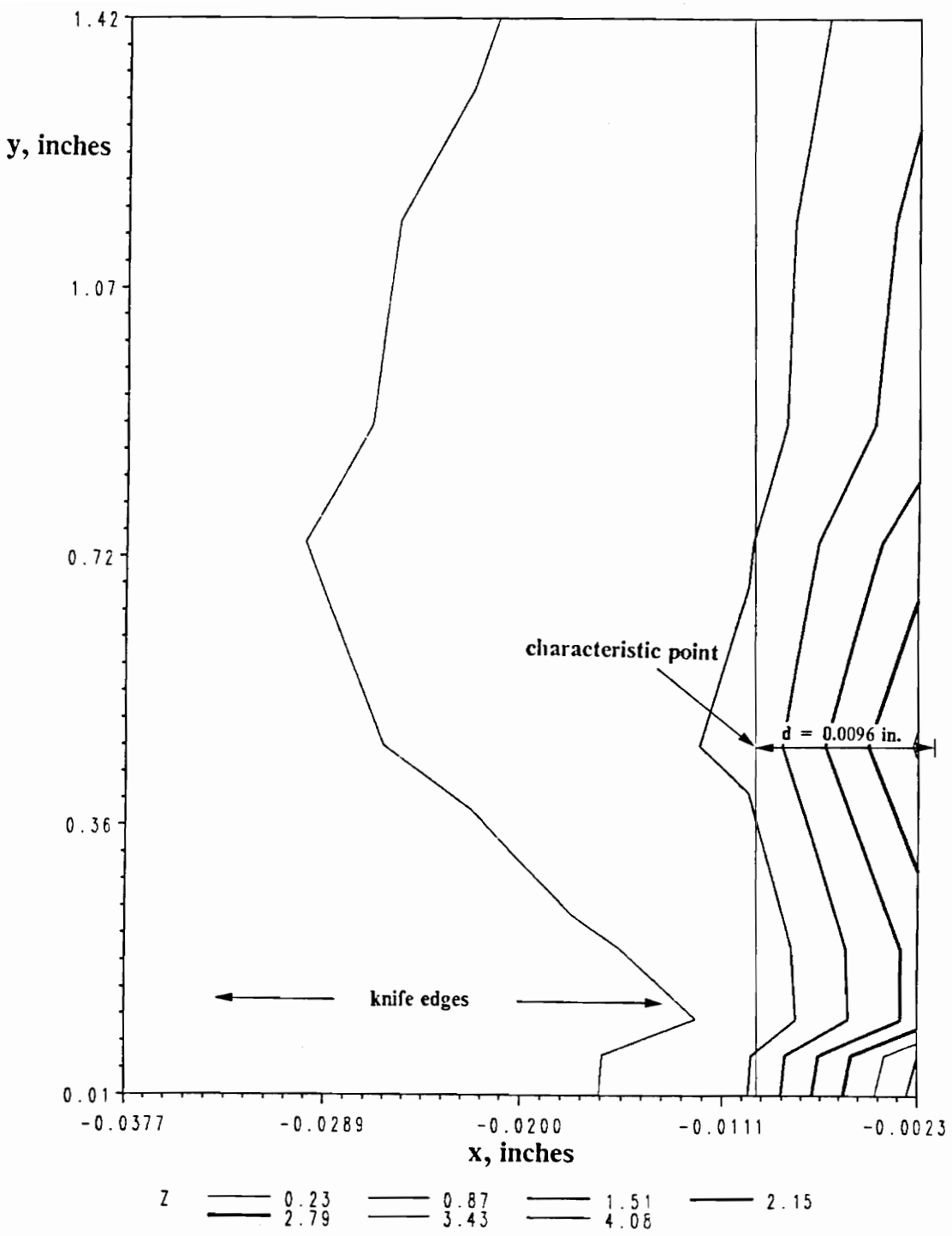

Figure 34. Contours of the delamination index in the upper interface for a nonlinear analysis: 3-in.-wide $[0_4]_T$ dropped-ply specimen at $N_x = 3{,}480$ lb/in, compression.

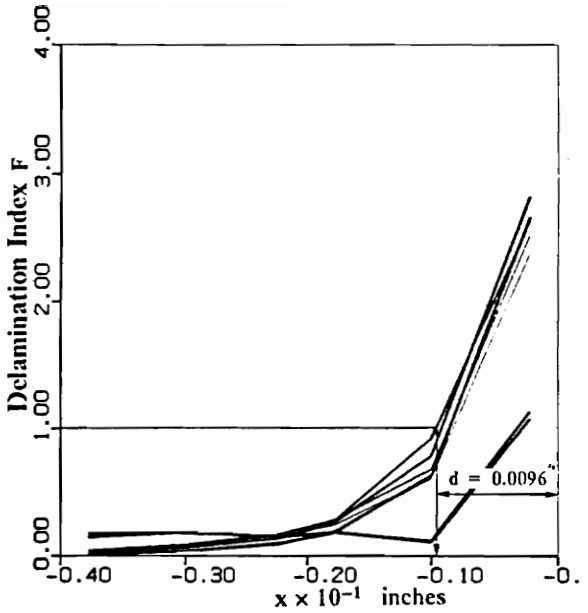

a) Linear analysis of 1-in-wide spec.

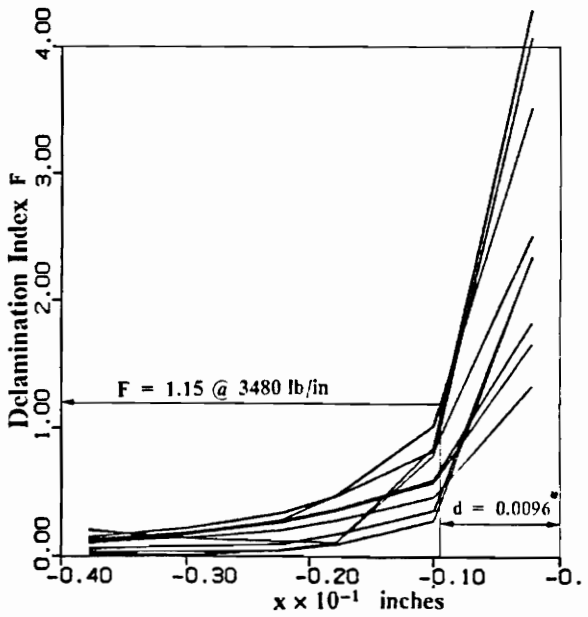

b) Nonlinear analysis of 3-in-wide spec.

Figure 35. Summary of linear/nonlinear delamination analysis: 1 and 3-in.-wide $[0_4]_T$ dropped-ply specimens

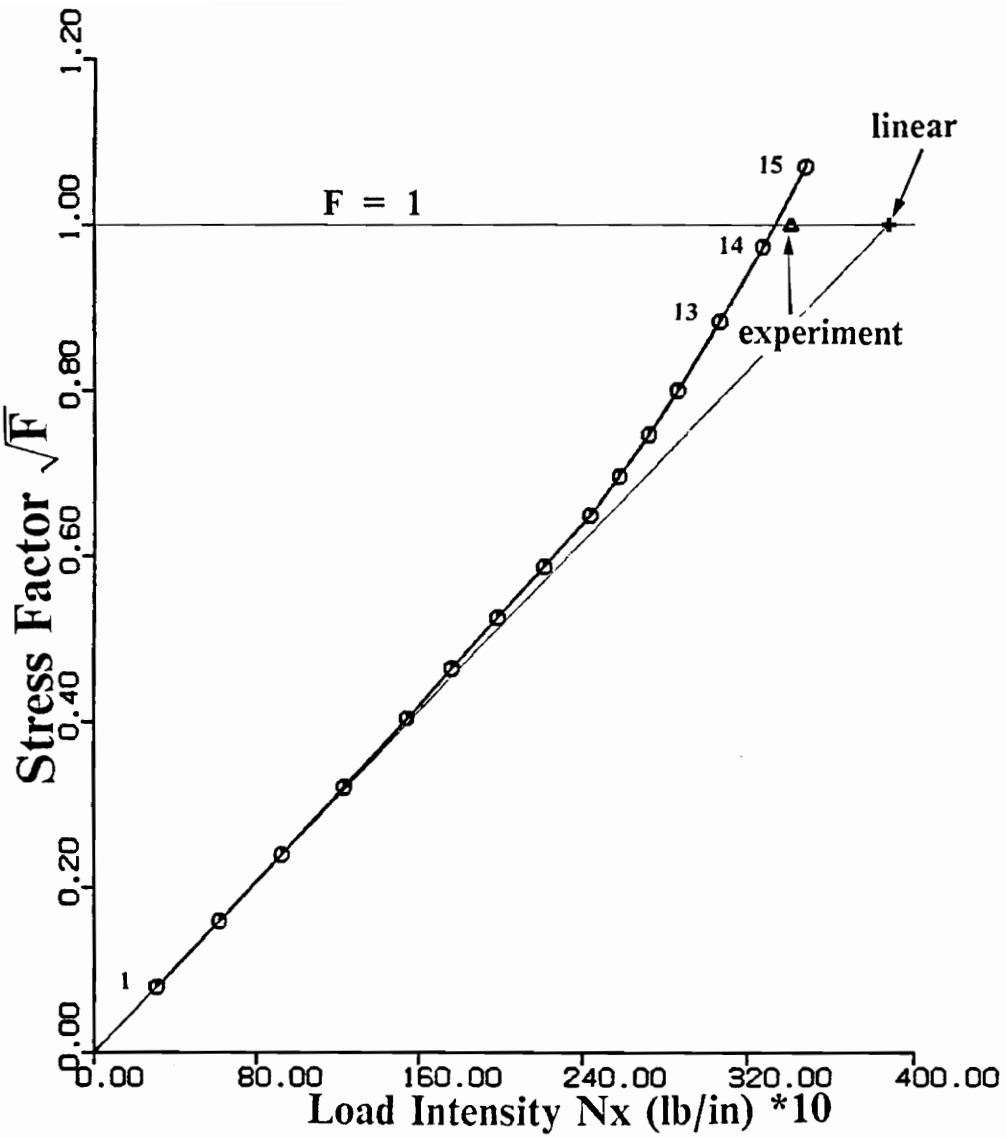

Figure 36. Stress index vs. applied load: out-of-plane deflections cause deviation from linear analysis for $[0_4]_T$ dropped-ply specimen.

5.3 Case 2 $[0_2]_T$ dropped-ply sublaminate

5.3.1 Linear analysis

The three $[0_2]_T$ 1-in.-wide specimens 13-3, 13-4 and 13-5 tested in compression by Curry started to delaminate at 5100, 5280 and 5060 lb/in, as reported in Table 4. Since the dimensions of the first specimen were not available, the average dimensions of the second and third specimens were used for this linear analysis: average width = 1.003 in., average ply thickness = 0.00495 in. (both thick and thin sides).

The distribution of the delamination index at the upper interface is shown in Figs. 37 and 38 at a load of 5100 lbs. The characteristic distance was found to be equal to 0.0093 inches. As for the $[0_4]_T$ case, the stresses at the lower interface were found not to be critical.

5.3.2 Nonlinear analysis

The out-of-plane deflections plotted in Fig. 39 show that the magnitudes of the deflections at the delamination load of the $[0_2]_T$ case are similar to the $[0_4]_T$ case. However, this thinner dropped-ply laminate fails at a somewhat (4%) higher load. No experimental out-of plane deflection data points are available for this specimen.

The distribution plot of the delamination index is shown in Fig. 40 for a load of 3575. lb/in., and the corresponding contour plot is shown in Fig. 41. The distribution of the index shown in Fig. 40 is significantly different than the distribution shown in Fig.

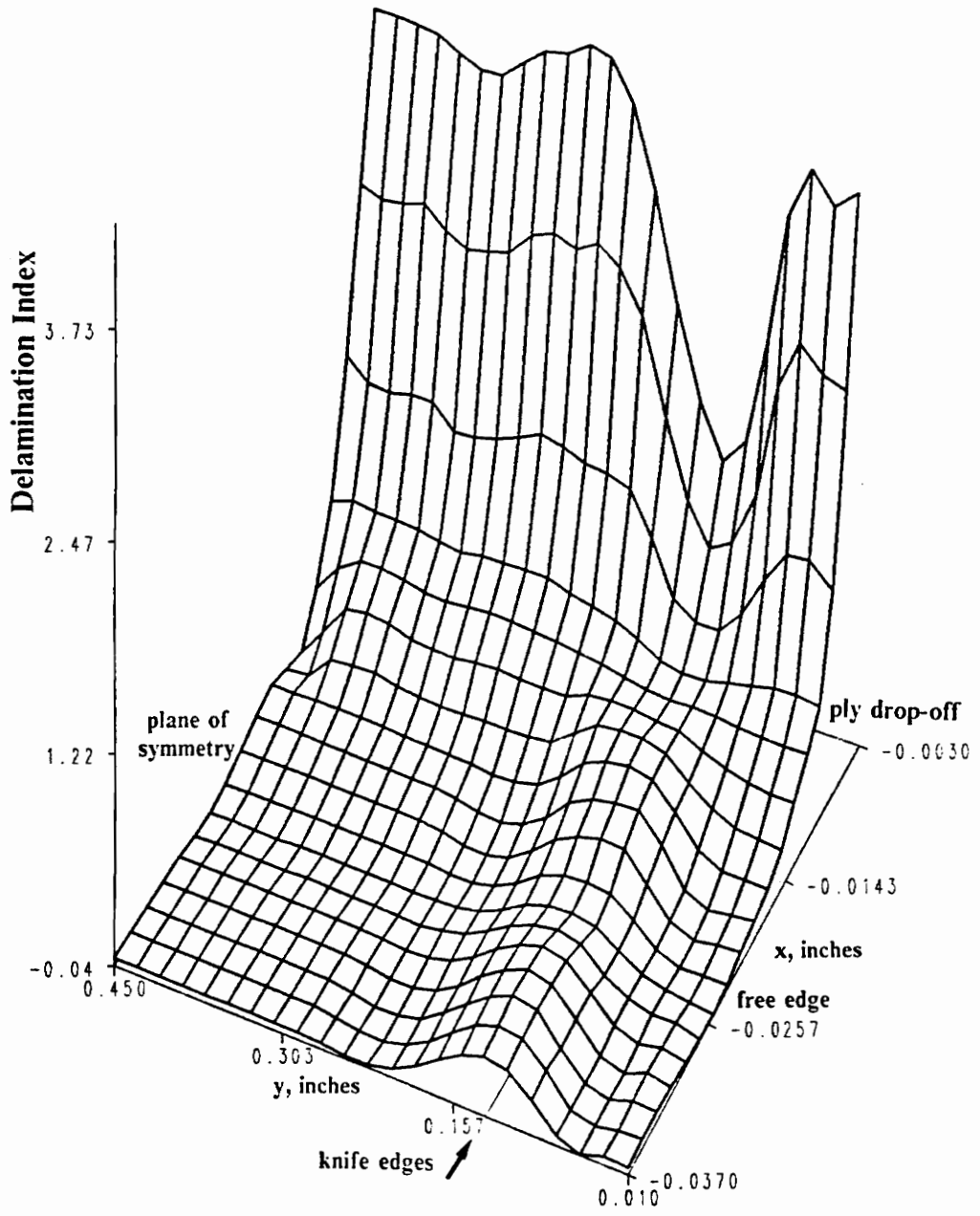

Figure 37. Distribution of the delamination index in the upper interface for a linear analysis: 1-in.-wide $[0_2]_T$ dropped-ply specimen at N_x = 5,100 lb/in, compression.

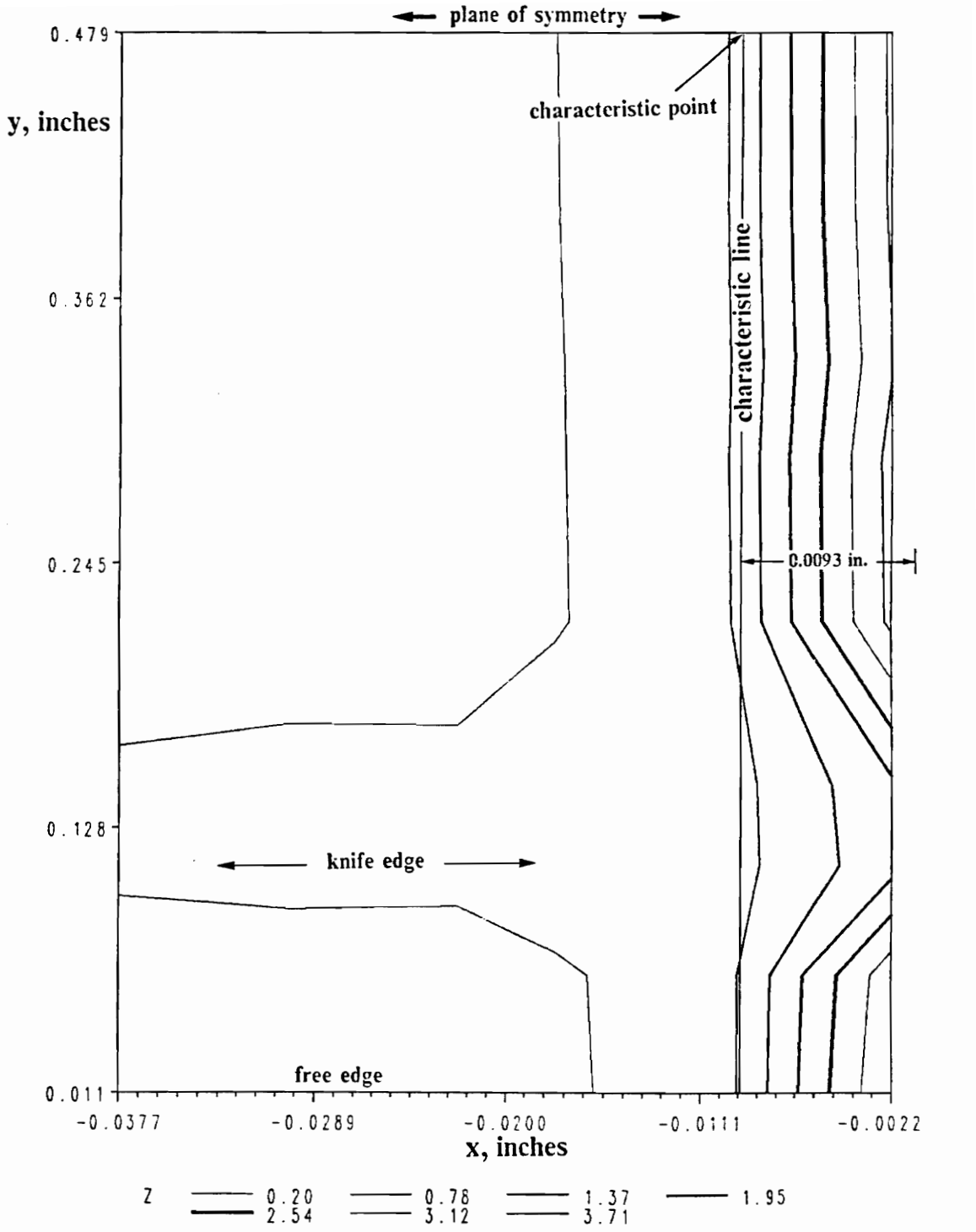

Figure 38. Contours of the delamination index in the upper interface for a linear analysis: 1-in.-wide $[0_2]_T$ dropped-ply specimen at $N_x = 5{,}100$ lb/in, compression.

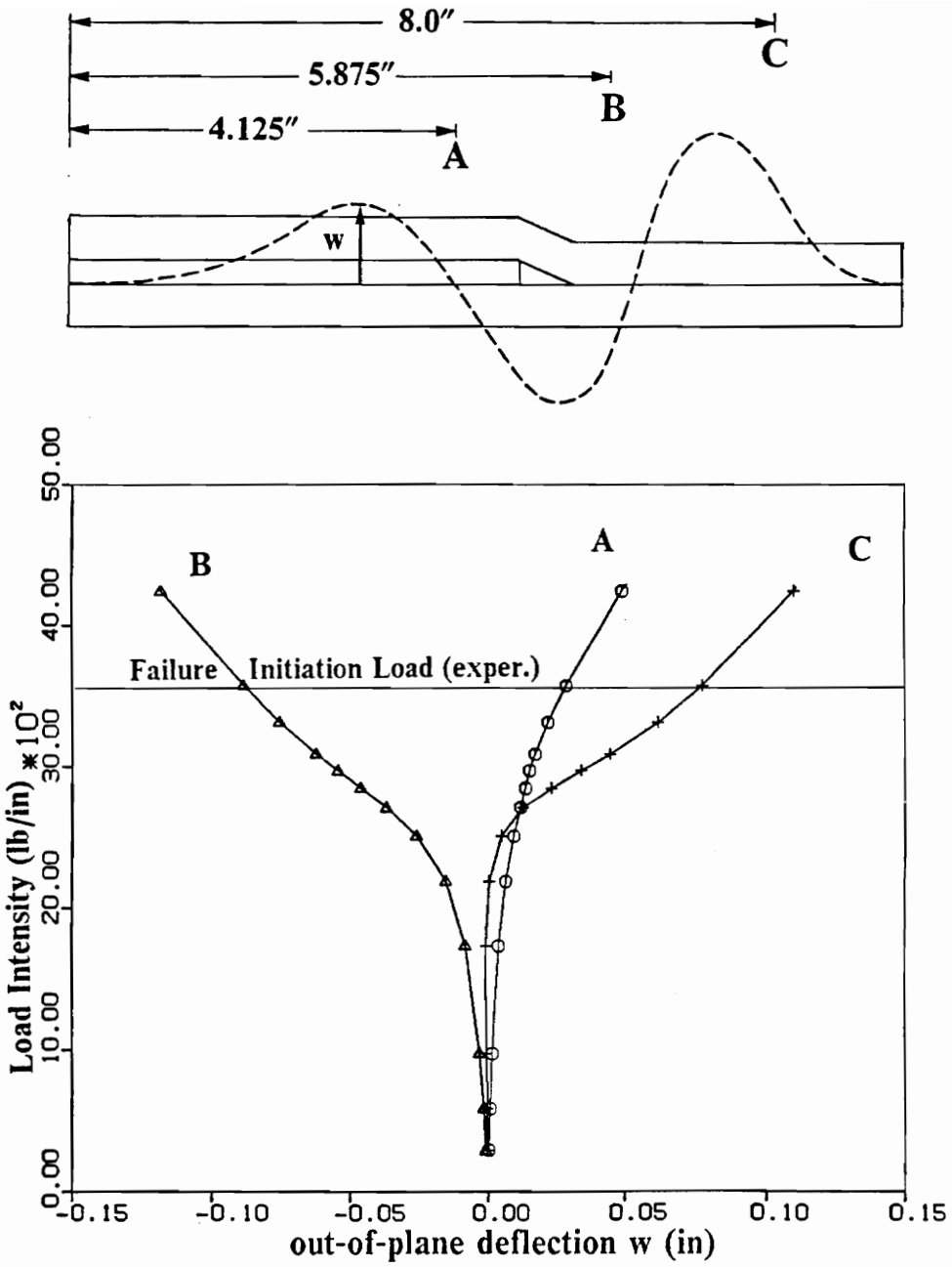

Figure 39. Compressive load intensity vs. out-of-plane deflection: 3-in.-wide $[0_2]_T$ dropped-ply specimen

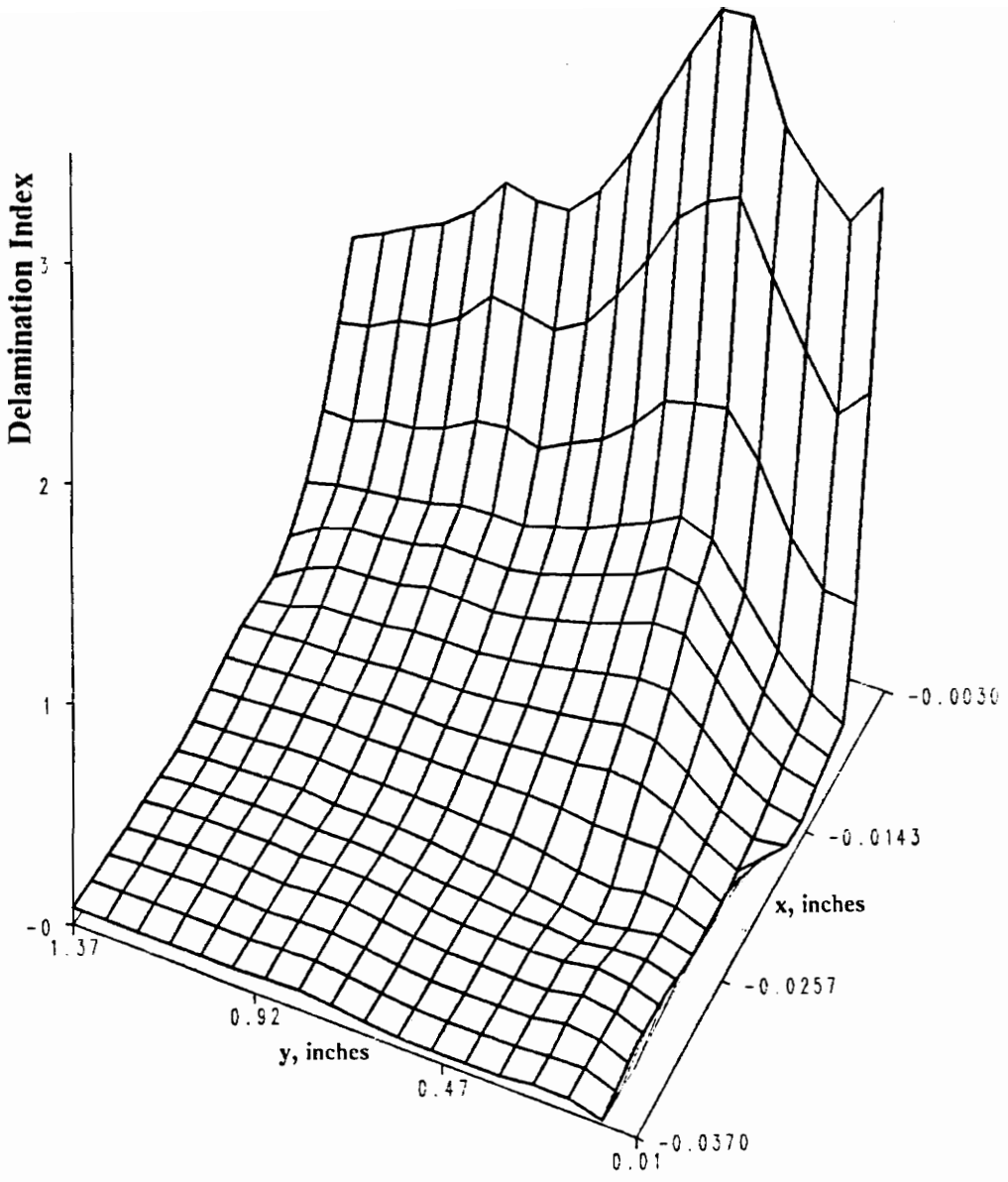

Figure 40. Distribution of the delamination index in the upper interface for a nonlinear analysis: 3-in.-wide $[0_2]_T$ dropped-ply specimen at $N_x = 3{,}575$ lb/in, compression.

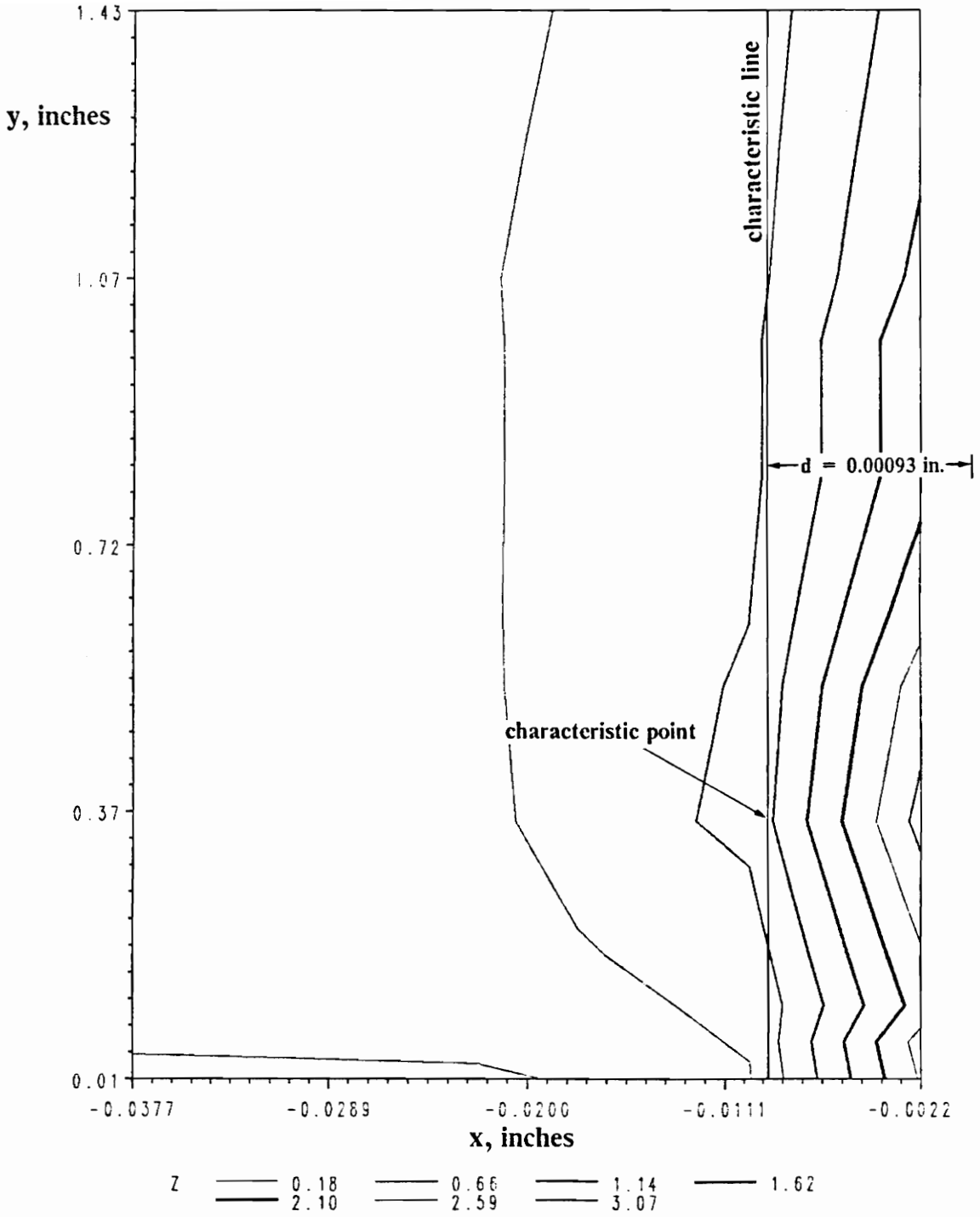

Figure 41. Contours of the delamination index in the upper interface for a nonlinear analysis: 3-in.-wide $[0_2]_T$ dropped-ply specimen at $N_x = 3{,}575$ lb/in, compression.

37 for the 1-in.-wide specimen. Also, the distribution shown in Fig. 40 is virtually identical, except at the free edge, to the $[0_4]_T$ case shown in Fig. 33 at 3480 lb/in. The difference in loads suggests that at equal load the interlaminar stresses for two plies dropped are lower than for four plies dropped. This is caused by a higher axial compliance of the $[0_2]_T$ with respect to the $[0_4]_T$ dropped-ply sublaminate, and by two differences in geometry. 1) The eccentricity in the load path, which acts primarily on a global level, and 2) a less abrupt thickness discontinuity which acts more locally. The thickness discontinuity causes the far-field compressive load to redistribute at the ply drop-off such that a local out-of-plane component of the load is present. This out-of-plane component tends to separate the dropped plies from the sublaminates encapsulating the dropped plies. For symmetric dropped-ply laminates where there is no geometric eccentricity, the abrupt thickness change at the drop-off can, by itself, initiate delamination in compression. Both of these geometric effects are detrimental to the strength of a laminate, and a higher number of plies dropped increases both factors.

At 3575 lb/in. compression, the delamination index F is 0.88 which, by extrapolation to F = 1 predicted an initial delamination load of 3660 lb/in., which is 4% higher than the experimental value.

5.4 Case 3 $[0_8]_T$ dropped-ply sublaminate

5.4.1 Linear analysis

The average delamination initiation load for the three $[0_8]_T$ 1-in.-wide laminates tested in compression by Curry was 3500 lbs. (See specimens 15-3, 15-4 and 15-5 in Ta-

ble 4) The average width of the three specimens is 1.002 in., and their average ply thickness 0.00508 and 0.00500 on the thin and thick sections, respectively. These average values were used in the analysis.

The distribution of the delamination index at the upper interface is shown in Fig. 42 and the contours in Fig. 43 for a compressive load of 3500 lbs. The characteristic distance is found equal to 0.0109 inches. Like for the previous two cases, the stresses at the lower interface were found to be less critical than those on the upper interface.

5.4.2 Nonlinear analysis

The out-of-plane deflection plot in Fig. 44 shows that the deflections are the smallest of all the zero-degree sublaminate cases analyzed. This thicker laminate fails at a lower load than the two previous thinner cases, which again shows that increasing the number of plies dropped has a detrimental effect on the strength of a laminate. No experimental out-of-plane deflection data points are available for this specimen.

The distribution of the delamination index is shown in Fig. 45 for a load of 3020 lb/in., and the corresponding contour plot is in Fig. 46. It is important to observe that the characteristic point in this nonlinear analysis has shifted from a region in-board of the knife edges to the free edge of the laminate. This did not occur with the thinner dropped sublaminates.

At a compressive load of 3020 lb/in., the delamination index at the free edge is 1.26. By interpolation, the predicted initial delamination load is 2820 lb/in., which is 4% lower than the experimental value.

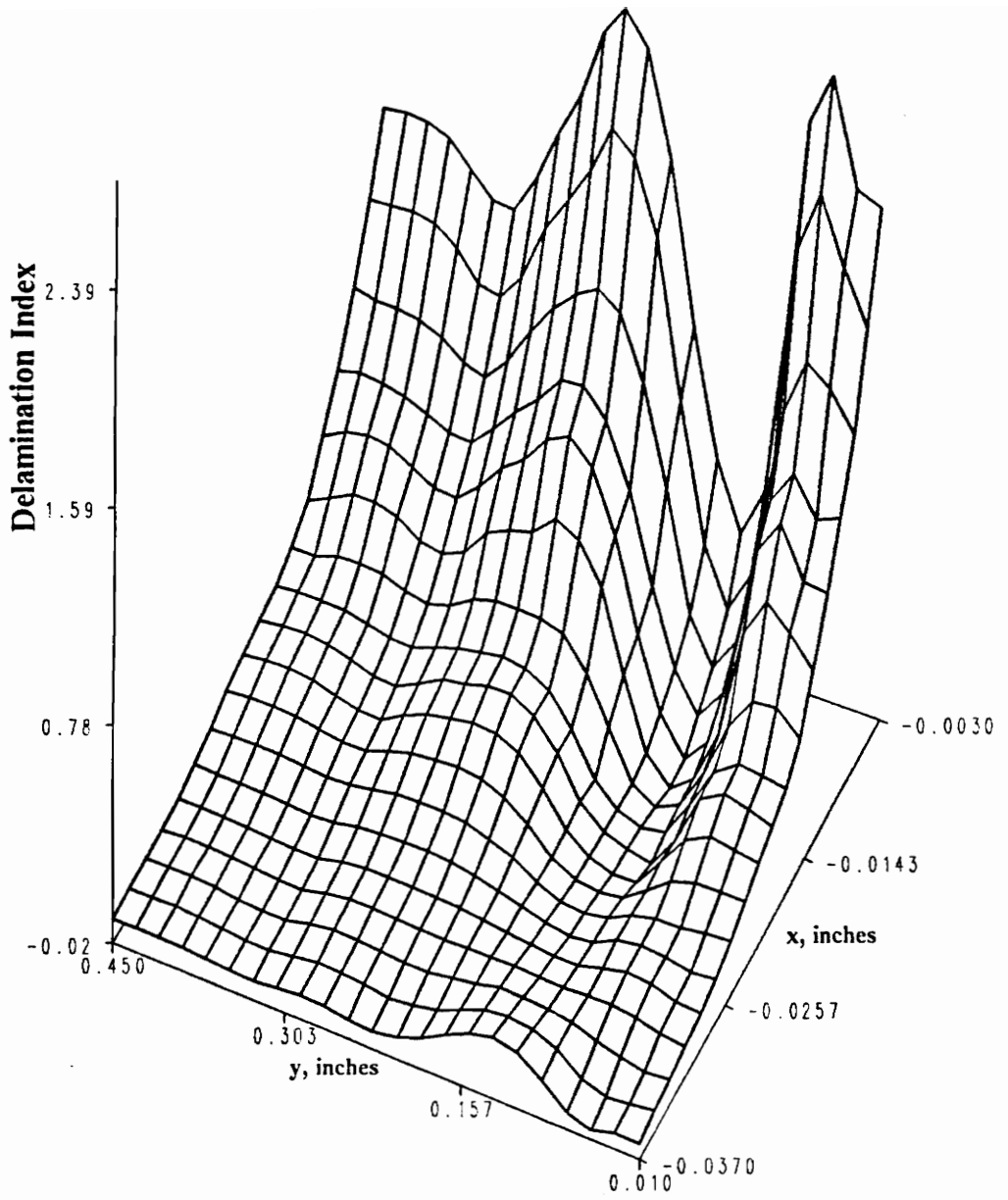

Figure 42. Distribution of the delamination index in the upper interface for a linear analysis: 1-in.-wide $[0_8]_T$ dropped-ply specimen at $N_x = 3{,}500$ lb/in, compression.

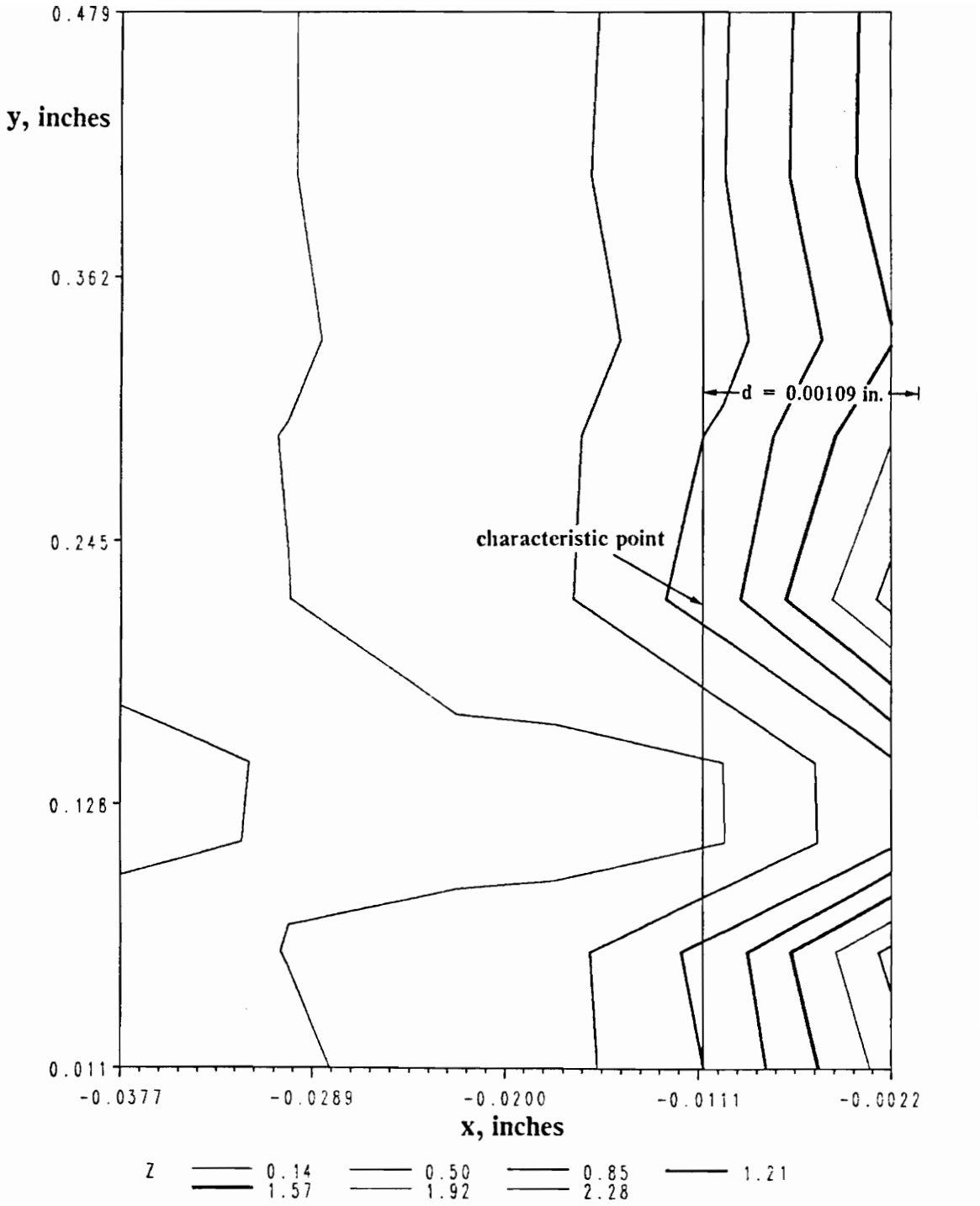

Figure 43. Contours of the delamination index in the upper interface for a linear analysis: 1-in.-wide $[0_8]_T$ dropped-ply specimen at $N_x = 3{,}500$ lb/in, compression.

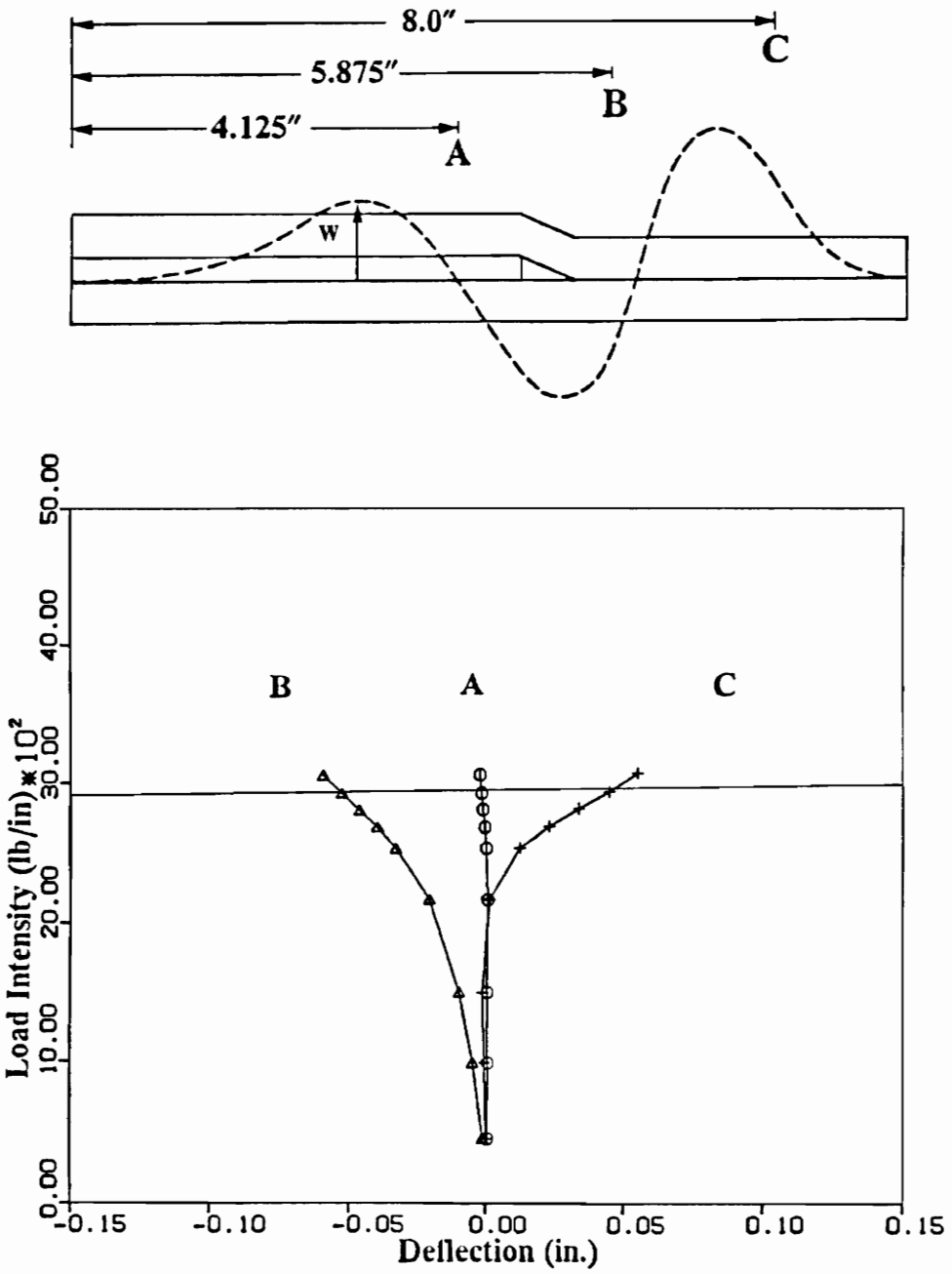

Figure 44. Compressive load intensity vs. out-of-plane deflection: 3-in.-wide $[0_8]_T$ dropped-ply specimen

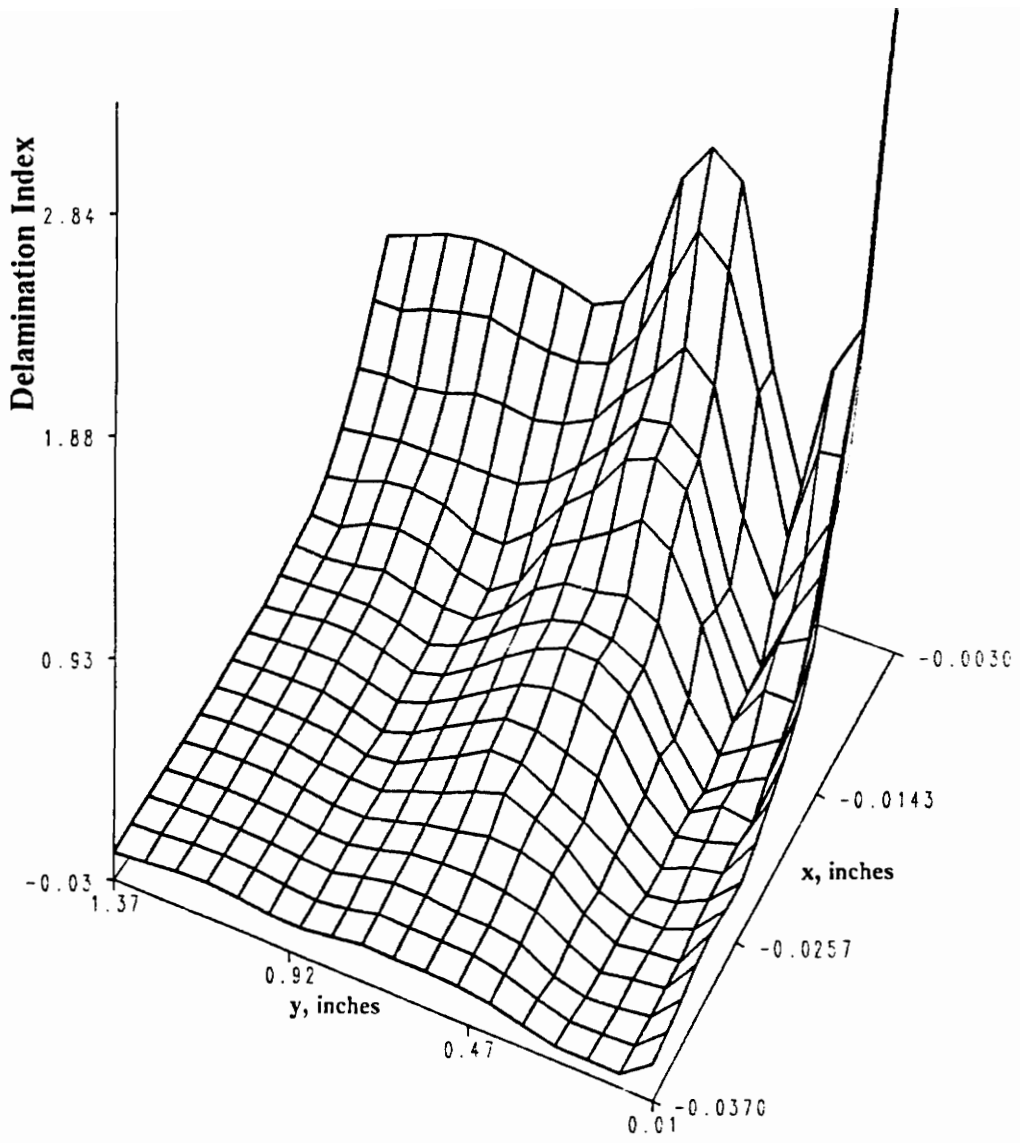

Figure 45. Distribution of the delamination index in the upper interface for a nonlinear analysis: 3-in.-wide $[0_8]_T$ dropped-ply specimen at $N_x = 3{,}020$ lb/in, compression.

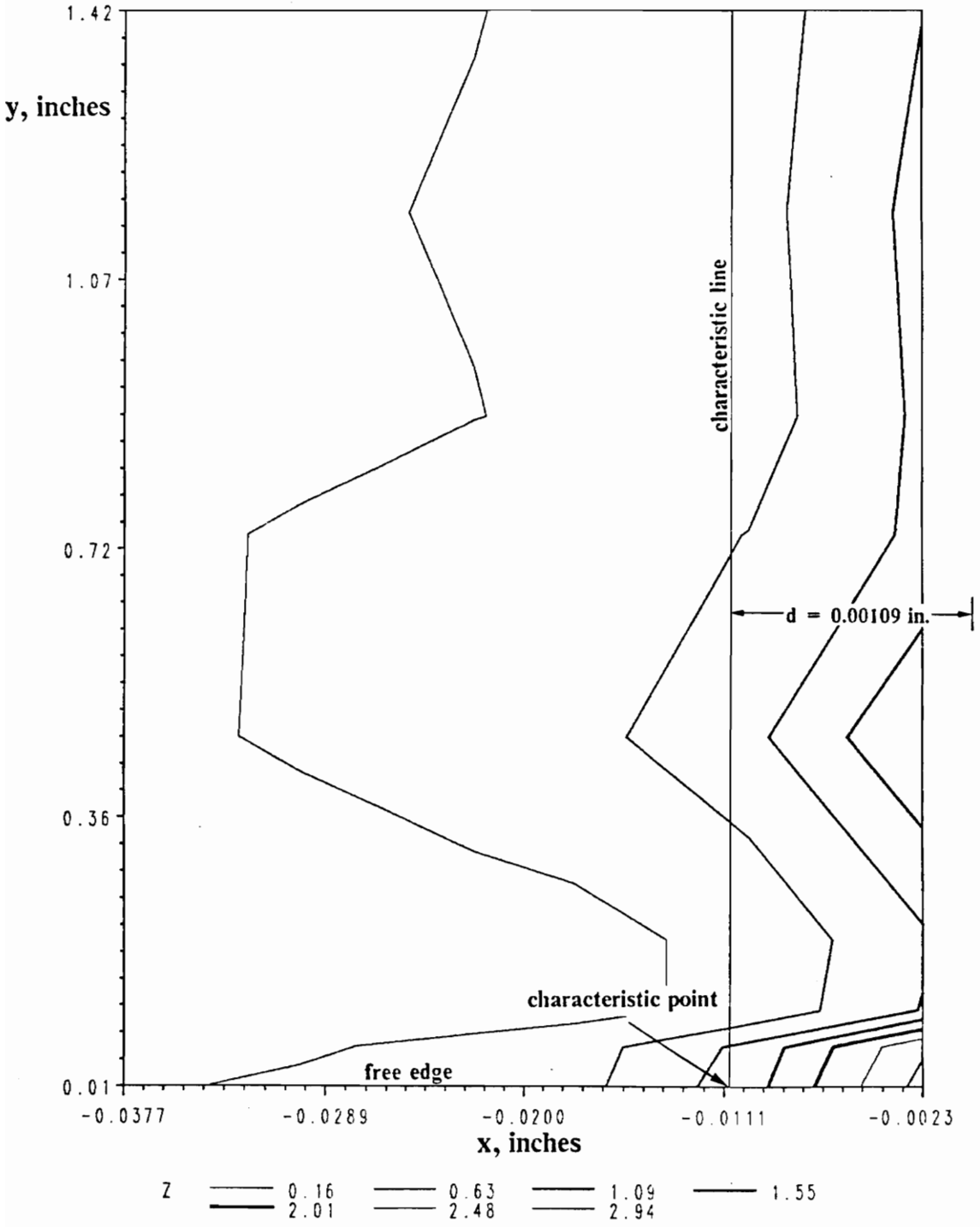

Figure 46. Contours of the delamination index in the upper interface for a nonlinear analysis: 3-in.-wide $[0_8]_T$ dropped-ply specimen at $N_x = 3{,}020$ lb/in, compression.

5.5 Case 4 $[\pm 45/0_2]_s$ dropped-ply sublaminate

5.5.1 Linear analysis

The $[\pm 45/0_2]_S$ 1-in.-wide laminate tested in compression by Curry started to delaminate at 3800 lb/in. (See specimens 12-3, 12-4 and 12-5 in Table 4). The average width of these specimens was 1.004 in., and their average ply thicknesses were 0.0050 in. on both thin and thick sides. These average values were used in the analysis.

The delamination index in the upper interface is shown in Figs. 47 and 48 at the initial delamination load. A characteristic distance of 0.0126 inches was found. As for all previous cases, the stresses at the lower interface were found to be lower than those at the upper interface.

5.5.2 Nonlinear analysis

The out-of-plane deflections plotted in Fig. 49 show that the magnitude of the deflections are small, and comparable to the $[0_8]_T$ dropped-ply sublaminate, where the same number of plies were dropped. The experimental failure load (3475. lb/in.) is somewhat higher than for the $[0_8]_T$ specimen (3309 lb/in.). The increase may be due to the lower axial stiffness of the dropped-ply sublaminate. No experimental out-of-plane deflection data is available for this specimen.

The plots of the delamination index are shown in Figs. 50 and 51 for a load of 3515 lb/in. The distribution of index F shows, like for $[0_8]_T$ specimen, that the critical lo-

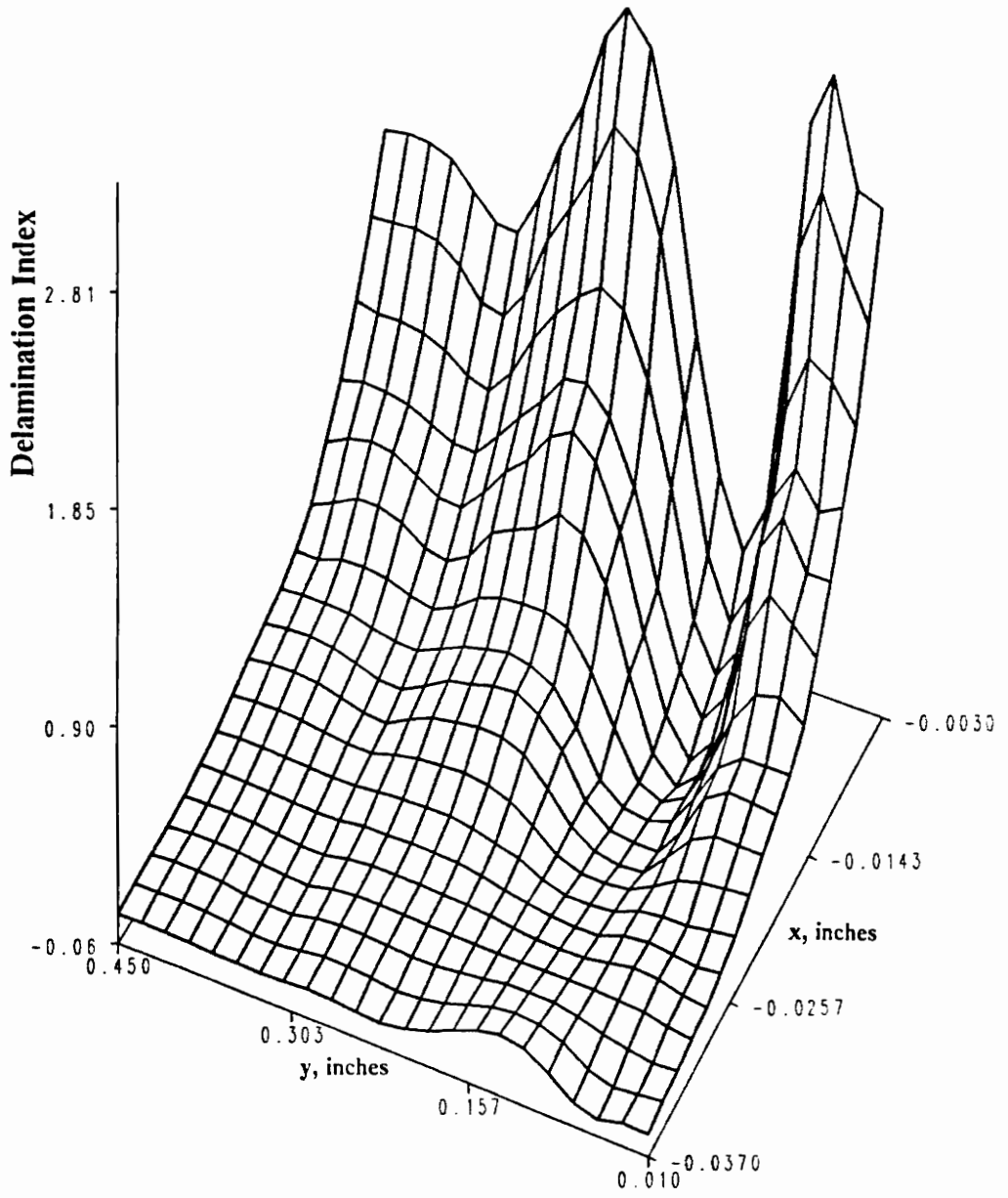

Figure 47. Distribution of the delamination index in the upper interface for a linear analysis: 1-in.-wide $[\pm 45/0_2]_S$ dropped-ply specimen at $N_x = 3{,}800$ lb/in, compression.

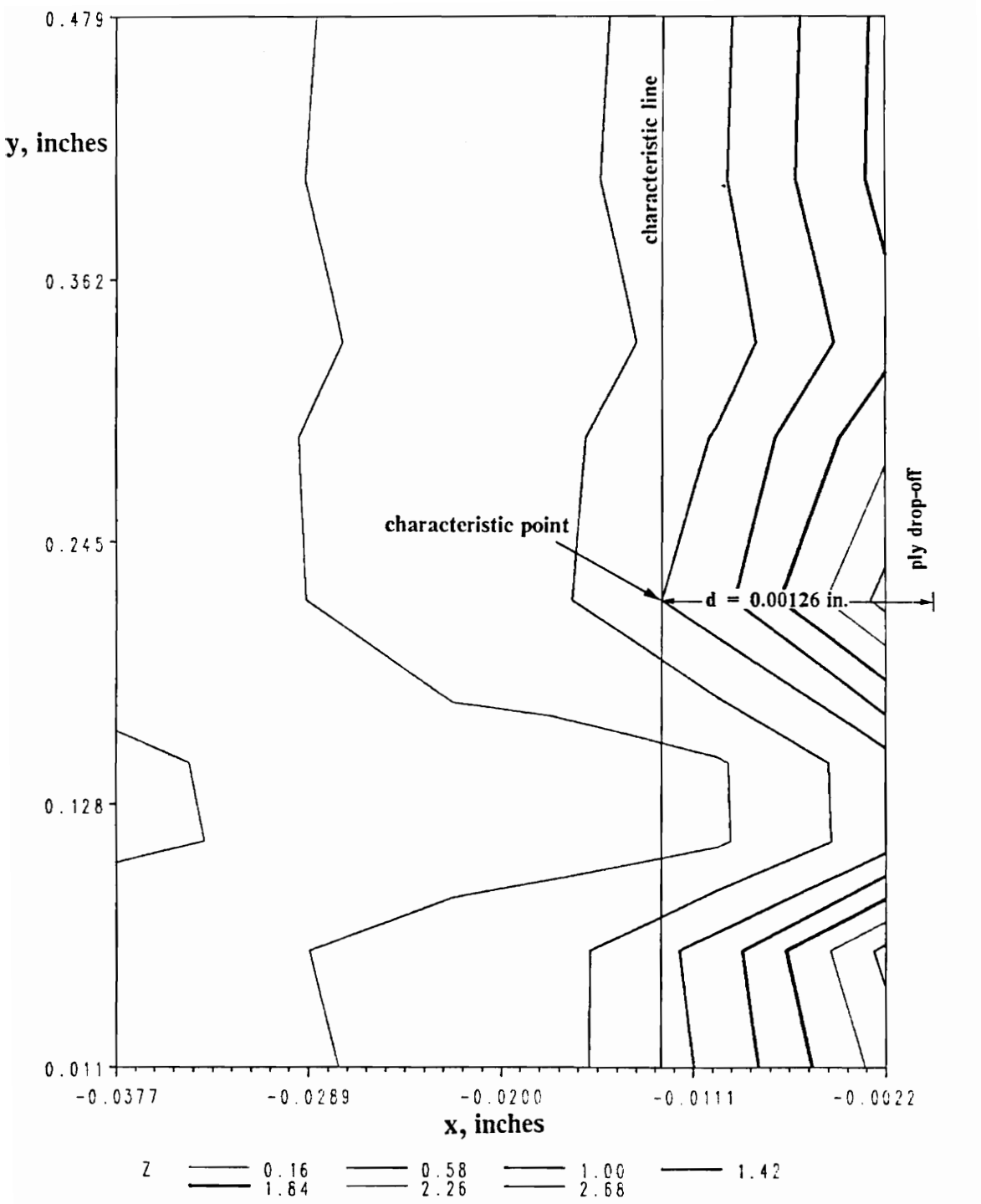

Figure 48. Contours of the delamination index in the upper interface for a linear analysis: 1-in.-wide $[\pm 45/0_2]_S$ dropped-ply specimen at $N_x = 3{,}800$ lb/in, compression.

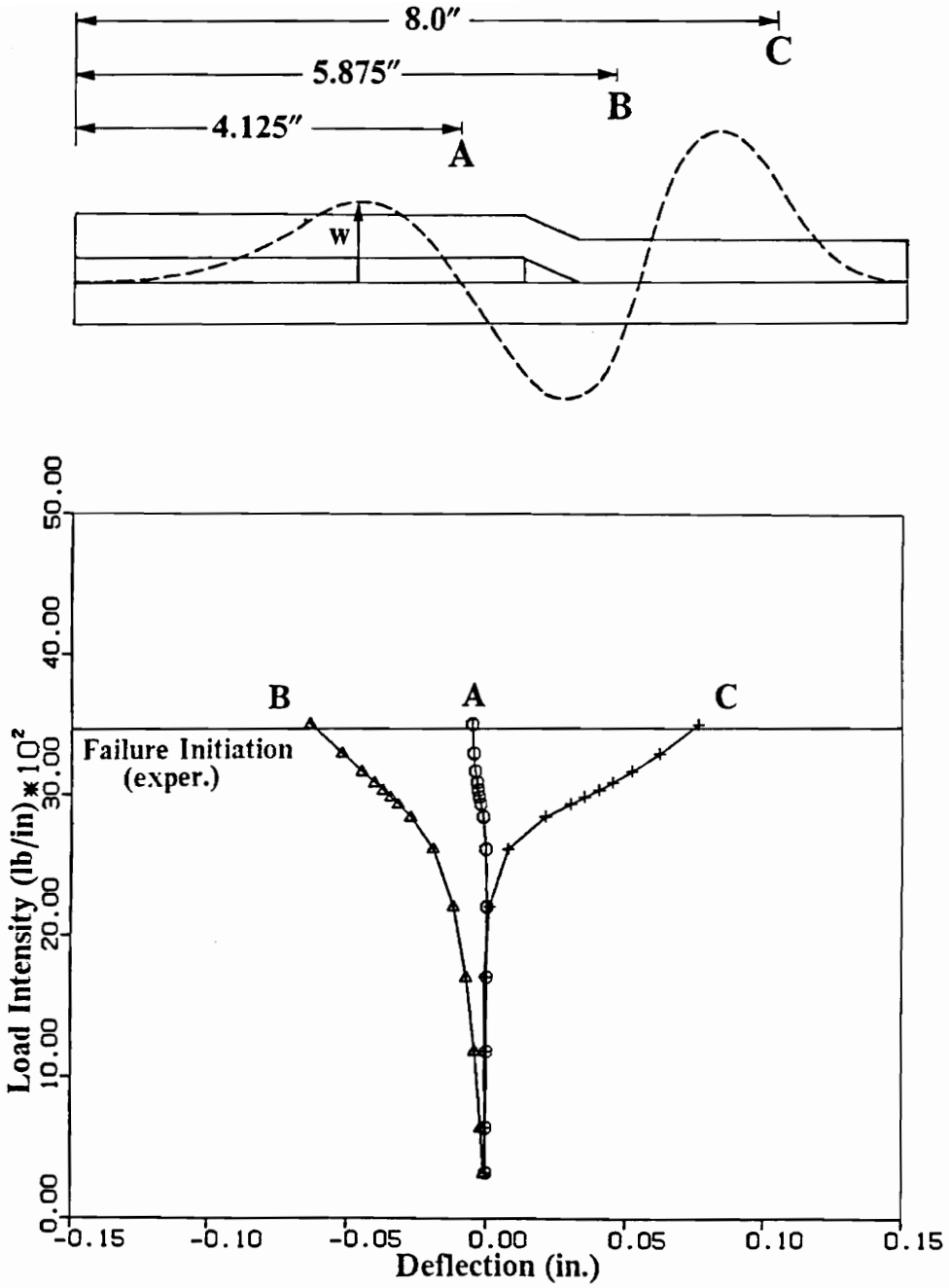

Figure 49. Compressive load intensity vs. out-of-plane deflection: 3-in.-wide $[\pm 45/0_2]_S$ dropped-ply specimen

cation is not in-board of the knife edges, but rather at the free edge. The delamination index on the characteristic line is 1.4 which, by extrapolation to F = 1, predicts an initial delamination load of 3170 lb/in. This prediction is 9% lower than the experimental value.

5.6 Summary and discussion of results

The results of the four cases analyzed above are compared in Fig. 52, which shows the delamination initiation loads for analysis and experiment. The values for the zero-degree specimens are connected by straight lines to show a trend. The values for the $[\pm 45/0_2]_S$ dropped-ply sublaminate are also shown for comparison.

Experiments and analysis clearly show a decrease in laminate strength with an increase in number of plies dropped. This is consistent with the fact that thicker (and therefore stiffer) dropped-ply sublaminates increase a specimen's propensity to delaminate by concentrating the interlaminar stresses into a small region near the drop-off site. In addition, the detrimental effects of load path eccentricity and the abrupt thickness change increase with the number of plies dropped (see discussion at the end of subsection 5.3.2).

It is often believed that geometric nonlinearity tends to relieve stresses and that linear analyses are, therefore, conservative with respect to design. However, the results shown in Figure 52 indicate that nonlinear effects cause a significant drop in strength. It was shown in the plots of the delamination index (Figs. 33, 40, 45 and 50) that the large out-of-plane deflections of the laminate unload the center of the laminate at the expense of increasing interlaminar stresses near the supports. This is particularly true

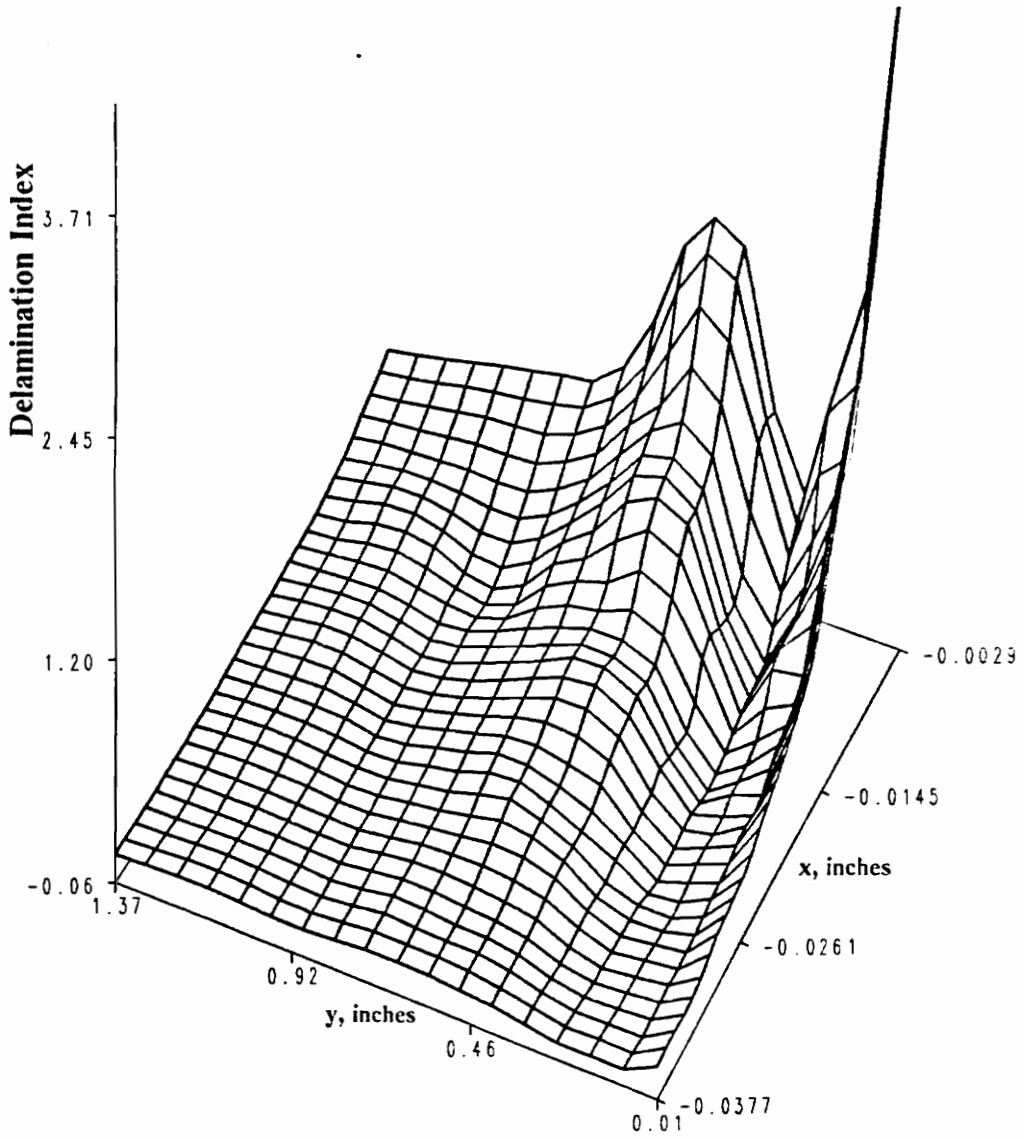

Figure 50. Distribution of the delamination index in the upper interface for a nonlinear analysis: 3-in.-wide $[\pm 45/0_2]_S$ dropped-ply specimen at $N_x = 3{,}515$ lb/in, compression.

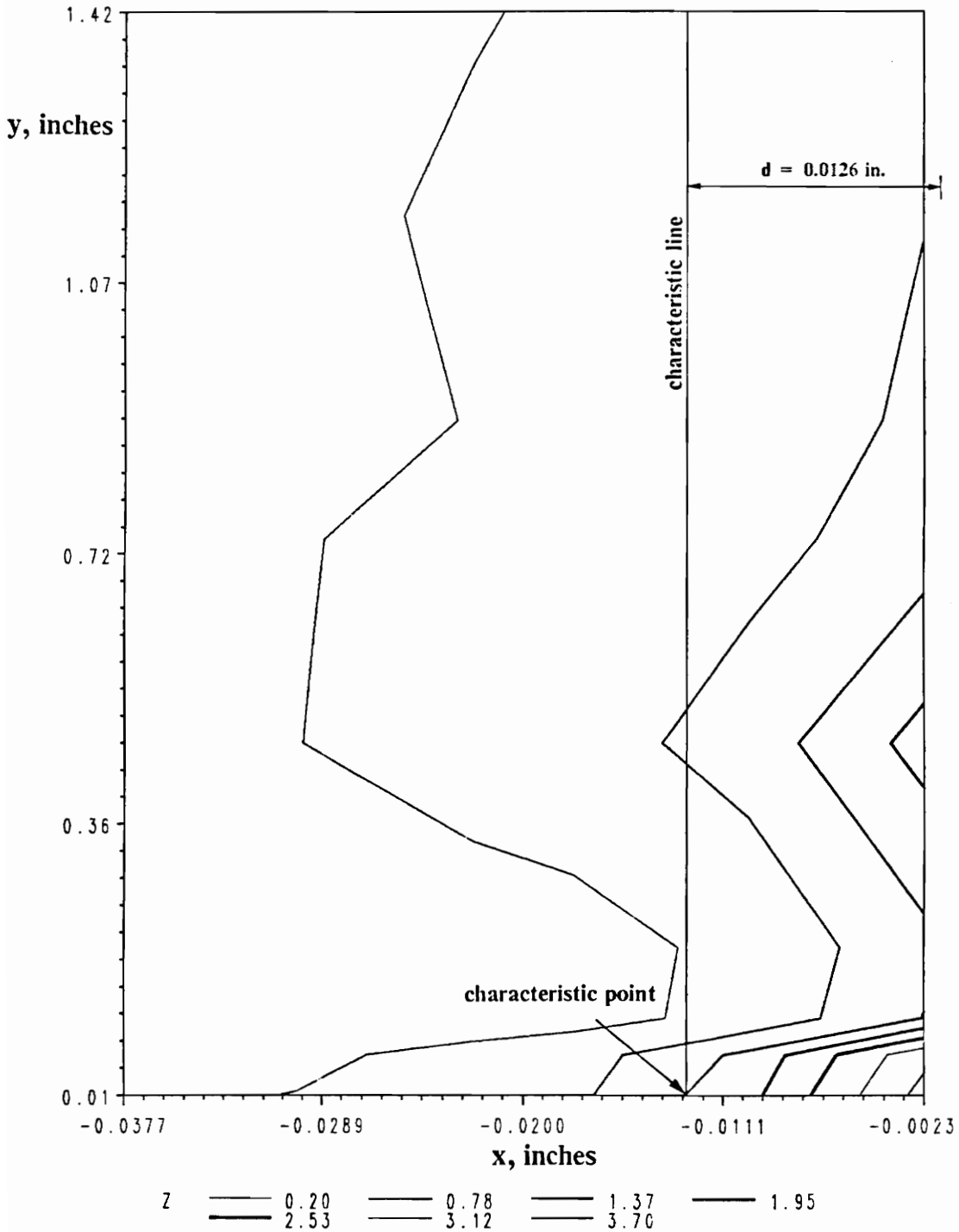

Figure 51. Contours of the delamination index in the upper interface for a nonlinear analysis: 3-in.-wide $[\pm 45/0_2]_S$ dropped-ply specimen at $N_x = 3{,}515$ lb/in, compression.

with the $[0_2]_T$ dropped-ply specimen, where its relative advantages of small load path eccentricity and thickness change are mostly offset by the large displacement (nonlinear) response.

The largest errors in the analysis are of 4 and 9%, and these errors correspond to the two cases of eight plies dropped. In both cases the analysis overpredicts the stresses (and underestimates the strength). The reason could be that in both of these cases the predicted location of the characteristic point is at the free edge, where the concept of characteristic line does not apply directly. These cases would require the use of a second characteristic line parallel to the free edge. However, the second characteristic distance could not be determined because none of the 1-in.-wide specimens were affected by a delamination initiation at the free edge.

The characteristic distance obtained for the four cases analyzed is shown in Fig. 53. The results indicate that the characteristic distance increases slightly with an increasing number of plies dropped for a fixed layup, and that the characteristic distance is a function of the stacking sequence.

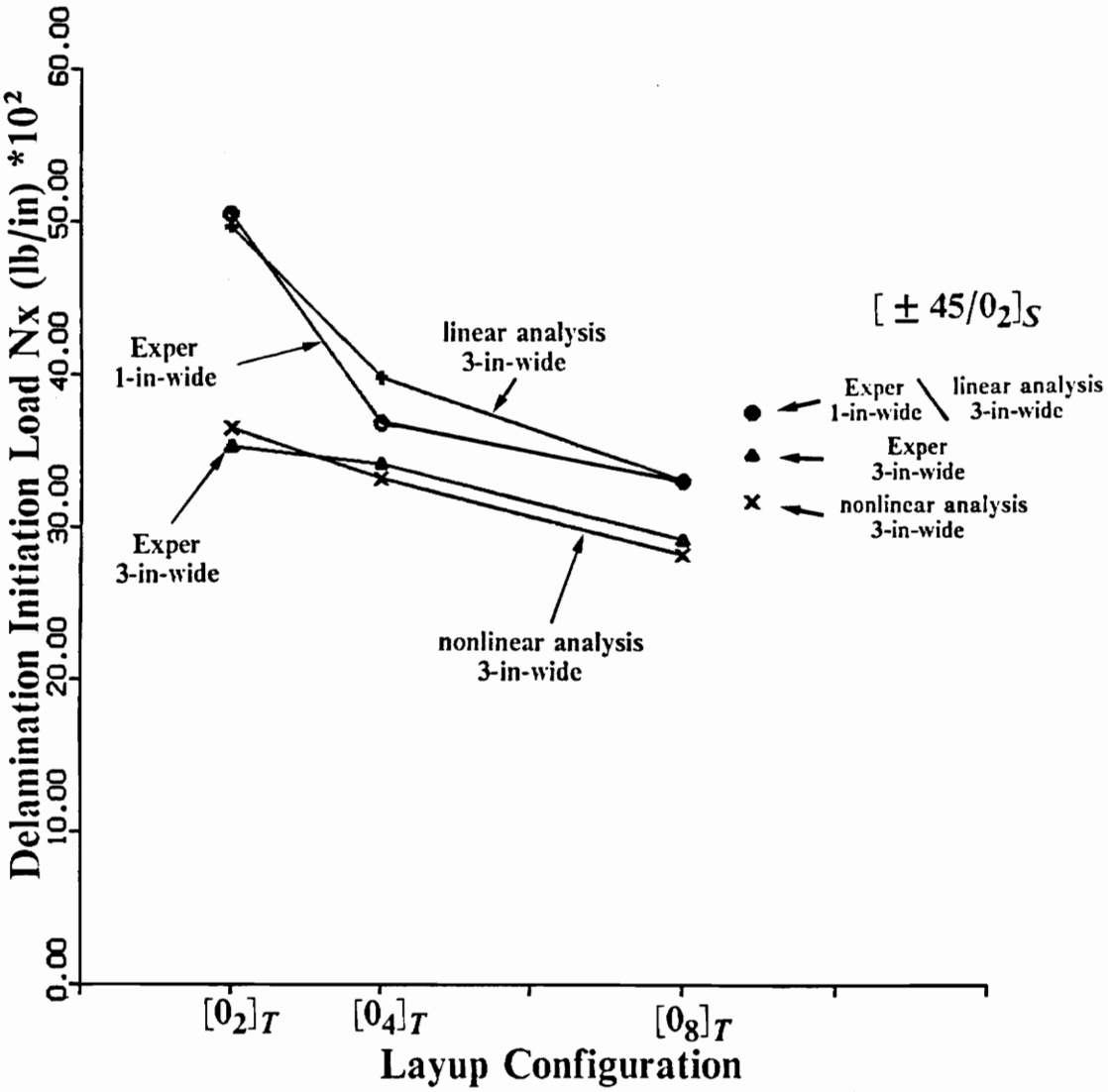

Figure 52. Initial delamination load for four cases analyzed: Summary of results

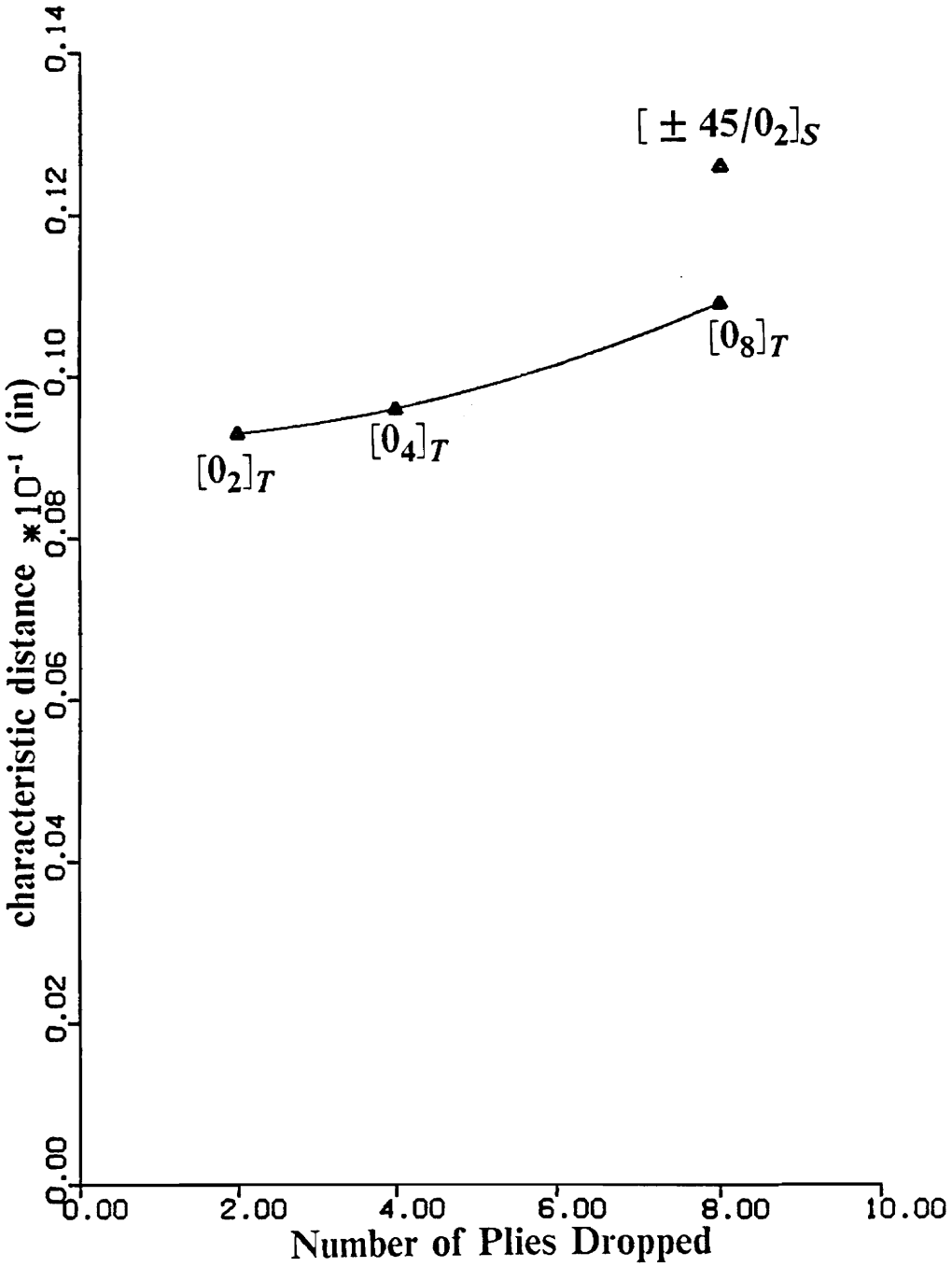

Figure 53. Characteristic distance

6 Concluding Remarks

Uniaxial compression testing[16] of dropped-ply, graphite-epoxy laminated plates has confirmed that delamination along the interfaces above and/or below the dropped plies is a common mode of failure initiation. The compression strength (load per unit plate width) of specimens exhibiting a linear response to delamination is greater than the compression strength of specimens with the same layup exhibiting a geometrically nonlinear response, or postbuckling response, to delamination. (A linear response was exhibited by the 1.0- and 1.5-inch-wide specimens in Ref. 16, while the three-inch counterpart of these narrow specimens exhibited a geometrically nonlinear response.) The purpose of this work is to determine the interlaminar stress distribution which causes the lower compression strength of the postbuckled specimens with respect to the linear response specimens, and to predict their strength. To achieve this purpose, a geometrically nonlinear finite element model of the dropped-ply specimens was developed to predict the interlaminar stress response in the critical interfaces surrounding the dropped plies, and a delamination methodology employing a quadratic interlaminar failure index computed at a characteristic distance from the drop-off was used to predict the strength.

A geometrically nonlinear finite element model which combines shell and solid elements was developed on the COmputational MEchanics Testbed (COMET) software system. COMET is managed by the Computational Mechanics Branch at the NASA Langley Research Center in Hampton, Virginia, and it provides a framework for research in structural analysis methods.

One of the principal thrusts of this work involved the development of analysis capabilities for dropped-ply laminate models that did not exist in COMET at the outset of this project. These new analysis capabilities are 1) the extension of the existing 20-node serendipity solid element from linear analysis only to include geometric nonlinearity in a total Lagrangian formulation, and 2) the development of a new 15-node transition element to connect shell and solid elements in both linear and geometrically nonlinear finite element models. These new analysis capabilities were validated with the few existing results available in the open literature (see Sec. 3.5), and were found to perform well. The transition element has the capability to connect a stack of solid elements through the thickness of the laminate to a single shell element. This feature is lacking in other transition elements reported in the literature. The transition element provides the interface between shell and solid elements, and may produce a stress concentration where the displacements of the three-dimensional field are constrained to match the shell field displacements. Therefore, it is recommended that stresses not be computed in the transition element. In modeling with shell, transition and solid elements, the purpose of including the solid elements is that these elements are to provide estimates of the three-dimensional state of stress, and not the transition elements.

The development of the transition element was essential for the reduction of the finite element model of the dropped-ply laminate to a reasonable number of degrees of

freedom. The computationally intensive solid elements were used only where three-dimensional effects are important; i.e., around the ply drop-off. Everywhere else, or about 96% of the laminate, nine-node shell elements were used. A parametric study on mesh size (see Sec. 4.4) showed that a relatively small model consisting of 2500 degrees of freedom was perfectly capable of generating reasonable interlaminar stress distributions.

Curry[16] tested about sixty specimens of dropped-ply laminates with eight layup configurations and three different widths. In four of these eight configurations, failure initiation was clearly identified as delamination along the ply drop-off, for all specimen widths. These four configurations were selected for this study. The other layup configurations led to other failure modes such as crushing at the grips or delamination at a nodal line in the thin section of the specimen.

The delamination analysis evaluated in this study is based on the quadratic delamination criterion which compares the state of stress at a point with allowable strengths. To avoid the problem of the stress singularities in the idealized model of the dropped-ply laminate, an extension of Nuismer and Whitney's[41] concept of characteristic distance was used. The characteristic line is defined as the two-dimensional counterpart of the characteristic distance. It defines a locus of points parallel to the ply drop-off where the stresses from the approximate analysis are assumed to be representative of the state of stress in the real structure.

The characteristic distance was determined from a linear analysis of a 1-in.-wide specimen, and was then used for the prediction of the delamination initiation of the postbuckled 3-in.-wide specimen.

Experimental and analytical results show that, contrary to common perception, geometric nonlinearity is not always accompanied by lower stress magnitudes with respect to linear response. In fact, the results for the laminates in this study show that a linear analysis is entirely inadequate, in particular for the case of just two zero-degree plies dropped, where the linear analysis is unconservative by about 35 percent.

The two most important factors influencing the compression strength of a dropped-ply laminate are the stacking sequence of the dropped plies, and the number of plies dropped. The stacking sequence, or the orientation of the fibers, changes the axial stiffness of the dropped plies. Higher axial stiffnesses increase the stress concentration at the corner of the drop-off, which lowers the strength of the laminate.

The number of plies dropped affects the strength of the laminate by adversely changing the geometry in two ways: 1) by increasing the eccentricity in the load path, which acts primarily on a global level, and 2) by increasing the abruptness of the thickness discontinuity, which acts more locally. The thickness discontinuity causes the far-field compressive load to redistribute at the ply drop-off such that a local out-of-plane component of the load is present. This out-of-plane component tends to separate the dropped plies from the sublaminates encapsulating the dropped plies. For symmetric dropped-ply laminates where there is no geometric eccentricity, the abrupt thickness change at the drop-off can, by itself, initiate delamination in compression. The detrimental effects of load path eccentricity and the abrupt thickness change increase with the number of plies dropped.

In addition to the stacking sequence and the number of dropped plies, geometrically nonlinear response can significantly reduce the strength of a laminate. The analytical results show that the large out-of-plane deflections associated with geometrically

nonlinear response cause a redistribution of the stresses from the center of the laminate towards the supports. The resulting stress peaks are substantially higher than those produced by a linear analysis, in particular for the laminates with the fewest plies dropped.

The concepts of a characteristic distance and a characteristic line are engineering solutions to the problem of stress singularities at a geometric discontinuity. Authors such as Brewer and Lagace[9] have performed studies aimed at determining the characteristic distances (or averaging distances) associated with particular laminates. It is important to recognize, however, that these values are just as dependent on finite element model and mesh size as they are on material properties and stacking sequences. In the analyses performed here, mesh size was kept nearly identical for linear and nonlinear analyses. The differences in mesh were in the width direction (y) where mesh refinement does not play an important role. This ensures that a characteristic distance obtained from a linear analysis can be used to scale the corresponding nonlinear analysis. As a result, the linear analysis is calibrated to compensate for some of the inaccuracies of the finite element discretization.

It should be stressed that the predicted delamination initiation loads are in remarkably good agreement with the experimental values. In all cases the error in the prediction is below 9%, even for the two cases where the characteristic point shifted to the free edge of the laminate.

The distributions of the delamination factor in Chapter 5 show that width effects for the 1-in.-wide specimens are not critical. For this reason, a linear quasi-three-dimensional analysis such as the one performed by Curry[16] is perfectly adequate. Three-in.-wide specimens, however exhibit large out-of-plane deflections which introduce

gradients in the width direction. This results in lower interlaminar stresses along the centerline of the laminate, and a shifting of the peak interlaminar stresses toward the supports. This clearly demonstrates the need for a geometrically nonlinear three-dimensional analysis such as the one performed in this work.

Future work

The usefulness of a transition element to connect a shell element to a solid element is not limited to dropped-ply laminates. Most laminated structures can be modeled with shell elements with details of critical areas such as holes, notches or free edges modeled by solid elements. The coupling of computationally less intensive shell elements with complex three-dimensional solid elements allows great modeling flexibility.

The 15-node transition element developed for this work, however, is not sufficient for many applications. This element possesses only one "shell" face and is designed for shell-to-solid transitions in only one direction - the direction normal to the shell face. For more general problems, a "corner" transition element with two shell faces is necessary. A 12-node corner element is a proposed addition to COMET's ES15 processor, as described in the manual for this processor in Appendix A.

Nonlinear analyses are computationally intensive. The full system of equations must be solved for the incremental displacements at least once at each load step. In spite of all the computational effort involved in intermediate load steps, it is usually only the solution at the last load step which is sought. The purpose of the entire analysis up to the last step is only to determine an estimate of the final solution. This seems inefficient

when considering that globally identical solutions can be obtained from models differing only in specific details.

A much more efficient procedure to obtain an estimate of the final solution is to perform a nonlinear analysis of a model without small-scale details. That solution can then be used for boundary conditions in a local linear analysis to estimate the displacements within the detail. The finite element model developed for this work is a perfect candidate for this procedure: a globally accurate solution can be obtained by replacing the three-dimensional elements around the ply drop-off with shell elements, and then the displacements of the three-dimensional nodes in the solid elements can be estimated from a local linear analysis. The combination of these two solutions, one nonlinear global, the other linear local, should provide a nearly converged initial estimate of the displacement field so that only a few iterations in the nonlinear solution method are needed to get to the final solution. Thus, a shell model is used for the nonlinear solutions at intermediate load magnitudes, and only at the final load is iteration performed on the fully detailed model.

The three-dimensional homogenization processor in COMET was used in this analysis to smear individual plies into stacks of up to eight plies per solid element. This analysis has shown that interlaminar stresses are relatively insensitive to these through-the-thickness discretizations. However, this homogenization procedure is designed for symmetric sublaminates, so it computes a homogeneous material stiffness matrix which is independent of position inside the element. An improved method would allow a variation in material properties through the thickness. For instance, 20-node solid elements work best with 3X3X3 integration points. The three planes of points can represent a quadratic variation of the material properties through the thickness. This would allow

greater flexibility in the discretization of a laminate into nonsymmetric sublaminate groups.

References

1. Yeager, J., and Rutan, D., *Voyager*, Harper & Row Publishers, New York, NY, 1987.
2. Aviation Week and Space Technology, "Piaggio Avanti, Beech Starship Offer Differing Performance Characteristics," October 2, 1989, pp. 75-78.
3. Madsen, C.B., Nuismer, R.J., and Bianca, C.J., "Space Shuttle Filament Wound Case Compressive Strength Study: Part I - Testing," AIAA Paper no. 86-1580, *Proceedings of AIAA/ASME/SAE/ASEE 22nd Propulsion Conference*, Huntsville, AL, June, 1986.
4. Messich, M.J., Nuismer, R.J., Jamison, G.T., and Graves, S.R., "Space Shuttle Filament Wound Case Compressive Strength Study: Part II - Analysis," AIAA Paper no. 86-1417, *Proceedings of AIAA/ASME/SAE/ASEE 22nd Propulsion Conference*, Huntsville, AL, June, 1986.
5. Adams, D.F., Ramkumar, R.L., and Walrath, D.E., "Analysis of Porous Laminates in the Presence of Ply Drop-Offs and Fastener Holes," Navy Technical Report No. N00019-82-C-0063, University of Wyoming College of Engineering, May, 1984.
6. Daoust, J., and Hoa, S.V., "Parameters Affecting Interlaminar Stresses in Tapered Laminates Under Static Loading Conditions," *Polymer Composites*, Vol 10, No. 5, October, 1989, pp. 374-383.

7. Fish, J.C., and Lee, S.W., "Tensile Strength of Tapered Composite Structures," *Proceeding of AIAA/ASME/ASCE/AHS 29th Structures, Structural Dynamics and Materials Conference*, Williamsburg, VA, April 1988, pp. 324-333.

8. Kim, R.Y., and Soni, S.R., "Failure of Composite Laminates due to Combined Interlaminar Normal and Shear Stresses," *Composites '86, Recent Advances in Japan and the United States*, 1986, pp. 341-350.

9. Brewer, J.C., and Lagace, P.A., "Quadratic Stress Criterion for Initiation of Delamination," *Journal of Composite Materials*, Vol 22, pp. 1141-1155, 1988.

10. Salpekar, S.A., Raju, I.S., and O'Brien, T.K., "Strain Energy Release Rate Analysis of Delamination in a Tapered Laminate Subjected to Tension Load," *Proceedings of the American Society for Composites Third Technical Conference*, Seattle, WA, September 1988, pp. 642-654.

11. Wisnom, M.R., "Delamination in Tapered Unidirectional Glass Fibre-Epoxy Under Static Tension Loading," AIAA Paper no. 91-1142-CP, *Proceedings of AIAA/ASME/ASCE/AHS 32nd Structures, Structural Dynamics and Materials Conf.*, Baltimore, pp. 1162-1172, 1991.

12. Wu, C.M.L., "Non-Linear Analysis of Tapered (in Steps) Laminated Plates under Uniform Inplane Load," *Composite Structures*, Vol 7, 1987, 205-223.

13. Kemp, B.L., and Johnson, E.R., "Response and Failure Analysis of a Graphite-Epoxy Laminate Containing Terminating Internal Plies," AIAA Paper no. 85-0608, *Proceedings of AIAA/ASME/ASCE/AHS 26th Structures, Structural Dynamics and Materials Conference*, Orlando, FL, 1985, pp. 12-24.

14. Kemp, B.L., and Johnson, E.R., "Response and Failure Analysis of a Graphite-Epoxy Laminate Containing Terminating Internal Plies," Master of Science Thesis in Aerospace Engineering, Virginia Polytechnic Institute and State University, Blacksburg, VA, July 1985.

15. Curry, J.M., Johnson, E.R., and Starnes, J.H., "Effect of Dropped Plies on the Strength of Graphite-Epoxy Laminates," AIAA Paper no. 87-0874, *Proceedings of AIAA/IASME/ASCE/AHS 28th Structures, Structural Dynamics and Materials Conference*, Monterey, CA, April 1987, pp. 737-747.

16. Curry, J.M., Johnson, E.R., and Starnes, J.H., "Effect of Dropped Plies on the Strength of Graphite-Epoxy Laminates," Center for Composite Materials and Structures Report No. CCMS-86-07, Virginia Polytechnic Institute and State University, Blacksburg, VA, December 1986.

17. Mikami, I., Dogaki, M., and Yonezawa, H., "Elastic Buckling of Orthotropic Plates with Abruptly Varying Rigidities under Compression," *Theoretical and Applied Mechanics, Vol.24, Proceedings of the 24th Japan National Congress for Applied Mechanics*, University of Tokyo Press, 1974, pp. 365-373.

18. Johnson, E.R., and Dávila, C.G., "Compression Buckling of Thick Orthotropic Plates with a Step Thickness Change," Proceedings of 12th Canadian Congress of Applied Mechanics, Ottawa, Canada, May 1989, pp. 140-144.

19. Jensen, D.W., and Lagace, P.A., "Influence of Mechanical Couplings on the Buckling and Postbuckling Behavior of Anisotropic Plates," *Proceedings of the AIAA/ASME/ASCE/AHS 27th Structures, Structural Dynamics, and Materials Conference*, May, 1986, pp. 132-141.

20. DiNardo M.T., and Lagace, P.A., "Buckling and Postbuckling of Laminated Composite Plates with Ply Dropoffs," *Proceedings of the AIAA/ASME/ASCE/AHS 28th Structures, AIAA Paper No. 87-0730, Structural Dynamics and Materials Conference*, Monterey, CA, April 1987, pp. 156-164.

21. Whitney, J.M., *Structural Analysis of Laminated Anisotropic Plates,* Technomic Publishing Co., Lancaster, PA, 1987, Chap 10.

22. Cohen, G.A., "Effect of Transverse Shear Deformation on Anisotropic Plate Buckling," *Journal of Composite Materials*, Vol. 16, July 1982, pp. 301-312.

23. Cohen, G.A., "Transverse Shear Stiffness of Laminated Anisotropic Shells," *Computer Methods in Applied Mechanics and Engineering,* , Vol. 13, 1978, pp. 205-220.

24. Huang, H. C., and Hinton, E., "A new Nine Node Degenerated Shell Element with Enhanced Membrane and Shear Interpolation," *International Journal for Numerical Methods in Engineering,* Vol. 22, 1986, pp. 73-92.

25. Park, K. C., Pramono, E., Stanley, G. M., and Cabiness, H. A., "The ANS Shell Elements: Earlier Developments and Recent Improvements," in *Analytical and Computational Models of Shells*, CED-Vol.3, edited by Ahmed K. Noor, Ted Belytschko, and Juan C. Simo, The American Society of Mechanical Engineers, New-York, NY, 1989, pp. 217-239.

26. Noor A. K., "Global-Local Methodologies and their Application to Nonlinear Analysis," *Proceedings of NASA Workshop on Computational Methods for Structural Mechanics and Dynamics-1985*, NASA CP-3034, Part 1, 1989, pp. 151-167.

27. Thompson, D. M., and Griffin, O. H., "2-D to 3-D Global/Local Finite Element Analysis of Composite Laminates," in the *Proceedings of the 4th Annual American Society for Composites Conference,* Fourth Technical Conference, October 3-5, 1989, Virginia Polytechnic Institute and State University, Blacksburg, VA, Technomic Publishing Co., Lancaster, PA, 1989, pp. 234-243.

28. Reddy J. N., "On Computational Schemes for Global-Local Stress Analysis," *Proceedings of NASA Workshop on Computational Methods for Structural Mechanics and Dynamics-1985*, NASA CP-3034, Part 1, 1989, pp. 123-133.

29. Bathe, K. J., *Finite Element Procedures in Engineering Analysis,* Prentice-Hall, Englewood Cliffs, N.J., 1982, pp. 250-256, and Chapter 6.

30. Bathe, K. J., and Bolourchi, S., "A geometric and material nonlinear plate and shell element," *Comp. Struct.,* Vol. 11, 1980, pp. 23-48.

31. Surana, K. S., "Transition finite elements for three-dimensional stress analysis," *Int. J. Numer. Methods Eng.,* Vol. 15, 1980, pp. 991-1020.

32. Surana, K. S., "Geometrically nonlinear formulation for the three dimensional solid-shell transition finite elements," *Comput. Struct.,* Vol. 15, 1982, pp. 549-566.

33. Liao, C. L., Reddy, J. N., and Engelstad, S. P., "A solid-shell transition element for geometrically non-linear analysis of laminated composite structures," *Int. J. Numer. Methods Eng.,* Vol. 26, 1988, pp. 1843-1854.

34. Stewart C. B., *The Computational Structural Mechanics Testbed User's Manual,* NASA Technical Memorandum 100644, Oct. 1989.

35. Vidussoni, M. A., "Global-Local Finite Element Analysis of Laminated Composites," Master of Science Thesis in Engineering Science and Mechanics, Virginia Polytechnic Institute and State University, Blacksburg, VA, July 1988.

36. Pitcher, E. J., "CSM Testbed Development and Large-Scale Structural Applications," *Science and Engineering on Cray Supercomputers,* Fourth International Symposium on Science and Engineering on Cray Supercomputers, Minneapolis, Minnesota, October 12-14, 1988, pp. 359-387.

37. Malvern, L.E., *Introduction to the Mechanics of a Continuous Medium,* Prentice-Hall, Inc., Englewood Cliff, NJ, 1969.

38. Knight, N.F., McCleary, S.L., and Stanley, G.M., *The Computational Structural Mechanics Testbed Procedure Manual,* NASA TM-100646, sect. 3.9, May 1990, pp. 1-35.

39. Davis, D.D., "Detailed Analysis and Test Correlation of a Stiffened Composite Wing Panel," *Proceedings of the 17th European Rotorcraft Forum,* Paper no. 91-85, Berlin, Germany, September 1991, pp. 85.1-85.15.

40. Tsai, S.W., *Composites Design - 1985,* Think Composites, Dayton, Ohio, 1985, Chapters 7, 8, and 10.

41. Nuismer, R.J., and Whitney, "Uniaxial Failure of Composite Laminates Containing Stress Concentrations," in *Fracture Mechanics of Composites,* ASTM STP 953, American Society for Testing and Materials, 1975, pp. 117-142.

42. Sun, C.T., and Sijian Li, "Three-Dimensional Effective Elastic Constants for Thick Laminates," *Journal of Composite Materials,* Vol. 22, July 1988, pp. 629-639.

Appendix A. Processor ES15 in the COMET Software System

1 GENERAL DESCRIPTION

Processor ES15 contains a 15-node transition element (TR15) based on the classical 20-node isoparametric serendipity element (BR20) developed at Virginia Polytechnic Institute and State University. Developers of element BR20 include M.A. Vidussoni (Ref. 1), D.M. Muheim, and O.H. Griffin, Jr. The TR15 transition element is designed to connect an EX97 nine-node shell element to one or more 20-node BR20 solid elements. A TR12 transition element which has two shell faces (for use as a corner element) is a planned addition.

Processor ES15 was developed by Carlos G. Dávila under the supervision of Professor Eric R. Johnson of Virginia Polytechnic Institute and State University. The theoretical development is presented in the Ph. D. dissertation (ref. 2) by the author. This research effort was supported by the Aircraft Structures Branch of the NASA Langley Research Center under Grant NAG1-537.

2 BASIC ELEMENT THEORY

The reader is encouraged to refer to the *Testbed User's Manual* (ref. 3, section 5.11) for a description of BR20 in processor ES10 on which this transition element is based.

2.1 Transition element for linear analysis

The stiffness matrix $\boldsymbol{K}_{Tr}$ for the transition element was obtained from the stiffness matrix $\boldsymbol{K}_S$ of the BR20 solid element by restricting the motion of one face of the element to be kinematically constrained by the Mindlin-Reissner plate theory. This theory assumes that the normal to the surface remains rigid in the deformation.

Except for the nodes on the transition face, all nodes on the transition element TR15 correspond to a node on the original solid element BR20, as shown in Fig. 54. The degrees of freedom for the nodes on the transition element are, like on the solid element, u, v and w. However, the three transition nodes 13, 14 and 15 are shell nodes, so their degrees of freedom additionally include the rotations α and β of the normal.

The kinematic relation between a solid element node k and its corresponding transition node j can be expressed as follows:

$$\begin{bmatrix} u_k \\ v_k \\ w_k \end{bmatrix}_S = \begin{bmatrix} 1 & 0 & 0 & 0 & d_{kj} \\ 0 & 1 & 0 & -d_{kj} & 0 \\ 0 & 0 & 1 & 0 & 0 \end{bmatrix} \begin{bmatrix} u_j \\ v_j \\ w_j \\ \alpha_j \\ \beta_j \end{bmatrix}_{Tr} \tag{1}$$

where $|d_{kj}|$ is the distance from the transition node j to the solid element node k.

If $\hat{u}_S$ is the complete displacement vector for the solid element and $\hat{u}_{Tr}$ is the vector of displacements and rotations for the transition element, then

$$\hat{u}_S = R\,\hat{u}_{Tr} \tag{2}$$

in which R is a restraint matrix composed of kinematic identities and submatrices obtained from Eq. (1) for nodes on the transition face.

The internal virtual work for the solid element is

$$\int_V \delta\varepsilon^T \sigma \, dV = \delta\,\hat{u}_S^T \, K_S \, \hat{u}_S \tag{3}$$

where $\delta\varepsilon$ is the virtual strain vector, σ is the conjugate stress vector, and K_S is the 60 X 60 stiffness matrix of the solid element. By substituting (2) into (3) we obtain the virtual work statement for the transition element

$$\int_V \delta\varepsilon^T \sigma dV = \delta\,\hat{u}_{Tr}^T \; R^T K_S R \;\; \hat{u}_{Tr} \tag{4}$$

from which it is clear that the stiffness matrix of the transition element is simply

$$K_{Tr} = R^T K_S R \tag{5}$$

Although similar in form to a multi-point constraint, Eq. (5) is applied to the solid element stiffness matrix *before* assembly of the matrix, i.e., at the element level. This frees the user from all matrix manipulations and allows the use of all Testbed solver and finite element processors.

2.2 *Geometrically Nonlinear Solid Element in an Incremental Formulation*

The restraint matrix $\boldsymbol{R}$ developed in Eq. (1) for a linear analysis is a function only of the difference in thickness coordinates d_{kj} from the brick node k to the transition node j in the undeformed configuration. This linear approximation, where displacements are proportional to rotation angles, is not valid for large rotations, in which case displacements are trigonometric functions of the rotations.

An approximate restraint matrix $\boldsymbol{R}$ for geometrically nonlinear problems was developed by the author for use in conjunction with incremental iterative methods. It is shown that $\boldsymbol{R}$, like the tangent stiffness, is a function of displacements as well as geometry.

The submatrix $[R_{kj}]$ which takes into account the combined effect of rotations and translations at the transition node can be written in a form similar to its linear counterpart, Eq. (1) (ref. 2). The total incremental displacement of solid-element node k in terms of the transition element node j is

$$\begin{bmatrix} \Delta u_k \\ \Delta v_k \\ \Delta w_k \end{bmatrix}_S = [R_{kj}]\{\Delta \hat{u}_j\}_{Tr} = \begin{bmatrix} 1 & 0 & 0 & d_{kj} fu_{\alpha j} & d_{kj} fu_{\beta j} \\ 0 & 1 & 0 & d_{kj} fv_{\alpha j} & d_{kj} fv_{\beta j} \\ 0 & 0 & 1 & d_{kj} fw_{\alpha j} & d_{kj} fw_{\beta j} \end{bmatrix} \begin{bmatrix} \Delta u_j \\ \Delta v_j \\ \Delta w_j \\ \Delta \alpha_j \\ \Delta \beta_j \end{bmatrix}_{Tr} \tag{3.4.6}$$

where the terms fu, fv and fw are functions of the accumulated displacements.

The formulation of the finite element stiffness matrix and internal force vector for the transition element are obtained directly from the formulations of the nonlinear solid element. By substituting $\Delta \hat{\boldsymbol{u}}_S = \boldsymbol{R}\, \Delta \hat{\boldsymbol{u}}_{Tr}$ into the principle of virtual work for incremental displacements, it is found that,

like in the linear case, the nonlinear transition element is easily constructed from the brick element and its associated constraint matrix:

$$\begin{aligned} K_{Tr} &= R^T K_S R \\ [K_{NL}]_{Tr} &= R^T [K_{NL}]_S R \\ F_{Tr} &= R^T F_S \end{aligned} \tag{7}$$

3 PROCESSOR INPUT/OUTPUT

3.1 Commands

Processor ES15 is based on the Generic Structural-Element Processor template, and hence employs the standard commands (e.g., FORM STIFFNESS, DEFINE FREEDOMS,...) described both in the Generic Structural-Element Processor Manual (ref. 4) and in Section 5.1 of the Testbed User's Manual (ref. 3).

3.2 Macro Symbols

Processor ES15 employs the standard macrosymbols, described in both the Generic Structural-Element Processor Manual (ref. 4) and in Section 5.1 of the Testbed User's Manual (ref. 3).

3.3 Research Parameters

There are two research parameters to be specified by the user in order for this processor to complete its task. The first research parameter is the number of integration points desired along one of the

local in-plane coordinate axes. The second research parameter is the number of integration points desired along the local out-of-plane coordinate axis. If *m* is the value of the first parameter, and *n* is the value of the second, *m*-by-*m*-by-*n* integration points will be used in the numerical integration. For more information, see the Element Selection Guidelines, Subsection 5.11.7 on BR20 in Ref. 3.

Note: This element has only been tested for a 3-by-3-by-3 (exact) order of integration.

3.4 Datasets

All input and output datasets for processor ES15 conform to the generic data structures described in Refs. 3 and 4.

4 ELEMENT DEFINITION

4.1 Geometry and Node Numbers

Element calculations are based on the *xyz* coordinate system relative to the element and known as the element local coordinate system. This system is based on the following Testbed convention: The local *xyz* origin is at node 1. Node 2 defines the positive local x-direction and lies on the local x-axis. Node 4 lies in the local *xy* plane in the positive y-direction and may or may not be un the local y-axis. Node 5 has a positive value of the local z-coordinate and may or may not lie on the positive local z-axis. Since no node-numbering convention has yet been established for transition elements, a numbering sequence was chosen which defines the same local coordinate system as in the original solid element.

The only geometry of TR15 that has been tested so far is a parallelopiped (solid "brick" with right angles at all corners). Other geometries are possible but may require internal modifications to the formulation. This results from the fact that since TR15 is based on the formulation of BR20 it must generate internally the coordinates of the "missing" nodes of the 20-node solid element from the coordinates of its 15 nodes.

4.2 Nodal Freedoms (displacements)

Element TR15 is designed to have one face compatible with a nine-node EX97 shell element. The three nodes on this face are therefore shell nodes which have five degrees of freedom per node. In the computational coordinate system *xyz* these displacement components are $\boldsymbol{d}_{Tr}{}^{T} = \{ u, v, w, \alpha, \beta \}$, where α and β are the rotation angles of the normal (see Section 5.2 in Ref. 2 on EX97 shell elements). The other 12 nodes of TR15 are solid nodes, and their displacements are composed only of three translations: $\boldsymbol{d}_{S}{}^{T} = \{ u, v, w \}$. The total number of degrees of freedom in TR15 is therefore 51.

4.3 Intrinsic Parameters

A summary of intrinsic parameters for each element type in ES15 is presented in Table 5.

5 ELEMENT RESULT INTERPRETATION (Stresses/Strain)

The elements in this processor should not be used to compute stresses or strains. Furthermore, transition elements TR15 and TR12 should not be used inside regions of significant three-dimensional effects where their inherent kinematic constraints could introduce a stress boundary layer.

Table 5. Processor ES15: Element Parameters

Parameter		Element Types	
Name	Description	TR15	TR12 (&)
C	Disp. Continuity	0	0
CLAS	Element Class	idSOLI	idSOLI
CNS	Constitutive Type	1	1
DIM	Intrinsic Dimensions	3	3
NDOF	No. of Freedoms/Node	6	6
NEE	No. of Element Equations	90	72
NEN	No. of Element Nodes	15	12
NIP	No. of Integration Points	*	*
NSTR	No. of Stress Components	6	6
NORO	Nodal Rotation Tolerance	0	0
PARS	No. of Research Parameters	2	2
PROJ	Projector Switch	0	0
SHAP	Element Shape	iQUAD	iQUAD
STOR	Inital Storage Space	0	0

& Planned addition to processor ES15. Not implemented yet.
* The user may select the number of integration points.

6 ELEMENT NONLINEARITY

6.1 Geometric Nonlinearity

The material and geometric components of the tangent stiffness matrix as well as the internal force vector were developed by the authors and added to the original 20-node solid element BR20. These terms are also used in TR15 where they are transformed into the corresponding terms for the transition element via the restraint matrices (see Section 2).

The nonlinear terms are developed in a Total Lagrangian formulation and the COROTATION option must be turned OFF.

6.2 Material Nonlinearity

Currently, only materials with linear elastic constitutive relations can be analyzed since processor LAU supplies the constitutive relations. Nonlinear constitutive processors are not available with this release version of COMET.

7 ELEMENT SELECTION GUIDELINES

7.1 General Element Selection

The transition elements TR15 and TR12 must be used in conjunction with the solid element BR20 and the shell element EX97. BR20 is recommended as a general-purpose, three-dimensional element, and it is particularly effective in the anlysis of composite laminates where elements with fewer nodes can be too stiff in their out-of-plane response. Similarly, EX97 is recommended as a robust "work horse" element for any shell structure application.

Note: Since a single transition element can be connected to an arbitrary number of solid elements, the bandwidth of the problem can become very large, which will drastically increase the length of execution of the equation solver. In addition, the maximum connectivity parameter (MAXCON) in the utilities may need to be reset to a value higher than the default.

7.2 Nodal Distribution

As for the 20-node BR20 element from which it was derived, the midside nodes of TR15 should be exactly half way between the corner nodes. As a midside node is moved away from that point and approaches the quarter point, the resulting stress distribution approaches singularity. This is

especially critical when elements have very small thickness, such as in the modeling of composite laminates.

The shell nodes 13, 14 and 15 of TR15 define the shell face of the transition element. Nodes 13 and 14 also define the vertical edges of the element on the shell face, and node 15 should be half way between them. Unlike the the solid nodes (all other nodes on the element) the shell nodes of TR15 are not required to be on the surface of the element. Instead, they can be outside the element on the transition face. This feature allows TR15 to be used to connect one shell element to several solid elements.

7.3 Aspect Ratio

There are certain element dimension considerations which must be made. For an element which is a rectangular parallelopiped with side lengths *a, b,* and *c*, the ratios a/b, a/c and b/c should ideally be in the range of 0.1 to 10. Experience has shown that ratios considerably outside this range can yield good results, but the user should carefully review any such results and possibly perform a parametric study of various ratios if the values are not within the ideal range.

7.4 Curvature Effects

It was mentioned in Section 4.1 that TR15 has only been tested in rectangular parallelopiped geometries. Other shapes, especially curved shapes require internal modifications or extensions of the algorithms now implemented in the element.

7.5 Skewness

See Curvature Effects.

7.6 Element Integration Option

TR15 has only been tested with a 3-by-3-by-3 order (exact) of integration. However, if the user is knowledgeable in the theory of finite elements and is confident of the loading conditions that are being applied on a particular element, then lower orders of integration schemes may be used, but with caution. The other possible integration schemes are 2 X 2 X 2 ; 2 X 2 X 3 and 3 X 3 X 2 .

8 IMPLEMENTATION STATUS

The implementation status of the functions for processor ES15 is indicated in Table 6, where a plus sign (+) indicates that the function has been implemented and a minus sign (—) indicates that it has not.

Table 6. Implementation Status in Processor ES15

Function	Subroutine	Status	Comments
Strains	ES15E	+	
Internal Forces	ES15FI	+	
Body Forces	ES15FB	—	
Surface Forces	ES15FS	—	
Geometric Stiffness	ES15KG	+	
Load Stiffness	ES15KL	—	
Material Stiffness	ES15KM	+	
Consistent Mass	ES15MC	—	
Diagonal Mass	ES15MD	—	
Stresses	CS	+	stresses for internal use only
Stress Transformation	ES15T	+	untested
Stress Extrapolation	ES15XP	+	untested
Auto-DOF-Suppression	ES15N	—	
Geometric Nonlinearity	—	—	
Material Nonlinearity	—	—	

REFERENCES

1. Vidussoni, M.A., "Global-Local Finite Element Analysis of Laminated Composites," Master of Science Thesis in Engineering Science and Mechanics, Virginia Polytechnic Institute and State University, Blacksburg, VA, July 1988.
2. Dávila, C.G., "Delamination Initiation in Postbuckled Dropped-Ply Laminates," Ph. D. Dissertation in Aerospace Engineering, Virginia Polytechnic Institute and State University, Blacksburg, VA, November 1991.
3. Stewart C.B., *The Computational Structural Mechanics Testbed User's Manual,* NASA Technical Memorandum 100644, Oct. 1989.
4. Stanley, Gary and Nour-Omid, Shahram: *The Computational Structural Mechanics Testbed Generic Structural-Element Processor Manual* . NASA CR 181728, 1989.

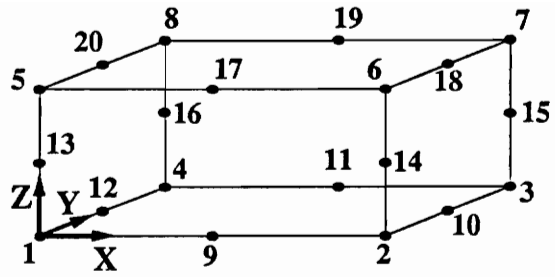

20-Node Solid Element BR20

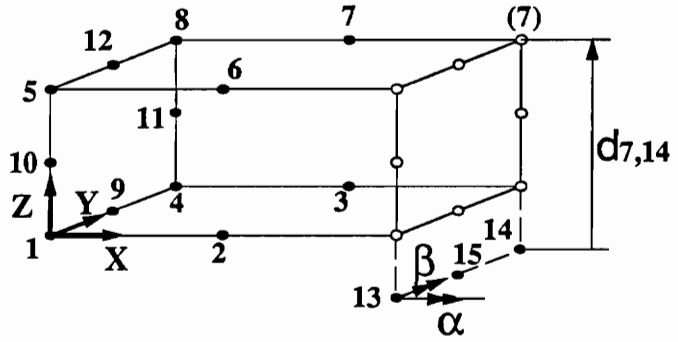

15-Node Transition Element TR15

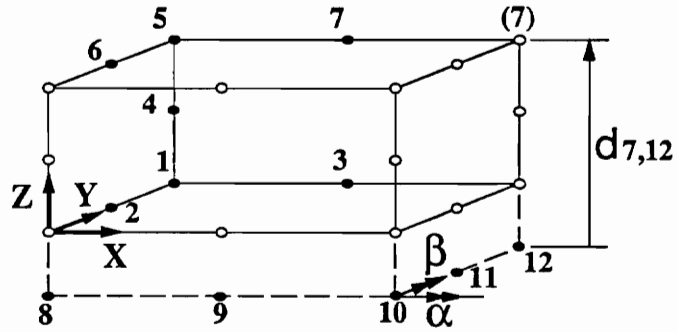

12-Node Transition Element TR12

● solid element nodes

○ "missing" solid element nodes

Figure 54. BR20 Solid Element. TR15 and TR12 Transition Elements

Appendix B. Homogenization of Material Properties

Equivalent single-layer material properties for a composite laminate can be computed with great efficiency with assumptions such as Classical Lamination Theory (CLT). These assumptions allow averaging of the material properties of stacks of plies into a single anisotropic layer. However, CLT and other higher-order theories are limited by their two-dimensional nature and cannot account for three-dimensional characteristics. Only recently have methods been developed which allow, under some circumstances, laminates to be represented by equivalent homogeneous anisotropic solids. The concept is based on the assumption that if the characteristic length of deformation of the global composite laminate is large compared with the stacking periodicity, then the properties of several plies can be smeared out into an equivalent cell where effective properties are used. In the absence of such homogenization, finite element models of thickness deformations in composite materials have typically involved the use of one element per ply, even when deformation fields did not justify such mesh refinement.

A smearing method was published by Sun et al.[42]. It is based on the application of conditions of inter- and intralaminar compatibility and equilibrium. The reader is referred to the latter reference for details on this theory.

In this work, great economy of resources was achieved by extensive use of smearing of properties. Sublaminates of up to eight plies are modeled with one solid element. However, the assumptions made by this method require caution. For instance, smearing does not account for lamination sequence, and was not developed for unsymmetric laminates.

The example shown in Fig. 55 was designed to test the capabilities of this method and to aid in the development of an appropriate finite element model of the dropped-ply laminate. This example consists of a twenty-inch long cantilever composite beam with a zero-degree ply above an eight-ply quasi-isotropic sublaminate. The width is 5 inches, and the thickness is 4.5 inches. An inplane load of 6,000 lb. is applied only to the free end of the zero-degree ply, as shown in Fig. 55. Load transfer to the quasi-isotropic laminate is through shear, much the same way as in a dropped-ply laminate. In order to prevent mesh refinement from entering in the comparison, the same number of elements is used for all three models. The mesh is refined near the free end of the beam in order to capture the boundary layer of the interlaminar shear. The top ply (0 degree) is modeled by one element through the thickness, and the quasi-isotropic $[\pm 45/0/90]_S$ sublaminate is subdivided into eight elements through the thickness.

The four smearing schemes shown in Fig. 56 were tested. H1 smears the properties of the entire quasi-isotropic sublaminate so the same properties are used for each of the 8 elements inside this sublaminate. H2 homogenization splits the eight layers in two, so that the properties of the 45-degree layers is used for the top two elements. H3 is similar,

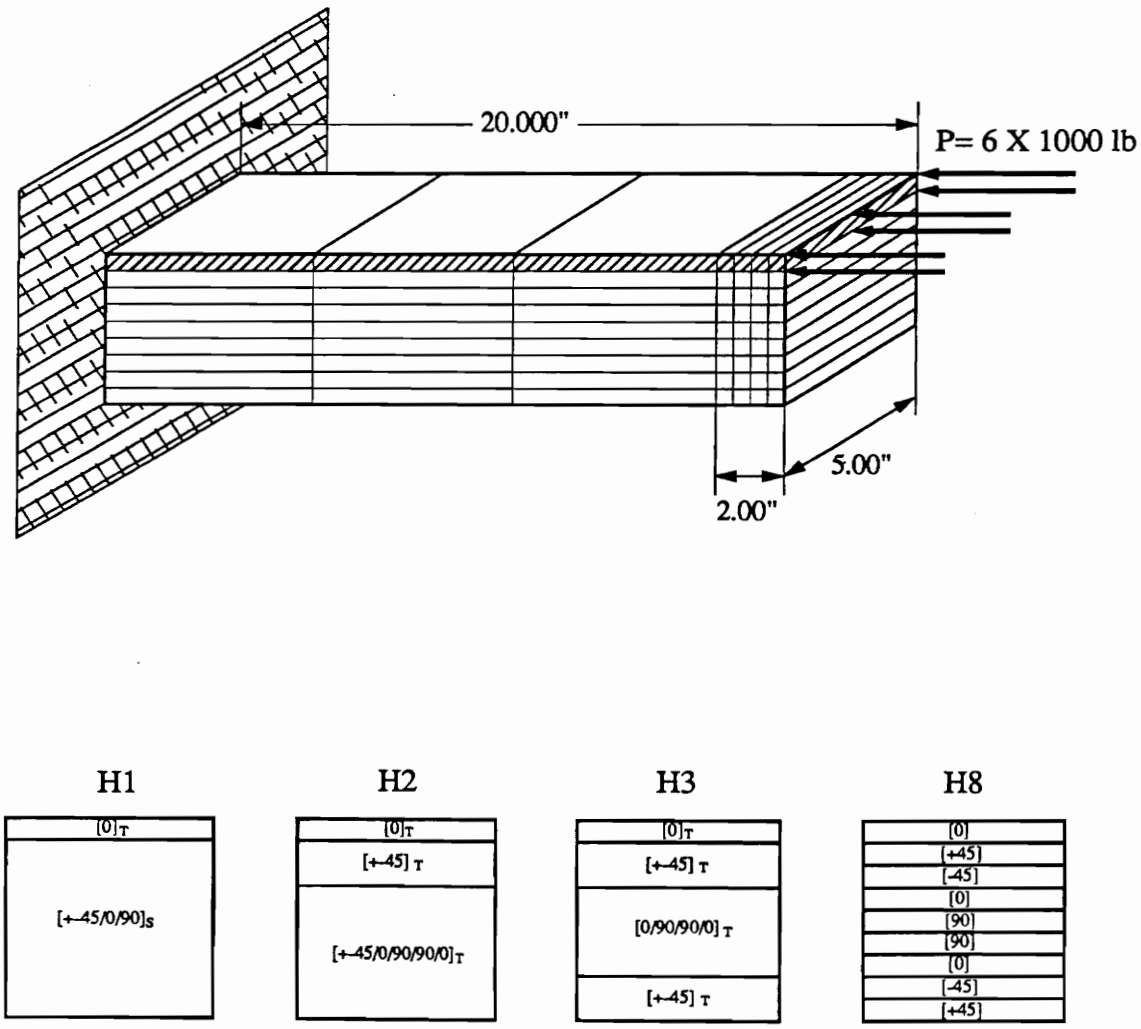

Figure 55. Modeling Schemes: Homogenization of layer properties

but the bottom 2 layers are also modeled separately. Finally, H8 uses the material properties for each ply and does not have any smearing.

All homogenization schemes produce virtually identical global deformations, so their virtues were determined from their predictions of interlaminar shear stress at the interface between the quasi-isotropic sublaminate and the zero-degree ply.

The interlaminar shear stress in the vicinity of the free edge at the interface between the quasi-isotropic sublaminate and the zero-degree ply is shown in Fig. 56. The stresses plotted are at the mid-width. The "refined model" consists of the curve-fit of a model with a mesh twice as refined as the test cases. This model produces the same displacements as H8 but was used to illustrate the exact form of the stress boundary layer at the free edge. The worst results correspond to H1, or the block smearing of the entire quasi-isotropic sublaminate. H2 homogenization, where the ± 45 degree layers in contact with the zero-degree ply are lumped together, offers the best compromise between efficiency and accuracy.

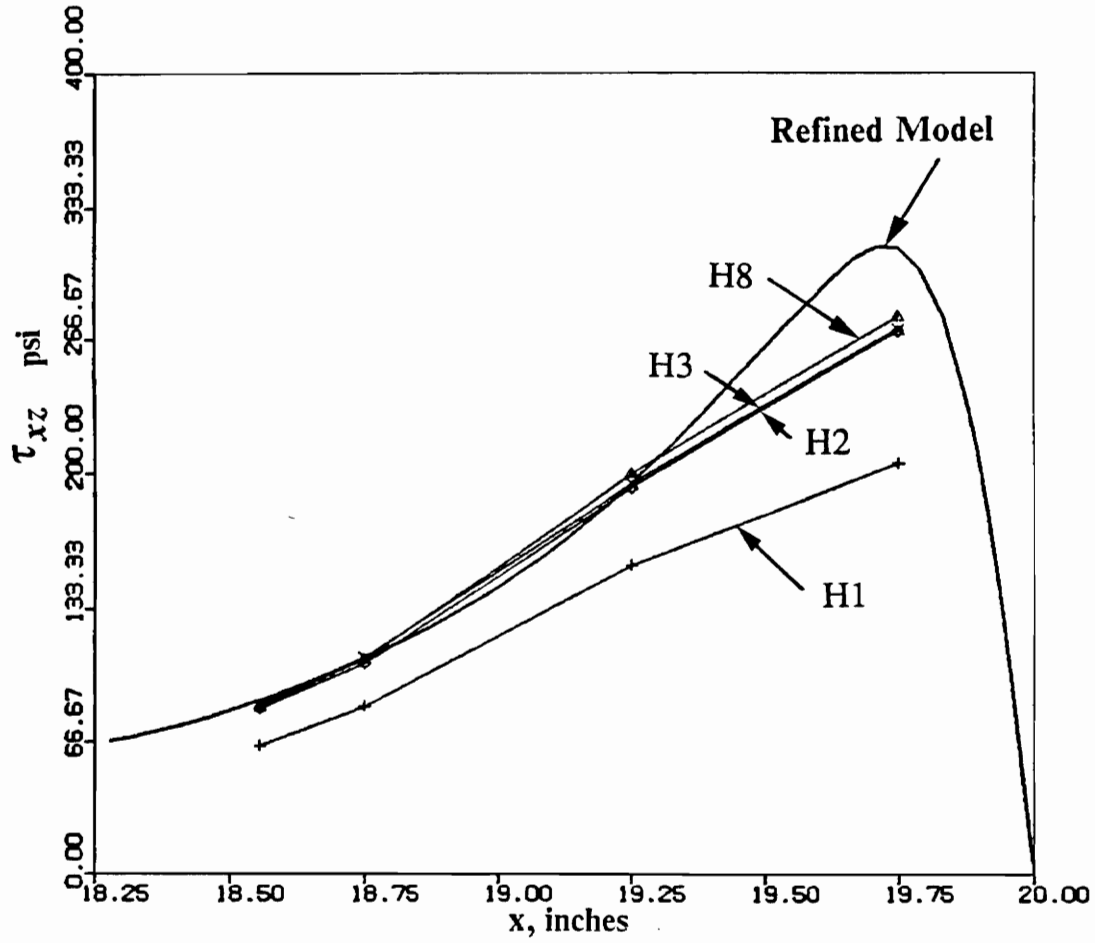

Figure 56. Interlaminar Shear Stress: Comparison of homogenization schemes

Appendix C. Runstream in COMET Software System

This Appendix contains the runstream for the generation an processing of the finite element model used in this work. The runstream contains CLAMP directives (the high-level command language of COMET), as well as processors (software elements that produce data structures) and macroprocessors (groups of related processors bundled as subroutines under a main program). The reader should refer to the COMET's User's Manual[33] for further information.

The runstream is followed by a condensed output file corresponding to the first step in a nonlinear analysis.

```
#
# @$-o spec02.3nl
# @$-eo
#
cd /scr/davila
/bin/time testbed <<\*EOI*
*set echo=off
*rem Ply-Drop Model    One solid element per quasi-isotropic sublaminate
*rem This model was modified from model.com for symmetry and free strip
*def/a Dbc = spec02.101
*def/a Dbr = spec02.103
*def/i beg_step = 1
*def/i max_step = 1
*def/a initial  = <true>
*def/a solut    = <true>
*def/a linear   = <false>
*def/a all_shell= <false>

*open 1 <Dbc>
*open/new 28 spec02.128
*set plib = 28

*add '/usr/u1/davila/research/esproc/basement/utilcgd.prc'
*add '/usr/u1/davila/research/esproc/basement/nl_static_1.clp'
*add '/usr/u1/davila/research/esproc/basement/l_static.clp'
*add '/usr/u1/davila/research/models/spec.nodloc'
*add '/usr/u1/davila/research/models/spec.eldef'

*def/a es_nameBR == BR20       . name of 20-node solid element
*def/a es_nameTR == TR15       . name of 15-node transition element
*def/a es_namePL == EX97       . name of 9-node shell element
*def/a es_procTR == es15       . name of processor for transition elem.
*def/a es_procPL == es1        . name of processor for shell elem.
*def/e Lx = 10.                . length of specimen
*def/e Lx1 = 4.72              . length of thick side of specimen
*def/e Lx2 = 4.88              . length of thin side of specimen
*def/e Ly =  1.50              . 1/2 width of laminate
*def/i nplyd = 2               . Number of dropped plies (for wall offset)
*def/e Lby = 0.125             . width of free edge strip
```

```
*def/e Lb =  0.375              . length of clamping area
*def/e r =   0.5                . radius factor (resin region)
*def/i nx1 = 4                  . number of shell divs. on thick side
*def/i nx2 = 4                  . number of shell divs. on thin side
*def/i ny = 3                   . y-divisions include strip outside knife edg
*def/i ndiv = 1                 . number of divisions from basic along span
*def/e plyt  = 0.00502          . ply thickness  (average for solids)
*def/e plyt1 = 0.00504          . ply thickness  Thick side
*def/e plyt2 = 0.00525          . ply thickness  thin side
*def/e z0 = <-8.*<plyt>>        . lower laminate surface (solid elements)
*def/e z1 = <-4.*<plyt>>
*def/e z2 =  .0                 . reference plane is at top of quasi-iso lami
*def/e z3 =  <1.*<plyt>>
*def/e z4 =  <2.*<plyt>>
*def/e z5 =  <6.*<plyt>>
*def/e z6 = <10.*<plyt>>        . upper laminate surface (solids, thick side)
*Procedure defs
   *if < <linear> > /then
    *def/a es_procBR = es10     . processor name for linear solid element
   *else
    *def/a es_procBR = es20     . processor name for nonlinear solid element
   *endif
*def/e Lt = <<Lx> - <Lx1> - <Lx2>>
*def/e Lhi = <<Lx1>+7*<Lt>/10>
*def/e Ltf = <<Lt>/<10*<ndiv>>>
*def/i nd = <7*<ndiv>>
*def/i ndz = <4*<ndiv>>
*def/i ndt = <2*<nd>>
*def/i nnx1 = <2* <nx1> +1>
*def/i nnx2 = <2* <nx2> +1>
*def/i nny = <2* <ny> +1>
*def/i nnod1 = <<nnx1>*<nny>>
*def/i nnod2 = <<nnx2>*<nny>>
*def/i nn = <<nnod1>+<nnod2>>
  *if <<all_shell>> /then
*def/i jnt = <<nn>+3*<nny>>
  *else
*def/e ndrt = < <<ndt>-1>/<ndt> >
*def/e ndr = < <<nd>-1>/<nd> >
*def/i ty = <2*<ny>>
*def/i nxt = <3*<nd>-2>
*def/i ny1 = <<ny>+1>
*def/e Lty = <<Ly>/<ty>>
*def/e Lty1 = <<Lby>+<<Ly>-<Lby>>/<2*<<ny>-1>>>
*def/e Lty2 = <<Ly>-<<Ly>-<Lby>>/<2*<<ny>-1>>>
*def/e Lh = <<Ly>*<1.-1./<ty>>>
*def/i nn0 = < <<ny>+1>*<2*<nd>-1> + <ny>*<<nd>-1> >
*def/i nn1 = < <<nd>-1>*<<ny>+1> >
*def/i nn2 = <nn0>
*def/i nn3 = < <<ndz>+<ndiv>-1>*<ny1> >
*def/i nn4 = < <10*<ndiv>-1>*<ny1> + <5*<ndiv>-1>*<ny> >
*def/i nn5 = <nn1>
*def/i nn6 = <nn0>
*def/i jnt = <<nn>+<nn0>+<nn1>+<nn2>+<nn3>+<nn4>+<nn5>+<nn6>>
*def/i nn01 = <<nn>+<nn0>>
*def/i nn02 = <<nn>+<nn0>+<nn1>>
*def/i nn03 = <<nn>+<nn0>+<nn1>+<nn2>>
*def/i nn04 = <<nn>+<nn0>+<nn1>+<nn2>+<nn3>>
*def/i nn05 = <<nn>+<nn0>+<nn1>+<nn2>+<nn3>+<nn4>>
*def/i nn06 = <<nn>+<nn0>+<nn1>+<nn2>+<nn3>+<nn4>+<nn5>>
*def/e td = <<z4>-<z2>>
*rem ********CONTROL PARAMETERS*********
*rem
*rem Critical Aspect Ratios:
*rem
*def/e SL = <Ltf>
*def/e SW = <<Ly>/<ny>>
*def/e SH = <td>
*rem Solid:  <SL> X <SW> X <SH> (DP solid el.)
*def/e SL = <Lb>
*rem Shell:  <SL> X <SW>            (clamped end)
*def/e SL = <<<Lx1>-<Lb>>/<<nx1>-1>>
*rem         <SL> X <SW>            (left side shells)
*def/e SL = <<<Lx2>-<Lb>>/<<nx2>-1>>
*rem         <SL> X <SW>            (right side shells)
  *endif
*end   .defs
*call defs
.
*Procedure constraints
```

```
  Con 1
  nonzero 1        : 1,<<nnod1>-<nnx1>+1>,<nnx1>      . Appl motion on left
    zero 6         : 1,<jnt>,1
    zero  2,3,4,5  : 1,<<nnod1>-<nnx1>+1>,<nnx1>       . A1C1  left clamp
    zero 1,2,3,4,5 : <<nnod1>+<nnx2>>,<nn>,<nnx2>      . B1D1  right clamp
    zero    3,4,5  : 2,<<nnod1>-<nnx1>+2>,<nnx1>       . A2C2  mid-pt (new
    zero     3     : 3,<<nnod1>-<nnx1>+3>,<nnx1>       . A2C2
    zero     3     : <<nnod1>+<nnx2>-2>,<<nn>-2>,<nnx2> . B2D2
    zero    3,4,5  : <<nnod1>+<nnx2>-1>,<<nn>-1>,<nnx2> . B2D2  mid-pt (new
    zero     3     : <1+2*<nnx1>>,<3*<nnx1>>,1         . A1A3
    zero     3     : <<nnod1>+1+2*<nnx2>>,<<nnod1>+3*<nnx2>>,1  . B3B1
    zero   2,4     : <<nnod1>-<nnx1>+1>,<nnod1>,1      . C1C3
    zero   2,4     : <<nn>-<nnx2>+1>,<nn>,1            . D3D1

  *if < <all_shell> > /then
    zero     3     : <<nn>+7>,<<nn>+9>,1                 . A3B3
    zero   2,4     : <<nn>+1+6*<ny>>,<jnt>,1             . C3D3
  *else
    zero   3   : <<nn>+3*<nd>-1>,<<nn>+5*<nd>-3>,1       . right z0
    zero   3   : <<nn06>+3*<nd>-1>,<<nn06>+5*<nd>-3>,1   . right z6 (new)
 nonzero   3   : <<nn06>+3*<nd>-1>,<<nn06>+3*<nd>+7*<ndiv>>,1  . right z6 (n
    zero   2   : <<nn>+<ny>*<3*<nd>-2>+1>,<nn01>,1       . left  z0
    zero   2   : <<nn01>+<ny>*<<nd>-1>+1>,<nn02>,1       . left  z1
    zero   2   : <<nn02>+<ny>*<3*<nd>-2>+1>,<nn03>,1     . left  z2
    zero   2   : <<nn03>+<ny>*<<ndz>+<ndiv>-1>+1>,<nn04>,1  . left  z3
    zero   2   : <<nn05>-10*<ndiv>+2>,<nn05>,1            . left  z4
    zero   2   : <<nn05>+<ny>*<<nd>-1>+1>,<nn06>,1        . left  z5
    zero   2   : <<nn06>+<ny>*<3*<nd>-2>+1>,<jnt>,1       . left  z6
  *endif

[xqt AUS
 ALPHA: CASE TITLES 1
   1'imposed transverse displacements
 sysvec: appl motions 1
  case 1
 i=1:  j=   1,<<nnod1>-<nnx1>+1>,<nnx1> : 0.004
*if <<1-<all_shells>>> /then
 i=3:  j=<<nn06>+3*<nd>-1>,<<nn06>+3*<nd>+7*<ndiv>>,1 : <1.e-4*<<z2>-<z6>>>
*endif
*end   .constraints
*Procedure printx
*rem 0.   1
*rem <<Lb>/2.>  2
*rem <Lb>  3
 *def/e dx1 = <<<Lx1>-<Lb>>/<<nnx1>-3>>
 *def/e dx2 = <<<Lx2>-<Lb>>/<<nnx2>-3>>
 *def/e xpt = <Lb>
*DO :Plate1 $ict = 1,<<nnx1>-3>
 *def/e xpt = <<xpt>+<dx1>>
 *rem <xpt>  <<$ict>+3>
:Plate1
 *def/e Xpt = <<Lx>-<Lx2>>
*DO :Plate2 $ict = 1,<<nnx2>-3>
 *rem <xpt>
 *def/e xpt = <<xpt>+<dx2>>
:Plate2
 *rem <<Lx>-<Lb>>
 *rem <<Lx>-<Lb>/2.>
 *rem <Lx>
*end

*call nodloc
*def/i p1 = <<nnod1>-<nnx1>+1>
*def/i p2 = <nnod1>
*def/i p5 = <<nn>-<nnx2>+1>
*def/i p6 = <nn>
 *call ES (function='DEFINE FREEDOMS')
 *def/i ns_overwrite = <true>
*Procedure Solve
*if < <solut> > /then
 *if < <linear> > /then
  *call L_STATIC ( print = <false> ; stress = <false> ; reaction = <false>
  *rem print coordinates:
  *call printx
    [xqt VPRT
    joints <p1>,<p2> : <p5>,<p6>
     joints 1,<jnt>,1
    components 1 3
    format=4
     print stat disp 1 1
```

```
    joints 1,<nn>,1
    components 1 3
     print stat reac 1 1
  *else
 *call NL_STATIC_1 ( beg_load = 1. ; max_load = 15.0; min_load = 0.; --
    beg_step = <beg_step> ; max_steps = <max_step> ; --
    des_iters = 5 ; max_iters = 8 ; max_cuts = 1 ; --
    nominal_dB = <Dbr> ; nominal_ds = <Dbc> ; --
    n_select = 8 ; TOL_E = .8e-4 ; --
    sel_nodes = 1,10,19,28,37,46,55,119 ; --
    sel_dofs = 1,1,1,1,1,1,1,3 ; --
    COROTATION = 0 )

 *rem print coordinates:
 *call printx
   [xqt VPRT
   joints <p1>,<p2> : <p5>,<p6>
   components 1 3
   format=1
   print tot disp  <max_step>
   joints 1,<nn>,1
   components 1 3
   print reac forc <max_step>
  *endif
 *endif  . solut
*end  . Solve
*call Solve
*close 28 /delete
[xqt exit
. \eof
\*EOI*

. ************************************************************************

*Procedure xlocA
  *if < <ic> /le <6*<ndiv>> > /then
   *def/e x == <<Lx1>+<ic>*<Ltf>>
  *else
   *def/e x == <<Lx1>+3*<Lt>/5+<<ic>-6*<ndiv>>*<Ltf>/2>
  *endif
*end
*Procedure xlocB
  *if < <ic> /le <3*<ndiv>> > /then
   *def/e x == <<Lx1>+<ic>*2*<Ltf>>
  *else
   *def/e x == <<Lx1>+3*<Lt>/5+<<ic>-3*<ndiv>>*<Ltf>>
  *endif
*end
*Procedure zdrop2
   *def/e zv == <z2>
   *def/e L = <<<x>-<Lhi>>*<pi>>
   *def/e c1 = <cos(<5*<L>/<Lt>>)>
   *def/e c12 = <cos(<10*<L>/<Lt>>)>
  *if < <x> /gt <Lhi> > /then
   *def/e zv == < <z2> - <td>*<<r>-1/2>*<1-<c12>> >
   *def/e x4 = <9*<Lt>/10+<Lx1>-<x>+<Lhi>>
   *def/e L4 = <<<x4>-<Lhi>>*<pi>>
   *def/e c14 = <cos(<5*<L4>/<Lt>>)>
   *def/e c124 = <cos(<10*<L4>/<Lt>>)>
   *def/e zv == <<z2>+<td>*<1+<c14>>/2-<td>*<1-<c124>>*<1-<c124>>*<1-<r>>/8
  *endif
  *if < <x> /gt <<Lx1>+8*<Lt>/10> > /then
   *def/e zv == < <z2> + <td>*<1+<c1>>/2 - <td>*<1-<c12>>*<1-<c12>>*<1-<r>>
  *endif
  *if < <x> /gt <<Lx1>+9*<Lt>/10> > /then
   *def/e zv == <z2>
  *endif
*end

*Procedure zdrop4
   *def/e zv == <z4>
  *if < <x> /gt <Lhi> > /then
   *def/e L = <<<x>-<Lhi>>*<pi>>
   *def/e c1 = <cos(<5*<L>/<Lt>>)>
   *def/e c12 = <cos(<10*<L>/<Lt>>)>
   *def/e zv == < <z2> + <td>*<1+<c1>>/2 - <td>*<1-<c12>>*<1-<c12>>*<1-<r>>
  *endif
*end

*Procedure zdrop5
```

```
   *def/e zv == <z5>
  *if < <x> /gt <Lhi> > /then
   *def/e L = <<<x>-<Lhi>>*<pi>>
   *def/e c1 = <cos(<5*<L>/<Lt>>)>
   *def/e c12 = <cos(<10*<L>/<Lt>>)>
   *def/e zv == < <z5> - <td>*<1-<c1>>/2 + <td>*<<r>-1/2>*<1-<c12>>/2 >
  *endif
  *if < <x> /ge <<Lx1>+9*<Lt>/10 > /then
   *def/e zv == <<z5>-<td>>
  *endif
*end
.
*Procedure zdrop6
   *def/e zv == <z6>
  *if < <x> /gt <Lhi> > /then
   *def/e L = <<<x>-<Lhi>>*<pi>>
   *def/e L = <cos(<5*<L>/<Lt>>)>
   *def/e zv == < <z6>-<td>*<1-<L>>/2 >
  *endif
  *if < <x> /ge <<Lx1>+9*<Lt>/10 > /then
   *def/e zv == <<z6>-<td>>
  *endif
*end
. ....................................................................
*Procedure nodloc
*if < <initial> > /then

       *if < 1-<all_shell> > /then
*rem NODES:
*rem        <nn>  Shell nodes
*rem        <<jnt>-<nn>>  Solid Element Nodes
*rem DEGREES OF FREEDOM
*rem        <nn> X 5 + <<jnt>-<nn>> *3 - BC = <2*<nn>+3*<jnt>> - BC
*rem ELEMENTS
*rem        <<ny>*<<nx1>+<nx2>>>  Shells
*rem        <5*<ny>>  Transition Elements
*rem        <<18*<ndiv>-5>*<ny>>  Solid Elements
      *endif

[xqt TAB
 START <jnt>
 jloc
*remark   First and Second Rows
    1      0.    0.    0.      <<Lb>/2>   0.    0.       2          1   2
  <nnx1>   0.  <<Lby>/2>  0.      <<Lb>/2.>  <<Lby>/2>  0.
 <1+2*<nnx1>>  0. <Lby> 0.   <<Lb>/2> <Lby> 0.  2  1 <2*<ny>-1>
  <nnx1>       0. <Ly>  0.   <<Lb>/2> <Ly>  0.
*remark   First Plate
    3     <Lb>  0.    0.       <Lx1>  0.    0.     <<nnx1>-2>     1   2
  <nnx1>  <Lb> <<Lby>/2>  0.        <Lx1> <<Lby>/2>  0.
 <3+2*<nnx1>> <Lb>  <Lby> 0.   <Lx1> <Lby> 0.    <<nnx1>-2>      1  <2*<ny>-1>
  <nnx1>      <Lb>  <Ly>  0.   <Lx1> <Ly>  0.
*remark   Second Plate
<<nnod1>+1> <<Lx>-<Lx2>>  0.   0. <<Lx>-<Lb>>  0.    0.    <<nnx2>-2> 1 2
  <nnx2>    <<Lx>-<Lx2>> <<Lby>/2> 0. <<Lx>-<Lb>> <<Lby>/2>  0.
<<nnod1>+1+2*<nnx2>> <<Lx>-<Lx2>> <Lby> 0. <<Lx>-<Lb>> <Lby> 0. --
       <<nnx2>-2> 1 <2*<ny>-1>
  <nnx2>    <<Lx>-<Lx2>> <Ly> 0. <<Lx>-<Lb>> <Ly>  0.
*remark   Last Two Rows
<<nnod1>+<nnx2>-1> <<Lx>-<Lb>/2>  0.  0.  <Lx>  0.    0.    2    1    2
  <nnx2>             <<Lx>-<Lb>/2> <<Lby>/2> 0.   <Lx> <<Lby>/2>  0.
<<nnod1>+3*<nnx2>-1> <<Lx>-<Lb>/2> <Lby> 0. <Lx> <Lby> 0. 2 1 <2*<ny>-1>
  <nnx2>             <<Lx>-<Lb>/2> <Ly> 0.   <Lx> <Ly>  0.
*if < <all_shell> > /then
*remark   Transition with SHELLS
<<nn>+1> <<Lx1>+7*<Lt>/20>  0. 0.   <<Lx1>+7*<Lt>/10>  0.   0.   2  1  2
   3     <<Lx1>+7*<Lt>/20> <<Lby>/2> 0. <<Lx1>+7*<Lt>/10> <<Lby>/2> 0.
<<nn>+7> <<Lx1>+7*<Lt>/20>   <Lby> 0. <<Lx1>+7*<Lt>/10> <Lby> 0. 2 1 <2*<ny>
   3     <<Lx1>+7*<Lt>/20> <Ly> 0. <<Lx1>+7*<Lt>/10> <Ly> 0.
<<nn>+3> <<Lx1>+17*<Lt>/20>  0. 0.   <<Lx1>+17*<Lt>/20>  <<Lby>/2>  0.  2 3
<<nn>+9> <<Lx1>+17*<Lt>/20> <Lby> 0.   <<Lx1>+17*<Lt>/20>  <Ly>  0. <2*<ny>-
*else
*remark   Transition with Solid Elements and Transition Elements
*remark     bottom   z0
 *Do :ALoop0 $i=1,<<ndt>-1>,1
  *def/i ic = <$i>
  *Call xlocA
  <<nn>+<ic>>       <x> 0. <z0>
  <<nn>+<ic>+<nxt>> <x> <Lby> <z0>  <x> <Ly> <z0> <ny> <nxt>
 :ALoop0
```

```
 *Do :BLoop0 $i=1,<<nd>-1>,1
  *def/i ic = <$i>
  *Call xlocB
  <<nn>+<ndt>-1+<ic>>       <x> <<Lby>/2> <z0>
  <<nn>+<ndt>-1+<ic>+<nxt>> <x> <Lty1> <z0>  <x> <Lty2> <z0> <<ny>-1> <nxt>
 :BLoop0
*remark     z1 Level
*def/i nnt = <<nn>+<nn0>>
 *Do :ALoop1 $i=1,<<nd>-1>,1
  *def/i ic = <$i>
  *Call xlocB
  <<nnt>+<ic>>        <x> 0. <z1>
  <<nnt>+<ic>+<nd>-1> <x> <Lby> <z1>  <x> <Ly> <z1> <ny> <<nd>-1>
 :ALoop1
*remark     z2 Level
*def/i nnt = <<nnt>+<nn1>>
 *Do :ALoop2 $i=1,<<ndt>-1>,1
  *def/i ic = <$i>
  *Call xlocA
  *Call zdrop2
  <<nnt>+<ic>>       <x> 0. <zv>
  <<nnt>+<ic>+<nxt>> <x> <Lby> <zv>  <x> <Ly> <zv> <ny> <nxt>
 :ALoop2
 *Do :BLoop2 $i=1,<<nd>-1>,1
  *def/i ic = <$i>
  *Call xlocB
  *Call zdrop2
  <<nnt>+<ndt>-1+<ic>>       <x> <<Lby>/2> <zv>
  <<nnt>+<ndt>-1+<ic>+<nxt>> <x> <Lty1> <zv>  <x> <Lty2> <zv> <<ny>-1> <nxt
 :BLoop2
*remark     z3 Level
*def/i nnt = <<nnt>+<nn2>>
 *Do :ALoop3 $i=1,<<ndz>+<ndiv>-1>,1
  *def/i ic = <$i>
  *Call xlocB
    *def/e zv3 = <z3>
   *if < <x> /gt <Lhi> > /then
    *call zdrop2
    *def/e zv2 = <zv>
    *call zdrop4
    *def/e zv3 = <<<zv2>+<zv>>/2>
   *endif
  <<nnt>+<ic>>        <x> 0. <zv3>
<<nnt>+<ic>+<ndz>+<ndiv>-1> <x> <Lby> <zv3> <x> <Ly> <zv3> <ny> <<ndz>+<ndi
 :ALoop3
*remark     z4 Level
 *def/i nnt = <<nnt>+<nn3>>
 *Do :ALoop4 $i=1,<10*<ndiv>-1>,1
  *def/i ic = <$i>
  *Call xlocA
  *Call zdrop4
  <<nnt>+<ic>> <x> 0. <zv>
  <<nnt>+<ic>+15*<ndiv>-2> <x> <Lby> <zv>  <x> <Ly> <zv> <ny> <15*<ndiv>-2>
 :ALoop4
 *Do :BLoop4 $i=1,<5*<ndiv>-1>,1
  *def/i ic = <$i>
  *Call xlocB
  *Call zdrop4
 <<nnt>+10*<ndiv>-1+<ic>> <x> <<Lby>/2> <zv>
 <<nnt>+25*<ndiv>-3+<ic>> <x> <Lty1> <zv> <x> <Lty2> <zv> <<ny>-1> <15*<ndi
 :BLoop4
*remark     z5 Level
 *def/i nnt = <<nnt>+<nn4>>
 *Do :ALoop5 $i=1,<<nd>-1>,1
  *def/i ic = <$i>
  *Call xlocB
  *Call zdrop5
  <<nnt>+<ic>>        <x> 0. <zv>
  <<nnt>+<ic>+<nd>-1> <x> <Lby> <zv>  <x> <Ly> <zv> <ny> <<nd>-1>
 :ALoop5
*remark     z6 Level
 *def/i nnt = <<nnt>+<nn5>>
 *Do :ALoop6 $i=1,<<ndt>-1>,1
  *def/i ic = <$i>
  *Call xlocA
  *Call zdrop6
  <<nnt>+<ic>>       <x> 0. <zv>
  <<nnt>+<ic>+<nxt>> <x> <Lby> <zv>  <x> <Ly> <zv> <ny> <nxt>
 :ALoop6
 *Do :BLoop6 $i=1,<<nd>-1>,1
```

```
  *def/i ic = <$i>
  *Call xlocB
  *Call zdrop6
  <<nnt>+<ndt>-1+<ic>>       <x> <<Lby>/2> <zv>
  <<nnt>+<ndt>-1+<ic>+<nxt>> <x> <Lty1> <zv>  <x> <Lty2> <zv> <<ny>-1> <nxt
 :BLoop6
*endif
*rem exiting nodloc
*call constraints
*call eldef
*endif . initial
*end

. ************************************************************************

*Procedure eldef
.
*if < 1-<all_shell> > /then
*rem First, the transition elements
.
*def/d es_pars[1:2] = 3,3
*call ES ( function = 'DEFINE ELEMENTS' ; es_proc = <es_procTR> ;--
           es_name = <es_nameTR>; es_count=<1-<all_shell>> ;--
           es_pars = <es_pars[1:2]> )
[xqt AUS
.
. build table of 3-D material data
.
table (ni=13,nj=2) : O3D DATA 1 1
. i=1,2,3,4,5,6,7,8,9
.       E11       E22       E33       G12       G23       G13     mu12 mu23 mu13
. j=1: 10.0e+6 10.0e+6 10.0e+6 3.85e+6 3.85e+6 3.85e+6  .3   .3  .3  .1 >
  j=1: 18.5e+6 1.64e+6 1.64e+6 0.87e+6 0.49e+6 0.87e+6  .3   .35 .3  .1 >
 1.E-4     1.E-4    1.E-4
  j=2: 0.5e+6 0.5e+6 0.5e+6 0.195e+6 0.195e+6 0.195e+6  .41  .41 .41 .1 >
 1.E-4     1.E-4    1.E-4
table (ni=3,nj=8,itype=0) : LAM O3D 1 1    . 8 layers of QI Sublaminates
  j=1: 1 <plyt>  45.
  j=2: 1 <plyt> -45.
  j=3: 1 <plyt>  0.0
  j=4: 1 <plyt> 90.0
  j=5: 1 <plyt> 90.0
  j=6: 1 <plyt>  0.0
  j=7: 1 <plyt> -45.
  j=8: 1 <plyt>  45.
table (ni=3,nj=2,itype=0) : LAM O3D 2 1    . Dropped plies
  j=1: 1 <plyt>  0.0
  j=2: 1 <plyt>  0.0
table (ni=3,nj=1,itype=0) : LAM O3D 3 1    . Resin
  j=1: 2 <plyt>  0.0
[xqt LAU
  reset et2d=0, et3d=1
  Online=1
[xqt ELD
    <es_expe_cmd>
     *def/i iu0 = 0
     *def/i iu1 = 0
     *def/i iu2 = 0
     *def/i iu3 = 0
     *def/i iu4 = 0
     *def/i iu5 = 0
     *def/i iu6 = 0
     *def/i lu = 0
     *def/i lur = 0
  *Do :TR2 $i = 1,<ny>,1
*rem Lower level of left transition elements  (A)
     nsect=1
     *def/i n1 = <<nn>+3*<nd>+<iu0>>
     *def/i n2 = <<nn>+3*<nd>-1+<iu0>>
     *def/i n3 = <<nn>+1+<iu0>>
     *def/i n4 = <<nn>+2+<iu0>>
     *def/i n5 = <<nn02>+3*<nd>+<iu2>>
     *def/i n6 = <<nn02>+3*<nd>-1+<iu2>>
     *def/i n7 = <<nn02>+1+<iu2>>
     *def/i n8 = <<nn02>+2+<iu2>>
     *def/i n9 = <<nn>+2*<nd>+<iu0>>
     *def/i n10 = <<nn01>+<nd>+<iu1>>
     *def/i n11 = <<nn01>+1+<iu1>>
     *def/i n12 = <<nn02>+2*<nd>+<iu2>>
     *def/i n13 = <3*<nnx1>+<lu>>
```

```
      *def/i n14 = <<nnx1>+<lu>>
      *def/i n15 = <2*<nnx1>+<lu>>
<n1> <n2> <n3> <n4> <n5> <n6> <n7> <n8> <n9> <n10> <n11> <n12> <n13> <n14>
*rem Bottom right level of transition  (B)
      nsect=1
      *def/i n1 = <<nn>+2*<nd>-2+<iu0>>
      *def/i n2 = <<nn>+2*<nd>-1+<iu0>>
      *def/i n3 = <<nn>+5*<nd>-3+<iu0>>
      *def/i n4 = <<nn>+5*<nd>-4+<iu0>>
      *def/i n5 = <<nn02>+2*<nd>-2+<iu2>>
      *def/i n6 = <<nn02>+2*<nd>-1+<iu2>>
      *def/i n7 = <<nn02>+5*<nd>-3+<iu2>>
      *def/i n8 = <<nn02>+5*<nd>-4+<iu2>>
      *def/i n9 = <<nn>+3*<nd>-2+<iu0>>
      *def/i n10 = <<nn01>+<nd>-1+<iu1>>
      *def/i n11 = <<nn01>+2*<nd>-2+<iu1>>
      *def/i n12 = <<nn02>+3*<nd>-2+<iu2>>
      *def/i n13 = <<nnod1>+1+<lur>>
      *def/i n14 = <<nnod1>+2*<nnx2>+1+<lur>>
      *def/i n15 = <<nnod1>+<nnx2>+1+<lur>>
<n1> <n2> <n3> <n4> <n5> <n6> <n7> <n8> <n9> <n10> <n11> <n12> <n13> <n14>
*rem Dropped ply transition (Left)  (C)
      nsect=2
      *def/i n1 = <<nn02>+3*<nd>+<iu2>>
      *def/i n2 = <<nn02>+3*<nd>-1+<iu2>>
      *def/i n3 = <<nn02>+1+<iu2>>
      *def/i n4 = <<nn02>+2+<iu2>>
      *def/i n5 = <<nn04>+15*<ndiv>+<iu4>>
      *def/i n6 = <<nn04>+15*<ndiv>-1+<iu4>>
      *def/i n7 = <<nn04>+1+<iu4>>
      *def/i n8 = <<nn04>+2+<iu4>>
      *def/i n9 = <<nn02>+2*<nd>+<iu2>>
      *def/i n10 = <<nn03>+<ndz>+<ndiv>+<iu3>>
      *def/i n11 = <<nn03>+1+<iu3>>
      *def/i n12 = <<nn04>+10*<ndiv>+<iu4>>
      *def/i n13 = <3*<nnx1>+<lu>>
      *def/i n14 = <<nnx1>+<lu>>
      *def/i n15 = <2*<nnx1>+<lu>>
<n1> <n2> <n3> <n4> <n5> <n6> <n7> <n8> <n9> <n10> <n11> <n12> <n13> <n14>
*rem Upper right level of transition  (D)
      nsect=1
      *def/i n1 = <<nn02>+2*<nd>-2+<iu2>>
      *def/i n2 = <<nn02>+2*<nd>-1+<iu2>>
      *def/i n3 = <<nn02>+5*<nd>-3+<iu2>>
      *def/i n4 = <<nn02>+5*<nd>-4+<iu2>>
      *def/i n5 = <<nn06>+2*<nd>-2+<iu6>>
      *def/i n6 = <<nn06>+2*<nd>-1+<iu6>>
      *def/i n7 = <<nn06>+5*<nd>-3+<iu6>>
      *def/i n8 = <<nn06>+5*<nd>-4+<iu6>>
      *def/i n9 = <<nn02>+3*<nd>-2+<iu2>>
      *def/i n10 = <<nn05>+<nd>-1+<iu5>>
      *def/i n11 = <<nn05>+2*<nd>-2+<iu5>>
      *def/i n12 = <<nn06>+3*<nd>-2+<iu6>>
      *def/i n13 = <<nnod1>+1+<lur>>
      *def/i n14 = <<nnod1>+2*<nnx2>+1+<lur>>
      *def/i n15 = <<nnod1>+<nnx2>+1+<lur>>
<n1> <n2> <n3> <n4> <n5> <n6> <n7> <n8> <n9> <n10> <n11> <n12> <n13> <n14>
*rem Upper level of left transition elements  (E)
      nsect=1
      *def/i n1 = <<nn04>+15*<ndiv>+<iu4>>
      *def/i n2 = <<nn04>+15*<ndiv>-1+<iu4>>
      *def/i n3 = <<nn04>+1+<iu4>>
      *def/i n4 = <<nn04>+2+<iu4>>
      *def/i n5 = <<nn06>+3*<nd>+<iu6>>
      *def/i n6 = <<nn06>+3*<nd>-1+<iu6>>
      *def/i n7 = <<nn06>+1+<iu6>>
      *def/i n8 = <<nn06>+2+<iu6>>
      *def/i n9 = <<nn04>+10*<ndiv>+<iu4>>
      *def/i n10 = <<nn05>+<nd>+<iu5>>
      *def/i n11 = <<nn05>+1+<iu5>>
      *def/i n12 = <<nn06>+2*<nd>+<iu6>>
      *def/i n13 = <3*<nnx1>+<lu>>
      *def/i n14 = <<nnx1>+<lu>>
      *def/i n15 = <2*<nnx1>+<lu>>
<n1> <n2> <n3> <n4> <n5> <n6> <n7> <n8> <n9> <n10> <n11> <n12> <n13> <n14>
      *def/i lu = <<lu>+2*<nnx1>>
      *def/i lur = <<lur>+2*<nnx2>>
      *def/i iu0 = <<iu0>+3*<nd>-2>
      *def/i iu1 = <<iu1>+<nd>-1>
      *def/i iu2 = <iu0>
```

```
      *def/i iu3 = <<iu3>+<ndz>+<ndiv>-1>
      *def/i iu4 = <<iu4>+15*<ndiv>-2>
      *def/i iu5 = <iu1>
      *def/i iu6 = <iu0>
  :TR2
  *rem Then, the Brick elements
*call ES ( function = 'DEFINE ELEMENTS' ; es_proc = <es_procBR> ;--
           es_name = <es_nameBR>; es_count=<1-<all_shell>> ;--
           es_pars = <es_pars[1:2]> )
[xqt ELD
    <es_expe_cmd>
*rem Lower sublaminate  (LA)
      *def/i n1 = <<nn>+2>
      *def/i n2 = <<nn>+4>
      *def/i n3 = <<nn>+3*<nd>+2>
      *def/i n4 = <<nn>+3*<nd>>
      *def/i n5 = <<nn02>+2>
      *def/i n6 = <<nn02>+4>
      *def/i n7 = <<nn02>+3*<nd>+2>
      *def/i n8 = <<nn02>+3*<nd>>
      *def/i n9 = <<nn>+3>
      *def/i n10 = <<nn>+2*<nd>+1>
      *def/i n11 = <<nn>+3*<nd>+1>
      *def/i n12 = <<nn>+2*<nd>>
      *def/i n13 = <<nn01>+1>
      *def/i n14 = <<nn01>+2>
      *def/i n15 = <<nn01>+<nd>+1>
      *def/i n16 = <<nn01>+<nd>>
      *def/i n17 = <<nn02>+3>
      *def/i n18 = <<nn02>+2*<nd>+1>
      *def/i n19 = <<nn02>+3*<nd>+1>
      *def/i n20 = <<nn02>+2*<nd>>
      nsect=1
      *Do :LAh $i=1,<<nd>-2>,1
      *def/i iv0 = 0
      *def/i iv1 = 0
      *def/i iv2 = 0
      *Do :LAv $j=1,<ny>,1
<<n1>+<iv0>> <<n2>+<iv0>> <<n3>+<iv0>> <<n4>+<iv0>> --
<<n5>+<iv2>> <<n6>+<iv2>> <<n7>+<iv2>> <<n8>+<iv2>> --
<<n9>+<iv0>> <<n10>+<iv0>> <<n11>+<iv0>> <<n12>+<iv0>> --
<<n13>+<iv1>> <<n14>+<iv1>> <<n15>+<iv1>> <<n16>+<iv1>> --
<<n17>+<iv2>> <<n18>+<iv2>> <<n19>+<iv2>> <<n20>+<iv2>>
      *def/i iv0 = <<iv0>+3*<nd>-2>
      *def/i iv1 = <<iv1>+<nd>-1>
      *def/i iv2 = <iv0>
 :LAv
 *def/i n1 = <<n1>+2>
 *def/i n2 = <<n2>+2>
 *def/i n3 = <<n3>+2>
 *def/i n4 = <<n4>+2>
 *def/i n5 = <<n5>+2>
 *def/i n6 = <<n6>+2>
 *def/i n7 = <<n7>+2>
 *def/i n8 = <<n8>+2>
 *def/i n9 = <<n9>+2>
 *def/i n10 = <<n10>+1>
 *def/i n11 = <<n11>+2>
 *def/i n12 = <<n12>+1>
 *def/i n13 = <<n13>+1>
 *def/i n14 = <<n14>+1>
 *def/i n15 = <<n15>+1>
 *def/i n16 = <<n16>+1>
 *def/i n17 = <<n17>+2>
 *def/i n18 = <<n18>+1>
 *def/i n19 = <<n19>+2>
 *def/i n20 = <<n20>+1>
 :LAh
*rem Dropped ply sublaminate  (LB)
      *def/i n1 = <<nn02>+2>
      *def/i n2 = <<nn02>+4>
      *def/i n3 = <<nn02>+3*<nd>+2>
      *def/i n4 = <<nn02>+3*<nd>>
      *def/i n5 = <<nn04>+2>
      *def/i n6 = <<nn04>+4>
      *def/i n7 = <<nn04>+15*<ndiv>+2>
      *def/i n8 = <<nn04>+15*<ndiv>>
      *def/i n9 = <<nn02>+3>
      *def/i n10 = <<nn02>+2*<nd>+1>
```

```
      *def/i n11 = <<nn02>+3*<nd>+1>
      *def/i n12 = <<nn02>+2*<nd>>
      *def/i n13 = <<nn03>+1>
      *def/i n14 = <<nn03>+2>
      *def/i n15 = <<nn03>+<ndz>+<ndiv>+1>
      *def/i n16 = <<nn03>+<ndz>+<ndiv>>
      *def/i n17 = <<nn04>+3>
      *def/i n18 = <<nn04>+10*<ndiv>+1>
      *def/i n19 = <<nn04>+15*<ndiv>+1>
      *def/i n20 = <<nn04>+10*<ndiv>>
      nsect=2    . Properties for the dropped plies
      *Do :LBh $i=1,<<ndz>+<ndiv>-2>,1
       *if <<$i> /gt <<ndz>-1> > /then
       *rem resin material loop
      nsect=3    . Properties for the resin material
       *endif
      *def/i iv2 = 0
      *def/i iv3 = 0
      *def/i iv4 = 0
      *Do :LBv $j=1,<ny>,1
<<n1>+<iv2>> <<n2>+<iv2>> <<n3>+<iv2>> <<n4>+<iv2>> --
<<n5>+<iv4>> <<n6>+<iv4>> <<n7>+<iv4>> <<n8>+<iv4>> --
<<n9>+<iv2>> <<n10>+<iv2>> <<n11>+<iv2>> <<n12>+<iv2>> --
<<n13>+<iv3>> <<n14>+<iv3>> <<n15>+<iv3>> <<n16>+<iv3>> --
<<n17>+<iv4>> <<n18>+<iv4>> <<n19>+<iv4>> <<n20>+<iv4>>
      *def/i iv2 = <<iv2>+3*<nd>-2>
      *def/i iv3 = <<iv3>+<ndz>+<ndiv>-1>
      *def/i iv4 = <<iv4>+15*<ndiv>-2>
 :LBv
 *def/i n1 = <<n1>+2>
 *def/i n2 = <<n2>+2>
 *def/i n3 = <<n3>+2>
 *def/i n4 = <<n4>+2>
 *def/i n5 = <<n5>+2>
 *def/i n6 = <<n6>+2>
 *def/i n7 = <<n7>+2>
 *def/i n8 = <<n8>+2>
 *def/i n9 = <<n9>+2>
 *def/i n10 = <<n10>+1>
 *def/i n11 = <<n11>+2>
 *def/i n12 = <<n12>+1>
 *def/i n13 = <<n13>+1>
 *def/i n14 = <<n14>+1>
 *def/i n15 = <<n15>+1>
 *def/i n16 = <<n16>+1>
 *def/i n17 = <<n17>+2>
 *def/i n18 = <<n18>+1>
 *def/i n19 = <<n19>+2>
 *def/i n20 = <<n20>+1>
 :LBh
*rem Top Left sublaminate  (LC)
      *def/i n1 = <<nn04>+2>
      *def/i n2 = <<nn04>+4>
      *def/i n3 = <<nn04>+15*<ndiv>+2>
      *def/i n4 = <<nn04>+15*<ndiv>>
      *def/i n5 = <<nn06>+2>
      *def/i n6 = <<nn06>+4>
      *def/i n7 = <<nn06>+3*<nd>+2>
      *def/i n8 = <<nn06>+3*<nd>>
      *def/i n9 = <<nn04>+3>
      *def/i n10 = <<nn04>+10*<ndiv>+1>
      *def/i n11 = <<nn04>+15*<ndiv>+1>
      *def/i n12 = <<nn04>+10*<ndiv>>
      *def/i n13 = <<nn05>+1>
      *def/i n14 = <<nn05>+2>
      *def/i n15 = <<nn05>+<nd>+1>
      *def/i n16 = <<nn05>+<nd>>
      *def/i n17 = <<nn06>+3>
      *def/i n18 = <<nn06>+2*<nd>+1>
      *def/i n19 = <<nn06>+3*<nd>+1>
      *def/i n20 = <<nn06>+2*<nd>>
      nsect=1
      *Do :LCh $i=2,<5*<ndiv>-1>,1
      *def/i iv4 = 0
      *def/i iv5 = 0
      *def/i iv6 = 0
      *Do :LCv $j=1,<ny>,1
<<n1>+<iv4>> <<n2>+<iv4>> <<n3>+<iv4>> <<n4>+<iv4>> --
<<n5>+<iv6>> <<n6>+<iv6>> <<n7>+<iv6>> <<n8>+<iv6>> --
<<n9>+<iv4>> <<n10>+<iv4>> <<n11>+<iv4>> <<n12>+<iv4>> --
```

```
<<n13>+<iv5>> <<n14>+<iv5>> <<n15>+<iv5>> <<n16>+<iv5>> --
<<n17>+<iv6>> <<n18>+<iv6>> <<n19>+<iv6>> <<n20>+<iv6>>
     *def/i iv4 = <<iv4>+15*<ndiv>-2>
     *def/i iv5 = <<iv5>+<nd>-1>
     *def/i iv6 = <<iv6>+3*<nd>-2>
 :LCv
 *def/i n1 = <<n1>+2>
 *def/i n2 = <<n2>+2>
 *def/i n3 = <<n3>+2>
 *def/i n4 = <<n4>+2>
 *def/i n5 = <<n5>+2>
 *def/i n6 = <<n6>+2>
 *def/i n7 = <<n7>+2>
 *def/i n8 = <<n8>+2>
 *def/i n9 = <<n9>+2>
 *def/i n10 = <<n10>+1>
 *def/i n11 = <<n11>+2>
 *def/i n12 = <<n12>+1>
 *def/i n13 = <<n13>+1>
 *def/i n14 = <<n14>+1>
 *def/i n15 = <<n15>+1>
 *def/i n16 = <<n16>+1>
 *def/i n17 = <<n17>+2>
 *def/i n18 = <<n18>+1>
 *def/i n19 = <<n19>+2>
 *def/i n20 = <<n20>+1>
 :LCh
 *rem Last row in top before thin laminate  (LD)
     *def/i iv2 = 0
     *def/i iv4 = 0
     *def/i iv5 = 0
     *def/i iv6 = 0
     *def/i n2 = <<nn02>+10*<ndiv>>
     *def/i n3 = <<nn02>+31*<ndiv>-2>
     *def/i n10 = <<nn02>+19*<ndiv>-1>
     *Do :LDv $j=1,<ny>,1
<<n1>+<iv4>> <<n2>+<iv2>> <<n3>+<iv2>> <<n4>+<iv4>> --
<<n5>+<iv6>> <<n6>+<iv6>> <<n7>+<iv6>> <<n8>+<iv6>> --
<<n9>+<iv4>> <<n10>+<iv2>> <<n11>+<iv4>> <<n12>+<iv4>> --
<<n13>+<iv5>> <<n14>+<iv5>> <<n15>+<iv5>> <<n16>+<iv5>> --
<<n17>+<iv6>> <<n18>+<iv6>> <<n19>+<iv6>> <<n20>+<iv6>>
     *def/i iv2 = <<iv2>+3*<nd>-2>
     *def/i iv4 = <<iv4>+15*<ndiv>-2>
     *def/i iv5 = <<iv5>+<nd>-1>
     *def/i iv6 = <<iv6>+3*<nd>-2>
 :LDv
*rem Top Right sublaminate  (LE)
     *def/i n1 = <n2>
     *def/i n2 = <<n1>+2>
     *def/i n3 = <<n1>+3*<nd>>
     *def/i n4 = <<n1>+3*<nd>-2>
 *def/i n5 = <<n5>+2>
 *def/i n6 = <<n6>+2>
 *def/i n7 = <<n7>+2>
 *def/i n8 = <<n8>+2>
     *def/i n9 = <<n1>+1>
     *def/i n12 = <n10>
     *def/i n10 = <<n12>+1>
     *def/i n11 = <<n4>+1>
 *def/i n13 = <<n13>+1>
 *def/i n14 = <<n14>+1>
 *def/i n15 = <<n15>+1>
 *def/i n16 = <<n16>+1>
 *def/i n17 = <<n17>+2>
 *def/i n18 = <<n18>+1>
 *def/i n19 = <<n19>+2>
 *def/i n20 = <<n20>+1>
     nsect=1
     *Do :LEh $i=<5*<ndiv>+1>,<<nd>-1>,1
     *def/i iv2 = 0
     *def/i iv5 = 0
     *def/i iv6 = 0
     *Do :LEv $j=1,<ny>,1
<<n1>+<iv2>> <<n2>+<iv2>> <<n3>+<iv2>> <<n4>+<iv2>> --
<<n5>+<iv6>> <<n6>+<iv6>> <<n7>+<iv6>> <<n8>+<iv6>> --
<<n9>+<iv2>> <<n10>+<iv2>> <<n11>+<iv2>> <<n12>+<iv2>> --
<<n13>+<iv5>> <<n14>+<iv5>> <<n15>+<iv5>> <<n16>+<iv5>> --
<<n17>+<iv6>> <<n18>+<iv6>> <<n19>+<iv6>> <<n20>+<iv6>>
     *def/i iv2 = <<iv2>+3*<nd>-2>
     *def/i iv5 = <<iv5>+<nd>-1>
```

```
     *def/i iv6 = <<iv6>+3*<nd>-2>
 :LEv
 *def/i n1 = <<n1>+2>
 *def/i n2 = <<n2>+2>
 *def/i n3 = <<n3>+2>
 *def/i n4 = <<n4>+2>
 *def/i n5 = <<n5>+2>
 *def/i n6 = <<n6>+2>
 *def/i n7 = <<n7>+2>
 *def/i n8 = <<n8>+2>
 *def/i n9 = <<n9>+2>
 *def/i n10 = <<n10>+1>
 *def/i n11 = <<n11>+2>
 *def/i n12 = <<n12>+1>
 *def/i n13 = <<n13>+1>
 *def/i n14 = <<n14>+1>
 *def/i n15 = <<n15>+1>
 *def/i n16 = <<n16>+1>
 *def/i n17 = <<n17>+2>
 *def/i n18 = <<n18>+1>
 *def/i n19 = <<n19>+2>
 *def/i n20 = <<n20>+1>
 :LEh
*endif  . <1-all_shell>
*rem Second, the PLATE elements
*call ES ( function = 'DEFINE ELEMENTS' ; es_proc = <es_procPL> ;--
   es_name = <es_namePL> ; es_count=<1-<all_shell>> )
[xqt AUS
.
. build table of 2-D material data
.
table (ni=16,nj=2) : OMB DATA 1 1
i = 1,2,3,4,5,6
j=1:   18.5e+6   .3   1.64e+6   0.87e+6   0.87e+6   0.49e+6
j=2:   18.5      .3   1.64      0.87      0.87      0.49
table (ni=3,nj=18,itype=0) : LAM OMB 1 1   . Thick Laminate
j=1:  1 <plyt1>   45.0
j=2:  1 <plyt1>  -45.0
j=3:  1 <plyt1>    0.0
j=4:  1 <plyt1>   90.0
j=5:  1 <plyt1>   90.0
j=6:  1 <plyt1>    0.0
j=7:  1 <plyt1>  -45.0
j=8:  1 <plyt1>   45.0
j=9:  1 <plyt1>       0.0
j=10:  1 <plyt1>      0.0
j=11:  1 <plyt1>  45.0
j=12:  1 <plyt1> -45.0
j=13:  1 <plyt1>   0.0
j=14:  1 <plyt1>  90.0
j=15:  1 <plyt1>  90.0
j=16:  1 <plyt1>   0.0
j=17:  1 <plyt1> -45.0
j=18:  1 <plyt1>  45.0
table (ni=3,nj=16,itype=0) : LAM OMB 2 1    . Thin Laminate (16-ply)
j=1:  1 <plyt2>  45.
j=2:  1 <plyt2> -45.
j=3:  1 <plyt2>  0.0
j=4:  1 <plyt2> 90.0
j=5:  1 <plyt2> 90.0
j=6:  1 <plyt2>  0.0
j=7:  1 <plyt2> -45.
j=8:  1 <plyt2>  45.
j=9:  1 <plyt2>  45.
j=10:  1 <plyt2> -45.
j=11:  1 <plyt2>  0.0
j=12:  1 <plyt2> 90.0
j=13:  1 <plyt2> 90.0
j=14:  1 <plyt2>  0.0
j=15:  1 <plyt2> -45.
j=16:  1 <plyt2>  45.
. Wall eccentricity
 table (ni=5,nj=2) : wall prop 1 1
i=1
.  j=1:  0.01072      . thick laminate offset
j=1:  <<plyt1>*<nplyd>/2> . thick laminate offset
*rem j=1:  <<plyt1>*<nplyd>/2>  thick laminate offset
[xqt LAU
reset et2d=1, et3d=0
Online=1
```

```
[xqt ELD
<es_expe_cmd>
nsect=1
*rem Left Plate
1 3 <2*<nnx1>+3> <2*<nnx1>+1> 2 <<nnx1>+3> <2*<nnx1>+2> <<nnx1>+1> --
<<nnx1>+2> 1 <nx1> <ny>
*rem Right Plate
      nsect=2
<<nnod1>+1> <<nnod1>+3> <2*<nnx2>+<nnod1>+3> <2*<nnx2>+<nnod1>+1> --
<<nnod1>+2> <<nnx2>+<nnod1>+3> <<nnod1>+2*<nnx2>+2> <<nnod1>+<nnx2>+1> --
<<nnod1>+<nnx1>+2> 1 <nx2> <ny>
.
    *if < <all_shell> > /then
.
 *def/i nu = 0
 *def/i nur = 0
 *def/i lu = 0
.
 *Do :TRLoop $i = 1,<ny>,1
.
*rem Left transition plate
     nsect=1
    *def/i n1 = <<nnx1>+<nu>>
    *def/i n2 = <<nn>+2+<lu>>
    *def/i n3 = <<nn>+8+<lu>>
    *def/i n4 = <3*<nnx1>+<nu>>
    *def/i n5 = <<nn>+1+<lu>>
    *def/i n6 = <<nn>+5+<lu>>
    *def/i n7 = <<nn>+7+<lu>>
    *def/i n8 = <2*<nnx1>+<nu>>
    *def/i n9 = <<nn>+4+<lu>>
 <n1> <n2> <n3> <n4> <n5> <n6> <n7> <n8> <n9>
*rem Right transition plate
     nsect=2
    *def/i n1 = <<nn>+2+<lu>>
    *def/i n2 = <<nnod1>+1+<nur>>
    *def/i n3 = <<nnod1>+2*<nnx2>+1+<nur>>
    *def/i n4 = <<nn>+8+<lu>>
    *def/i n5 = <<nn>+3+<lu>>
    *def/i n6 = <<nnod1>+<nnx2>+1+<nur>>
    *def/i n7 = <<nn>+9+<lu>>
    *def/i n8 = <<nn>+5+<lu>>
    *def/i n9 = <<nn>+6+<lu>>
    <n1> <n2> <n3> <n4> <n5> <n6> <n7> <n8> <n9>
 *def/i lu = <<lu>+6>
 *def/i nu = <<nu>+2*<nnx1>>
 *def/i nur = <<nur>+2*<nnx2>>
:TRLoop
*endif
*end
```

```
*************************************************************************
*                                                                       *
*                            OUTPUT FILE                                *
*                                                                       *
*************************************************************************
```

N L _ S T A T I C _ 1

CSM Testbed Procedure for Nonlinear Statics:

- o Corotational Newton/Raphson algorithm
- o Linearized Crisfield/Riks arc-length control
- o Applied forces and/or displacements

```
NO. OF    9-NODE ELEMENTS=     24
NO. OF   15-NODE ELEMENTS=     15
NO. OF   20-NODE ELEMENTS=     39
```

BEGINNING STEP 1

```
** BEGIN K     **    DATA SPACE=  2000000 WORDS
```

```
Determinant of K = 0.1732E+01 * 10 ** 0.7420D+04

 ITER=1  LD=0.1000E+01  ERR=0.9999D+00  REF=0.1677D+01
           delta_d_max=4.000000000000001E-03  node=1    dof=1
           resid_f_max=-124.933339124389  node=28 dof=1
           ERR_RF=0.1000D+01          ERR_DI=0.1000D+01

            Forming TANGENT Stiffness Matrix
** BEGIN INV  **   DATA SPACE=  2000000 WORDS

 ITER=2  LD=0.9998E+00  ERR=0.1204D-04  REF=0.1677D+01
           delta_d_max=5.372954373229622E-05  node=118   dof=5
           resid_f_max=-124.907894723274  node=28 dof=1
           ERR_RF=0.1000D+01          ERR_DI=0.4684D-02

         CONVERGENCE AT STEP 1.

STEP 1 SUMMARY :

Load Factor ____________________ 0.999807559597927
Load Direction _________________ 1
Stiffness determinant __________ 0.2796E+10 * 10 ** 0.7410D+04
Number of negative roots _______ 0
Path_length_increment __________ 4.923758107387853E-02
Relative energy_error __________ 0.1204D-04
Number of Iterations ___________ 2
Number of Step Cuts ____________ 0
Total Number of Iterations _____ 2
Total Number of Factorizations_____ 2

Displacements of shell nodes along Centerline
          U            W
    55  0.400E-02   0.000E+00
    56  0.394E-02   0.000E+00
    57  0.388E-02   0.000E+00
    58  0.363E-02   0.174E-04
    59  0.337E-02   0.550E-04
    60  0.311E-02   0.111E-03
    61  0.285E-02   0.181E-03
    62  0.259E-02   0.251E-03
    63  0.233E-02   0.124E-03
   118  0.217E-02  -0.164E-03
   119  0.183E-02  -0.367E-03
   120  0.150E-02  -0.264E-03
   121  0.116E-02  -0.158E-03
   122  0.816E-03  -0.778E-04
   123  0.474E-03  -0.243E-04
   124  0.148E-03   0.000E+00
   125  0.729E-04   0.000E+00
   126  0.000E+00   0.000E+00
Reaction Forces at loaded end (thick end)
  Node      U            W
     1 -0.118E+02   0.403E-03
    10 -0.299E+02   0.424E-03
    19 -0.404E+02   0.347E-03
    28 -0.125E+03   0.907E-02
    37 -0.606E+02   0.850E-02
    46 -0.121E+03   0.216E-01
    55 -0.302E+02   0.581E-02
      425.6 real      224.0 user       53.9 sys
```

Vita

Carlos G. Dávila was born on April 5th, 1961 in Lima, Peru. He began his studies of engineering in Brussels, Belgium, but graduated at Virginia Tech in 1984 with a bachelor's degree, and in 1986 with a Master's degree in mechanical engineering. Since 1987 he has pursued a Ph.D. degree in aerospace engineering and this dissertation is the result of his research.